

FEDERAL UNIVERSITY OF ESPÍRITO SANTO

TECHNOLOGICAL CENTER

GRADUATE PROGRAM IN ELECTRICAL ENGINEERING

LETICIA MUNHOZ AVELLAR

DOCTORAL THESIS

**Photonic Textiles: Optical Fiber Integrated
Smart Textile for Healthcare Applications**

Vitória, ES, Brazil
2022



UFES

FEDERAL UNIVERSITY OF ESPÍRITO SANTO

DOCTORAL THESIS

Photonic Textiles: Optical Fiber Integrated Smart Textile for Healthcare Applications

Author:

Leticia Munhoz Avellar

Supervisors:

Prof. Dr. Arnaldo Leal-Junior

Prof. Dr. Anselmo Frizera

Dr. Eduardo Rocon de Lima

*A thesis submitted in fulfillment of the requirements
for the degree of Doctor in Electrical Engineering*

in the

Telecommunications Laboratory
Electrical Engineering Department

Vitória, ES, Brazil
2022



UFES

Ficha catalográfica disponibilizada pelo Sistema Integrado de Bibliotecas - SIBI/UFES e elaborada pelo autor

A949p Avellar, Letícia Munhoz de, 1995-
Photonic Textiles: Optical Fiber Integrated Smart Textile for
Healthcare Applications / Letícia Munhoz de Avellar. - 2022.
161 f. : il.

Orientador: Arnaldo Gomes Leal Júnior.

Coorientadores: Anselmo Frizera Neto, Eduardo Rocon de Lima.

Tese (Doutorado em Engenharia Elétrica) - Universidade Federal do Espírito Santo, Centro Tecnológico.

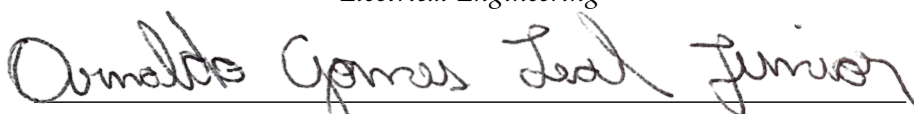
1. Biomedical Engineering. 2. Optical Fiber Sensors. 3. Movement Analysis. 4. Remote Healthcare Monitoring. I. Leal Júnior, Arnaldo Gomes. II. Frizera Neto, Anselmo. III. Lima, Eduardo Rocon de. IV. Universidade Federal do Espírito Santo. Centro Tecnológico. V. Título.

CDU: 621.3

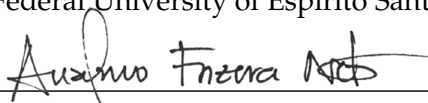
LETICIA MUNHOZ AVELLAR

Photonic Textiles: Optical Fiber Integrated Smart Textile for Healthcare Applications

Thisis presented to the Graduate Program in Electrical Engineering of the Federal University of Espírito Santo, as a partial requirement for the degree of Doctor in Electrical Engineering



Prof. Dr. Arnaldo Gomes Leal Júnior - Advisor
Graduate Program in Electrical Engineering
Federal University of Espírito Santo



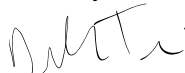
Prof. Dr. Anselmo Frizera Neto - Co-Advisor
Graduate Program in Electrical Engineering
Federal University of Espírito Santo



Dr. Eduardo Rocon de Lima - Co-Advisor
Centre for Automation and Robotics (CAR)
Spanish National Research Council (CSIC)




Dr. Carlos Alberto Ferreira Marques
I3N & Physics Department
University of Aveiro



Prof. Dr. Daniele Tosi
School of Engineering and Digital Sciences
Nazarbayev University



Prof. Dr. Santosh Kumar
School of Physics Science and Information Technology
Liaocheng University



Prof. Dr. Camilo Arturo Rodríguez Díaz
Graduate Program in Electrical Engineering
Federal University of Espirito Santo

Abstract

In recent years, technologies in the scope of Internet of Things (IoT) have been employed as strategical approaches for decentralized decision making through the connection of the digital and physical worlds. Smart Healthcare is an IoT application, which aims at the improvement of the everyday quality of life in the end-user community. Sensor devices are employed to collect medical data and vital signs from patients to monitor diagnose conditions, track progress and indicate anomalies. Moreover, the combination of IoT and Artificial Intelligence (AI) algorithms in the healthcare sector has a higher potential of making intelligent decisions in real-time for patient medical records.

The miniaturization and advancements of flexible sensors have boosted the development of wearable technologies to track health-related parameters or to extract practical features from multi-modal sensors on the wearable device. There are popular wearable devices in the market, such as inertial sensors embedded in elastic bands, smart watches and instrumented insoles, for movement and posture analysis, physiological parameters monitoring and pressure plantar detection. However, simultaneous monitoring of different health-related parameters requires the use of several individual devices, which lead to issues related to devices' connection and synchronization, in addition to discomfort related to long-term use of these wearable devices. Sensors integration with clothing, so-called smart textiles, are attractive solutions to overcome these drawbacks. The smart textiles present the advantages regarding to sensors compactness and higher transparency between the sensor and the user, which leads to the monitoring of the natural activity without inhibiting the user's movement. Furthermore, smart textiles are easily handled, with simple installation and removal, which represents an advantage in terms of usability.

Optical fiber sensors (OFS) have attractive features for smart textile technology, including compactness, lightweight and multiplexing capabilities. In addition, OFS are not susceptible to electrical discharges and they are immune to electromagnetic interference. The polymer optical fiber (POF) sensors have additional advantages since they present high flexibility and biocompatibility. This PhD Thesis presents a promising remote healthcare monitoring solution based on the combination of different optical fiber sensors approaches with AI algorithms and the integration of such systems in textiles and clothing accessories. Such approach leads to innovative optical fiber-based solutions capable of accurately identify activities, assess movement-related parameters, including physiological and gait parameters. The approaches proposed in this work includes the multiplexed intensity variation-based sensors, fiber Bragg gratings (FBGs) and transmission-reflection analysis (TRA) systems for distributed and quasi-distributed sensors systems. These approaches are applied in different protocols and applications, including balance assessment, movement analysis and classification. In addition, this PhD Thesis also presents the development of a Smart Environment based on Heterogeneous OFS Network for remote healthcare monitoring. This leads to the improvement of the communication between patients and clinicians leading to a high potential of making intelligent real-time decisions in a homecare assessment, which not only indicate an important improvement in Healthcare 4.0 systems, but also lead to the possibility of developing innovative multifunctional devices for healthcare applications.

Keywords: Photonic Textiles, Optical Fiber Sensors, Remote Healthcare Monitoring, Machine Learning

Resumo

Nos últimos anos, tecnologias no âmbito da Internet das Coisas (IoT) têm sido empregadas como abordagens estratégicas para a tomada de decisão descentralizada por meio da conexão dos mundos digital e físico. *Smart Healthcare* é uma das aplicações de IoT, que visa a melhoria da qualidade de vida cotidiana na comunidade dos usuários finais. Sensores são empregados para coletar dados médicos e sinais vitais de pacientes para monitorar condições de diagnóstico, acompanhar o progresso e indicar anomalias. Além disso, a combinação de IoT e Inteligência Artificial (AI) no setor de saúde aumenta o potencial na tomada de decisões inteligentes em tempo real para casos clínicos de pacientes.

A miniaturização e os avanços dos sensores flexíveis impulsionaram o desenvolvimento de tecnologias vestíveis para rastrear parâmetros relacionados à saúde ou extrair atributos dos sensores multimodais. Existem dispositivos vestíveis populares no mercado, como sensores inerciais, relógios inteligentes e palmilhas instrumentadas, para análise de movimento e postura, monitoramento de parâmetros fisiológicos e detecção de pressão plantar. No entanto, o monitoramento simultâneo de diferentes parâmetros relacionados à saúde exige o uso de vários dispositivos individuais, o que leva a problemas relacionados à conexão e sincronização dos dispositivos, além do desconforto relacionado ao uso prolongado desses dispositivos vestíveis. A integração de sensores com roupas (ou tecidos inteligentes) são soluções atraentes para solucionar essas desvantagens. Os tecidos inteligentes apresentam compacidade dos sensores e maior transparência entre o sensor e o usuário, o que leva ao monitoramento da atividade natural sem inibir o movimento do usuário. Além disso, os tecidos inteligentes são facilmente manuseados, com instalação simples, o que representa uma vantagem em termos de usabilidade.

Os sensores em fibra óptica (OFS) têm recursos atraentes para a tecnologia de tecidos inteligentes, incluindo compacidade, leveza e a capacidade de multiplexação. Além disso, os OFS não possuem descargas elétricas e são imunes a interferências eletromagnéticas. Os sensores em fibra óptica polimérica (POF) apresentam vantagens adicionais por apresentarem alta flexibilidade e biocompatibilidade. Esta Tese apresenta uma solução promissora de monitoramento remoto de saúde baseada na combinação de diferentes sensores em fibra óptica com algoritmos de AI e a integração de tais sistemas em tecidos e acessórios flexíveis. Essa abordagem leva a soluções inovadoras baseadas em fibra óptica capazes de identificar atividades com precisão, avaliar parâmetros relacionados ao movimento, incluindo parâmetros fisiológicos e de marcha. As abordagens propostas neste trabalho incluem os sensores multiplexados baseados em variação de intensidade, sensores em grades de Bragg (FBGs) e sistemas baseados na análise de transmissão-reflexão (TRA) para sistemas de sensores distribuídos e quase-distribuídos. Essas abordagens são aplicadas em diferentes protocolos e aplicações, incluindo avaliação do equilíbrio, análise e classificação do movimento. Além disso, esta Tese também apresenta o desenvolvimento de um Ambiente Inteligente baseado em Rede Heterogênea de OFS para monitoramento remoto de saúde. Isso leva à melhoria da comunicação entre pacientes e médicos levando a um alto potencial de tomada de decisões inteligentes em tempo real em uma avaliação de atendimento domiciliar, o que não apenas indica uma melhoria importante na tecnologia *Healthcare 4.0*, mas também leva ao desenvolvimento de soluções inovadoras multifuncionais para aplicações de saúde.

Palavras-chave: Tecidos Fotônicos, Sensores em Fibra Óptica, Monitoramento Remoto de Saúde, Inteligência Artificial, *Healthcare 4.0*.

Acknowledgements

First of all I would like to thank God. Without His support I wouldn't be here. I'm also grateful because in addition to His support he sent me angels that I can call family. Definitely the support of my family brought me here. I would like to thank my mother (Janice Munhoz), my father (Celino Avellar) and my brother (Leandro Munhoz de Avellar) for all the love during my entire life and for being patient with me in all my unbearable moments. I would also like to thank all my friends for all their support and understanding too. Special thanks to Giselle who never left me and always tries to cheer me up. Also, I would like to thank my friends and colleagues from LABTEL and LABSensores for friendship and support during this Thesis.

I want to express my special gratitude to my Co-Advisor Dr. Eduardo Rocon, who offered me one of the greatest opportunities of my career and life by inviting me to work in Spain. It was a peculiar and wonderful chapter of my life, in which I learned a lot about a lot of things. Thanks for the support and the talks during the pandemic. In addition, I would like to thank all Gnec's group. The 2020 year was tough, but things became easier with this group that I really miss.

I also would like to thank my co-advisor Prof. Dr. Anselmo Frizera Neto, who has supported me since my undergraduate degree, and for always trusting in me and my work. He introduced me to the research area, where I found my way, and always remembers me at every opportunity that comes along, I am really grateful for that. It's been 7 years of working together and I hope this partnership will last for many years to come.

Finally, I would like to thank my advisor Prof. Dr. Arnaldo Leal-Junior. He is crucial in my life. I met him when he was a student and he was once an inspiration to me. He has become one of the most important people in my life. I would like to thank him for helping me to be my best version (as a person and researcher). He is a phenomenon that I admire a lot and I hope to share more achievements like this with him.

This research is financed by FAPES (320/2020 and 84336650) and BenchBalance European Union (EU) Project (EU-H2020-779963-FSTP1-BenchBalance).

Contents

Abstract	ii
Resumo	iii
Acknowledgements	iv
1 Introduction	1
1.1 Motivation	1
1.2 Research Objectives	2
1.3 Justification	4
1.3.1 Optical Fiber Sensors	6
1.4 Contributions	6
1.4.1 Publications	7
1.4.2 Patents	9
1.5 Organization of the Thesis	9
2 Theoretical Background	11
2.1 Optical Fiber Overview	11
2.1.1 Numerical Aperture	13
2.1.2 Modes in Optical Fibers	13
2.1.3 Refractive Index Profiles	14
2.1.4 Optical Fiber Losses	15
2.1.5 Optical Fiber Materials	16
2.2 Sensing Techniques	18
2.2.1 Intensity Variation-based Sensors	18
2.2.2 Fiber Bragg Gratings Sensors	21
2.2.3 Transmission-Reflection Analysis for Distributed Sensors	22
2.3 Biomechanics of Human Movement	23
2.3.1 Human gait	23
2.3.2 Spatio-temporal Gait Parameters	24
2.3.3 Human Balance during Gait	24
2.4 Artificial Intelligence in Sensors Technology	27
2.4.1 Machine Learning	28
k-Nearest Neighbor (kNN) algorithm	28
2.4.2 Deep Learning	28
Feed-Forward Neural Network	30
2.4.3 Data Dimensionality Reduction	31
Principal Component Analysis (PCA)	32
3 Development and Performance Analysis of Optical Fiber Sensors for Kinetic and Kinematic Monitoring	33
3.1 Kinematic Parameters (Angle and Angular Velocity) Influence in OFS Responses	33

3.1.1	Materials and Methods	34
3.1.2	Experimental Procedures	34
3.1.3	Statistical analysis and angular velocity compensation	35
3.1.4	Results and Discussion	38
	Analysis of different light source central wavelengths	38
	Analysis of different angular velocities	40
3.2	Force assessment using Intensity Variation-based OFS	43
3.2.1	Materials and Methods	43
3.2.2	Experimental procedures	44
3.2.3	Results and Discussion	45
	Force characterization on different support materials	45
	Impact location detection protocol	47
3.3	Final Remarks	49
4	Optical Fiber Sensors Integration in Textiles and Flexible Structures	50
4.1	POF Smart Textile: Preliminary Study	50
4.1.1	Materials and Methods	50
4.1.2	Experimental procedures	51
4.1.3	Results and Discussion	51
4.2	Spatial Characterization of a Rubber Blanket-embedded FBG Matrix	55
4.2.1	Materials and Methods	56
4.2.2	Experimental procedures	56
4.2.3	Results and Discussion	58
4.3	TRA-based Sensor using Different DNP Fibers	61
4.3.1	Materials and Methods	61
4.3.2	Experimental procedures	62
4.3.3	Results and Discussion	63
4.4	TRA-based Distributed Sensor using a DNP-doped Fiber: Multiple Simultaneous Disturbances Analysis	68
4.4.1	Materials and Methods	68
4.4.2	Experimental procedures	68
4.4.3	Results and Discussion	70
4.5	Final Remarks	72
5	Optical Fiber Sensors in a Balance Assessment Protocol	73
5.1	Balance assessment protocol	73
5.2	Perturbator System based on POF-embedded Force Sensor	74
5.2.1	Materials and Methods	74
5.2.2	Experimental procedures	75
5.2.3	Results and Discussion	76
5.3	POF Smart Garment for Impact Identification	79
5.3.1	Development of the POF Smart Garment	79
	Sensors' design	79
	Data processing and analysis	80
5.3.2	Experimental procedures	82
5.3.3	Results and Discussion	84
	Sensors' characterization	84
	Experimental protocol validation	85
5.4	Final Remarks	90

6	Smart Textile for Remote Healthcare Monitoring	91
6.1	POF Smart Garment: Human Activity Classification	92
6.1.1	POF Smart Garment	92
6.1.2	Experimental procedures	92
	Human activity recognition protocol	92
	Data processing and Machine Learning training model	92
	Human movement-related parameters extraction	93
6.1.3	Results and Discussion	93
	Sensors' characterization	93
	Human activities classification	95
	Data dimensionality reduction	98
	Human movement-related parameters extraction	100
6.2	POF Smart Pants: Gait Analysis and Movement Recognition	103
6.2.1	Materials and Methods	103
6.2.2	Experimental procedures	103
6.2.3	Results and Discussion	105
6.3	POF Smart Carpet: Gait Analysis	110
6.3.1	Development of the POF Smart Carpet	110
6.3.2	Experimental procedures	112
6.3.3	Results and Discussion	113
	POF Smart Carpet Characterizations	113
	POF Smart Carpet Validation in Walking Test	116
6.4	Final Remarks	117
7	Heterogeneous OFS Network for Smart Environment	119
7.1	Smart Environment using a TRA-based Sensor	120
7.1.1	Experimental procedures	120
7.1.2	Results and Discussion	120
7.2	Instrumented Carpet based on FBG Matrix for Gait Analysis	124
7.2.1	Materials and Methods	124
7.2.2	Experimental procedures	124
7.2.3	Results and Discussion	125
7.3	Heterogeneous OFS Network based on FBG, Intensity Variation and TRA techniques	128
7.3.1	Materials and Methods	128
7.3.2	Experimental procedures	128
7.3.3	Results and Discussion	128
7.4	Final Remarks	129
8	Conclusions and Future Works	131
8.1	Summary and Final Remarks	131
8.2	Future Works	132
	Bibliography	135

List of Figures

1.1	Market overview of wearable devices in healthcare applications [17].	3
1.2	Schematic representation of the Thesis outline.	10
2.1	Optical Fiber overview.	12
2.2	Principle of the total internal reflection in the optical fiber.	12
2.3	Representation of the NA of silica and polymer fibers.	13
2.4	SI profile fiber.	14
2.5	GI profile fiber.	14
2.6	Optical fiber losses.	15
2.7	Schematic representation of the steps followed in the fiber fabrication.	17
2.8	Intensity variation technique approach: a straight fiber with an attenuation in the output, and a bending in the fiber with a high power variation in the output provoked by the physical variation.	19
2.9	Schematic representation of the sensitive zone.	19
2.10	Multiplexing technique for intensity variation-based sensors.	20
2.11	Working principle of an FBG.	21
2.12	The traditional nomenclature for describing events of the normal human gait.	24
2.13	Terms used to describe foot placement on the ground.	25
2.14	Margin of Dynamic Stability.	26
2.15	Artificial Intelligence overview: Machine Learning and Deep Learning.	27
2.16	Classification principle. (a) NN. (b) kNN.	29
2.17	FFNN architecture.	30
2.18	Pareto chart for the PCA technique.	32
3.1	Experimental setup for evaluating the curvature sensor based on CYTOP fiber.	34
3.2	State machine diagram of the angular velocity compensation.	36
3.3	(a) Flexion and extension applied on CYTOP fiber showing the sensitivity and hysteresis concept. (b) Exponential regression of one curvature test showing the determination coefficient R^2	37
3.4	Sensor's response in the curvature characterization with fitted curves: (a) Power variation of each central wavelength in angle range of 50 degrees. (b) Normal distribution of sensitivity for each central wavelength.	39
3.5	Raw measurements for each angular velocity.	40
3.6	Mean of the cycles at each angle presenting the mean hysteresis for each angular velocity.	42
3.7	Angle curves with and without angular velocity compensation compared with the reference of one test.	43
3.8	Experimental setup for evaluating the force sensor using CYTOP fiber.	44
3.9	Results of the CYTOP response under six different forces on the support I.	45

3.10	Results of the CYTOP response under six different forces on the support II.	46
3.11	Results of the vertical forces applied along the fiber (d=1,2,3,4 and 5cm to the sensor).	48
4.1	Smart Textile overview: picture and schematic representation of the proposed smart textile system.	51
4.2	Temperature analysis of the LPS-POF embedded textile. (a) Temperature characterizations. (b) Temperature responses of each sensor for different heat spots.	52
4.3	Force analysis of the LPS-POF embedded textile. (a) Transmitted optical power attenuation as function of time for forces applied at different sensors. (b) Force characterizations. (c) Force map from the sensors responses with a force applied on the textile.	54
4.4	Sensors responses with angular displacement on different planes.	55
4.5	FBGs spectra. Top spectra: fiber 1. Bottom spectra: fiber 2.	56
4.6	Experimental setup of the rubber blanket-embedded FBG matrix.	57
4.7	Feed-forward Neural Network model.	57
4.8	Force characterization of each FBG. (a) FBG 1. (b) FBG 2. (c) FBG 3. (d) FBG 4. (e) FBG 5. (f) FBG 6. (g) FBG 7. (h) FBG 8. (i) FBG 9. (j) FBG 10.	59
4.9	Metrics of the FFNN model with 40 epochs for the spatial characterization. (a) Loss. (b) Accuracy	60
4.10	Experimental procedure. (a) Setup using the transmission-reflection analysis for disturbance location characterization. (b) Disturbance location characterization inset.	62
4.11	Relationship between the normalized reflected and transmitted optical powers at different disturbance locations. (a) Fiber A. (b) Fiber B.	64
4.12	Results of disturbance location characterization using the Fiber C. (a) Relationship between the normalized reflected and transmitted optical powers at different disturbance locations. (b) Behavior of the normalized reflected optical power related to the disturbance location.	65
4.13	SR and SNR parameters during the disturbance location characterization using the Fiber C.	66
4.14	Results of Fiber D and Fiber E. (a) Relationship between the normalized reflected and transmitted optical powers at different disturbance locations for Fibers D (top panel) and E (bottom panel). (b) Normalized reflected power variation for Fibers D and E related to the disturbance location.	67
4.15	Experimental setup of the multiple simultaneous disturbances characterization.	68
4.16	Feed-forward neural network (FFNN) model.	70
4.17	Transmitted and reflected optical powers under three conditions. (a) Single point perturbation. (b) 2-points perturbation. (c) 3-points perturbation.	71
4.18	Metrics of the designed model for 40 epochs. (a) Loss. (b) Accuracy	71
4.19	Confusion matrices of each label for the single and multiple perturbation detection using FFNN model.	72
5.1	Balance assessment overview.	74

5.2	LPS-POF force sensor. (a) System description. (b) Characterization setup.	74
5.3	Viscoelastic transient pattern: creep and recovery.	75
5.4	Viscoelasticity compensation model to improve the sensor recovery response.	76
5.5	Perturbator system using the LPS-POF force sensor.	76
5.6	LPS-POF force sensor characterization.	77
5.7	Viscoelastic behavior of the POF force sensor.	77
5.8	Uncompensated and compensated responses of LPS-POF force sensor compared to reference system.	78
5.9	Results of the LPS-POF force sensor used as gait perturbation system without compensation.	78
5.10	Results of the perturbation test with uncompensated and compensated responses.	79
5.11	Smart Garment overview: Sensors arrangement in the Smart Garment.	80
5.12	Sensors fabrication process. (a) Removal of part of the fiber material creating a lateral section. (b) LED coupling to the fiber lateral section in a 3D printed part. (c) Sensor encapsulation using clear urethane rubber mixture. (d) Encapsulated sensor. (e) Sensor incorporated in the garment.	81
5.13	POF pressure sensors operating setup.	81
5.14	Proposed technique to identify impacts on the sensors by using outliers identification algorithm in the derivative of the sensors' optical power: example using the sensor 18.	82
5.15	Experimental setup. (a) Force characterization and sensitivity calculation based on the optical power variation and reference system. (b) Impact location identification with a sample of the sensors responses. (c) Perturbation protocol with the back, front, right and left perturbations in the volunteer. All sub-regions are also presented.	83
5.16	Force characterization of 10 sensors, where the right axis shows the force measured in the reference system and left axis shows the derivative normalized optical power for 10 sensors, which indicates the signal variation of the active sensors during the impacts.	84
5.17	Impacts on different body regions.	86
5.18	Results of the perturbation protocol to impacts on volunteer's back. (a) Smart Garment overview with description of the back sub-regions and the sensors related to these sub-regions. (b) Results of the activated sensors, the applied vertical forces (force z) for each sub-region and the volunteer' trunk angles (mediolateral, anteroposterior and longitudinal).	87
5.19	Results of the perturbation protocol to impacts on volunteer's front. (a) Smart Garment overview with description of the front sub-regions and the sensors related to these sub-regions. (b) Results of the activated sensors, the applied vertical forces (force z) for each sub-region and the volunteer' trunk angles (mediolateral, anteroposterior and longitudinal).	88

5.20	Results of the perturbation protocol to impacts on volunteer's right. (a) Smart Garment overview with description of the right sub-regions and the sensors related to these sub-regions. (b) Results of the activated sensors, the applied vertical forces (force z) for each sub-region and the volunteer' trunk angles (mediolateral, anteroposterior and longitudinal).	89
5.21	Results of the perturbation protocol to impacts on volunteer's left. (a) Smart Garment overview with description of the left sub-regions and the sensors related to these sub-regions. (b) Results of the activated sensors, the applied vertical forces (force z) for each sub-region and the volunteer' trunk angles (mediolateral, anteroposterior and longitudinal).	89
6.1	Chapter 6 overview: Smart Textiles applications.	91
6.2	POF Smart Garment overview and the sensor response when a force is applied on the top of the sensor 10.	94
6.3	Response of sensors 27-30 when a predefined loading is applied to each sensor.	95
6.4	Clustering of six classes (activities) using the response of 3 sensors.	96
6.5	Confusion matrix regarding 10 trials including the dataset of all volunteers in the kNN classification.	98
6.6	Sensors activation for each activity. (a) Optical power variation between the standing and sitting activities of sensors 1, 30, 21 and 10. (b) Response of sensors 26 and 21 during the squatting activity and response of sensors 5 and 26 during the up-and-down arms activity. (c) Sensors activation during the walking and running activities.	99
6.7	Results of walking and running tests of the volunteer 1 for cadence estimation: temporal response and FFT of the IMU data (yaw) and the response of sensor 8.	101
6.8	FFT of the IMU data (pitch) and the response of sensor 17 during standing activity of the volunteer 1 for breathing rate estimation.	101
6.9	Results of the up-and-down arms test of the volunteer 1: temporal response of sensors 5 (right arm) and 26 (left arm) and identification of the shoulder flexion and extension by outliers detection using the temporal response derivative.	103
6.10	Smart Pants overview. (a) Sensors system schematic. (b) Sensors system incorporated in the pants.	104
6.11	Curvature characterization setup.	104
6.12	Activities recognition protocol.	105
6.13	Metrics of the FFNN model with 40 epochs for activities classification. (a) Loss. (b) Accuracy	107
6.14	Pareto chart for the PCA technique.	108
6.15	Selected sensors by analyzing the principal components weights resulted from the PCA technique.	108
6.16	Metrics of the FFNN model with 30 epochs for activities classification after the sensors selection. (a) Loss. (b) Accuracy	109
6.17	Selected sensors during the gait performance: left and right legs.	110
6.18	POF Smart Carpet overview.	111
6.19	Characterizations protocols setup: (a) Force characterization. (b) Spatial characterization.	112

6.20	Sensor's response in the force characterization with fitted curves: (a) Right sensors 1 and 2 using photodetector P1. (b) Left sensors 1 and 3 using photodetector P2. (c) Right sensors 3-10 using photodetector P1. (d) Left sensors 2 and 4-10 using photodetector P2.	114
6.21	Sensitivity as a function of the sensor position: (a) Right sensors using photodetector P1. (b) Left sensors using photodetector P2.	114
6.22	Response of sensors 1–5 when a loading is applied to sensor 3. The applied forces are of 10 N to 50 N, respectively, with steps of 10 N. . . .	115
6.23	Results of spatial characterization in the two tests.	116
6.24	Results of one walking test: (a) Normalized GRF curves. (b) Foot placement including the step lengths.	117
7.1	Chapter 7 overview: heterogeneous OFS network for smart environment.	119
7.2	Results of transmitted and reflected optical power using the TRA setup for place identification in the smart environment.	121
7.3	Metrics of the FFNN model with 70 epochs for the identification of the accessed places in the house. (a) Loss. (b) Accuracy	122
7.4	Results of the classification of new data using the designed FFNN model for three different conditions. (a) Two persons at home. (b) One person at home. (c) No person at home.	123
7.5	System setup for the FBG-based Instrumented Carpet in the Heterogeneous OFS network protocol.	124
7.6	Sensors responses after normalization during a gait performance. . . .	125
7.7	Sensors responses of FBG 4 and FBG 5, and the estimation of support periods (single and double) of two consecutive contralateral steps during the gait.	126
7.8	Sensors responses of FBG 7 and FBG 9 and the estimation of stance and swing phase duration during a gait cycle.	126
7.9	Examples of the classification of locations pressed by the volunteer during a gait performance using the designed FFNN model: comparison between the real output and the FFNN output, which presents the probabilities of each class. (a) Double support at locations L1 and L15. (b) Double support at locations L5 and L19. (c) Single support at location L23.	127
7.10	Graphical interface for data management and acquisition control. . . .	129
7.11	Result of the Smart Environment protocol using the synchronized systems. (a) FBG-based Instrumented Carpet. (b) POF Smart Pants. (c) TRA-based Smart Environment.	130

List of Tables

2.1	Spatio-temporal gait parameters used for Clinical Gait Assessment. . .	25
3.1	FoM of sensor performance for each central wavelength.	38
3.2	Mean(SD) of sensor performance factors for each angular velocity. . . .	40
3.3	Mean(SD) RMSE of angle measurements for each angular velocity with uncompensated and compensated responses. *Excluding outliers.	41
3.4	Sensor performance using two different supports.	47
3.5	Sensor performance for force applied along the fiber.	49
4.1	Comparison of different DNP fibers employed in this work.	66
4.2	Combination of the multiple simultaneous disturbances.	69
5.1	Sensor's sensitivities of all 30 sensors in the smart garment.	85
6.1	Classification results for each volunteer.	97
6.2	Estimated parameters from IMU (reference) and POF Smart Garment sensors: errors between the measurements obtained from the two sys- tems.	102
6.3	Sensitivities of sensors in the fiber 1.	106
6.4	Sensitivities of sensors in the fiber 2.	106
6.5	Spatio-temporal gait parameters in three walking tests.	117
7.1	FBGs sensors' sensitivities.	125

Chapter 1

Introduction

1.1 Motivation

Life expectancy has continuously increased since the early days of human history, which resulted in population aging. From 1950 to 2000, the elderly population (over 65 years) rose from 131 million in 1950 to 418 million in 2000, more than a threefold increase in 50 years [1]. The longevity increase is the reflection of the society evolution with advances on public health, medicine, economy and social development [2]. All these advances contribute to the control of diseases, injuries prevention and reduction of premature deaths. Therefore, many health conditions that were deadly in the past nowadays are treatable or curable. According to United Nations (UN) reports, there are four trends in the global population: (i) population growth, (ii) urbanization, (iii) international migration and the (iv) population ageing [2].

The elderly population is defined as number of people over 65 years. The working ages are defined as the interval between 25 and 64 years. In addition, there are the children (whose ages 0 to 14 years) and the youth population, ages between 15 and 24 years. Common metrics to set the scene of population ageing are the percentage composition of the population, considering all four groups, i.e., children, youth, working-age adults, and older population. Therefore, common metrics that defines population ageing are the percentage composition of the elderly population, considering all population groups [2].

The demographic transition in world population sets new challenges in different areas, in an economical and healthcare perspectives of the elderly population, especially the ones who suffer from inherent conditions of normal ageing such as immunosenescence, urologic and sensory changes [3]. Such conditions lead to variation in physical functions, including the reduction of walking speed, mobility disability, difficulty in activities of daily living and increase of fall risk [3]. The degradation of physical functions in conjunction with the cognitive reduction can also lead to psychological and social issues [3]. The population ageing also results in increase of clinical conditions that affect the human health the so-called chronic age-related diseases and geriatric syndromes [4]. These conditions include osteoarthritis, rheumatoid arthritis, Alzheimer's disease, Parkinson's disease and weakness of the skeletal muscles. All these conditions lead to degradation of physical and/or cognitive functions [4]. It is worth noting that strokes, spinal cord injuries and musculoskeletal injuries can also lead to major locomotor impairments [5].

In this way, wearable sensors can be used on healthcare applications [6], where the health condition assessment is not limited to clinical environments [7]. Thus, it is also possible to monitor different physiological parameters for patients at home, especially for the elderly population and people with locomotor disabilities [8]. These parameters can be divided in kinect (or dynamic) and kinematic parameters for a biomechanics perspective to acquire the angle/displacement and torques/forces in

the human movement. In addition, the gait, as a key human movement, involves many parameters such as ground reaction forces (i.e. forces applied in the ground), spatio-temporal parameters (which is related to length and times related to the gait) and plantar pressure mapping (i.e. pressure distribution on the feet during gait) [8]. Important parameters for health assessment also include the physiological ones, which are related to the health indicators of the patient. Such parameters include the pulse oximetry, breath rate, arterial pressure and heart rate, disturbances or abnormalities in these parameters can indicate different diseases [9]. Although there are also biomarkers and hormones detections approaches, the biomechanics and physiological parameters are the ones addressed in this PhD Thesis.

This background in conjunction with new developments in data transmission, signal processing and sensors' technologies lead to the development of human-friendly and integrated technologies for patients monitoring. The possibility of monitoring parameters of movement as well as physiological parameters for human health enables novel developments in healthcare in which it is possible to assess the patient's condition for the continuous monitoring of health conditions as well as the possibility of anticipating some diseases and/or disorders. Furthermore, the dynamic evaluation of kinetic and kinematic parameters of human gait can also aid clinicians on the gait related pathologies diagnosis [10]. The measurement and analysis of joint angles can also provide benefits for clinicians and therapists. It is used on the evaluation and quantification of surgical interventions and rehabilitation exercises [11].

Among many important physiological parameters, abnormalities on the heart rate (HR) and breathing rate (BR) are also important indicators of some cardiovascular diseases [9], fatigue [12], apnea [12] and respiratory abnormalities [13]. These new advances in healthcare technology provide important information for therapeutics in rehabilitation field, where a widespread of wearable technologies has been observed in the last years [14]. From the user perspective, methods for increasing the patient engagement on the use of such technologies are also proposed [15]. Furthermore, challenges related to the technology sustainability, failure rates, privacy and security have been addressed [16]. The widespread of wearable assistive technologies in conjunction with the increase on the patient engagement result in a continuous increase on the market of wearable healthcare devices [17]. Figure 1.1 shows a market overview on healthcare wearable devices, in which it is possible to observe a large increase on the market with the forecast of even higher increase in the next years. In addition, Figure 1.1 also shows that almost a half (42%) of the wearable devices are focused on healthcare applications and this value can be even higher if we consider that other healthcare applications are related to monitoring and sensing (16% of all applications).

Thus, the continuous ageing of the population as well as the increase on chronic diseases and physical impairments in the world population encourage the development of new smart devices for human assistance and health condition assessment.

1.2 Research Objectives

The main goal of this Doctoral Thesis is the development and application of novel photonic smart textiles systems based on embedded optical fiber sensors (OFS). The sensors are developed using different sensing approaches for quasi-distributed

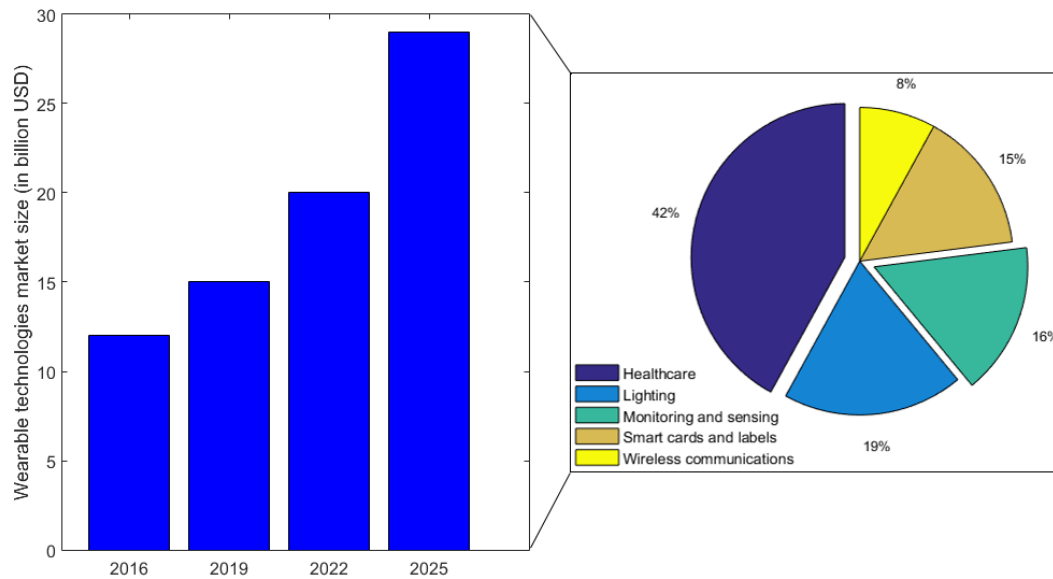


FIGURE 1.1: Market overview of wearable devices in healthcare applications [17].

and distributed systems. Such approaches include multiplexed intensity variation-based sensors, fiber Bragg gratings (FBGs) and transmission-reflection analysis (using nanoparticle-doped optical fibers), where all systems enable the development of sensors arrays for multiparameter sensing. The proposed systems include smart textiles used as clothing accessories, carpets and smart devices (such as tables and beds) using the aforementioned OFS approaches. Such heterogeneous OFS systems are integrated in smart environments.

In order to achieve these objectives, the investigation of the sensors performance under bending angles and forces are performed to evaluate the sensors responses for kinematic and kinetic parameters, which also include the analysis of different nanoparticle-doped optical fibers with respect to their performance in transmission-reflection analysis systems. In addition, the optical fiber integration in different textiles and flexible materials for angle and force assessment are developed with the use of machine learning and deep learning algorithms for feature extraction and activities recognition. These lead to the specific objectives of this Thesis listed as follows:

1. Characterization of polymer optical fibers sensors for kinetic and kinematic parameters;
2. Analysis and comparison of different compounds of nanoparticle-doped optical fibers;
3. Integration of multiplexed intensity variation-based sensors in textiles: clothing accessories and carpets;
4. Integration of FBGs in rubber carpets;
5. Embedment of nanoparticle-doped optical fibers in smart structures and textiles;
6. Development of machine learning and deep learning algorithms for feature extraction and activities recognition of the photonic smart textiles;

7. Development of human-machine interfaces and data transmission;
8. Definition of a framework for the integration of the heterogeneous optical fiber sensor system.

1.3 Justification

The continuous population ageing and the evolution as well as the widespread of the technology in general, but mostly in sensors technologies have enable the development of wearable sensors technologies. Such new advances lead to increasing demands on the sensors technologies, especially in terms of wireless connectivity, portability and autonomy. Moreover, there are also increasing demands for new (and high performance) sensors for parameters monitoring in wearable applications for healthcare. These parameters include the biomechanical and physiological parameters.

The biomechanical parameters can be subdivided into kinematics and kinetics. These parameters provide important information regarding the human physical condition and can be related to the efficiency on the daily activity performance and the locomotion [18]. The biomechanics of human movement is defined as the study of the human movement using methods of mechanical engineering [19]. The human movement analysis includes gait analysis, which comprises the systematic study of human walking, performed by collecting kinematic and kinetic data [20]. The kinematics studies the description of motion of the body without considering the causes of motion [20]. The kinematic parameters include joint angles, center of mass (CoM) displacement velocity, and spatiotemporal gait parameters such as cadence, stride and step length, among others as discussed in [18]. The spatio-temporal gait parameters describe the gait relating the foot placement, gait events timing and velocity variables [18], and their measurement forms the basis of any gait analysis as it complements the angular and displacement data in gait. In contrast, kinetics studies the forces and torques that initiate the motion. It considers the forces generated internally in the body that result in human movement [20]. In general, kinetics parameters include ground reaction forces (GRF), plantar pressure distribution and joint momentum [21].

The kinematic parameters assessment are applied on rehabilitation, training athletes and diagnosis of neurological disorders that affects the movement [22]. Camera-based motion capture systems are capable of providing reliable measurements in three dimensions of body joint positions and estimate spatio-temporal gait parameters and joint angles. However, it is a costly and time-consuming technique. As it is limited to laboratory or clinical environment, it cannot be applied on the continuous monitoring of human movement, especially in remote (or in-home) [22]. Therefore, for gait analysis, the motion capture and kinematic measurement are limited to few gait cycles. To address these limitations, another line of research is the development of wearable technologies for joint assessment, which include electrogoniometers and potentiometers for joint angle assessment in a single axis. However, these technologies present the important drawback of large dimensions and weight that not only limit natural patterns of movement, but also are sensitive to misalignments that commonly occur in polycentric joints [23]. Flexible goniometers, generally based on strain gauges, provide better adaptation to body parts and they are not sensitive to misalignments in the polycentric joints' movement. Moreover, digital goniometer using encoders is developed to measure joint angles in sagittal plane as an attempt to

make a contactless sensor. However, its high sensitivity to misalignment and limitations in speed range discourages its application. Inertial measurement units (IMUs) have experienced a widespread due to advances in MEMS. The combination of a tri-axial magnetometer with tri-axial accelerometer and tri-axial gyroscope is an IMU, which are attached onto the surface of the human body, collecting the linear acceleration and angular velocities, in addition to the magnetic field response, allowing the combination of these data to estimate the joint angles and spatio-temporal gait parameters, commonly performed using sensor fusion algorithms. Despite the wide range of applications of IMUs and their advantages, they present high sensitivity to magnetic field interferences and frequent recalibrations are required [22]. The measurement of joint kinematics results in a system capable of recognizing the daily activities performed by the user, such as walk, sit, run and so on.

In contrast, kinetic parameters include ground reaction forces (GRF), plantar pressure distribution and joint momentum [21]. The plantar pressure and ground reaction forces (GRFs) are assessed using three major monitoring techniques, which include imaging technologies [24], force/pressure distribution platforms [25] and instrumented insoles [26]. The imaging technologies generally use expensive equipment and complex signal processing [27]. Moreover, when the analysis is performed in computed tomography machines, the inability of performing dynamic analysis of plantar pressure during gait or other dynamic movements are additional issues in the gait assessment [24]. To overcome the drawback of inability in performing dynamic analysis, and as a lower cost alternative, force platforms are used on the plantar pressure assessment. These platforms generally have a matrix of pressure sensing elements arranged in a rigid and flat platform [27]. They provide measurements of the foot plantar pressure and 3D dynamics, however they also lack in portability, restricting the tests to laboratory or clinical environments, with a limitation on the number of steps per trial. This drawback inhibits the application on remote and home health monitoring, which is a trend on healthcare applications with the advances in wireless sensor and communication technologies [28]. Another drawback of force platforms is the change of the natural gait pattern when the users try to correctly place the foot on the platform, which leads to inaccuracies on the analysis [29]. Consequently, it leads to the necessity of hidden the platform on the ground, and the test need to be repeated until a natural gait pattern is obtained with the foot placed within the platform boundaries [25].

The instrumented insoles are a feasible option to the force platforms. The portability allowing its use outside the laboratory environment during daily activities with the natural gait pattern of the users is an important advantage of the instrumented insoles, since it enables remote health monitoring and wearable robotics applications [27]. Such insoles can present instability on the measurement (with false positives and false negatives) and lack of resistance to the impact loads that commonly occurs in the gait cycle, especially insoles based on capacitive and resistive technologies [30]. The number of sensors per insole can also be regarded as an additional drawback in the instrumented insole technology, since the small number of sensor results in a low spatial resolution for the plantar pressure analysis [27]. According to [26], the human foot has 15 critical pressure areas that support most of the body weight, and for this reason, an ideal sensor system for complete monitoring of the plantar pressure needs, at least, 15 sensors positioned these predefined points. A higher number of sensors can lead to higher spatial resolution as well as the accuracy in the plantar pressure mapping, and it can be achieved with custom fabrics with flexible capacitive sensors. However, they generally present performance limitations due to material features such as low repeatability, hysteresis, creep and

nonlinearities [27].

1.3.1 Optical Fiber Sensors

Optical fiber sensors present the intrinsic advantages of lightweight, compactness, chemical stability, immunity to electromagnetic field and multiplexing capabilities [31], which enable their application in different fields. They are employed for industrial [32], medical [33] and structural health monitoring [34] applications, also including immunosensors [35], biochemical detection [36] and environmental monitoring [37]. The OFS are already employed for the measurement of the aforementioned kinematics, kinetics and physiological parameters, such as in the measurement of angle [38], refractive index [39], temperature [40], humidity [41], acceleration [42], pressure [43], breathing rate [44] and oxygen saturation [45]. Moreover, the geometric and material features of optical fibers enable their embedment in different structures, from metals and concrete to fabrics and textiles, which can be used for sensing applications [44], [46]. In this way, there is also the creation of optical fiber-based textiles, the so-called photonics textiles [45], which represents a clothing accessory or signaling devices in their first reports [47]. Recently, different application using the photonics textiles are reported, such as the body temperature sensing [48], breath and heart rates [49]. Smart textile approaches offer the advantages of higher transparency between the sensor and the user, in addition to not influence or inhibit the user's natural movements [50]. Thus, sensor's compactness and flexibility allow easy installation and removal, which facilitate the system's usability [8]. The features of OFS in smart textile also enable the development of new platforms for force assessment that can be embedded in carpets for remote monitoring with the mitigation of the targeting effect.

Optical fiber sensors are also compatible with the requirements of the internet of things (IoT) technology [51], which mainly relies on the wireless connectivity of devices with their miniaturization as well as low energy consumption. This new paradigm is related to the remote healthcare applications [52], which has its widespread motivated by the population ageing scenario. Such sensor systems allow the continuous monitoring of patients activities, resulting in remote assistive services, including diagnosis, early detection of health issues and their transport in case of emergencies [53]. It is worth noting that the patient health monitoring at home instead of hospitals or clinical facilities is a positive component (emotional and psychological) due to the possibility of performing their daily activities and the sense of independent growth in the community [54].

1.4 Contributions

The contributions of this Thesis include the development of OFS and their integration in smart textiles, used as clothing accessories and smart devices, to monitor biomedical parameters without influencing or inhibiting the user's natural movements. In addition, a Smart Environment using heterogeneous OFS network is proposed to improve the quality of the remote healthcare monitoring at home. This Thesis also includes the combination of proposed sensors with AI algorithms to increase the potential of making intelligent decisions in real-time. These developments improve the communication between patients and clinicians without face-to-face medical consultation.

1.4.1 Publications

In the time frame of the Thesis, about 19 journal papers (J), 4 conference works (C) and 2 book chapters (B) were either published, accepted or under review. These works also include the collaboration with other researchers and international groups. The works are divided into the ones used in the Thesis and the ones from collaborations and parallel researches. In addition, there are also 4 patent applications under consideration on the university. The publications resulting from this Thesis are listed below:

1. **Journal - L. Avellar**, A.G. Leal-Junior, C.A.R. Diaz, C. Marques and A. Frizera, "POF Smart Carpet: A Multiplexed Polymer Optical Fiber-Embedded Smart Carpet for Gait Analysis", *Sensors*, vol. 19, no. 15, p. 3356, 2019.
2. **Journal - L. Avellar**, A. Leal-Junior, C. Marques and A. Frizera, "Performance Analysis of a Lower Limb Multi Joint Angle Sensor Using CYTOP Fiber: Influence of Light Source Wavelength and Angular Velocity Compensation", *Sensors*, vol. 20, no. 2, p. 326, 2020.
3. **Journal - L. Avellar**, G. Delgado, E. Rocon, C. Marques, A. Frizera and A. Leal-Junior, "Polymer Optical Fiber-Embedded Force Sensor System for Assistive Devices With Dynamic Compensation", *IEEE Sensors Journal*, vol. 21, no. 12, pp. 13255-13262, 2021.
4. **Journal - L. Avellar**, G. Delgado, C. Marques, A. Frizera, A. Leal-Junior and E. Rocon, "Polymer Optical Fiber-Based Smart Garment for Impact Identification and Balance Assessment", *IEEE Sensors Journal*, vol. 21, no. 18, pp. 20078-20085, 2021.
5. **Journal - L. Avellar**, A. Frizera, E. Rocon and A. Leal-Junior, "Characterization and analysis of a POF sensor embedded in different materials: Towards wearable systems for stiffness estimation", *Optics and Laser Technology*, vol. 145, 2022.
6. **Journal - A. Leal-Junior, L. Avellar**, A. Frizera and C. Marques, "Smart textiles for multimodal wearable sensing using highly stretchable multiplexed optical fiber system", *Scientific Reports*, vol. 10, no. 1, p. 13867, 2020.
7. **Journal - C. Bayón, G. Delgado-Oleas, L. Avellar**, F. Bentivoglio, F. Di Tommaso, N.L. Tagliamonte, E. Rocon, E.H.F. van Asseldonk, "Development and Evaluation of BenchBalance: A System for Benchmarking Balance Capabilities of Wearable Robots and Their Users", *Sensors*, vol. 22, no. 1, p. 119, 2022.
8. **Journal - L. Avellar**, M. Silveira, C.A.R. Diaz, C. Marques, A. Frizera, W. Blanc and A. Leal-Junior, "Performance Analysis of a Transmission-Reflection Analysis (TRA)-based Distributed Sensing using Different Oxide Nanoparticle-doped High Scattering Fibers", *Photonic Technology Letters*, **(Under Review)**.
9. **Journal - L. Avellar**, C.S. Filho, G. Delgado, G. Castellano, A. Frizera, E. Rocon and A. Leal-Junior, "Photonic Smart Garment: an optical fiber-integrated and AI-enabled clothing for biomedical analysis", *Scientific Reports*, **(Under Review)**.
10. **Conference - L. Avellar**, A. Leal-Junior, A. Frizera, "Polymer Optical Fiber Sensors for Treadmill Instrumentation", in *Proceedings IMOC*, Aveiro, Portugal, 2019.

11. **Conference** – **L. Avellar**, A. Leal-Junior, C. Marques, E. Rocon and A. Frizera, “Proof-of-Concept of POF-Based Pressure Sensors Embedded in a Smart Garment for Impact Detection in Perturbation Assessment”, in *Converging Clinical and Engineering Research on Neurorehabilitation IV*, ICNR, Biosystems & Biorobotics, vol 28. Springer, 2020.
12. **Conference** – A. Leal-Junior, **L. Avellar**, M.J. Pontes, C.A.R. Diaz, C. Marques and A. Frizera, “Proof-of-concept of a carpet-embedded heterogeneous optical fiber sensor system for gait analysis”, in *Proceedings SPIE*, Limassol, Chipre, 2019.

In addition, the publications which include works from collaborations and parallel researches during the development of this Thesis are listed as follows:

1. **Journal** - C.A.R. Diaz, A. Leal-Junior, **L. Avellar**, P.F.C. Antunes, M.J. Pontes, C. Marques, A. Frizera and M.R.N. Ribeiro, “Perrogator: A Portable Energy-Efficient Interrogator for Dynamic Monitoring of Wavelength-Based Sensors in Wearable Applications”, *Sensors*, vol. 19, no. 13, p. 2962, 2019.
2. **Journal** - A. Leal-Junior, C.A.R. Diaz, **L. Avellar**, M.J. Pontes, C. Marques and A. Frizera, “Polymer optical fiber sensors in healthcare applications: A comprehensive review”, *Sensors*, vol. 19, no. 14, pp. 1-30, 2019.
3. **Journal** - A. Leal-Junior, **L. Avellar**, C.A.R. Diaz, A. Frizera, C. Marques and M.J. Pontes, “Fabry–Perot Curvature Sensor With Cavities Based on UV-Curable Resins: Design, Analysis, and Data Integration Approach”, *IEEE Sensors Journal*, vol. 19, no. 21, pp. 9798-9805, 2019.
4. **Journal** - A. Leal-Junior, **L. Avellar**, J. Jaimes, C.A.R. Diaz, W. Santos, A.A.G. Siqueira, M.J. Pontes, C. Marques and A. Frizera, “Polymer Optical Fiber-Based Integrated Instrumentation in a Robot-Assisted Rehabilitation Smart Environment: A Proof of Concept”, *Sensors*, vol. 20, no. 11, p. 3199, 2020.
5. **Journal** - A. Leal-Junior, **L. Avellar**, C.A.R. Diaz, M.J. Pontes and A. Frizera, “Polymer Optical Fiber Sensor System for Multi Plane Bending Angle Assessment”, *IEEE Sensors Journal*, vol. 20, no. 5, pp. 2518-2525, 2020.
6. **Journal** - A. Leal-Junior, A. Theodosiou, C.A.R. Diaz, **L. Avellar**, K. Kalli, C. Marques and A. Frizera, “FPI-POFBG Angular Movement Sensor Inscribed in CYTOP Fibers With Dynamic Angle Compensator”, *IEEE Sensors Journal*, vol. 20, no. 11, pp. 5962-5969, 2020.
7. **Journal** - A. Leal-Junior, **L. Avellar**, A. Frizera, P. Antunes, C. Marques, and C. Leitão, “Polymer optical fibers for mechanical wave monitoring”, *Optics Letters*, vol. 45, no. 18, pp. 5057-5060, 2020.
8. **Journal** - A. Leal-Junior, D. Ribeiro, **L. Avellar**, M. Silveira, C.A.R. Diaz, A. Frizera, W. Blanc, E. Rocon and C. Marques, “Wearable and Fully-Portable Smart Garment for Mechanical Perturbation Detection With Nanoparticles Optical Fibers”, *IEEE Sensors Journal*, vol. 21, no. 3, pp. 2995-3003, 2021.
9. **Journal** - V. Biazzi, **L. Avellar**, A. Frizera, and A. Leal-Junior “Influence of Two-Plane Position and Stress on Intensity-Variation-Based Sensors: Towards Shape Sensing in Polymer Optical Fibers” *Sensors*, vol. 21, no. 23, p. 7848, 2021.

10. **Journal** - Leal-Junior, A.; **Avellar, L.** ; Biazi, V. ; Soares, M. S. ; Frizera, A. ; Marques, C. "Multifunctional Flexible Optical Waveguide Sensor: on the Bioinspiration for Ultrasensitive Sensors Development", *Opto-Electronic Advances*, 2021, (Accepted).
11. **Book Chapter** - **L. Avellar**; Leal-Junior, A.; Frizera, A. ; "Optical fiber sensing technologies", in *Optical Fiber Sensors for the Next Generation of Rehabilitation Robotics*, Elsevier, 2021.
12. **Book Chapter** - **L. Avellar**; Leal-Junior, A.; Frizera, A. ; "Smart structures and textiles for gait analysis", in *Optical Fiber Sensors for the Next Generation of Rehabilitation Robotics*, Elsevier, 2021.
13. **Conference** - A. Leal, **L. Avellar**, M. J. Pontes, C. A. Díaz, C. Marques, and A. Frizera Neto, "Proof-of-concept of a carpet-embedded heterogeneous optical fiber sensor system for gait analysis," in *Seventh European Workshop on Optical Fibre Sensors*, p. 130, 2019.

1.4.2 Patents

1. "Smart Garment based on optical fiber sensors for monitoring of biomedical parameters", **L. Avellar**, E. Rocon, A. Frizera and A. Leal-Junior, *Under Consideration*, (Process: 23068.001955/2022-19).
2. "Smart Pants based on optical fiber sensors for monitoring of gait parameters", **L. Avellar**, A. Frizera and A. Leal-Junior, *Under Consideration*, (Process: 23068.001962/2022-11).
3. "Multifunctional intelligent structure with built-in optical sensors for human-robot and human-environment interfaces", **L. Avellar**, A. Frizera and A. Leal-Junior, *Under Consideration*, (Process: 23068.001961/2022-76).
4. "Smart Carpet based on optical fiber sensors for gait analysis", **L. Avellar**, A. Frizera and A. Leal-Junior, *Under Consideration*, (Process: 23068.001963/2022-65).

1.5 Organization of the Thesis

This Ph.D. Thesis is divided into eight chapters separated in four main parts as follows: Introduction and Background, which comprises Chapter 1 and Chapter 2; Sensors Development and Performance Analysis, which comprises Chapter 3 and Chapter 4; Protocols and Applications, which comprises Chapters 5, 6 and 7; and Final Remarks and Future Works, which comprises Chapter 8.

1. Part 1: Introduction and Background

Chapter 1 presents the motivation, justification, the objectives and the contributions of this Thesis.

Chapter 2 provides the theoretical background of this work. Some knowledge prior to the understanding of following chapters, such as optical fiber overview, materials, optical fiber sensing techniques and biomedical concepts are presented in this chapter.

2. Part 2: Sensors Development and Performance Analysis

In Chapter 3, the development and the performance analysis of different OFS under kinetic and kinematic parameters are performed. Different performance factors are evaluated in this Chapter, such as sensitivity, hysteresis and linearity.

Thereafter, in Chapter 4, OFS are developed and integrated in textiles and flexible structures for performance analysis. Different sensing techniques are employed and different parameters are evaluated.

3. Part 3: Protocols and Applications

Chapter 5 presents a development of different OFS systems for a balance assessment protocol.

In Chapter 6, photonic textiles are developed and applied in different protocols for monitoring several biomedical parameters.

Chapter 7 presents an heterogeneous sensor network based on sensors with different OFS techniques applied in the Smart Healthcare.

4. Part 4: Final Remarks and Future Works

Finally, the main conclusions, as well as the future works and new research topics, are presented in Chapter 8.

All these chapters comprise important parts of this Thesis, as presented in the flowchart of Figure 1.2.

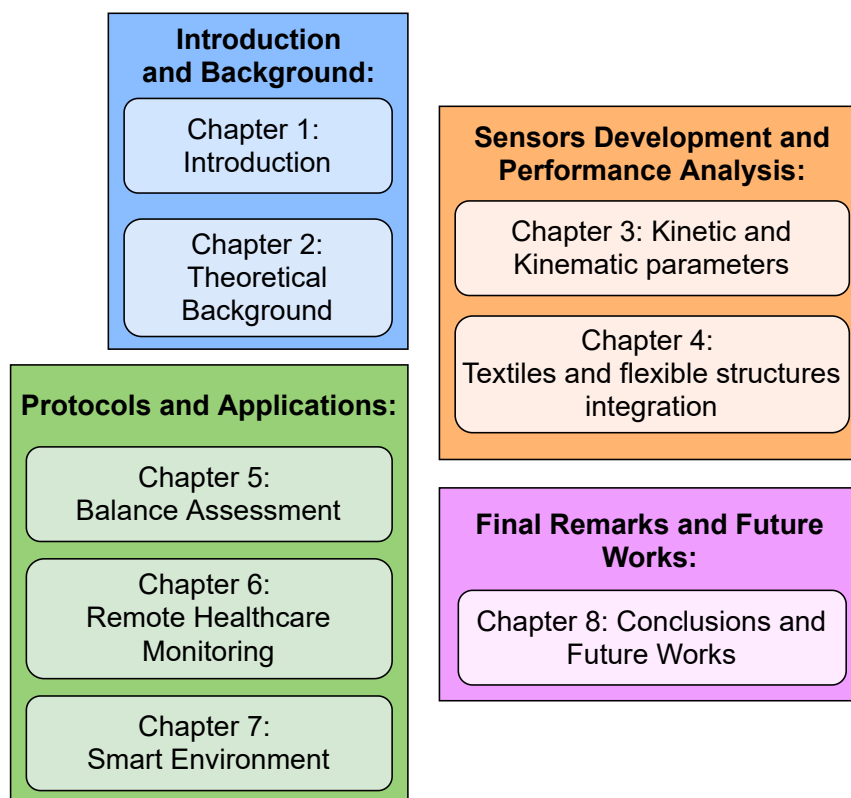


FIGURE 1.2: Schematic representation of the Thesis outline.

Chapter 2

Theoretical Background

Measurement is a process of collecting information from a physical world, performed by instruments designed and manufactured for specific tasks or parameters [55]. Sensors are used as the primary elements to provide information of the physical, chemical or biological measurand of interest and converting it into a form of energy (e.g. electrical or optical signal), which can be processed and correlated to the measurand of interest [56]. In ideal cases, the sensors measurements should be consistent without any errors, drift, or hysteresis. However, there are several sources of error when measuring parameters in the physical world, such as changes in component performances (e.g., gain shift, changes in chemistry, aging, and offsets drifts), external and ambient influences such temperature, pressure and humidity. Thus, it is important to identify these sources to select or design the sensor for a particular application [56].

Optical Fiber Sensing (OFS) technology is based on the interaction of a measurand with the light guided in the optical fiber, which leads to variations in optical signal related to the parameter of interest. The advantages of OFS over traditional electronic sensors include compactness, lightweight, flexibility, immunity to electromagnetic interference, chemical stability and multiplexing capabilities. Since the early studies of OFS in the 70s, there are a growing number of research groups dedicated to the exploration of this technology [57]. Decades of research led to the development of accurate optical fiber sensing, including several application fields: health-care, robotics, structural health monitoring, environmental monitoring, medicine and many industrial technologies [56].

In this chapter, fundamentals and key concepts on the study of OFSs will be addressed. This Chapter presents the optical fiber overview, sensing techniques that will be employed in this Ph.D. Thesis. In addition, an overview and fundamentals of biomechanics and machine learning are discussed, since they are the main application field in this Ph.D. Thesis.

2.1 Optical Fiber Overview

An optical fiber is defined as a cylindrical dielectric waveguide, made of glass (silica fibers) or plastic materials (Polymer Optical Fiber, POF), which is composed of two parts: a core, a cladding with a coating to increase the waveguide robustness [58], as shown in Figure 2.1. The core is where the light is transmitted, whereas the cladding is a layer which reduces the optical losses from the core to the environment (generally air) and reduces scattering loss at the surface of the core. The coating is a layer used to protect the optical fiber from physical damage and contaminants. Fibers can be produced in different geometries, dimensions and materials.

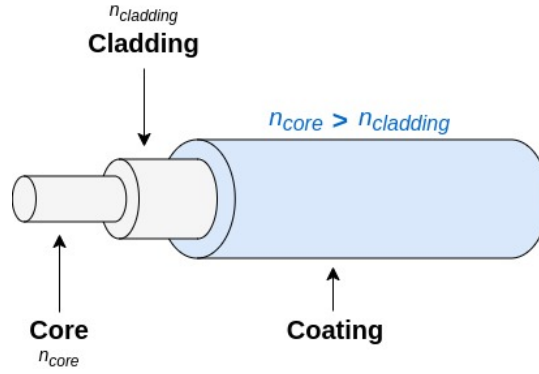


FIGURE 2.1: Optical Fiber overview.

The light transmission in optical fibers is based on the principle of *total internal reflection*, which is related to a light beam incident on the boundary between two materials with different refractive indices. When light is incident from a medium with a higher index (n_{core}) to one with a lower index ($n_{cladding}$), the transmitted beam emerges at an angle higher than the incident angle. If the incident angle increases, it will reach a point at which the refracted angle is 90° ; at this point, the value of the incident angle is known as the critical angle. If the incident angle is higher than the critical angle, there is no refraction of the light, and all of the rays become totally internally reflected in the material with higher refractive index (core). Figure 2.2 presents an illustration of the principle of *total internal reflection* in the optical fiber.

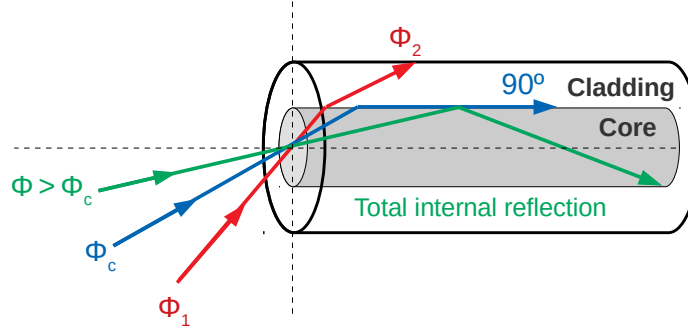


FIGURE 2.2: Principle of the total internal reflection in the optical fiber.

The critical angle can be calculated using the Equation 2.1:

$$\phi_c = \sin^{-1} \left(\frac{n_{cladding}}{n_{core}} \right) \quad (2.1)$$

In addition, only the light rays with angles lower than the acceptance angle are propagated inside the optical fiber. The acceptance angle (ϕ_{max}) is a function of the core refractive index (n_{core}), external refractive index (n_{ext}) and the critical angle (ϕ_c), as presented in Equation 2.2.

$$\frac{\sin(\phi_{max})}{\sin(\phi_c)} = \frac{n_{core}}{n_{ext}} \quad (2.2)$$

2.1.1 Numerical Aperture

As previously presented, the acceptance angle (ϕ_{max}) is the maximum incident ray angle that can be propagated [58]. The fiber numerical aperture (NA) represents the angles of the incident light beam accepted by the fiber core through the acceptance cone (as shown in Equation 2.3) and the full aperture angle is given by $2\phi_{max}$.

$$NA = \sin(\phi_{max}) = \sqrt{n_{core}^2 - n_{cladding}^2} \quad (2.3)$$

Thus, the value of NA is dependent on the difference between the refractive indices of the core and cladding material. Compared with other optical fibers, multimode POFs (with 1 mm core diameter) has the highest NA , which leads to lower cost of the connectors that are commonly made of simple plastic structures with fabrication tolerances orders of magnitude higher than the ones for silica fibers [58]. Figure 2.3 shows a representation of the NA in a silica fiber and in a POF.

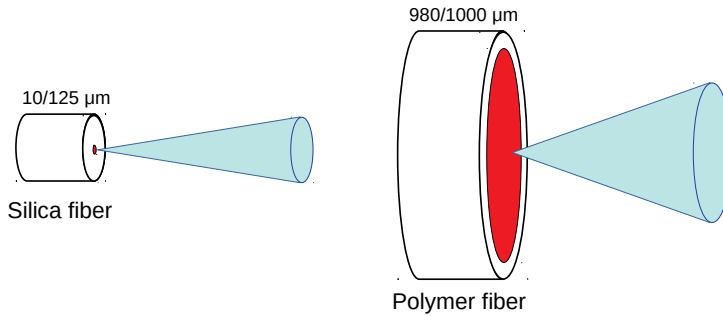


FIGURE 2.3: Representation of the NA of silica and polymer fibers.

2.1.2 Modes in Optical Fibers

In the theory of the principle of total internal reflection, all the rays with incident angle higher than the critical angle ($\phi > \phi_c$) are transmitted through the optical fiber. However, to obtain a complete description of the wave guiding phenomenon, the wave properties of light are also be considered, which means that not all guided waveforms, so-called modes in which $\phi < \phi_{max}$ can propagate [58]. Each mode represents one particular solution of the Maxwell equation. The classification regarding the number of propagation modes inside the fiber can be divided into single-mode and multimode fibers. Single-mode fibers only support one waveform (mode), whereas in multimode fibers hundreds to thousands of modes are supported. The number of modes (N_m) in a step index fiber can be defined as presented in Equation 2.4:

$$N_m = \frac{V^2}{2} \quad , \quad (2.4)$$

where V represents the normalized frequency. The normalized frequency of an optical fiber is defined in Equation 2.5, in which a represents the core radius, λ represents the wavelength and NA is the numerical aperture.

$$V = \frac{2\pi a}{\lambda} NA \quad (2.5)$$

In this way, if $V > 2.405$ the optical fiber is multimode, otherwise the optical fiber is a single-mode waveguide.

2.1.3 Refractive Index Profiles

The core can present different refractive index profiles, and the two major types are: (i) step index (SI) and graded index (GI) profiles. In a SI fiber, the core is homogeneous and the refractive index is constant across the cross section of the core. Thus, the light rays propagate along straight lines in the core and are completely reflected at the core/cladding interface [58]. Figure 2.4 presents the principle of a fiber with a SI profile and the light rays traveling through the fiber at different angles of incidence, where n_1 represents the core refractive index and n_2 represents the cladding refractive index.

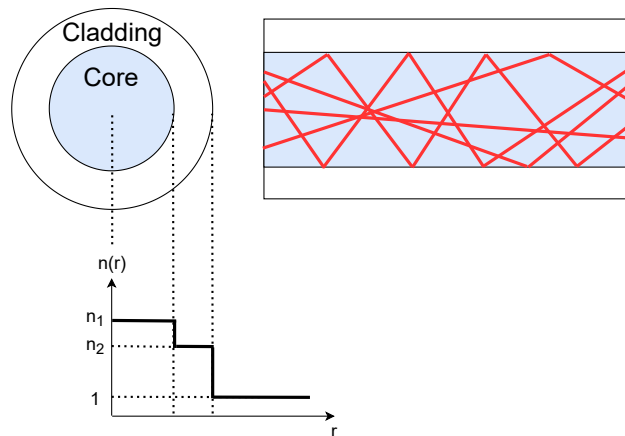


FIGURE 2.4: SI profile fiber.

In a GI fiber, the core has a radius-dependent refractive index with a gradient distribution, in which the refractive index is higher at the core center and lower at the extremities [58]. The rays propagating in the center travel a shorter distance. However, due to the higher refractive index at the center, these rays travel at a lower speed. On the other hand, the smaller refractive index (near the core extremities) causes the rays traveling with higher velocity in a longer distance. This refractive index gradient distribution in GI profiles results in a non-straight ray propagation, as shown in Figure 2.5.

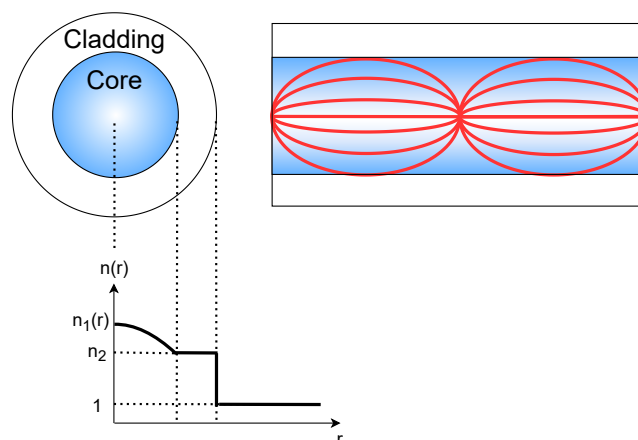


FIGURE 2.5: GI profile fiber.

2.1.4 Optical Fiber Losses

In an optical fiber, the power decreases exponentially with the distance z . Equation 2.6 shows the calculation of the attenuation in an optical fiber, in which α is called attenuation coefficient of the optical fiber and it represents the value of the attenuation as a function of the fiber length [59].

$$P(z) = P(0)10^{-\alpha \cdot z/10} \quad (2.6)$$

The expression of the attenuation in decibels is presented in Equation 2.7.

$$\alpha = \frac{10}{z} \cdot \log \left(\frac{P(0)}{P(z)} \right) \quad [\text{dB/km}] \quad (2.7)$$

The attenuation depends on the material, dimensions and geometry of the optical fiber. Improvements in optical fiber materials and fabrication process with reduction of impurities led to attenuation as low as 0.15 dB/km (at 1550 nm wavelength) in silica optical fibers [60]. Polymer materials are less efficient for light transmission, with lowest attenuation of 125 dB/km (at 650 nm wavelength) [57], and it is related to the lower transparency of the materials. Also, the attenuation is dependent on the spectral width and on the NA of the light source employed [58]. There are regions of the spectrum where the attenuation is minimum, so-called transmission windows. In silica fibers the window is centered at 1550 nm , whereas in POF, the window is centered at 650 nm .

The attenuation can be classified into two main groups: *intrinsic and extrinsic*. The *intrinsic losses* are related to the composition of the optical fiber. Absorption and the Rayleigh scattering are examples of *intrinsic losses*. They are caused by the molecular vibrational absorption within the molecular bonds and by the scattering from composition, orientation and density fluctuations [61]. The *extrinsic losses* are regarding external influences in the fiber, such as the absorption caused by organic pollutants and the dispersion provoked by dust particles, microfractures, bubbles, and other structural imperfections in the fiber. Moreover, another *extrinsic loss* is related to radiation losses, originated by perturbations in the fiber geometry (microbends or macrobends). Figure 2.6 presents a diagram including the *intrinsic and extrinsic losses*.

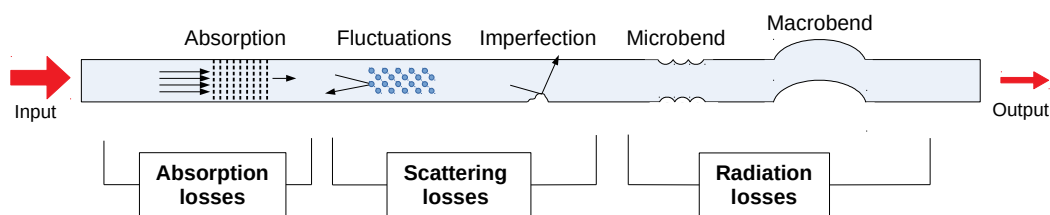


FIGURE 2.6: Optical fiber losses.

2.1.5 Optical Fiber Materials

In general, the optical fiber materials are divided into silica and polymers. Due to their lower attenuation, silica fibers are the preferred material for telecommunication and remote sensing applications, since they guarantee an optical signal transmission in long distances ($\sim km$). However, POFs are attractive for sensors applications due to their material's properties, including mechanical and thermal properties. In terms of temperature, conventional silica fibers have high glass transition temperature (T_g) which leads to the silica fibers as the best option for application at higher temperatures, in applications with temperatures higher than $300^\circ C$ [60]. On the other hand, silica fibers present a small strain limit of below 5%, which makes these fibers fragile and applicable only to small strains, whereas commercial POFs present strain limits as high as 10%. Furthermore, the elastic modulus of POFs are at least ten times lower than silica fibers, indicating higher mechanical flexibility of the POFs and enabling their application in high bending conditions.

There are different POF materials and, among them, the polymethyl methacrylate (PMMA) is the most employed in POF applications. The PMMA presents some aspects in the sensing applications which can be improved with the use of other polymers, which will be discussed below. Additional fabrication methods for POFs enable the fabrication of POFs with higher flexibility, where there are reports of POFs with elastic modulus in the range MPa [40] and even kPa [35]. As an example, there are fibers which are created through the light polymerization spinning (LPS) process, where a mixture of monomers are polymerized with UV light, resulting in a higher degree of customization for the so-called LPS-POF. The LPS-POFs have elastic modulus more than 100 times lower than PMMA, which is even lower than the elastic modulus of cotton and other textile materials [62]. Moreover, LPS-POF presents strain limits higher than 200% [40]. PMMA also presents low T_g and high attenuation when compared with other polymers, such as polycarbonate (PC) and cyclic transparent optical polymer (CYTOPs), respectively. The CYTOPs offer advantages due to their lower attenuation, particularly in the 1550 nm wavelength region. This advantage enables the employment of commercially available optical components, which are generally designed to work within the 1550 nm wavelength region. Another issue regarding the PMMA is the higher moisture absorption capability, which can harm its application in temperature or strain sensing where a humidity cross-sensitivity is undesirable [63]. POFs made of cyclic olefin copolymers (COC) present a humidity sensitivity at least 30 times lower than the one of PMMA, which enable the use of COC fibers to mitigate the humidity cross-sensitivity.

In addition to the POF advantages previously mentioned, silica optical fibers have attractive features for sensing applications, since glass has high chemical stability, mechanical strength and high transparency [64]. Recent advances in glass science show that the incorporation of nanoparticles can significantly change certain properties of this material [65]. The enhancement of some spectroscopic characteristics of silica optical fibers, such as broaden emission spectra and higher energy transfer, can be achieved by incorporating rare-earth (RE)-ions within dielectric (oxide) nanoparticles (DNP) in the fiber's core [66], [67].

The presence of DNPs in the core of silica fibers leads to higher optical losses due to the Rayleigh scattering in comparison with the losses found on single-mode fibers [68]. This higher backscattering motivates the implementation of DNP-doped fibers in Rayleigh scattering-based distributed sensing system applications [69], such as temperature monitoring during laser ablation of the porcine liver phantom [70], 3D shape sensing [69] or optical backscatter reflectometer (OBR)-based refractive index

sensor [71]. Another technique for these fibers is the Transmission-Reflection Analysis (TRA), where the Rayleigh backscattering is used for determining the position of a disturbance event along the length of a silica fiber [72]. Therefore, DNP-doped high scattering fibers are an attractive solution to enhance the spatial resolution of TRA-based systems such as presented in [73].

As a general description of the fiber fabrication (detailed description can be found in [74], [75], there is the preparation of the silica preform with nanoparticles with their formation triggered by the use of magnesium (Mg) or other components (depending on the fiber composition), an alkaline earth element, in conjunction with erbium ions dispersed in an ethanol solution to obtain the doping solution [74]. In the first step, a germanium-doped silica porous layer is obtained in Modified Chemical Vapor Deposition process. Then, it is immersed in the solution and dried at high temperature (1000 °C), represented in Figure 2.7 as step 2.

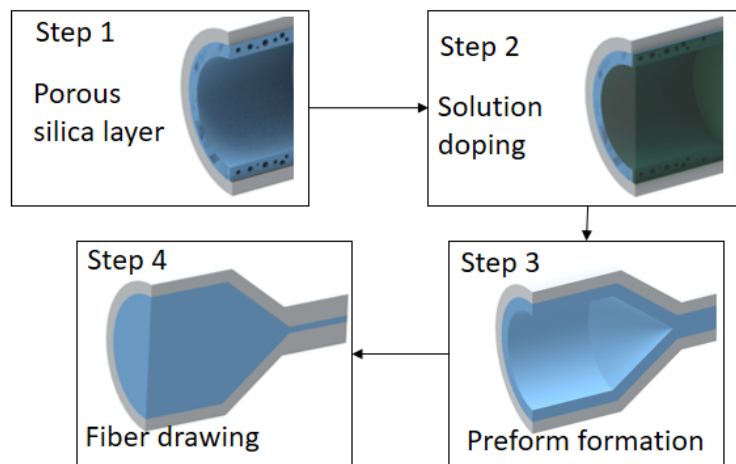


FIGURE 2.7: Schematic representation of the steps followed in the fiber fabrication.

After thermal treatments, the porous layer is densified and resulted in a preform with 10 mm diameter with 1 mm core [74], in step 3. Following this procedure, there is an immiscible system, which results in one phase with silica predominance in the core of preform and one phase majorly composed by the Mg-based nanoparticles [74]. Finally, in step 4, the optical fiber takes its final shape using a draw tower with 2200 °C, resulting in a total diameter of 125 μm of the fiber. As a final step in the fiber fabrication, a polymer coating is applied to increase the mechanical robustness of the optical fiber, especially against bending and impact, which is important for the proposed application, where the fiber is subjected to sequential mechanical perturbations. It is worth noting that the nanoparticle composition depends on its size, also resulting in a refractive index change on the particles [74]. The size of nanoparticles ranges from few nanometers to 160 nm with variations in shape as well. These unique characteristics of the optical fiber points to the necessity of a mechanical perturbations characterizations at different positions in the optical fiber prior to the sensor's application in perturbation assessment during gait. The fabrication process is summarized in Figure 2.7, where the fabricated fiber represented by this method has an attenuation of 2.6 dB/m and a scattering gain of 2.0 dB, which make it suitable for the transmission of optical signals in the order of 10 mW for a few meters. It is also worth noting that there are different compositions of the optical fibers with different performances, as discussed in Section 4.3. For example, comparing with

the MgO-based nanoparticle fibers previously reported [76], [77], in this case, the fiber has an outer ring with the MgO-based nanoparticles, which resulted in smaller optical attenuation than the ones with MgO-based nanoparticles inside the fiber's core [77].

2.2 Sensing Techniques

The optical fiber-based sensing technology aims to convert a physical parameter to an optical output. An important key of this technology is the transducer, i.e. the device which converts one form of energy associated with the physical parameter into another form of energy (optical output). Different types of sensors can be achieved depending on the transducer employed in the OFS detection system. Thus, OFS can be classified based on different categories based on working principle, spatial positioning and measurement parameters.

The working principle depends on the light property which is modified according to the change in the measurand to be evaluated. The sensors can be classified into: intensity-modulated sensors, detection through the light power; phase-modulated sensors, detection using the phase of the light beam; polarimetric sensors, detection of changes in the state of polarization of the light; or spectrometric sensors, detection of changes in the wavelength change of the light. Furthermore, the OFS can be classified based on the spatial positioning, in which the sensors can measure punctually or along the fiber. This classification is divided into punctual, quasi-distributed or distributed sensors. The punctual sensors provide the value of the physical parameter of interest locally, whereas distributed sensors provide the value of the physical parameter over a distance and as a function of the position along the fiber. In the quasi-distributed sensors, the variable is measured at discrete points along the fiber. Finally, the sensors can be classified based on the measurement parameters, i.e. physical sensors such as temperature, strain and pressure; chemical sensors, such as pH and gas sensors; and biosensors, such as DNA, blood flow and glucose sensors.

There are several techniques with different classifications used for optical fiber sensing. In this chapter, the techniques employed in the development of this Ph.D. Thesis will be addressed.

2.2.1 Intensity Variation-based Sensors

The intensity variation technique is one of the simplest sensing techniques employed in the OFS development. In the intensity variation approach, the optical signal is transmitted from a light source through optical fibers and a transducer converts the optical power in electrical power related to the variation of the medium through the light is transmitted. Thus, the sensitivity is related to the sensor alignment. Figure 2.8 shows the intensity variation technique approach, where a physical variation in the optical fiber provokes a power variation in the output, in addition to the fiber attenuation, which is present even in a straight fiber. The main advantages of intensity-variation sensors are the ease of fabrication, simple detection system, simplicity in signal processing and the low-cost performance.

A typical intensity-variation-based POF sensor generally consists of a POF with a lateral section. The lateral section is made by removing the cladding and part of the fiber core, and it creates a sensitive zone, which increases the sensor sensitivity and linearity of the signal attenuation when the fiber is under a bending. The light

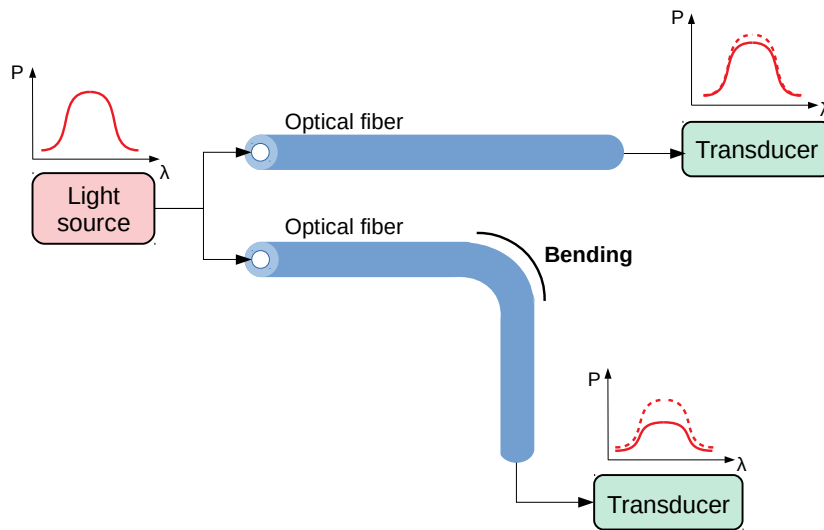


FIGURE 2.8: Intensity variation technique approach: a straight fiber with an attenuation in the output, and a bending in the fiber with a high power variation in the output provoked by the physical variation.

losses are due to absorption and frustrated total internal reflection when in contact with the surface [57]. When the bending occurs, the incident angle increases and creates a variation on the transmitted signal. When the sensitive zone of the fiber is bending, there are higher losses due to this POF region that has no cladding, increasing the radiation losses. Another source of loss is the surface scattering caused by the coupling between higher and lower guided modes [78]. Figure 2.9 presents the description of a fiber geometry considered in the POF sensor modeling. The sensitive zone is represented by the section length given by c and the section depth of removed material on the fiber core denoted by p . The optical fiber length in Figure 2.9 is given by L , meanwhile the optical fiber diameter is d , and the curvature radius is R .

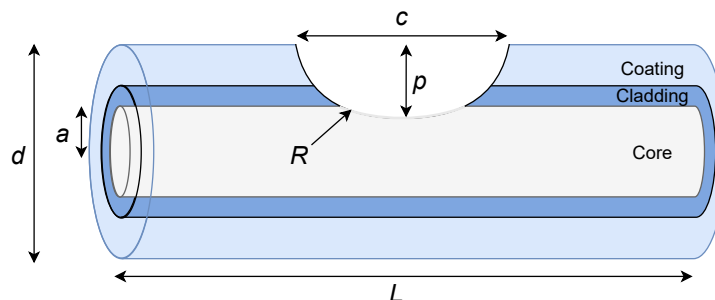


FIGURE 2.9: Schematic representation of the sensitive zone.

The setup of the Figure 2.8 represents a punctual sensor, since the whole fiber comprises an unique measurement point and it is not possible to identify where the physical variation was performed. With the creation of the sensitive zone, the sensor consists of this lateral section, and it also represents a punctual sensor. However, it is possible to achieve a quasi-distributed sensor using a multiplexing technique in

intensity variation-based sensors [79]. The multiplexing technique consists of laterally coupling light sources, i.e. light emitting diodes (LEDs), to lateral sections, and photodetectors at the fiber ends. An aluminum foil can be placed on the end facet of the fiber to increase the reflectivity, and hence increase the optical power in the phototransistor. Each LED side-coupled to the respective lateral section represents one sensor, which leads to discrete points along the fiber, i.e. a quasi-distributed system. The LEDs activation is time multiplexed, thus each LED is activated at time and its response is acquired by the photodetector, and in the end all the sensors' responses are sent to a microcontroller. In this way, it is possible to identify the physical variation applied to all these points (sensors) in the fiber. Figure 2.10 presents the setup of the intensity variation-based quasi-distributed sensors using the multiplexing technique.

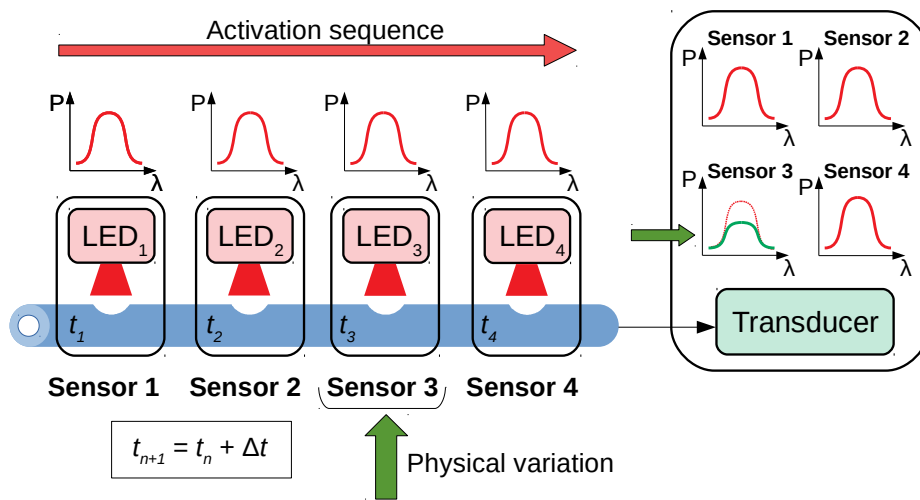


FIGURE 2.10: Multiplexing technique for intensity variation-based sensors.

One limitation of the technique is the maximum number of sensors that can be multiplexed. Since there is a power attenuation at each sensor's lateral section, when the fiber presents a high number of sensors, the output power decreases and may be too low to be detected. The initial power attenuation due to lateral section and sensor sensitivity depends on the lateral section parameters (c and p) of each optical fiber sensor [30], [80]. Since the sensors work with the power attenuation principle, the sensors sensitivities and dynamic range are factors which need to be considered in the POF output power estimation. Taking these parameters into account, the power attenuation with respect to all aforementioned effects is estimated as follows:

$$\frac{P_0}{P_{in}} = \frac{(S_c - NS_0)}{S_c} - \alpha L - \sum \text{sens}_i r_i \quad (2.8)$$

In the Equation 2.8, N is the number of sensors, L is the fiber's length, α is the attenuation coefficient, sens_i and r_i are the sensitivity and dynamic range of each sensor, respectively. Since the two first terms of the Equation 2.8 are constant, only the last term is considered in the output power estimation. Therefore, Equation 2.9 presents the simulation of the sensors responses, where i is the sensor ($i = 1, 2, 3$ in this case) and j is the photodetector ($j = 1, 2$) [60].

$$\left(\frac{P_0}{P_{in}}\right)_{i,j} = \sum_{i=1}^n sens_i r_i \quad (2.9)$$

Equation 2.9 shows the response calculation of each sensor based on the sum of the previous sensors, i.e., the power of Sensor 3 consists of the sum of the responses of Sensors 1, 2, and 3, whereas Sensor 2 is the sum of 1 and 2. Therefore in order to obtain the response of a single sensor without the influence of other sensors, it is necessary to compensate the response of the other sensors. In this case, Equation 2.9 is rewritten as Equation 2.10. Thus it is noticeable the need of characterization of each sensor individually, prior to their applications for simultaneous measurements [60],

$$r_i = \frac{P_i - P_{i-1}}{sens_i} \quad (2.10)$$

2.2.2 Fiber Bragg Gratings Sensors

The Fiber Bragg Gratings (FBGs) are spectrometric (wavelength-based) sensors, i.e. when the fiber is interacted by an external perturbation the sensor exhibits a change in the propagating optical wavelength. The FBGs are created by periodic modulations of the fiber core's refractive index. Among several methods, the modulation can be achieved with the interference of two laser beams [81], where there is a photo-degradation of the silica when the grating is inscribed [82], and this photo-degradation is related to the wavelength intensity of the light source employed [83]. The periodic index-modulated structure leads to the reflection of a specific wavelength (the Bragg wavelength). Figure 2.11 presents a schematic representation of FBGs working principle.

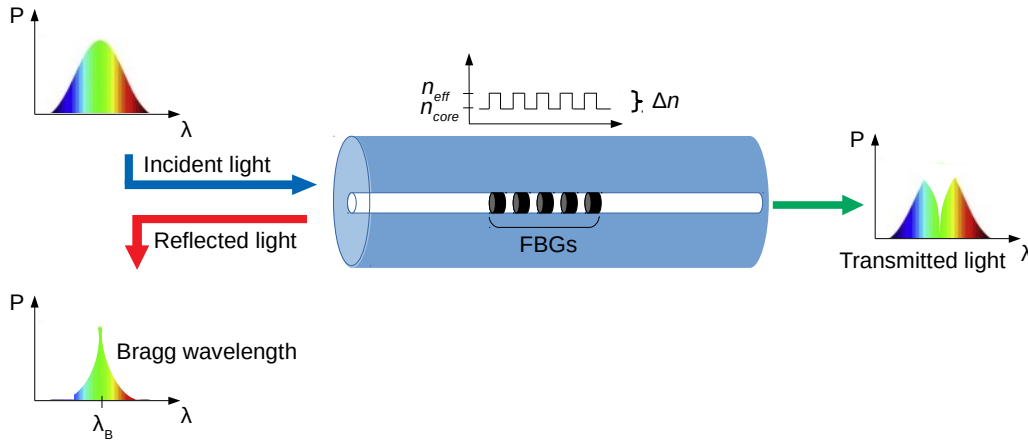


FIGURE 2.11: Working principle of an FBG.

In the fabrication of an FBG, the Bragg wavelength (λ_B) depends on the material effective refractive index (n_{eff}) and modulation period (Λ), as shown in Equation 2.11.

$$\lambda_B = 2n_{eff}\Lambda \quad (2.11)$$

The Bragg wavelength of FBG sensor strongly depends on applied strain to the FBG and local temperature surrounding it. The shift in the Bragg wavelength due to

the strain and temperature is given by Equation 2.12. For this sensibility to strain and temperature, the Bragg wavelength is sensitive to a range of physical parameters, and thus, an FBG can be used as a sensor in a variety of applications [60].

$$\frac{\Delta\lambda_B}{\lambda_B} = (1 - P_e)\epsilon + (\alpha_T + \xi)\Delta T, \quad (2.12)$$

where $\Delta\lambda_B$ is the Bragg wavelength shift, λ_B is the Bragg wavelength, P_e is the photoelastic constant, α_T is the thermal expansion coefficient of the fiber, ξ is the thermo-optic coefficient, ΔT is the temperature variation, and ϵ is the strain [60].

2.2.3 Transmission-Reflection Analysis for Distributed Sensors

In detection systems along an optical fiber sensor, the distributed [84] and quasi-distributed [85] approaches are employed for disturbances location assessment in a kilometer range. Distributed optical fiber sensors are mainly based on optical time-domain reflectometry (OTDR) and optical frequency-domain reflectometry (OFDR) with spatial resolution on the ranging from centimeters to meters [84]. Although such spatial resolution is proportionally high when sensing lengths in the order of kilometers are considered, such spatial resolution in order of meters is regarded as a low spatial resolution in systems with sensing lengths as small as 8 meters, for example. In addition, such approaches have a complex interrogation system with bulk and costly components such as modulated light sources and, in some cases, microwave photonic circuits [84]. Such systems can also present acquisition rate of a few samples per second, which inhibit their application in dynamic events assessment.

As an alternative approach for distributed optical fiber sensors, the transmission-reflection analysis (TRA) has been proposed [86]. In this case, the transmitted and reflected optical powers are measured and correlated with the location and amplitude of mechanical perturbations on the optical fiber [87]. Therefore, a distributed sensor system is obtained with portable and low cost components, which is suitable for mechanical perturbation detection in different (including wearable) applications. Although there are many reports of TRA-based distributed sensors for parameters such as leak localization (through the mechanical disturbances in the optical fiber due to polymer swelling) [88], intrusion detection [89] and strain sensing [87], most of the reports are dated back to the early 2000s. The reason for this more than 10 years' gap can be related to the poor spatial resolution of the sensor (in the order of meters). Such low spatial resolution is due to the low Rayleigh scattering coefficient of standard single mode fibers (SMFs), which result in a low backscattered optical signal. However, a novel optical fiber was recently proposed [74] in which the fiber core is composed of silica and sub-200 nm oxide nanoparticles. In this optical fiber, there is an increase of the Rayleigh scattering (when compared with standard SMFs), which results in a higher backscattered optical power, leading to an increase in the spatial resolution of TRA-based systems [73].

Thus, in distributed sensors using TRA, there is an increase on the backscattered optical power without high transmission losses. It is well known that mechanical disturbances, such as bending, lead to variations on the transmitted optical power and such variations are proportional to the bending angle or momentum [90]. Such mechanical disturbances also influence the backscattered optical power, which is commonly used in distributed sensing for estimating the disturbance location [86]. For the mechanical disturbance localization using TRA, the ratio between transmitted and reflected optical powers are employed and their unique relation at each

disturbance location and amplitude result in the disturbance location estimation. In this case, the disturbance location along the fiber can be achieved with unmodulated light source, which reduces the system cost, when compared with the reflectometry-based distributed systems [87].

In TRA, the transmitted optical power is affected by the amplitude of the displacement in the fiber and has relative insensitivity to the location of such disturbance as commonly occurs in intensity variation-based sensors [91], whereas the reflected (backscattered) is mainly affected by the location where the perturbation is applied in the fiber [73]. If the perturbation occurs close to the light source, there will be a lower backscattered power. In contrast, higher backscattered power is obtained as the distance between source and perturbation location increases. Thus, mechanical perturbation and its localization can be estimated by the analysis of both transmission and reflection optical signals, where unique relations of transmission and reflection are obtained for each location and amplitude of the mechanical perturbation [73].

As any intensity variation-based system, the TRA system is not immune to light source power fluctuations. Thus, the light source power is monitored, where the transmission and reflection optical powers are normalized as a function of the light source in order to obtain a self-compensation for optical power fluctuations [57].

2.3 Biomechanics of Human Movement

The biomechanics of human movement can be defined as the interdisciplinary that describes, analyzes, and assesses human movement. A wide variety of physical movements are involved, from the gait of the physically handicapped to the performance of an athlete. The physical and biological principles that apply are the same in all cases, excepting the specific movement tasks and the level of detail that is being assessed the performance of each movement for each application [92]. The human movement analysis mainly includes gait analysis, posture and trunk movement analysis, and upper limb movement analysis [20].

2.3.1 Human gait

The human gait can be defined as a complex and cyclical process, characterized by periods of loading and unloading of the limbs [18]. It requires the synergy of muscles, bones, and nervous system, mainly aimed at supporting the upright position and maintaining balance during static and dynamic conditions [93]. The gait cycle is defined as the time interval between two successive occurrences of the same event of walking [94]. Such gait events have different classifications in the literature. However for all classifications the cycle is divided in two phases: *stance* and *swing*. The *stance* phase is a term used to designate the period when the foot is on the ground [94]. This phase begins with the first contact of one foot and ends with the next contact of the same (ipsilateral) foot, which will be the initial contact of the next cycle [18]. The *stance* phase can be divided in five subphases, according to the classification of [95]:

1. *Heel strike*, initiates the gait cycle and represents the point at which the body's center of gravity is at its lowest position.
2. *Foot-flat*, is the time when the plantar surface of the foot touches the ground.

3. *Midstance*, occurs when the swinging (contralateral) foot passes the stance foot and the body's center of gravity is at its highest position.
4. *Heel off*, occurs as the heel loses contact with the ground and pushoff is initiated.
5. *Toe off*, terminates the *stance* phase as the foot leaves the ground.

The *swing* phase corresponds to the moment when the foot is oscillation, without contact with the ground. This phase begins when the foot leaves the ground. The *swing* phase can be divided in three subphases, according to the classification of [95]:

1. *Acceleration*, begins as soon as the foot leaves the ground and the subject activates the hip flexor muscles to accelerate the leg forward.
2. *Midswing*, occurs when the foot passes directly beneath the body, coincidental with midstance for the other foot.
3. *Deceleration*, describes the action of the muscles as they slow the leg and stabilize the foot in preparation for the next *heel strike*.

Figure 2.12 shows the gait cycle divided in phases and subphases, according to a traditional nomenclature [95].

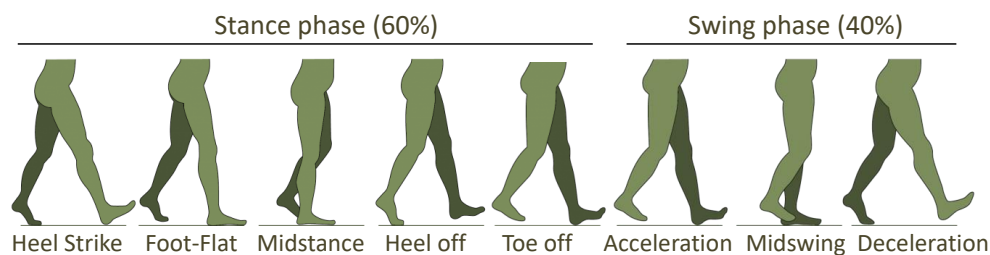


FIGURE 2.12: The traditional nomenclature for describing events of the normal human gait.

2.3.2 Spatio-temporal Gait Parameters

There are several gait parameters used as indicators for gait assessment. [96] mentions many interesting spatio-temporal gait parameters, and some of these ones are presented in Table 2.1. Figure 2.13 shows some spatio-temporal gait parameters cited on Table 2.1 through the foot placement on the ground.

The *step duration* is the temporal difference between the moment of each heel contact, meanwhile the *cycle time* is the temporal difference between the heel contact of the same foot. The division of step length by step duration resulted in *step velocity*. The *walking speed* is the division of the performed distance by the time taken to complete the trajectory. Moreover, the *cadence* is the number of steps taken in a given time, the usual units being steps per minute [94].

2.3.3 Human Balance during Gait

Center of mass (CoM) is a point equivalent of the total body mass in the global reference system and is the weighed average of the CoM of each body segment in 3D space. It is a passive variable controlled by the balance control system. The

Spatio-temporal gait parameters	
Length	Step length Step width Stride length
Time	Step duration Stance time Swing time Cycle time
Velocity	Step velocity Walking speed Cadence

TABLE 2.1: Spatio-temporal gait parameters used for Clinical Gait Assessment.

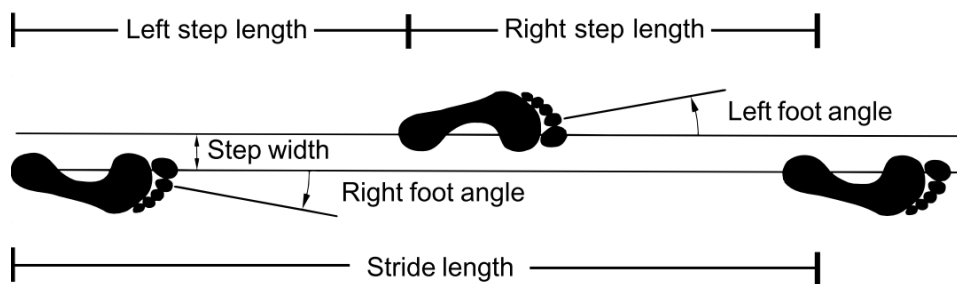


FIGURE 2.13: Terms used to describe foot placement on the ground.

Source: Adapted from [94]

vertical projection of the CoM onto the ground is often called the centre of gravity (CoG). Its units are metres (m) [97].

Stable gait is achieved as a function of the CoM position and velocity at the moment of foot placement [98]. The condition for human stability is the confinement of the CoM in static situations or extrapolated center of mass (XCoM) in dynamic situations within the base of support (BoS). The CoM–BoS interaction is indicative of both static and dynamic balance control ability [99], and there is more noticeable deviations in balance control in elderly people [98].

Margin of dynamic stability (MDS) is determined by CoM or XCoM position relative to BoS boundaries [99], as shown in Figure 2.14, and was used as a measure of balance [98]. MDS reflects the CoM–BoS interaction, and is influenced by voluntary changes in two gait parameters (step width and length) and can be increased by longer steps (larger anterior-posterior BoS) and wider steps (larger medial-lateral BoS) [99].

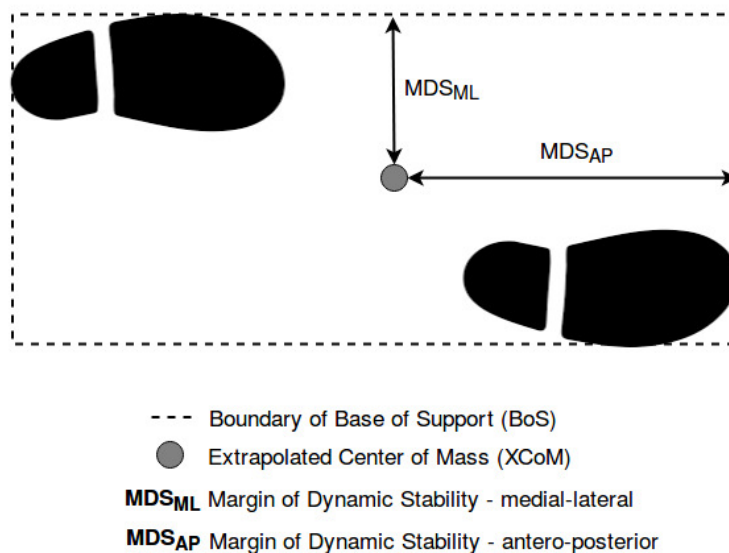


FIGURE 2.14: Margin of Dynamic Stability.

The investigation on human balance during gait has been a research interest for many years, where center of mass and center of pressure investigations under different standing and gait conditions are reported [97]. In this context, the gait analysis under mechanical perturbations provides important insight on human balance control, including the spatiotemporal parameters and dynamic stability in gait [100]. The neuromuscular activity on forward and backward perturbations during gait was also measured, where the magnitude and location of the perturbation can lead to different muscular responses [101]. Thus, the detection of the location and amplitude of the perturbation provide additional information regarding the natural strategies of balance control in humans.

The widespread of wearable robots for gait assistance [5] points towards the development of bioinspired devices from the design with approaches such as the human-in-the-loop design [102] to the device control [103], including bioinspired actuation [104]. The investigation of the human balance control can lead to the development of novel robust control strategies for wearable robots with disturbance rejection [105]. In addition, experimental protocols for mechanical disturbances during exoskeleton-assisted gait provide quantitative and qualitative data regarding the

exoskeleton control robustness, which also indicates the importance of a wearable impact detection system in biomechanical and health monitoring applications.

For impact detection systems, electronic sensors based on capacitive and resistive technologies are commonly used [106]. Recently, the developments of conductive polymers also resulted in pressure sensors embedded in textiles [107]. However, the electromagnetic field sensitivity, lack of multiplexing capabilities as well as the sensor wiring are significant drawbacks in these systems especially when their use with wearable robots is proposed [108]. To that extent, optical fiber sensors have been proposed through the years, since they rely on advantages such electromagnetic field immunity, chemical stability, galvanic isolation as well as compactness and multiplexing capabilities [109], as discussed in Section 2.2.

2.4 Artificial Intelligence in Sensors Technology

Artificial Intelligence, so-called AI, is one area of computer science that focuses on the creation of intelligent machines that normally requires human intelligence [110], [111]. It includes adaptations, learning processes, planning and even problem solving. AI algorithms are designed to make artificial machines capture, store and analyze massive amounts of data. This actionable intelligence allows for a more real-time decision-making process based on a situation that is as human as possible [110].

Machine Learning (ML) is a core part of AI that deals with the simulation of intelligent behaviour in computers. ML is a branch of data science that enables computers to learn from existing “training” data without explicit programming to make predictions about new data points. The another approach Deep learning (DL) is a subset of ML based on neural networks, containing a large number of layers, made possible due to recent computational advances [111]. Figure 2.15 presents the diagram of the AI overview subdivided into Machine Learning and Deep Learning.

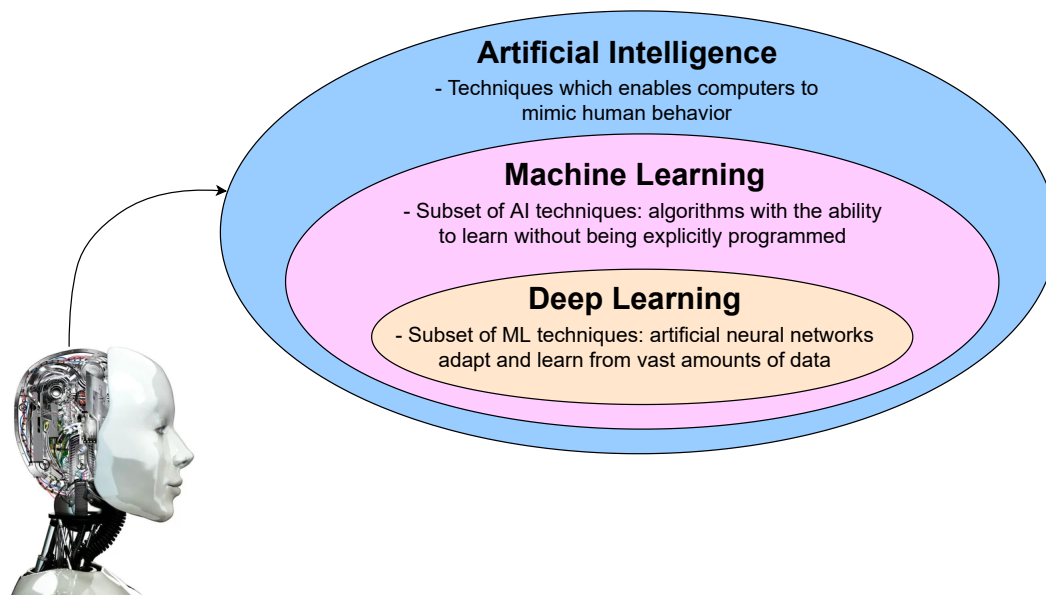


FIGURE 2.15: Artificial Intelligence overview: Machine Learning and Deep Learning.

Source: Adapted from [111]

2.4.1 Machine Learning

Machine Learning, or ML, works by finding and learning a pattern from multiple inputs, and then the machine can perform classification or regression to determine suitable outputs. In this context, ML focuses on using the data to establish correlations and make predictions. When providing sufficient examples of the different classes, algorithms “learn” how to classify novel data.

The learning technologies (ML and DL) can be categorized into unsupervised learning and supervised learning. Unsupervised learning is defined as output which is not supervised, which results in a set of unexplained variables due to unstructured and unlabeled data. A typical example of ML-unsupervised algorithm is the k-means clustering, which can generate novel groupings or categories from complex and unlabeled data sets [111]. In contrast, the supervised learning can be defined as a statistical model that will predict and estimate outputs based on one or more labeled inputs [110]. ML-supervised learning include different types of algorithms, including probabilistic classification models, such as Naive Bayes classifier; or distance-based algorithms, such as k-Nearest Neighbor (kNN). Moreover, ML algorithms also include support vector machines, random forests and decision trees. This Ph.D. Thesis focuses on using the kNN algorithm due to its simple implementation and significant classification performance for sensors applications [112], and, for this reason, the theory behind this technique is addressed below.

k-Nearest Neighbor (kNN) algorithm

The KNN classification is based on a similarity measure, usually a distance function, to the already stored available data. Before understanding the kNN method, it is essential to present the Nearest Neighbor (NN) algorithm. The NN algorithm involves the data partition into training and testing and stores the training data to classify new data (testing). Each sample from the testing data (v) is associated with the nearest sample from the training data (x_i), and this testing sample is labeled according to the label (y_k) of sample x_i , as presented in Equation 2.13. The classification performance is evaluated by comparing the estimated labels with the actual labels.

$$\{v, y_k\} \rightarrow k = \underset{i}{\operatorname{argmin}}[\operatorname{dist}(v, x_i)] \quad (2.13)$$

The kNN is an extension of the NN algorithm, since kNN considers not only the nearest neighbor, but the k nearest neighbors. Figure 2.16 presents the classification principle of NN and kNN methods. The value k is a parameter that need to be optimized and can be selected by associating with the best classification accuracy in a predefined range. The use of k nearest neighbors may improve the classification efficiency, since it is a more reliable way to classify new data, such presented in Figure 2.16(b), in which the use of the NN method would result in a misclassified output due to the outlier in the training data, but the use of the kNN method resulted in a correct classification of the new data.

2.4.2 Deep Learning

Deep Learning, or DL, involves the adaption and learning of artificial neural networks from a great amount of data. A DL architecture includes a multilayer stack of simple modules, which are subject to learning, and compute non-linear input–output

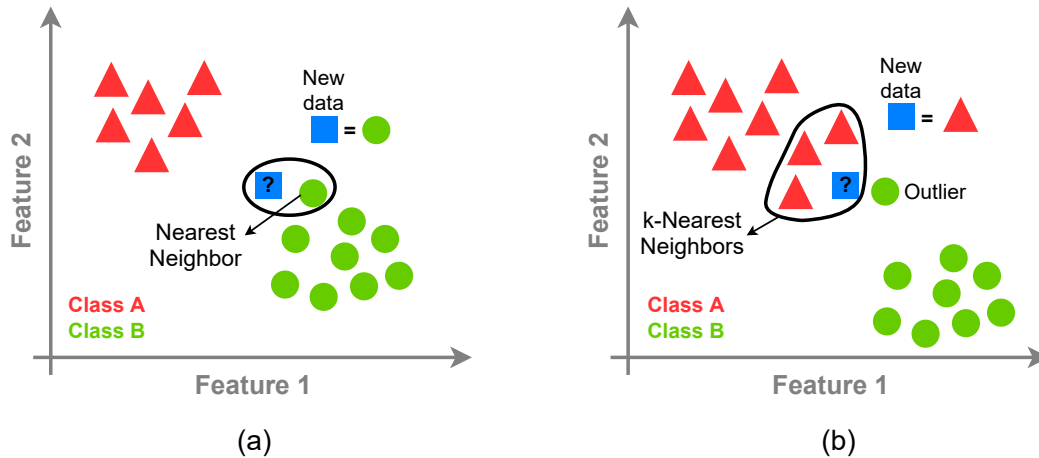


FIGURE 2.16: Classification principle. (a) NN. (b) kNN.

mappings [110], [113]. For classification tasks, multiple non-linear layers of representation amplify aspects of the input that present more influence in the discrimination and suppress irrelevant variations [113]. The key aspect of deep learning is that the layers of features are learned from data using a learning procedure. Thus, the system creates a decision-making function.

The DL process works as follows: (i) during training, the machine produces an output in the form of a vector of scores, one for each category; (ii) an objective function that measures the error (or distance) between the output scores and the desired pattern of scores is computed; (iii) the machine then modifies its internal adjustable parameters to reduce this error. These adjustable parameters, often called weights, are real numbers that define the input–output function of the machine [113].

Many applications of deep learning use feedforward neural network (FFNN) architectures, which learn to map a fixed-size input to a fixed-size output with only one way from input to output, without feedback loops [114]. The convolutional neural network (CNN) is one particular type of deep, that is easier to train and better than networks with full connectivity between adjacent layers. CNNs are designed to process data in the form of multiple arrays, such as a colour image composed of three 2D arrays containing pixel intensities in the three colour channels. Typically, CNNs, a class of FFNN, have been used for image-based problems. Another type of deep network is the recurrent neural networks (RNNs). RNNs process an input sequence one element at a time, maintaining in their hidden units a ‘state vector’ that contains information about the history of the past elements of the sequence [113]. Although their main purpose is to learn long-term dependencies, theoretical and empirical evidence shows the difficulty of storing information for very long. To overcome this difficulty, one idea is to augment the network with an explicit memory, and one proposal is the long short-term memory (LSTM) networks that use special hidden units, called the memory cell, to remember inputs for a long time [115].

Among various deep learning algorithms, different applications require specific neural network types. In the applications of this Ph.D. Thesis, the data did not have a dependency on past samples. For this reason, the use of neural networks with memory (RNN or LSTM) was not the most adequate. Furthermore, the data were not in the multi-array format, such as the cases in which CNN is designed. Therefore, the traditional FFNN is the only model applied in this Ph.D. Thesis, and the theory is discussed as follows.

Feed-Forward Neural Network

As previously discussed, the FFNN is a simple type of neural network commonly employed in several applications. The FFNNs have three main layers: input layer, hidden layer, and output layer, as shown in Figure 2.17. The input layer is connected to the hidden layer (or layers), which is (are) connected to the output layer. The raw data comprise the input layer. There are weights on the connections between the input and hidden layers, and these weights combined with the input layer determine the activities of the hidden units. Similarly, there are weights on the connections between the hidden layers and output layer, and these weights combined with the hidden layers determine the activities of the output layer. The advantage of the FFNN architecture is the ability of the hidden layers in choosing their representations of the inputs by suitably modifying these weights [113].

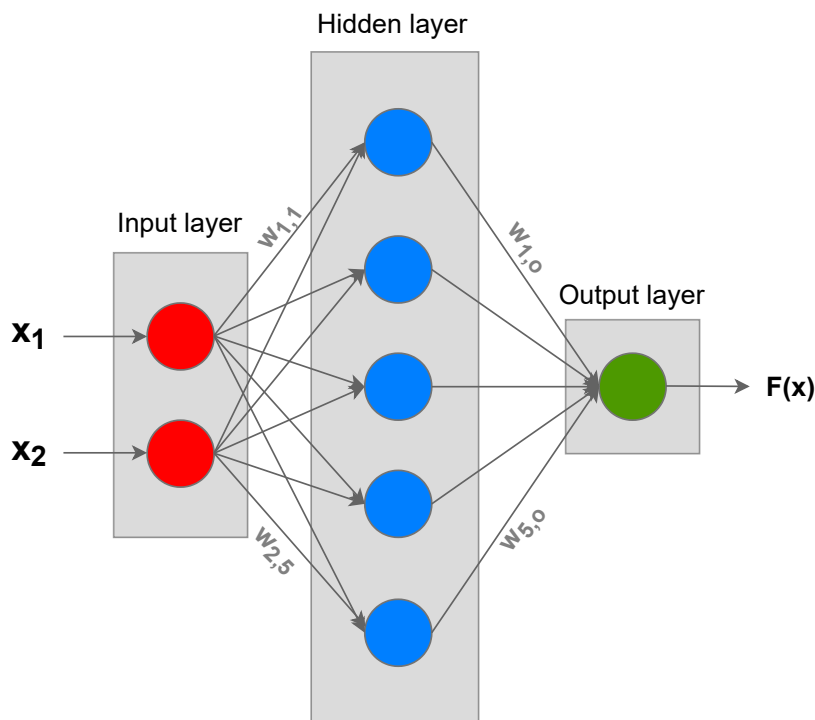


FIGURE 2.17: FFNN architecture.

After training, the network learns to recognize certain inputs and returns the correct outputs. Therefore, the objective of the network training algorithm is to build a mapping between the input-outputs samples to form the relationship. This mapping could be a classifier (in classification problems) or a regression function (in approximation problems). For a single training example, the loss error is computed to measure the performance of this sample. The average of the loss function of the entire training set is called cost function [116]. A cost function is introduced to measure the performance of the neural network. The commonly used cost function is the mean squared error (MSE), defined in Equation 2.14,

$$E = \frac{1}{L} \sum_{i=1}^L \|y_i - \hat{y}_i\|^2, \quad (2.14)$$

where L is the number of training samples, and y_i and \hat{y}_i represent the desired and actual outputs corresponding to the input of the i_{th} sample. Different types of

loss function are used in the literature, such as root mean squared error (RMSE) loss or mean absolute error (MAE) loss, for regression loss functions, and binary cross-entropy or categorical cross-entropy, for classification loss functions.

Cross-entropy is the outstanding part of the category of probability-based loss functions [117]. For binary classification, the binary cross-entropy loss function measures how distant from the true value (which is either 0 or 1) the prediction is for each of the classes and then averages these class errors to obtain the final loss [116]. The standard binary cross-entropy (BCE) function is defined in Equation 2.15 [116], where N is the number of training samples, y_n is the target label for sample n , x_n is the input for sample n and h_θ is the model with neural network weights θ .

$$BCE = -\frac{1}{N} \sum_{n=1}^N [y_n \cdot \log(h_\theta(x_n)) + (1 - y_n) \cdot \log(1 - h_\theta(x_n))] \quad (2.15)$$

For multi-class classification, the categorical cross-entropy loss function is applied when the output can be classified as categorical classes. A technique called one-hot encoding is employed in multi-class classification to convert the categorical class to binary format, and the distribution of the predicted and true labels are compared [116]. The standard categorical cross-entropy (CCE) function is defined in Equation 2.16, where N is the number of training samples, K is the number of classes, y_n^k is the target label for sample n for class k , x_n is the input for sample n and h_θ is the model with neural network weights θ [116].

$$CCE = -\frac{1}{N} \sum_{k=1}^K \sum_{n=1}^N y_n^k \cdot \log(h_\theta(x_{n,k})) \quad (2.16)$$

2.4.3 Data Dimensionality Reduction

In general, the traditional supervised approaches need feature reduction, also called data dimensionality reduction. It is necessary to reduce model complexity and avoid overfitting, i.e., memorizing the training sample cases rather than learning the relevant pattern [111]. Different data dimensionality reduction techniques are employed in the literature. Principal Component Analysis (PCA) is a statistical procedure which uses an orthogonal transformation, i.e., PCA converts a group of correlated variables to a group of uncorrelated variables. Another popular dimensionality reduction approach is the Linear Discriminant Analysis (LDA), which aims to project a dataset with high number of features onto a less-dimensional space with good class-separability [118]. Different from PCA, the LDA is a supervised linear mapping. As well as PCA, the Independent Component Analysis (ICA) is an unsupervised linear dimensionality reduction technique. ICA is a process of extracting independent components from linear transformations of the original data. Different from PCA, the ICA components do not have to be orthogonal. Moreover, PCA tries to maximize the variance of the input signal along with the principal components, whereas ICA minimizes mutual information in found components. Thus, the features obtained in the PCA are sorted from most significant to least significant, and it is possible to discard some of the features to reduce the dimension, whereas components obtained in ICA are fundamentally unordered and equivalent and can not be sorted [119]. For this reason, PCA is the technique employed in this Ph.D. Thesis, and the theory behind the technique is addressed below.

Principal Component Analysis (PCA)

PCA is not an attribute selection technique, but a technique from the field of linear algebra which converts an attribute set to a new dataset linearly uncorrelated, obtained from the linear combination of the original attributes, so-called principal components. As the principal components have a sample-like pattern with a weight for each attribute, we can use the weights to visualize the influence of each attribute on the dataset [120].

Considering the matrix $X_{n \times D}$, in which the rows represent the samples and the columns represent the attributes, each sample is normalized by subtracting the attribute mean (μ_j) and dividing by the attribute standard deviation (σ_j), as shown in Equation 2.17.

$$\hat{x}_{i,j} = \frac{x_{i,j} - \mu_j}{\sigma_j}, \quad j = 1, 2, \dots, d \quad i = 1, \dots, N \quad (2.17)$$

With the new matrix X (with mean 0), the correlation matrix C is calculated by using the Equation 2.18. From this matrix, the eigenvalues (λ) and eigenvectors (V) are obtained.

$$C = \frac{1}{(N-1)} \hat{X}^T \hat{X} \quad (2.18)$$

For the dimensionality reduction, the k eigenvectors associated to the largest eigenvalues are selected to compose the new dataset (Ω_x), calculated by the Equation 2.19. The k eigenvectors are defined by analyzing the variance explained by each principal component, in which the variance might be higher than 99%, and the number of attributes is reduced.

$$\Omega_X^T = X \cdot V_{N \times k} \quad (2.19)$$

The variance explained can be checked by analyzing the pareto chart, which presents the accumulative variance explained according to the principal components, as shown in Figure 2.18.

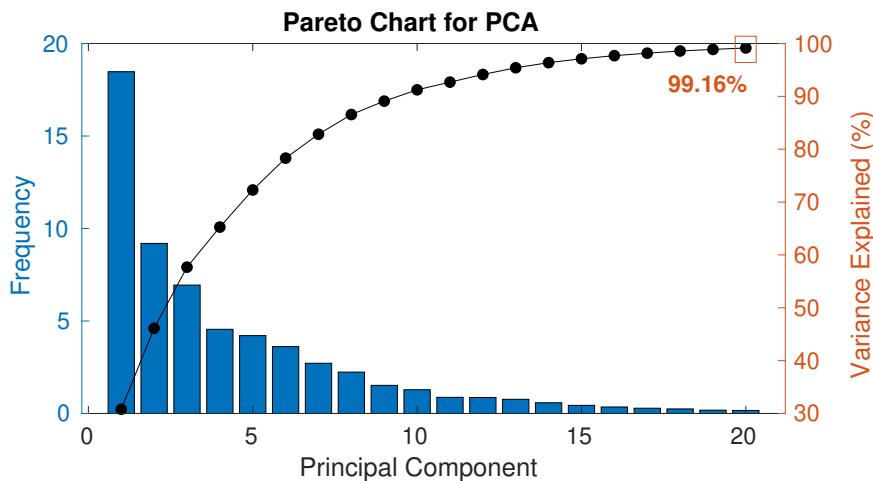


FIGURE 2.18: Pareto chart for the PCA technique.

In this way, by using the PCA technique it is possible to reduce the computational costs by maintaining similar classification performance, which is interesting for online applications or cases which include a great amount of data.

Chapter 3

Development and Performance Analysis of Optical Fiber Sensors for Kinetic and Kinematic Monitoring

The biomechanical parameters in human movement depend on kinetic and kinematic parameters, where the forces/torques and angle/displacements in human movement need to be assessed. For this reason, the performance analysis of optical fiber sensors under forces and angles can indicate the feasibility of using optical fiber sensors in biomechanical applications. This chapter presents the development and the performance analysis of optical fiber sensors (using the intensity variation approach) for the analysis of kinetic and kinematic parameters employed in biomechanical applications (displacements and forces). First, an intensity variation-based curvature sensor using POF is evaluated under different conditions to analyze the influence of light source wavelengths and angular velocities in angle measurement performance. Second, an intensity variation-based force sensor is developed and evaluated embedded in different materials. The objective is to characterize the sensor response and to analyze the ability of estimating the stiffness and the force sensitivity of these optical fibers at different stiffness conditions commonly obtained along the body. It can be employed in several biomedical applications, such as in human-robot interaction, in which the human stiffness feedback is not only valuable for the system control, but it is also a security issue for the robot user. In this context, the analysis presented in this Chapter can provide the data regarding the sensors responses under the kinetic and kinematic conditions of movement analysis.

3.1 Kinematic Parameters (Angle and Angular Velocity) Influence in OFS Responses

Curvature sensors are widely employed in joint angle assessment and they present important information in the human motion analysis [22]. Generally, human joints have large range of movement in the order of tens degrees, e.g. hip, knee, shoulder and elbow with different ranges of angular velocities. For this reason, a POF was used in this analysis due to its higher strain limits and flexibilities, which make them compatible with the large range of movement in human joints. The use of POFs lead to the possibility of using optical fiber sensors for the analysis of different joint movements. Furthermore, the intensity variation principle leads to a portable,

compact and low cost system for movement analysis due to the use of low cost components, i.e., LEDs and photodetectors.

3.1.1 Materials and Methods

The POF was made of a commercial gradient index multimode CYTOP fiber (Chromis Fiberoptics Inc, USA) with a core diameter of $120\ \mu\text{m}$, a cladding thickness of $20\ \mu\text{m}$ and a polycarbonate overcladding. The light sources were five light emitting diodes (LEDs) with different central wavelengths (λ): $430\ \text{nm}$, $530\ \text{nm}$, $660\ \text{nm}$, $870\ \text{nm}$ and $950\ \text{nm}$ (IF-E92A, IF-E93, IF-E97, IF-E91D and IF-E91A, respectively, Industrial Fiber Optics, USA). The selected LEDs correspond to different central wavelength of visible light region (blue - $430\ \text{nm}$, green - $530\ \text{nm}$ and red - $660\ \text{nm}$) and different central wavelength of infrared region ($870\ \text{nm}$ and $950\ \text{nm}$). The optical power was converted into an electrical signal using a phototransistor IF-D92 (Industrial Fiber Optics, USA) and the acquisition was made through a microcontroller FRMD-KL25Z (NXP Semiconductors, Netherlands), at a sampling rate of $100\ \text{Hz}$. The data was filtered through the moving average filter with span of 5% , in order to eliminate the outliers observed in the measurements. The angle and the angular velocity were controlled using a servo motor to emulate the joints movement (although there is a constant center of rotation). Figure 3.1 shows the experimental setup for evaluation of the POF-based curvature sensing performance using CYTOP fiber.

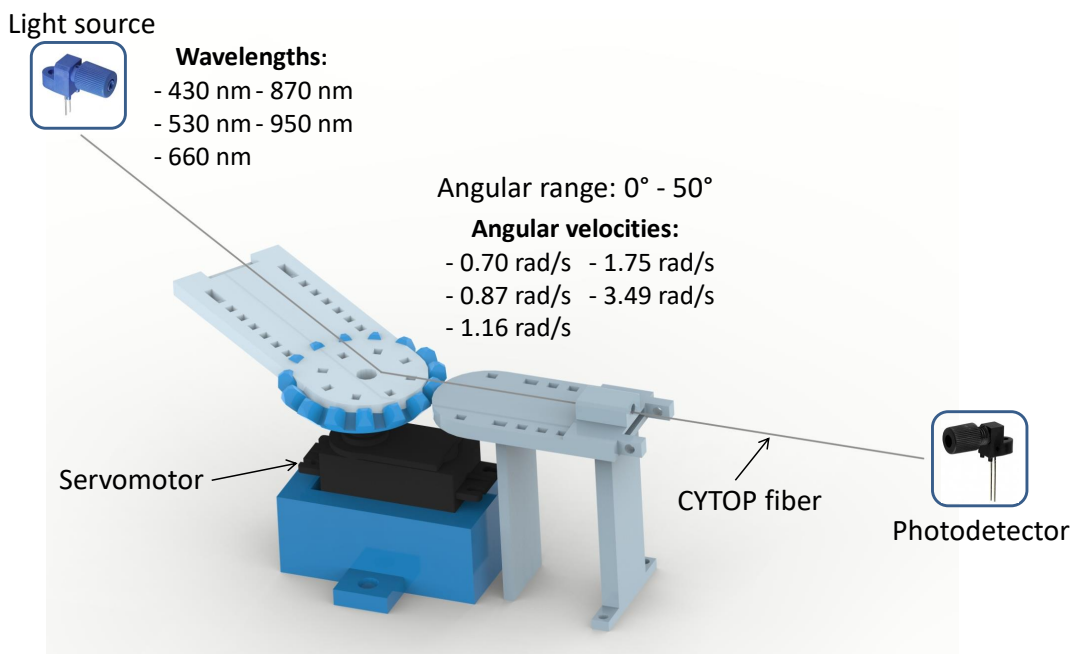


FIGURE 3.1: Experimental setup for evaluating the curvature sensor based on CYTOP fiber.

3.1.2 Experimental Procedures

The experimental protocol was divided into two parts to evaluate the performance of the CYTOP fiber under curvature: (i) influence of different light source central wavelengths and (ii) influence of different angular velocities due to the frequency dependency of the viscoelastic materials, resulting velocity-dependent performance. Both approaches consisted of curvature tests with angular range from 0 to $50\ \text{degrees}$

and steps of 10 *degrees*, where the angular velocity and angles are applied on the fiber through the servo motor shown in Figure 3.1. This range was defined according to lower limb joints angles during gait and limited at 50 *degrees* to ensure the possibility of using higher angular velocities due to the servo motor angular range and velocity limitations. However, it is important to mention that such range is sufficient to analyze the sensors' performance as a function of the kinematic parameters. The analysis of the opposite bending (−50 to 0 *degrees*) can be performed through lateral sections made in the fiber to create a sensitive zone. In the case of concave bending, there is an increase in reflections on the convex side of the curvature and a decrease on the concave side. Thus, if the lateral section is made in the concave side, the output power is higher for concave bending and lower for convex bending, and it is possible to identify the bending direction [30].

In the analysis of light source influence in angle responses, curvature tests with angular velocity of 0.87 *rad/s* were performed to ensure a constant velocity throughout the light source tests. In addition, LEDs with different central wavelengths were employed to compare the responses related to wavelength. Sensitivity, hysteresis and R^2 were analyzed, and through these factors, the figure of merit (FoM) was calculated, as shown in Equation (3.1) in order to characterize the wavelength which results in the higher FoM, consequently the best sensor performance. In Equation (3.1), S is the sensitivity, h is the hysteresis, R^2 is the determination coefficient, and α , β , θ are coefficients which define the weight of each performance factor defined considering the possibility of hysteresis compensation and requirements of low errors and resolution. It is important to mention that different weights can be attributed for each parameter considering the sensor application. Thus, these parameters were chosen to provide a first analysis of the sensor and can be changed or even optimized for specific applications.

$$FoM = \alpha \cdot S - \beta \cdot h + \theta \cdot R^2 \quad (3.1)$$

Thereafter, tests with different angular velocities (0.70 *rad/s*, 0.87 *rad/s*, 1.16 *rad/s*, 1.75 *rad/s* and 3.49 *rad/s*), which were chosen considering the viscoelastic response of the material at different frequencies [60] and the light source central wavelength previously defined by FoM were conducted to evaluate the influence of velocity in the curvature sensor performance (sensitivity, hysteresis and R^2).

Based on these tests, an angular velocity compensation technique was proposed to reduce the root-mean-square error (RMSE) in different angular velocities (see section 3.1.3). In both approaches, 10 tests were performed.

3.1.3 Statistical analysis and angular velocity compensation

A Shapiro-Wilk test was used to verify the data normality. Since the data are normal, one-way ANOVA (analysis of variance) was applied to determine if significant differences in sensitivity, hysteresis and angular error existed among different angular velocities with a significance level of 0.05, and the significant angular velocity groups were defined through this analysis.

In order to reduce the RMSE of angle measurements, compensation models were developed for each angular velocity group. Figure 3.2 shows the state machine diagram describing the proposed angular velocity compensation, in which "QS" block comprises the model obtained on a quasi-static test, i.e. calibration curve with the lowest influence of the sensor angular velocity, and C_i comprises the compensation

models for respective angular velocity range. The models were obtained by using the Least Squares Method.

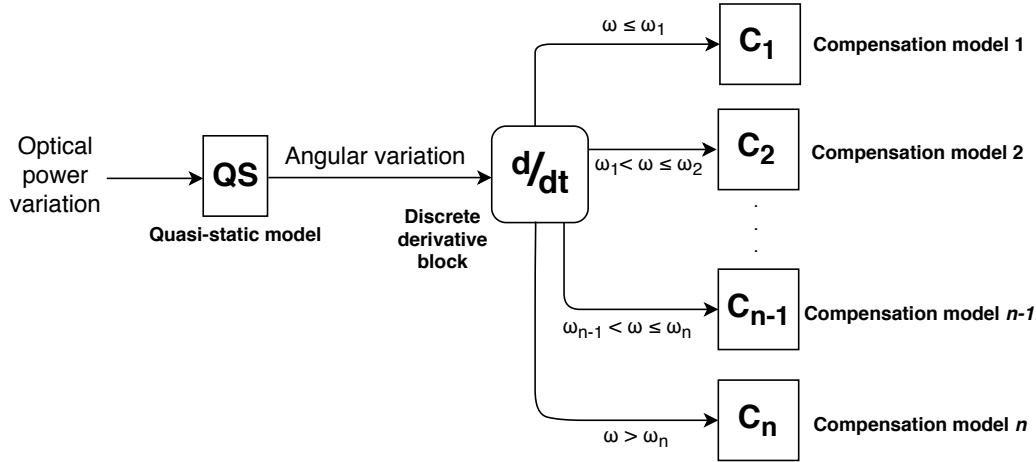


FIGURE 3.2: State machine diagram of the angular velocity compensation.

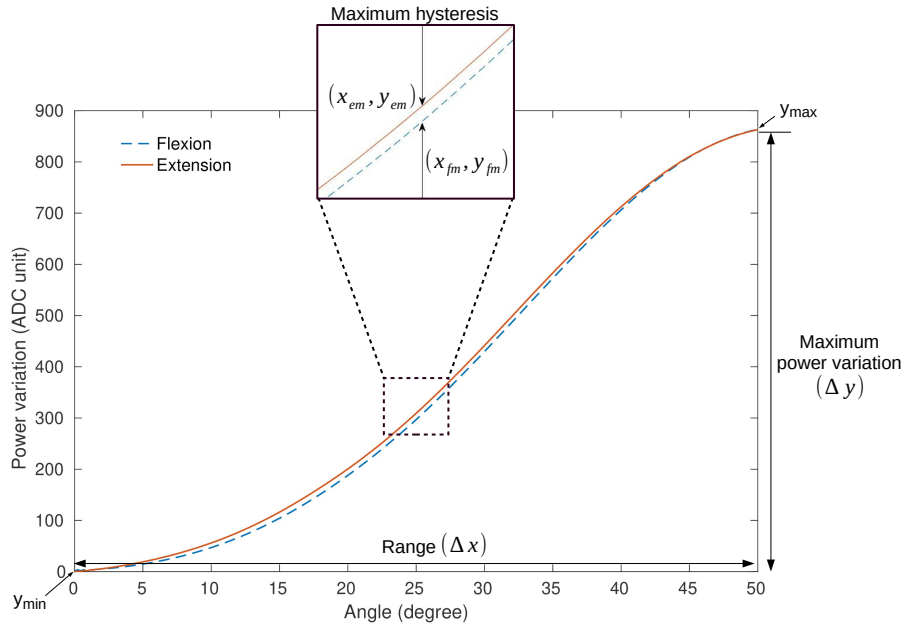
Since the CYTOP is a viscoelastic material, its strain response depends on the time and the polymer relaxation can lead to the sensor hysteresis and possible variations on its linearity. In order to obtain a response close to the ideal (servo motor input), i.e. linear response, the compensation models were based on a sum of exponential with order 2 (since the fiber has a combination of two materials: perfluorinated polymer in the core/cladding and polycarbonate in the overcladding) as shown in Equation (3.2), where a_n are the model coefficients, α is the compensated angle ($^\circ$) and P is the sensor power variation (ADC unit).

$$\alpha = a_1 \cdot e^{a_2 \cdot P} + a_3 \cdot e^{a_4 \cdot P} \quad (3.2)$$

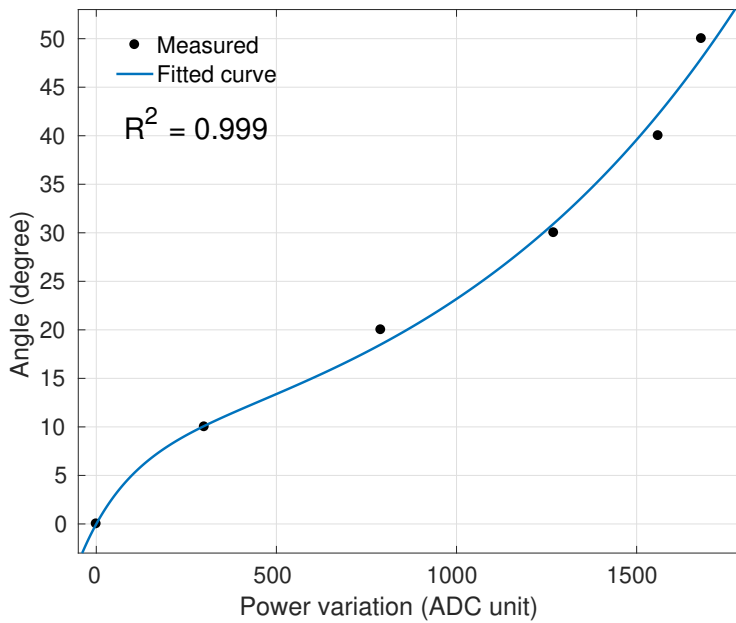
The analysis of POF curvature sensor in CYTOP fiber is based on three performance factors: sensitivity, hysteresis and R^2 . Figure 3.3(a) shows the concept of sensitivity and hysteresis applied in one result, where R^2 corresponds to the determination coefficient with a exponential regression, as shown in Figure 3.3(b). The sensitivity is defined as the variation of the optical signal as a function of the measurand variation, which is acquired as the slope in the characterization curve, as also shown in Equation (3.3). The hysteresis is the differences between loading and unloading curves, where the relative difference between these curves is considered and can be calculated with Equation (3.4).

$$Sensitivity = \frac{\Delta y}{\Delta x} \quad (3.3)$$

$$Hysteresis(\%) = \frac{100 \cdot (y_{em} - y_{fm})}{\Delta y} \quad (3.4)$$



(a)



(b)

FIGURE 3.3: (a) Flexion and extension applied on CYTOP fiber showing the sensitivity and hysteresis concept. (b) Exponential regression of one curvature test showing the determination coefficient R^2 .

3.1.4 Results and Discussion

Analysis of different light source central wavelengths

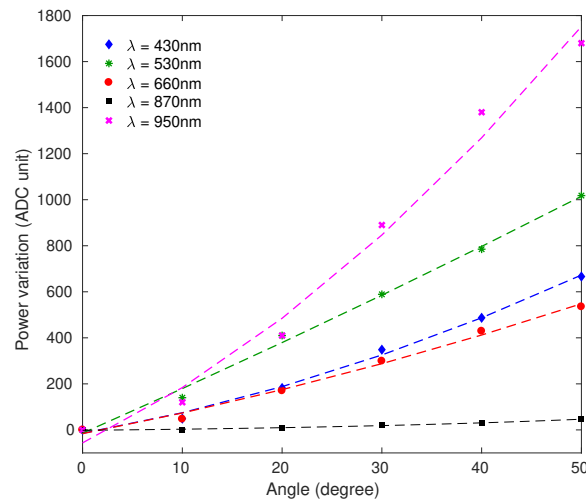
Figure 3.4(a) presents the sensors' responses to the curvature applied to the CYTOP fiber (angular range from 0 to 50 *degrees* and constant angular velocity of 0.87 *rad/s*) for different central wavelengths (λ), in which the markers represent the measured output and the dashed lines represent the sensors fit. The sensors' responses presented exponential behavior with R^2 higher than 0.99 in all characterization tests. It is possible to observe the normal distribution of sensitivities in Figure 3.4(b), in which the light source central wavelength of 950 *nm* provide the highest sensitivity (32.63 *ADC unit/deg*) of the sensor, whereas the light source central wavelength of 870 *nm* provide the lowest sensitivity (0.94 *ADC unit/deg*). This may occur due to the some reasons, such as the decreasing optical attenuation curve of CYTOP fiber that presents higher attenuation for $\lambda = 430$ *nm* and lower optical attenuation for $\lambda = 950$ *nm* [31]. In addition, the photodetector as a function of the wavelength presents higher responsivity for 800 *nm* < λ < 950 *nm*.

The photodetector presents the maximum photosensitivity at 870 *nm*, and higher than 90% of the normalized photosensitivity in a range from 800 *nm* up to 950 *n*. The $\lambda = 870$ *nm* should present the second highest sensitivity. However, the current of the tests is lower than the forward current presented in the light source datasheet [121]. Since the currents used in all tests has the same value and the $\lambda = 870$ *nm* need a higher current value, the optical power is relatively lower, as the sensitivity when compared with others light source central wavelengths. In addition, the $\lambda = 660$ *nm* presented the lower sensitivity among the visible spectrum ($\lambda = 430$ *nm*, 530 *nm*, 660 *nm*) due to the lowest full-spectral bandwidth of the light source, resulting in a lower output power, since the photodetector acquires the integral of the light source spectrum, and, consequently, lower sensitivity. For these reasons, the best sensor performance is using the LED with central wavelength of $\lambda = 950$ *nm*.

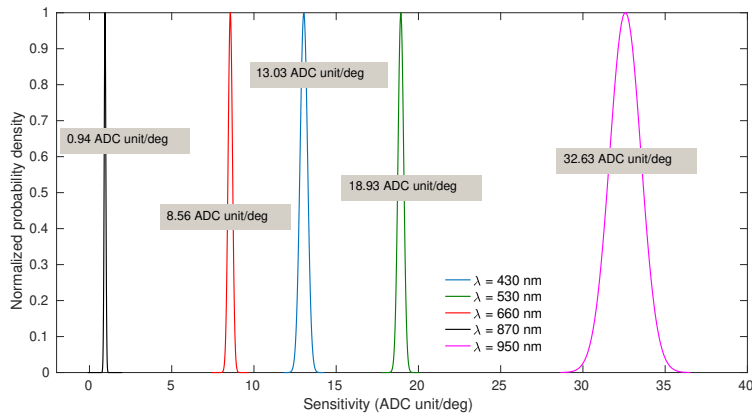
Based on these performance factors, a FoM was applied to calculate the weighted sum of the factors and to select the central wavelength that results the higher FoM. For this analysis, the weighted coefficients for FoM calculation were defined as $\alpha = 0.5$, $\beta = 0.2$, $\theta = 0.3$, since the sensitivity is a important factor which significantly decreases as the angular velocity increases, and hysteresis can be smoothed through some compensation technique [38]. The definition of these factors were made considering previous works in the literature and can be adjusted or optimized for each case or application [122]. Table 3.1 presents the results of each FoM, in which the light source central wavelength of 950 *nm* provides the higher FoM, being the best option for following applications. Although this configuration presented higher hysteresis than other ones, such undesirable parameter is compensated through the proposed hysteresis compensation technique.

TABLE 3.1: FoM of sensor performance for each central wavelength.

λ	Sensitivity	Hysteresis (%)	R^2	FoM
430 <i>nm</i>	13.03	1.78	0.997	6.81
530 <i>nm</i>	18.93	1.66	0.998	9.76
660 <i>nm</i>	8.56	1.44	0.998	4.58
870 <i>nm</i>	0.94	2.60	0.996	0.77
950 <i>nm</i>	32.63	2.73	0.993	16.58



(a)



(b)

FIGURE 3.4: Sensor's response in the curvature characterization with fitted curves: (a) Power variation of each central wavelength in angle range of 50 degrees. (b) Normal distribution of sensitivity for each central wavelength.

Analysis of different angular velocities

After the first set of tests to select the light source central wavelength, tests with the angular range from 0 to 50 degrees and different angular velocities are performed, as shown in Figure 3.1. Figure 3.5 shows the results of measurements without data treatment for the different angular velocities with the light source central wavelength selected in the previous analysis. All graphs show curvature cycles performed during the same time variation at different angular velocities. It is noticeable that the sensor responses present low noise. However, the moving average filter is used to eliminate the outliers observed in the measurements. The filter has order 1 and did not resulted in significant delays in the signal. The three performance factors (sensitivity, hysteresis and R^2) are analyzed, and Table 3.2 shows the mean and the standard deviation (SD) of sensitivity (ADC unit/°), hysteresis (%) and angular error (°) of tests for each angular velocity.

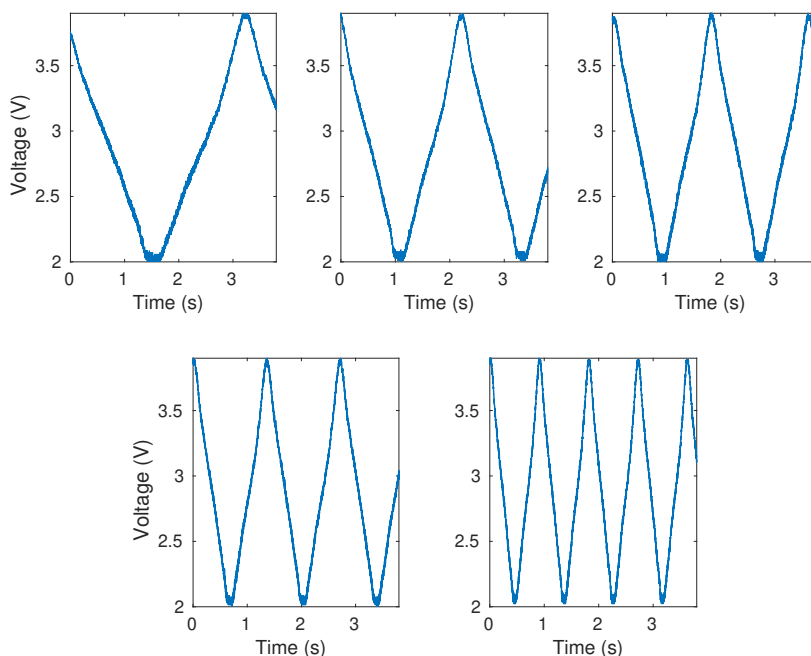


FIGURE 3.5: Raw measurements for each angular velocity.

TABLE 3.2: Mean(SD) of sensor performance factors for each angular velocity.

Angular velocity	Sensitivity	Hysteresis (%)	Angular error (°)
3.49 rad/s	12.85(2.14)	3.12(2.82)	25.25(2.00)
1.75 rad/s	33.01(0.48)	2.37(2.14)	1.31(0.77)
1.16 rad/s	33.33(0.38)	1.17(0.89)	0.82(0.55)
0.87 rad/s	32.63(0.39)	2.73(2.48)	1.16(0.63)
0.70 rad/s	33.33(0.36)	1.72(1.13)	0.78(0.58)

According to Table 3.2, it is noticeable that $w = 3.49 \text{ rad/s}$ presented worst performance compared with others velocities, with lower sensitivity, equivalent to approximately 40% of the others, error of $25.25^\circ (\pm 2.00^\circ)$, corresponding to 50%

of error and highest hysteresis of $3.12\%(\pm 2.82\%)$. Excluding this angular velocity ($w = 3.49 \text{ rad/s}$), all data are normal and the one-way ANOVA test showed that the sensitivities did not showed significant difference ($p = 0.1831$), as well the hysteresis ($p = 0.1042$) and the angular error ($p = 0.1841$). In addition, the maximum angular error was of $1.31^\circ(\pm 0.77^\circ)$, which corresponds to 2.62% of error, and the minimum angular error was of $0.78^\circ(\pm 0.58^\circ)$, which corresponds to 1.56% of error. These results show that the sensor is repeatable and presents similar responses for this angular velocity range (0.70 to 1.75 rad/s) and as the velocity increases, the sensor performance decline. All angular velocities presented R^2 higher than 0.99. The mean of the cycles at each angle for all tested angular velocities presented low hysteresis, as shown in Figure 3.6, in which h is the hysteresis and ω is the angular velocity.

In addition to angular errors, the sensor responses presented high RMSE with maximum mean of $12.41^\circ(\pm 1.49^\circ)$ and minimum of $6.45^\circ(\pm 0.43^\circ)$. For this reason, the angular velocity compensation technique was applied in order to decrease the RMSE of angle measurements according to the angular velocity. Since the angular velocity range from 0.70 to 1.75 rad/s did not present significant differences, the angular velocity compensation technique was fitted for two groups: first group (angular velocities lower than or equal to 1.75 rad/s) and second group (angular velocities higher than 1.75 rad/s). The C_1 and C_2 blocks comprise the compensation models for two angular velocity groups. Equations (3.5), (3.6) and (3.7) show the compensation models QS, C1 and C2 (see Figure 3.2) relating the optical power variation (P) with angle, respectively.

$$QS(P) = 16.43 \cdot e^{-0.0007 \cdot P} - 16.40 \cdot e^{-0.0061 \cdot P} \quad (3.5)$$

$$C_1(P) = 8.93 \cdot e^{0.0010 \cdot P} - 9.75 \cdot e^{-0.0080 \cdot P} \quad (3.6)$$

$$C_2(P) = 12.53 \cdot e^{0.0025 \cdot P} - 12.84 \cdot e^{-0.0091 \cdot P} \quad (3.7)$$

Figure 3.7 shows the angle curves of characterized sensors responses in a quasi-static tests (uncompensated) and with the angular velocity compensation (compensated) compared to the servo motor input (reference) in one test, and Table 3.3 shows the RMSE of angle measurements for uncompensated and compensated response in each angular velocity.

TABLE 3.3: Mean(SD) RMSE of angle measurements for each angular velocity with uncompensated and compensated responses.
*Excluding outliers.

Angular velocity	Uncompensated	Compensated
3.49 rad/s	$12.41^\circ(1.49^\circ)$	$3.62^\circ(1.32^\circ)^*$
1.75 rad/s	$6.93^\circ(1.30^\circ)$	$1.94^\circ(0.97^\circ)$
1.16 rad/s	$6.45^\circ(0.43^\circ)$	$1.67^\circ(0.27^\circ)$
0.87 rad/s	$6.90^\circ(1.07^\circ)$	$2.03^\circ(0.63^\circ)$
0.70 rad/s	$7.97^\circ(1.27^\circ)$	$2.33^\circ(0.72^\circ)$

The compensated responses presented a RMSE decrease up to 74% ($w = 1.16 \text{ rad/s}$), with minimum error of $1.67^\circ(\pm 0.27^\circ)$ for angular velocity of $w = 1.16 \text{ rad/s}$. The

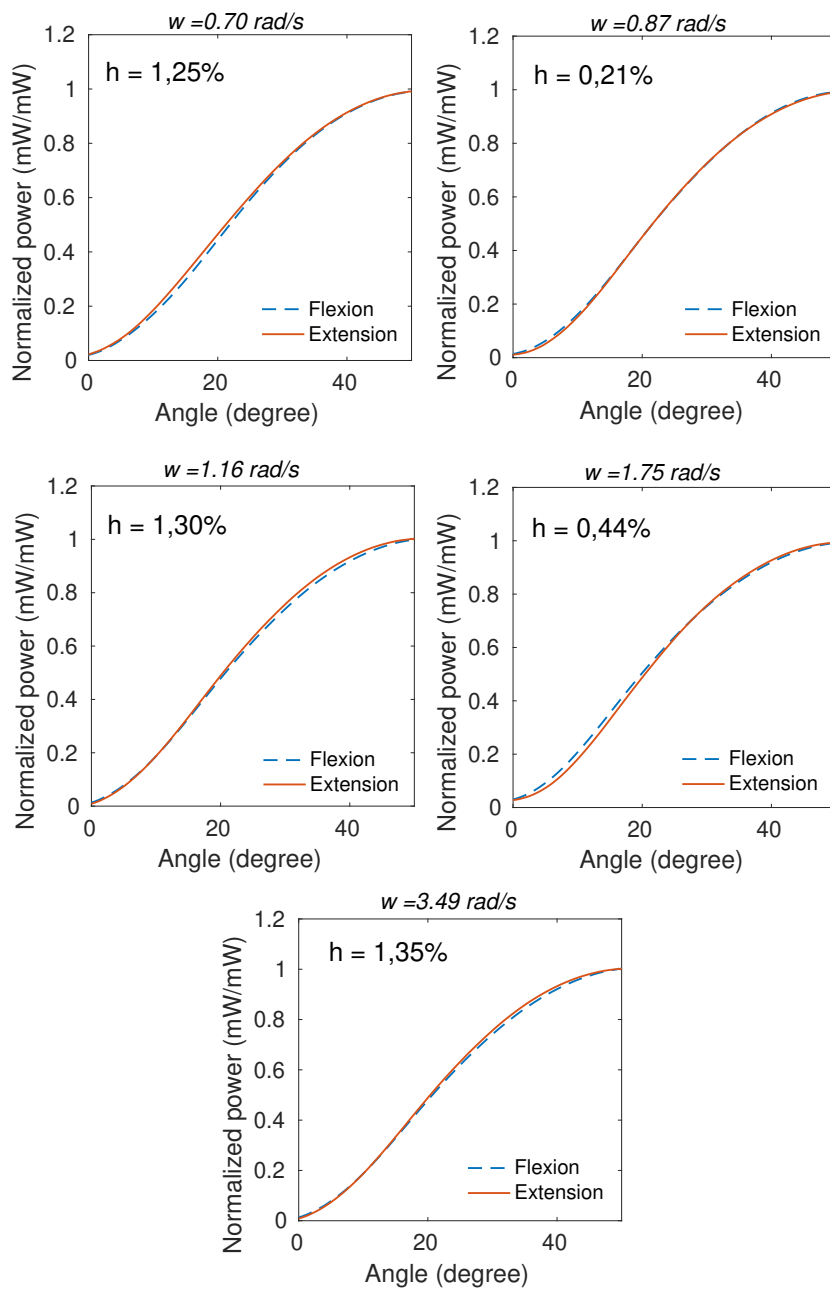


FIGURE 3.6: Mean of the cycles at each angle presenting the mean hysteresis for each angular velocity.

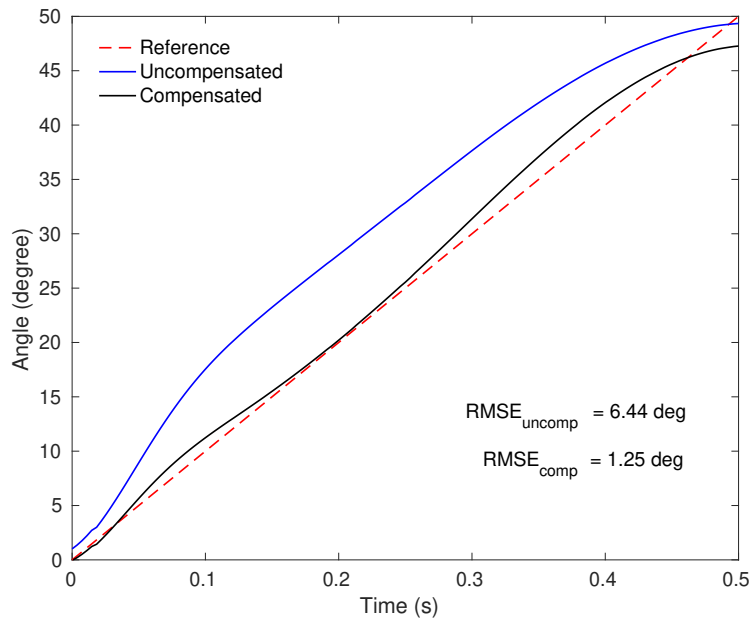


FIGURE 3.7: Angle curves with and without angular velocity compensation compared with the reference of one test.

higher angular velocity ($w = 3.49 \text{ rad/s}$) presented two cycles with major differences from the others, resulting in $\text{RMSE } 6.85^\circ (\pm 5.23^\circ)$. However, excluding these two cycles the RMSE was $3.62^\circ (\pm 1.32^\circ)$. Although the responses demonstrate worst performance in this angular velocity, the two different cycles may be related to servo motor performance at high velocities, presenting errors up to three times higher than the mean, which can be considered outliers.

3.2 Force assessment using Intensity Variation-based OFS

After the analysis of the optical fiber sensor performance under kinematic parameters, the POF was analyzed in force application conditions in which it is possible to infer the sensor responses under kinetic parameters. Such analysis enable the evaluation of the proposed sensor in the dynamic conditions of the disturbances protocols as well as in the ground reaction forces and plantar pressure sensors.

3.2.1 Materials and Methods

The POF was made of a commercial gradient index multimode CYTOP fiber with a core diameter of $120 \mu\text{m}$, a cladding thickness of $20 \mu\text{m}$ and a polycarbonate overcladding, resulting in a diameter of 0.5 mm . The sensor consists of a light source laterally coupled to the fiber in order to transmit the light to the fiber core (see Figure 3.8). The light source used is a LED flexible lamp belt. To increase the light transmission to the core and, hence, increase the sensor sensitivity, a lateral section is made on the fiber, following the guidelines presented in [30].

The transmitted optical power was converted into an electrical signal using a phototransistor IF-D92 (Industrial Fiber Optics, USA) positioned at the fiber end facet, and the acquisition was made through a microcontroller FRMD KL25Z, at a sampling rate of 100 Hz and a 16-bit ADC resolution. A reference for the applied

force was acquired by a load cell LCM201 (Omega, USA). The proposed force sensor not only can measure the force applied directly on the LED coupled region of the sensor, but also can detect the impact along the fiber. In this analysis, the tests were made with only one sensor. However, this setup enables the addition of more multiplexed sensors, since each sensor can have its own light source. Thus, the analysis of the laterally coupled light source is performed, which also leads to higher sensitivity, since minor variations on the LED positioning as a function of the fiber position also results in optical power variations.

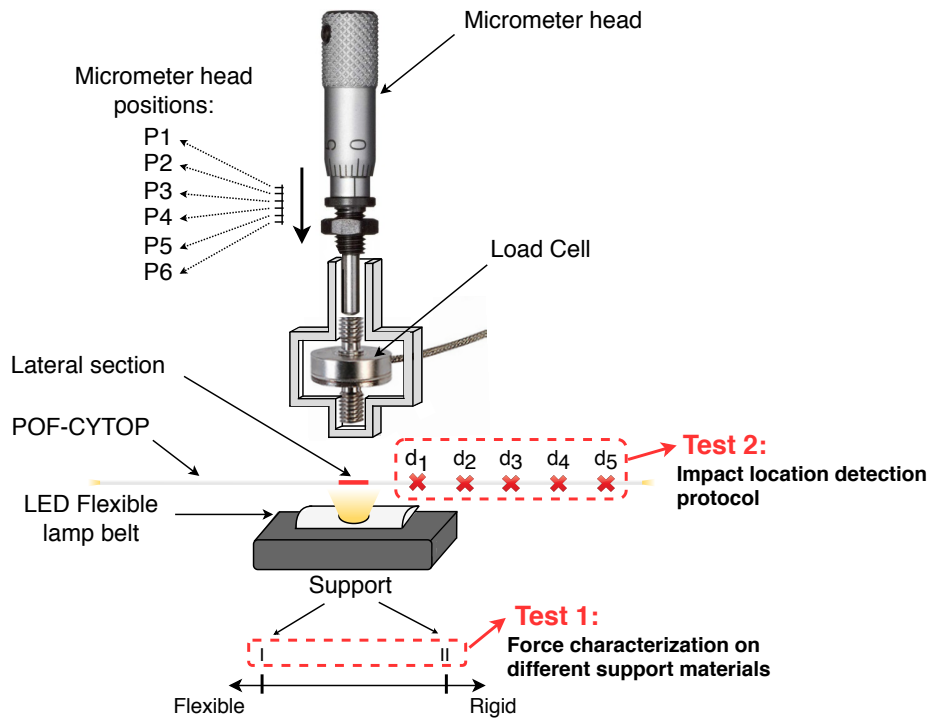


FIGURE 3.8: Experimental setup for evaluating the force sensor using CYTOP fiber.

3.2.2 Experimental procedures

The experimental setup consists of a micrometer head vertically positioned in a structure to control the millimeter position of this structure, where such structure also contains a load cell for the force acquisition. The whole structure is positioned on supports of different rigid and flexible materials. Two different tests were performed in this work: the force characterization on different support materials (Test 1) and impact localization detection protocol (Test 2), as shown in Figure 3.8. First, the force characterization on different support materials consisted of turning the micrometer head in six different millimeter positions (P1=1 mm up to P6=6 mm, with 1mm steps) applying vertical force on the top of the sensor positioned on supports with two different stiffness (flexible and rigid). Support I (flexible) is a polyurethane foam, with elastic modulus of 18.6 MPa and support II (rigid) is a 3D structure manufacture made of acrylonitrile butadiene styrene (ABS) using a 3D printer Sethi3D s3 (Sethi, Campinas, SP, Brazil), with elastic modulus of 1.6 GPa.

The goal of this protocol is to relate the optical power variation to the force on the fiber for each support stiffness, since different regions in human body present

different stiffness characteristics that should be considered in the sensors analysis. The impact location detection protocol consisted of turning the micrometer head in six different millimeter positions (P1-P6) applying vertical force along the fiber (outside the sensor sensitive zone) on five positions along the fiber (d1-d5) which correspond to distances of 1 cm-5 cm with steps of 1 cm.

3.2.3 Results and Discussion

Force characterization on different support materials

In this characterization, the CYTOP was positioned on two different supports and six different forces were applied on the sensor based on the micrometer head positions. First, the CYTOP was positioned on the support I, which is the most flexible (elastic modulus of 18.6MPa). Three tests were made and the results are shown in Figure 3.9. The markers and the vertical bars represent the mean and the standard deviation (SD) of the measured force (in N) in three trials, respectively, and the continuous line represent the fitted curve obtained from the mean of the measured values.

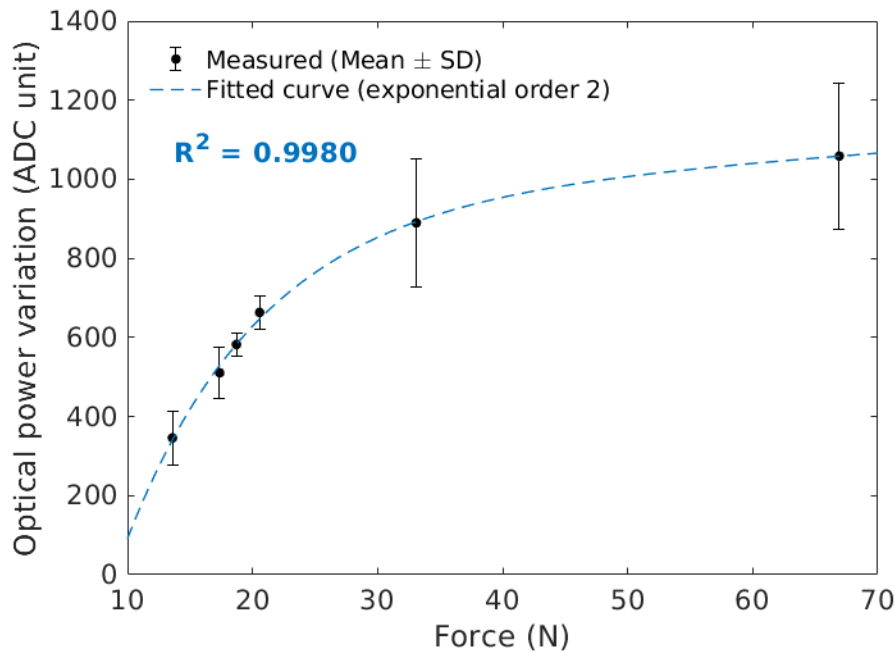


FIGURE 3.9: Results of the CYTOP response under six different forces on the support I.

The POF force sensor response presented an exponential behavior with order 2 ($R^2 = 0.9980$), as shown in Figure 3.9 and it is noticeable that the optical power variation increases as the force increases. Using a setup containing a fiber, a LED and a photodetector (one at each fiber end), the sensor present a linear decreasing behavior when the force increases, as presented in [123]. This is due to the attenuation of the transmitted optical signal power caused by fiber bending as well as the variation on the refractive index due to the stress-optical effect. Since the current setup is using a LED side-coupled to a lateral section, there is the coupling influence in addition to the attenuation of the transmitted optical power. The force applied on the POF by the micrometer head decrease the displacement between the LED flexible lamp belt

and the fiber lateral section, which increase the light coupling of the flexible lamp belt. Since the support is flexible, the applied force is not high enough result in a significant stress in the fiber due to the force damping caused by the flexible material. It means that this force range provoke higher light coupling (which increase the optical power) than the stress in the fiber (which decrease the optical power). For this reason, there is an increase of the optical power variation. In addition, there is a saturation tendency on the optical power variation due to displacement reduction between the LED and POF as the forces increase, resembling the stress-strain curve of the materials, where there is a linear region, followed by another region with smaller slope as the stress (or force) continues to increase.

Thereafter, the CYTOP was positioned on the support II, which is the most rigid among the ones tested (elastic modulus of 1.6 GPa) and the micrometer head was put in the same six positions (P1-P6) presented in Figure 3.8. Figure 3.10 shows the results of the sensor response of three trials. The markers and the vertical bars represent the mean and the standard deviation of the measured force (in N) in three tests, respectively. The continuous line represent the fitted curve obtained from the mean of the measured values.

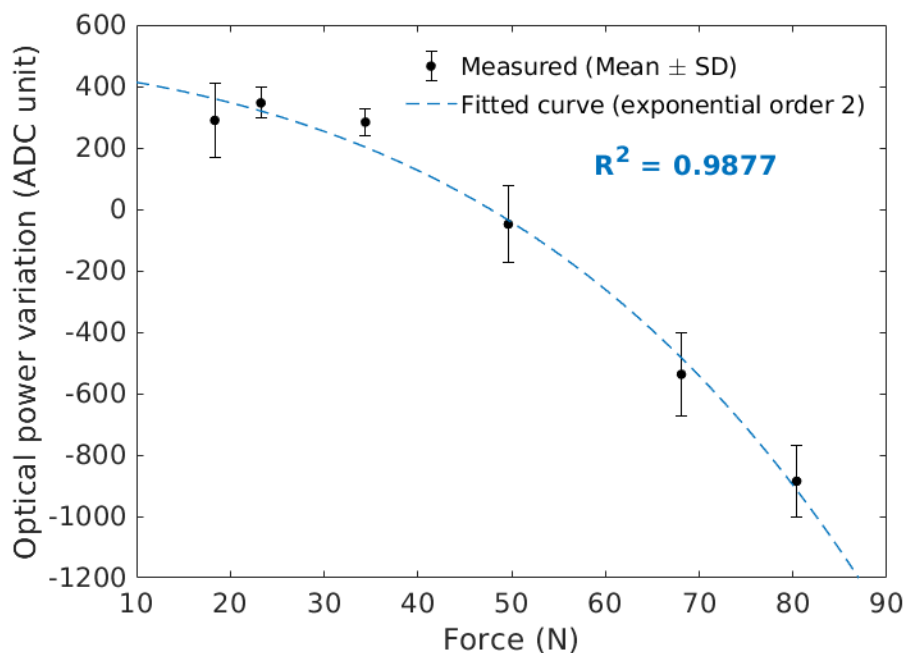


FIGURE 3.10: Results of the CYTOP response under six different forces on the support II.

The force sensor response presented a determination coefficient of 0.9877 with a second degree exponential, as shown in Figure 3.10. The response presented a small increase in the optical power in forces lower than 40 N, followed by a decrease of the optical power in higher forces. The results show a different behavior when compared with the results using support I, which only presented an increase of the optical power. As the support has a higher Young Modulus, the strain on the support due to the applied load is smaller, leading to only a minor increase in the optical power. As the force continues to increase, there is a higher stress concentrated in the fiber (since there is no significant strain in the rigid support), which results in a

transmitted optical power attenuation due to the stress-optical effect.

In order to compare the behavior of both rigid and flexible supports, Table 3.4 shows the sensor performance using the two different supports in these experimental protocol.

On the flexible support the sensor presented sensitivity of 15.78 ADC unit/N in a force range of 0-67 N, whereas on a rigid support the sensitivity was 10.98 ADC unit/N in a force range of 0-80 N. These results were obtained under the same micrometer head positions, which show that on a more flexible support there is a greater force damping due to the smaller Young modulus of such material. Thus, the stress-strain curve has a smaller slope, which indicates that larger strain is obtained with smaller force when compared with the rigid support with a Young modulus two orders of magnitude higher. This is also the reason of the higher sensitivity of the sensor in the flexible support when compared with the one in the rigid support. Moreover, the exponential regression presents lower determination coefficient in the rigid support due to the duality in the optical power variation behavior, where there is an increase on the optical power in lower forces, followed by a decrease as the forces increase due to the strain in the optical power.

Therefore, the comparison between both structures shows not only the possibility of measuring forces using the proposed sensor (previously characterized for each structure), but also the possibility of estimating the structural stiffness through the feature extraction of the sensors responses, e.g. sensitivity and determination coefficient analyses. The latter possibility plays an important role in the stiffness mapping of the user in wearable sensors applications, where it is possible to estimate the recovery of a patient by analyzing the stiffness evolution of affected regions, such as presented in [124], as well as on the development of customized assistive devices. In addition, it also has influence on the design of flexible (and rigid) wearable robots and their control, where the possibility of obtaining the contact stiffness between robot and user can lead to a natural control of the robot with variable stiffness where its stiffness mimics the one of the users [125], as well as presented in [126] in which an interface is designed for a more natural interaction between human and robot.

TABLE 3.4: Sensor performance using two different supports.

	Flexible	Rigid
OPV (ADC units)	1059	885
Fitted curve	Exp. order 2	Exp. order 2
R^2	0.9980	0.9877
Force range (N)	67	80

Impact location detection protocol

In practical applications, the force may not be directly applied in the sensor region. In order to verify the sensor behavior under different forces along the fiber, the POF was placed on support II and the micrometer head was positioned in the same positions of the previous characterization (P1-P6) along the fiber ($d = 1, 2, 3, 4$ and 5 cm), in which d is the distance between the applied force caused by the micrometer head and the lateral section. Figure 3.11 shows the sensor responses for each d , presenting the measured values and the fitted curves (exponential order 2) with their respective determination coefficients. In this case, there is not the influence of the displacement

between the LED flexible lamp belt and the sensor, i.e. the influence of the light coupling in the sensor responses, since the micrometer head was not pressured on the top of the sensor. For this reason, the sensor responses were entirely influenced by the fiber strain and did not present an increase in the optical power, as showed in the previous test with support II (see Figure 3.10).

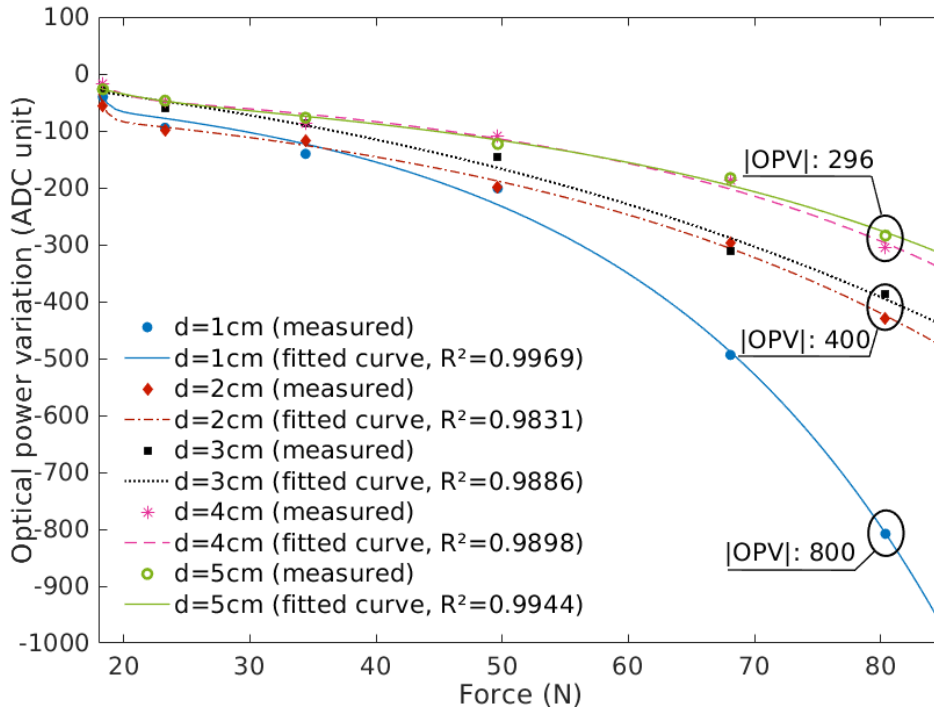


FIGURE 3.11: Results of the vertical forces applied along the fiber ($d=1,2,3,4$ and 5cm to the sensor).

Figure 3.11 shows the sensor responses for all distances d in a smaller force range. As the force increases, it is possible to identify differences in the sensor responses, e.g., for an applied force of 80 N , approximately, it is possible to identify 3 clusters (C1: $d = 1\text{ cm}$, C2: $d = 2 - 3\text{ cm}$ and C3: $d = 4 - 5\text{ cm}$). It shows that the impact location detection is more evident under higher forces with spatial resolution of 2 cm . However, it is worth noting that each distance presents its own correlation curve, where all cases show a strong correlation ($R^2 > 0.98$) with an exponential curve.

Table 3.5 shows the comparison of the optical signal variation and determination coefficient for each case at 80 N . As expected, the smaller distances result in higher signal variation, since it is closer to the light source, whereas the higher distances lead to lower signal variations. Considering the system's resolution, it is possible to infer that the sensor is able of tracking changes as far as 10 cm of the lateral section. These results indicate the possibility of a real-time assessment of mechanical disturbances localization using a multiplexed system able of tracking simultaneous perturbations such as the one presented in [62]. The use of the proposed system may enable to pinpoint the disturbance along the fiber and not only on the sensors, using the response of the multiplexed sensors, increasing the spatial resolution of the system. Furthermore, the analysis of each sensor also results in the assessment of the stiffness in the region at which the sensor was pressed with important implications on rehabilitation and wearable robots control, where an application of optical fiber sensors in the stiffness assessment can be proposed.

TABLE 3.5: Sensor performance for force applied along the fiber.

	d_1	d_2	d_3	d_4	d_5
OPV (ADC units)	800	428	386	305	284
Fitted curve			Exp. 2		
R^2	0.997	0.983	0.989	0.990	0.994
Force range (N)			80		

3.3 Final Remarks

This Chapter presented the development and performance analysis of intensity variation based sensors using CYTOP fiber for monitoring kinetic and kinematic parameters. First, a curvature sensor is proposed, and tests under different conditions are performed for evaluating the influence of angular velocity and the central wavelength of the light source. Curvature tests with an angular range from 0 to 50 *degrees* using five light sources with different central wavelengths were performed. Three factors were analyzed to achieve the best sensor performance: sensitivity, hysteresis and R^2 . After this, tests with the same angular range were performed under five different angular velocities using the light source with the central wavelength which obtained the best performance in the first tests. A compensation model was designed to reduce angular errors. These analyses result in an enhanced sensor for application in the joint assessment during the gait.

Second, a force sensor is proposed, and two tests were performed: force characterization on different support materials and impact location detection. Both tests consisted of applying a strain in the fiber using a micrometer head. The first test aimed to characterize the sensor response embedded in materials with different stiffness since the human body presents a variety of stiffness characteristics throughout the body that should be considered in the analysis of wearable sensors. The second test aimed to evaluate the sensor response with force application outside the sensor sensitive zone and the ability to identify the impact.

Chapter 4

Optical Fiber Sensors Integration in Textiles and Flexible Structures

This Chapter presents works developed for the integration of optical fiber sensors in different textiles and flexible structures. In the first analysis, a preliminary study of a POF-integrated textile is presented, where the force, temperature and bending analyses of the multiplexed intensity variation-based sensors are analyzed for each condition. FBG sensors inscribed in silica fibers incorporated in a rubber blanket are evaluated for application as an intelligent carpet for gait analysis. The rubber blanket is characterized by force and space using neural network. Moreover, for TRA-based sensors integration in smart structures, a preliminary analysis of a TRA-based distributed sensor using different oxide DNP-doped fibers as well as a comparison of these fibers according to the distributed sensor performance to define the suitable DNP-doped optical fiber for the biomechanical applications. Finally, a deep learning-based analysis of multiple simultaneous disturbances applied on a TRA-based distributed sensor using an oxide DNP-doped fiber is performed to address one of the major problems in the TRA-based approach, i.e., the ability of detecting simultaneous perturbations along the optical fiber.

4.1 POF Smart Textile: Preliminary Study

Before the development of textile applications, a preliminary study using a textile model is performed. A light polarization spinning (LPS) POF was used in the preliminary tests due to its promising mechanical features and properties for mechanical sensing with the possibility of embedding on textiles without changing the textile stiffness [40], which makes it suitable for multiparameter sensing in smart textiles.

4.1.1 Materials and Methods

The LPS-POF has a diameter of $580 \mu\text{m} \pm 30 \mu\text{m}$ with a core refractive index of 1.54, whereas the fiber cladding (with $20 \mu\text{m}$ thickness) has a refractive index of 1.45. For the multiparameter sensing, the technique proposed by [79] is used, which is based on light source lateral coupling and temporal multiplexing. The light source is activated at a time and the correspondent optical power is acquired. The light source is a LED in flexible substrate to ensure a high flexibility to the system embedded in the textile fabric, and the optical power is acquired by a photodetector IF-D92 (Industrial Fiber Optics, USA). The sensor system (comprised of the LPS-POF and the flexible LEDs) is sewed between two layers of a neoprene textile fabric, as shown in Figure 4.1. The LEDs activation control as well as the optical power acquisition are performed by a microcontroller FRMD-KL25Z (NXP Semiconductors, Netherlands).

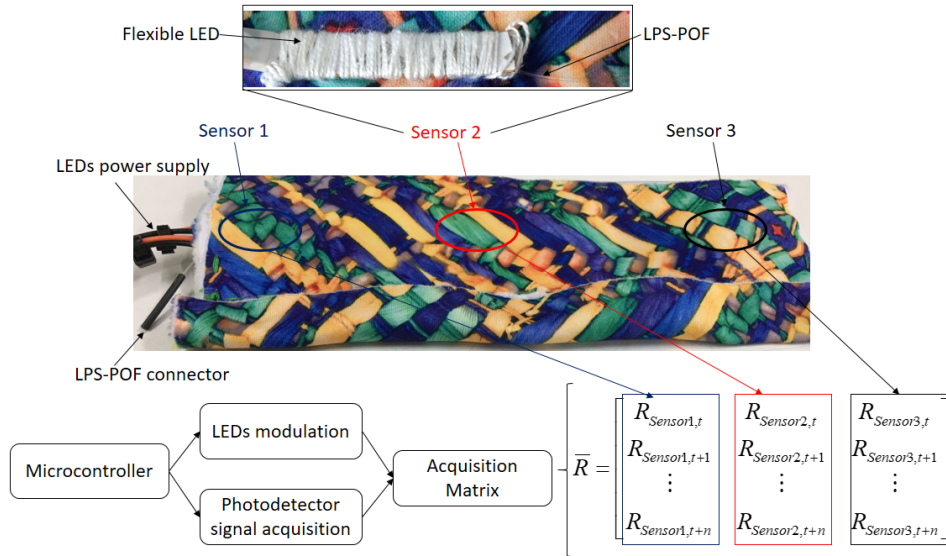


FIGURE 4.1: Smart Textile overview: picture and schematic representation of the proposed smart textile system.

4.1.2 Experimental procedures

In order to characterize the sensors, different tests are performed. In the temperature tests, Sensors 1, 2 and 3 were positioned in a thermoelectric Peltier plate TEC-12706 (Heibei IT, China) with closed loop temperature control TED 200C (Thorlabs, USA). The temperature range was 20–40 °C in 5 °C steps, where the isothermal period was 5 *min* to ensure a constant temperature at each sensor. For the temperature profile tests, a temperature-controlled hot air blower 858D (QWERTOUY, USA) was employed and positioned at different regions of the smart textile.

For the force characterization, calibrated weights with a known mass were positioned on the top of each sensor for about 10 s. All the sensors were tested in a range of 0–150 *N*. However, Sensors 1 and 3 have different forces due to the dimensions of the weights, which can apply a force on Sensor 2 due to the proximity of such sensors. In addition, the force map characterization was performed by position a weight with larger dimensions in the center of the smart textile, leading to a force distribution in the sensors.

The angular displacement tests were performed by manually bending the textile with the aid of a goniometer at the different planes, where the goniometer was previously aligned with the bending plane and the angular displacements in the range of 0° to 90° for bending and 0° to 180° for torsion were performed.

4.1.3 Results and Discussion

The POF-embedded smart textile was tested in different conditions in order to verify its suitability for measuring multiple parameters, where the multiplexing technique based on the LEDs modulation enables the simultaneous measurement of multiple parameters in multiple points on the POF. In this case, the tests were performed in the textile with three measurement points. Figure 4.2 presents the temperature response of each sensor, where the tests were performed in a range of 20–40 °C due to both the intended application (room temperature monitoring and on-body applications). The temperature characterization of each sensor, in Figure 4.2(a), shows a

linear behavior of all sensors in the mean and standard deviations of five tests, where the sensor 1 presented the highest temperature sensitivity. The temperature increase in the LPS-POF leads to refractive index variation due to the thermo-optic effect, which results in variations in the transmitted optical power, the differences in the sensitivities can be related to anisotropy in the fiber material [127]. From the linear regressions obtained in the sensors characterizations in Figure 4.2(a), it is possible to estimate a temperature distribution in the textile, as shown in Figure 4.2(b). In this case, a thermal blower is positioned in different locations along the fiber, leading to both distributed and concentrated temperature increase in different regions.

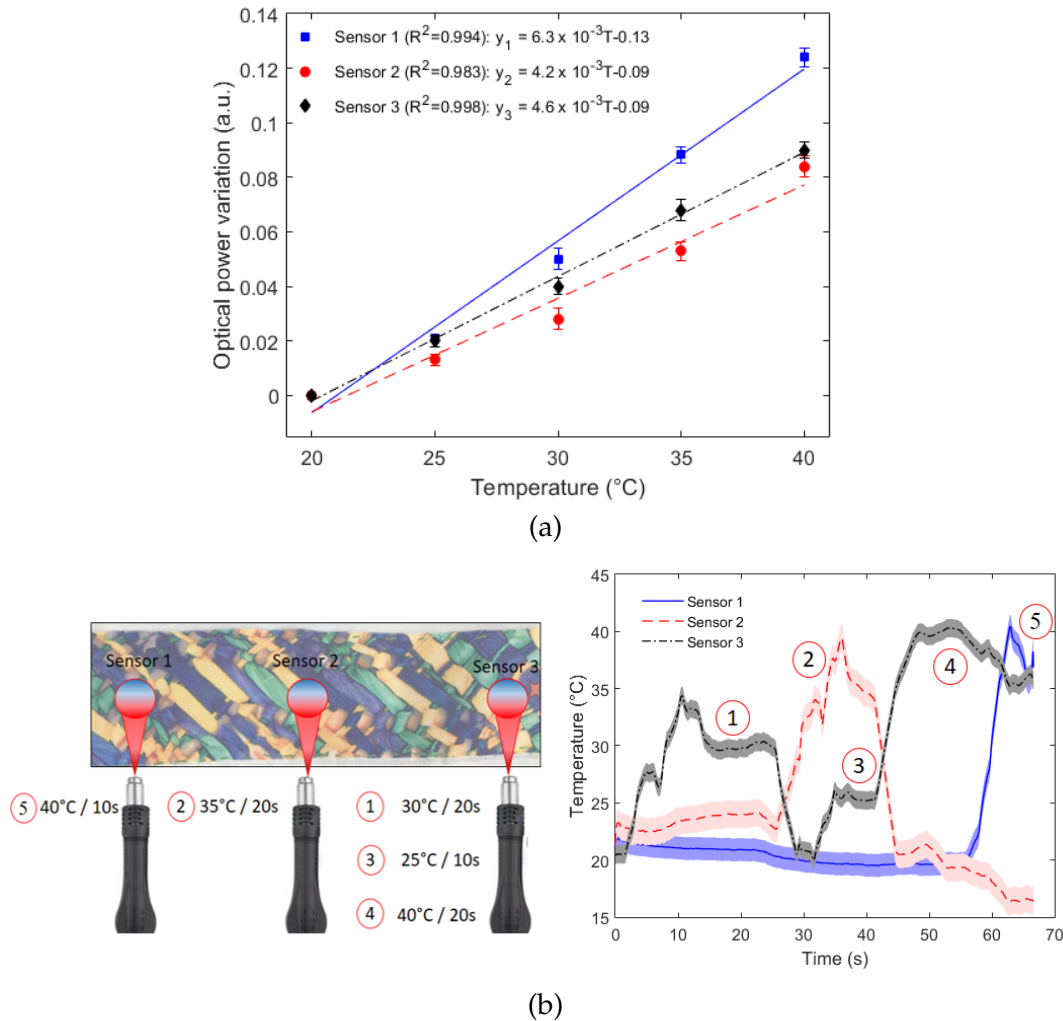


FIGURE 4.2: Temperature analysis of the LPS-POF embedded textile. (a) Temperature characterizations. (b) Temperature responses of each sensor for different heat spots.

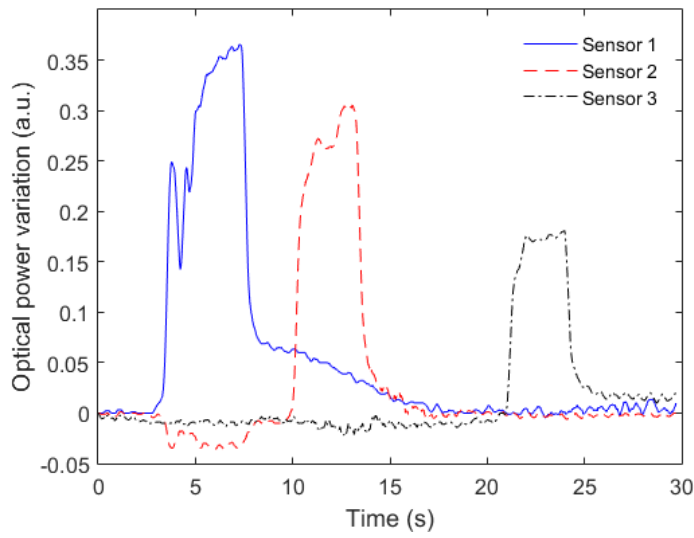
The capability of sensing the temperature distribution in the textile was demonstrated, where the sensors also presented low cross-sensitivity between them, demonstrating the feasibility of the proposed multiplexing technique. Regarding the temperature responses, the solid lines are the responses of the sensors applying the linear regressions, whereas the shaded lines are the temperature uncertainty of the sensors, considering the standard deviations on the characterizations shown in Figure 4.2(a). The positions and temperatures of the heating spots on the optical fiber are also presented in Figure 4.2(b), where it can be seen a temperature increase starting

in the Sensor 3 and ending in Sensor 1. Thus, the proposed sensor system can be used for body temperature monitoring and can be applied in the interface between the user and an assistive device for microclimate assessment.

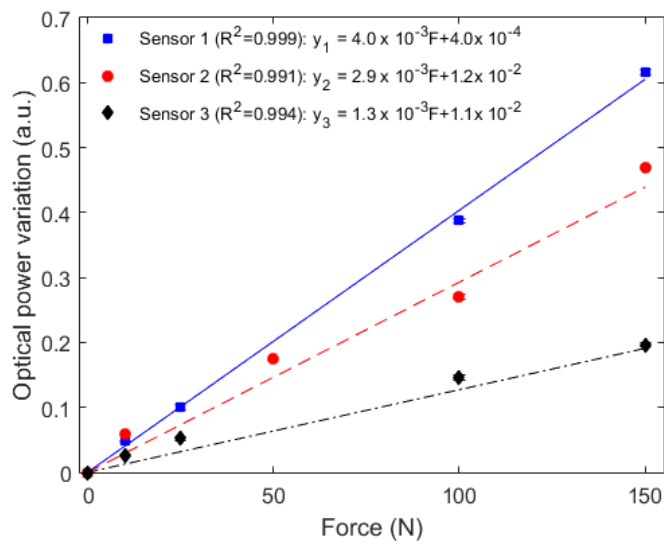
Thereafter, different forces are applied at each sensor to obtain their responses at transverse force conditions, which can be correlated to the applied pressure by considering the area of each sensor. In order to show the low crosstalk between sensors, Figure 4.3(a) shows the sensors responses as a function of time for a force of 100 N applied at one sensor at a time (starting from Sensor 1). It is possible to observe the low cross-sensitivity between sensors, i.e., when the force is applied directly on one sensor, there is no significant signal variation in the others, showing the feasibility of the proposed LED modulation multiplexing technique for intensity-based sensors. In Figure 4.3(b), the force characterization is presented, where high linearity of all sensors and low standard deviation between tests is shown. By applying the linear regression in the sensors responses, it is possible to obtain a pressure/force map of the interaction between the sensor and the user (or environment), as shown in Figure 4.3(c). In this case, a rectangular object (resembling a chair support) is positioned on the textile and the force map is presented in Figure 4.3(c), which indicates the possibility of using the proposed smart textile with a mesh of sensors to evaluate the interaction pressure between the user and the environment, such as chairs and beds. Such evaluation is important to provide a remote monitoring of the user's activities and prevent pressure ulcers.

The smart textile sensors responses under displacements applied at different planes are presented in Figure 4.4. Bending at different planes and torsions were applied with controlled angles. For the bending, the angles were 0° to 90° and 0° to -90° , whereas, in the torsion assessment, angular displacements ranging from 0° to 180° were applied, as depicted in Figure 4.4 inset. Comparing the responses of each sensor, which are obtained at the angular displacements in different planes, it is possible to observe differences in the sensors behavior, which can be used for the classification of each movement in multiple planes. It is also noteworthy that Sensors 1 and 2 presented the highest bending sensitivity, related to the region where the bending was applied (see Figure 4.4 inset), resulting in a higher stress in Sensors 1 and 2. In the torsion case, the highest optical power variation was also obtained in Sensor 1, whereas, once again, the Sensor 3 presented the lowest signal variation. However, the differences in the sensors sensitivities obtained in each case can be used for the estimation of the multiplane displacements applied on the textile, using techniques such as transfer matrix for 3D plane displacements assessment [128], where a system of equations obtained in the sensors characterizations are used for the angle assessment of each plane. It enables the remote human movement analysis using wearable sensors that do not inhibit the natural pattern of the user's movements.

As shown in Figure 4.2, the sensors are also sensitive to temperature variations. Thus, temperature variations interfere on the bending and force assessment. Although the results presented in Figures 4.3 and 4.4 were obtained in constant temperature conditions, temperature variations can occur in practical applications. In order to mitigate the temperature influence on the sensors' responses, two approaches are considered. The first approach is based on the difference between sensors responses for temperature and strain-related parameters (as previously validated in temperature-compensated systems [129]), considering their previously characterized sensitivities with respect to temperature, angle and force, in this case. Furthermore, the use of the smart textile in dynamic movement applications leads to an additional possibility of temperature compensation. In practical applications of the



(a)



(b)



(c)

FIGURE 4.3: Force analysis of the LPS-POF embedded textile. (a) Transmitted optical power attenuation as function of time for forces applied at different sensors. (b) Force characterizations. (c) Force map from the sensors responses with a force applied on the textile.

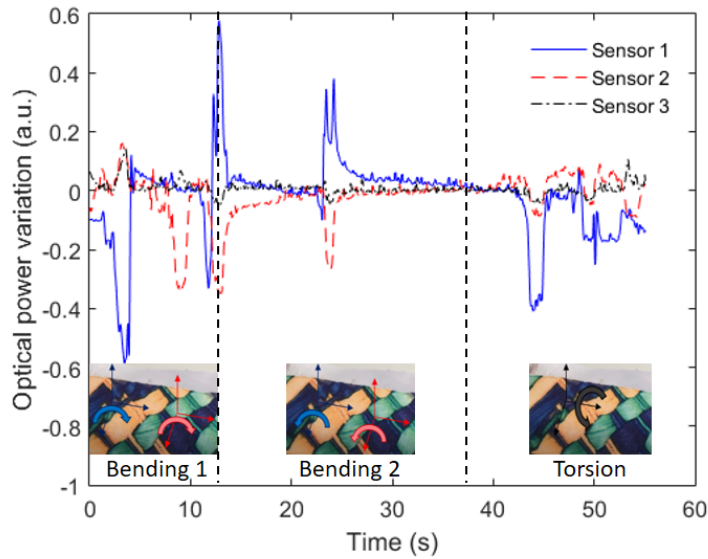


FIGURE 4.4: Sensors responses with angular displacement on different planes.

proposed textile, the temperature variation rate is lower than the one of the strain-related parameters (such as force and angle). This behavior leads to differences in the frequency components of the temperature and strain, where the lower frequencies are related to the temperature. Therefore, the temperature influence on the strain response is mitigated by filtering the low frequencies components on the sensor responses, as demonstrated in previous works [130].

It is also worth noting that the smart textile characterization with respect to temperature and force show a high repeatability of the sensors with low standard deviation (0.004 a.u.) in the temperature assessment after 3 sequential tests (see the error bars in Figure 4.2(a)). Moreover, the error bars are not visible in Figure 4.3(b) due to its low standard deviation (0.005 a.u.). As another indicator of the sensors' consistency, the bending tests, whose results are shown in Figure 4.4, show the sensor reversibility, since the sensors responses returned to their initial condition without significant residual strains after the bending is performed. The maximum reversibility error (obtained by the comparison between the sensors responses before and after the bending) is 0.03 a.u. , considering all three sensors.

4.2 Spatial Characterization of a Rubber Blanket-embedded FBG Matrix

In order to develop a OFS-based system incorporated in a flexible structure for gait analysis, the rubber blanket-embedded FBG matrix is proposed. The use of FBG sensors in this work is mainly related to the heterogeneity of the systems proposed in this PhD Thesis and to the evaluation of the ability to integrate different systems in the same application, as presented in the Chapter 7. This Section aims to characterize each sensor (force) and the whole system (disturbance location) to evaluate the ability of measuring kinetic and kinematic gait parameters. A deep learning technique is proposed to provide an accurate identification of disturbance location which are useful for gait applications in smart environments, as presented in the Chapter 7.

4.2.1 Materials and Methods

In this setup, 10 FBGs inscribed in 2 silica fibers (5 FBGs in each fiber, separated by 20 *cm*) are used embedded in a rubber blanket. The FBGs were inscribed in a photosensitive single mode fiber GF1B (ThorLabs, Newton, NJ, EUA) using a 248 nm KrF pulsed laser through the phase mask technique [131]. Figure 4.5 presents the FBGs spectra of each fiber.

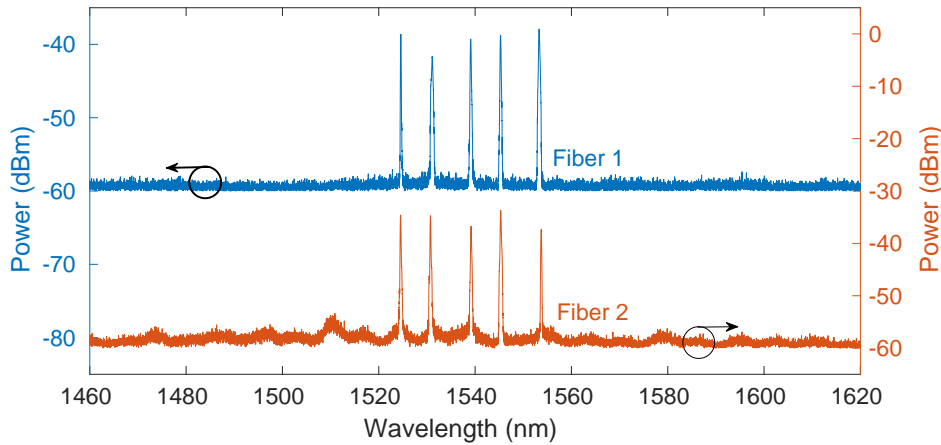


FIGURE 4.5: FBGs spectra. Top spectra: fiber 1. Bottom spectra: fiber 2.

The rubber blanket is made of nitrile rubber with dimensions of 200 *cm* (length), 60 *cm* (width), and 1.5 *mm* (height). Since the system consists of the silica fibers between two layers of the rubber blanket, the total height of the system is 3 *mm*.

4.2.2 Experimental procedures

Two tests are performed to evaluate the system: the force and spatial characterizations. The force characterization aims to estimate the sensitivity and the linearity of each FBG, in addition to normalize all the sensors. The force characterization of the FBGs is performed (at a constant temperature) by positioning predefined weights (5-10 *kg* with steps of 1 *kg*) on the top of each FBG. The spatial characterization aims to identify the disturbance location based on a neural network model. It consists of applying the same force on 23 predefined points and relate the sensors responses with these points to design a neural network model for classification of the disturbance location in the rubber blanket. This classification model is evaluated using accuracy and loss metrics. The setup of each characterization, as well as the FBGs incorporated in the rubber blanket are shown in Figure 4.6.

A feed-forward neural network (FFNN), presented in the Section 2.4.2, is designed to perform a multi-label classification of simultaneous disturbances location on the rubber blanket. The FFNN comprises of an input layer with 10 nodes (FBG responses), two hidden layers with 600 and 300 neurons and an output layer (23 binary values). Moreover, the data are divided into training (80%) and testing (20%), and randomly permuted. The batch size is 50 and 40 epochs are used in the FFNN.

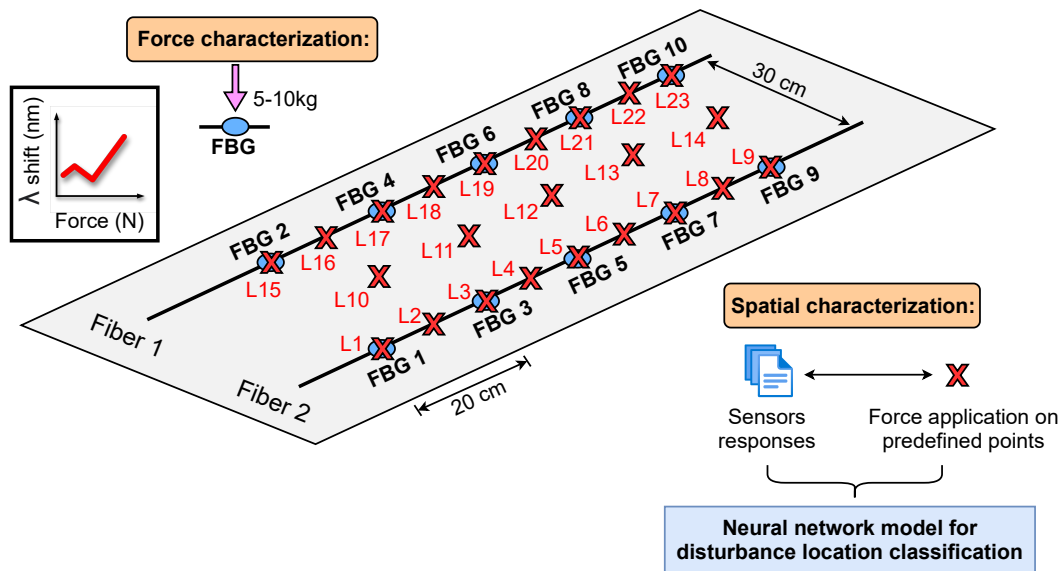


FIGURE 4.6: Experimental setup of the rubber blanket-embedded FBG matrix.

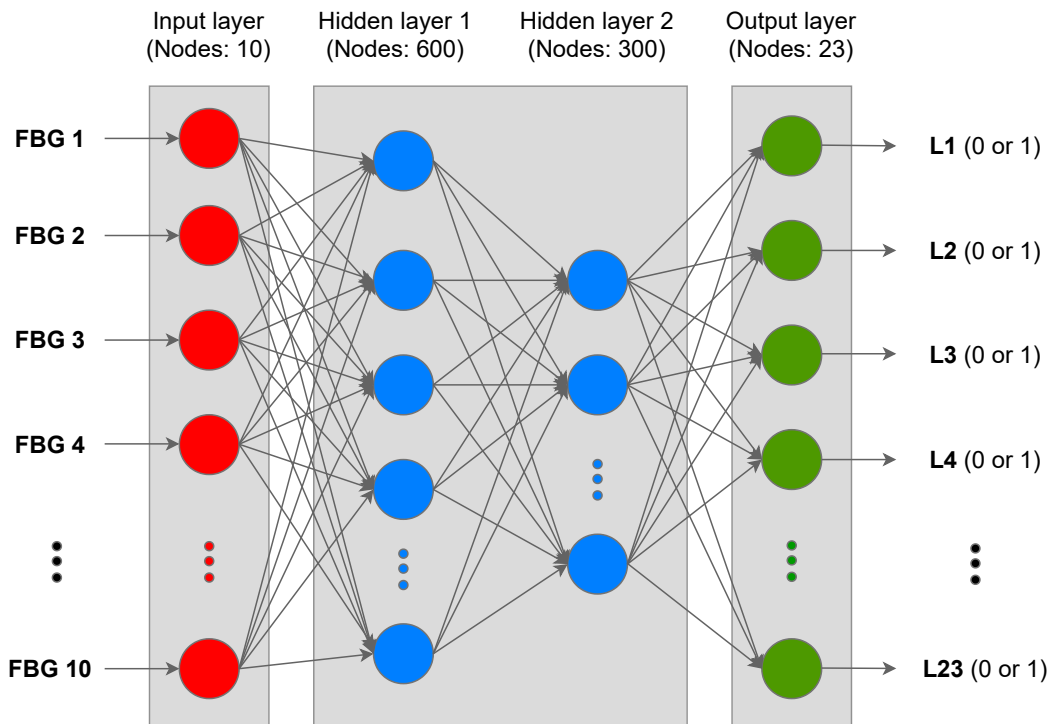


FIGURE 4.7: Feed-forward Neural Network model.

4.2.3 Results and Discussion

Figure 4.8 presents the results of the FBGs in the force characterization. The tests were performed at constant temperature (22°C). All sensors presented a linear relation between wavelength shift and force, with determination coefficient (R^2) higher than 0.98. The sensors' sensitivities are different, as presented in Figure 4.8, where it is possible to observe the differences in the sensors sensitivities, obtained by the slope of the characterization curves. The FBG 8 presented the highest sensitivity (4.12 pm/N) among the tested ones, which is similar to FBG 2 sensitivity (3.87 pm/N), whereas the lowest sensitivities are obtained in FBGs 5 and 6 with sensitivities of 0.49 pm/N and 0.79 pm/N, respectively. The reason for this behavior is related to the positioning of the FBGs in the rubber carpet, where there are some deviations on the rubber carpet thickness ($1.6 \pm 0.2\text{mm}$). The higher thickness of the carpet leads to lower force sensitivity of the sensors, whereas the lower thickness results in higher force sensitivity. Thus, the variation on the carpet thickness leads to such differences in the sensitivities of each FBG.

Since the FBGs presented different sensitivities, all the sensors are normalized by their sensitivities prior to the application in the FFNN. The results of the FFNN classification model are presented in Figure 4.9, which shows the high accuracy of the proposed approach, where there is the classification of the foot position based on 23 predefined positions, as shown in Figure 4.6. The accuracy value converged to 99.58% and the loss value to 0.0115. Thus, the results show the feasibility of impact detection on the FBG-embedded rubber carpet, where it is possible to estimate the spatio-temporal parameters of the gait and the ground reaction forces of the users in the FBG-embedded carpet.

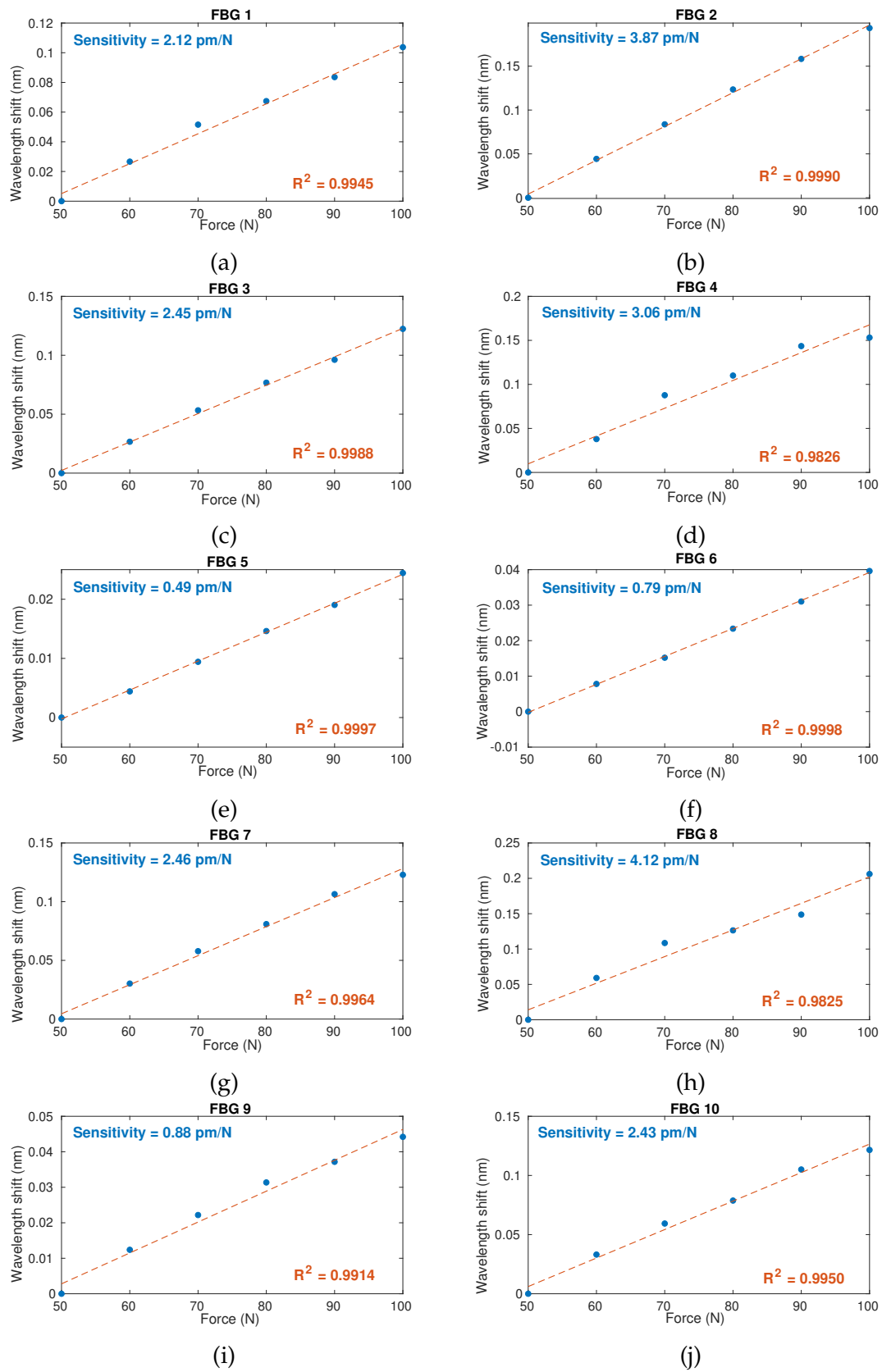
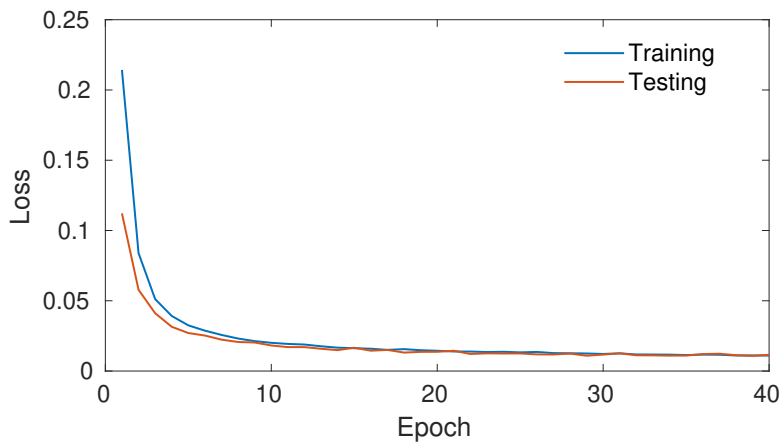
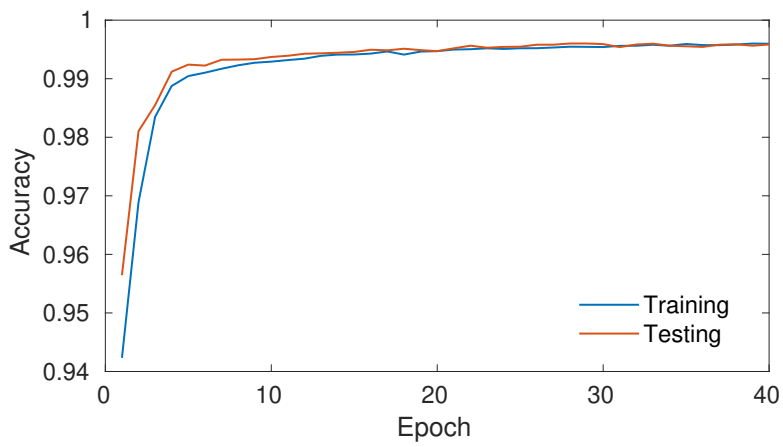


FIGURE 4.8: Force characterization of each FBG. (a) FBG 1. (b) FBG 2. (c) FBG 3. (d) FBG 4. (e) FBG 5. (f) FBG 6. (g) FBG 7. (h) FBG 8. (i) FBG 9. (j) FBG 10.



(a)



(b)

FIGURE 4.9: Metrics of the FFNN model with 40 epochs for the spatial characterization. (a) Loss. (b) Accuracy

4.3 TRA-based Sensor using Different DNP Fibers

This Section presents an experimental characterization of a TRA-based sensor system using five different DNP-doped fibers with the same length. A disturbance location protocol is proposed to evaluate the influence of different DNPs (with various compositions and sizes) on the sensing performance. The sensors' performance is evaluated and related to the fiber fabrication and the DNPs presented in the fiber core. These analyses enable the selection of the DNP-doped fiber with the best performance for biomedical applications, such as in wearable sensors or smart environments (as presented in Chapter 7).

4.3.1 Materials and Methods

The materials used in this setup are divided into three parts: the light source, the acquisition system and the optical fibers. The super-luminescent diode centered at 1550 nm with a bandwidth of 60 nm (SLED, DL-BP1-1501A, Ibsen Photonics, Farum, Denmark) was employed as the light source. The acquisition system consists of two photodetectors (PD, GT322D, Go4fiber, China), two transimpedance amplifiers (TIA, TLV3541, Texas Instruments, USA), a microcontroller unit (MCU, Kinetis K64F, NXP Semiconductors, Eindhoven, Netherlands) and a computer. An optical circulator (OC) is employed to connect the reflected optical power to one PD, whereas the another PD is directly connected at the optical fiber to acquire the transmitted optical power. Each PD is coupled to the TIAs and the signal acquisition is performed by the microcontroller and transmitted to the computer for data processing.

Regarding the optical fibers, five different DNP-doped fibers were used in the experiments. The Fibers A, B and C are fabricated following the guidelines presented in [66]. The standard solution doping technique is employed to incorporate RE ions within DNPs in silica-based optical fibres. Fiber A contains SrO oxide in its composition, whereas Fiber B and Fiber C contain CaO and MgO oxides, respectively. In these optical fibers (A, B and C), erbium ions are incorporated into the DNP to broaden the emission spectrum. In addition, germanium (1.85 mol%) and small amounts of phosphorus (0.8 mol%) were added to raise the core refractive index and ease the fabrication of these fibers. It is important to mention that no particle bigger than 100 nm was observed in the Fiber C, which is different from fibers A and B.

Fiber D (La_2O_3 -doped fiber) is fabricated using the gradual time doping technique [132], which is used to prepare fibers with longitudinally varying characteristics (concentration, refractive index, core diameter) along the fiber. The preform core contains Ge. Two doping solutions are used, Solution I: $[LaCl_3] = 0.01 \text{ mol/l}$, $[ErCl_3] = 0.01 \text{ mol/l}$; Solution II: $[LaCl_3] = 0.7 \text{ mol/l}$, $[ErCl_3] = 0.01 \text{ mol/l}$. The entire preform is soaked with the Solution I for more than one hour to reach the stationary concentration. Solution I is removed and the Solution II is injected up to the middle of the preform, in which the rising time is around one minute. The Solution II is slowly drained until the 1/3 of the preform. The draining time is about 20-30 minutes. The lower part of the preform is soaked for more than one hour with the Solution II in order to reach the complete equilibrium in this part. Finally, the Solution II is removed and the process is completed. Using this process, [132] reported a variation of the fiber characteristics over 100 to 500 meters. However, it is important to mention that the length of the optical fiber under test is 150-cm in this work, since this size is compatible with wearable applications.

Fiber E was fabricated using a non-conventional solution doping method to dope the preform fiber with $ZnGa_2O_4$ DNPs: the doping solution was injected in the horizontally rotating tube and then dried at room temperature by an oxygen gas flow. The solution was sonicated before being introduced in the tube. However, ultrasonic waves only broke the micrometric clusters and slightly reduce the diameter of the smaller clusters down to about 150 nm [67]. The Fiber E presented an optical attenuation of 275 dB/m .

4.3.2 Experimental procedures

A disturbance location characterization is performed to evaluate the transmitted and reflected optical power as a disturbance is applied along the fiber. The purpose of this protocol is to evaluate the performance of each fiber to localize the disturbance by using the transmission-reflection analysis. The setup of the disturbance location characterization is presented in Figure 4.10. This characterization consists of applying the same force in different points in the fiber, in a range of 15 cm up to 150 cm , with steps of 15 cm , i.e., the first point is 15 cm distant from the fiber end near to the optical source, whereas the last point is 150 cm from the start.

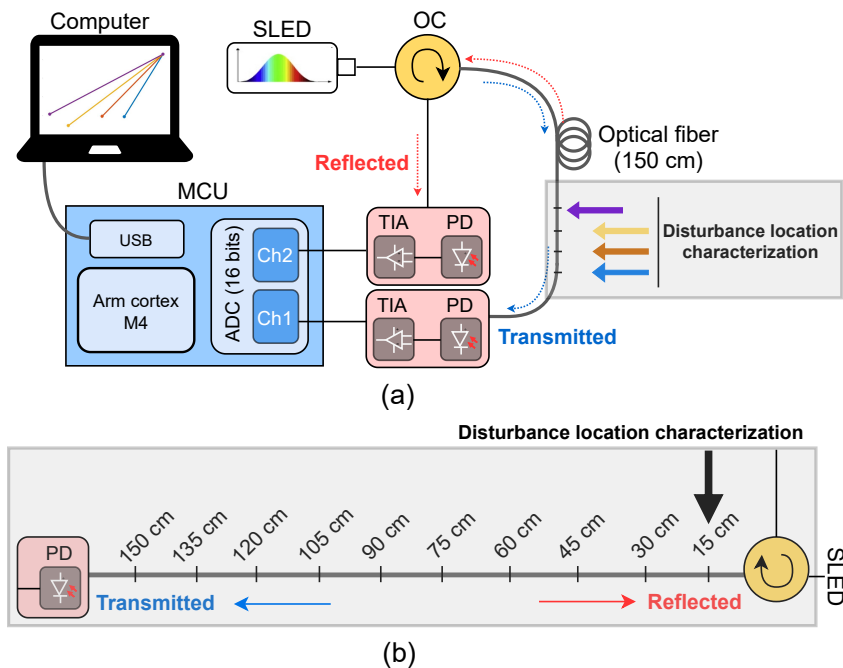


FIGURE 4.10: Experimental procedure. (a) Setup using the transmission-reflection analysis for disturbance location characterization. (b) Disturbance location characterization inset.

Two different parameters are calculated to evaluate the performance of the distributed sensor during the disturbance location characterization: Signal-to-Noise Ratio (SNR) and Spatial Resolution (SR). The SNR comprises the relation between the desired signal and the noise, and it is estimated by dividing the normalized reflected optical power under strain (R_{norm}) by the standard deviation of the normalized noise (σ_{noise}), as shown in Equation 4.1.

$$SNR = \frac{1 - R_{norm}}{\sigma_{noise}} \quad (4.1)$$

Moreover, the SR represents the smallest distance that can be detected by the sensor, and it is estimated by the Equation 4.2:

$$SR = \frac{\Delta L \cdot \delta n_{max}}{\Delta R_{norm}}, \quad (4.2)$$

where ΔL represents the distance variation between adjacent disturbance locations, δn_{max} represents the maximum noise amplitude and ΔR_{norm} is the difference between the normalized reflected optical powers associated with adjacent disturbance locations.

4.3.3 Results and Discussion

The results of the disturbance location characterization using Fiber A are presented in Figure 4.11(a). The Fiber A presented a perceptible variation in the transmitted optical power (~ 0.05 a.u.) when comparing the unstrained fiber to the strained fiber (when a disturbance is applied). From the distance of 15 cm up to 45 cm the normalized reflected power variation is 0.3518 a.u., as observed in Figure 4.11(a). On the other hand, the reflected optical power presents low variation between the disturbances on 45 cm up to 150 cm (0.0033 a.u.). It may be related to the high attenuation of the Fiber A (~ 40 dB/m) attributed to the presence of the bigger sized particles (~ 100 nm) [64], which leads to a reflected power variation only closer to the reflection-related PD. Moreover, in this fiber region (15-45 cm), the worst case presented SR of 0.1 cm with SNR of 31 dB, whereas the best case presented SR of 0.07 cm with SNR of 27 dB. Thus, It is recommended for this protocol the use of smaller lengths of the Fiber A, since the Rayleigh backscattering loss is high, leading to high spatial resolution in TRA-based sensors systems.

Fiber B presented a different behavior when compared to the Fiber A. In Figure 4.11(b) it is possible to note that the Fiber B presented a negligible variation in the transmitted optical power under strain (~ 0.0035 a.u.), approximately 15 times lower than the transmitted power variation using the Fiber A. Both fibers (Fiber A and Fiber B) have bigger DNPs (mean size around 100 nm and bigger particles were observed) in the optical fiber core when compared to Fiber C. The large particles influence the Rayleigh backscattering along the fiber and increase the attenuation [66]. In the case of Fiber B, the high attenuation (~ 55 dB/m) is observed in all fiber, with maximum normalized reflected power variation of 0.01 a.u. (from 15 cm up to 150 cm), different from Fiber A, which the reflected power variation increases for disturbances applied on the last 30 cm of the fiber. Due to the higher attenuation of Fiber B when compared with the Fiber A, it is necessary smaller length of Fiber B for its application in this protocol.

Figure 4.12 presents the results of the disturbance location characterization using Fiber C. Figure 4.12(a) shows the relation between the normalized reflected and transmitted optical powers as the disturbance location increased and Figure 4.12(b) shows the exponential behavior (order 2) of the relation between the reflected optical power and the disturbance location in the fiber, with determination coefficient (R^2) of 0.9956. This result is in agreement with the previous work [73], which used the Fiber C. Such optical fiber has smaller particles (mean size of ~ 40 nm) incorporated in its core when compared with the Fibers A and B, which may be cause of lower attenuation in Fiber C. There is a reflected power variation in all 150 cm-along fiber, different from the Fiber A that presented optical power variation only at 30 cm close to the reflection-related PD. Moreover, the SNR and SR by using the Fiber C are estimated by following the Equation 4.1 and Equation 4.2, respectively, presented in

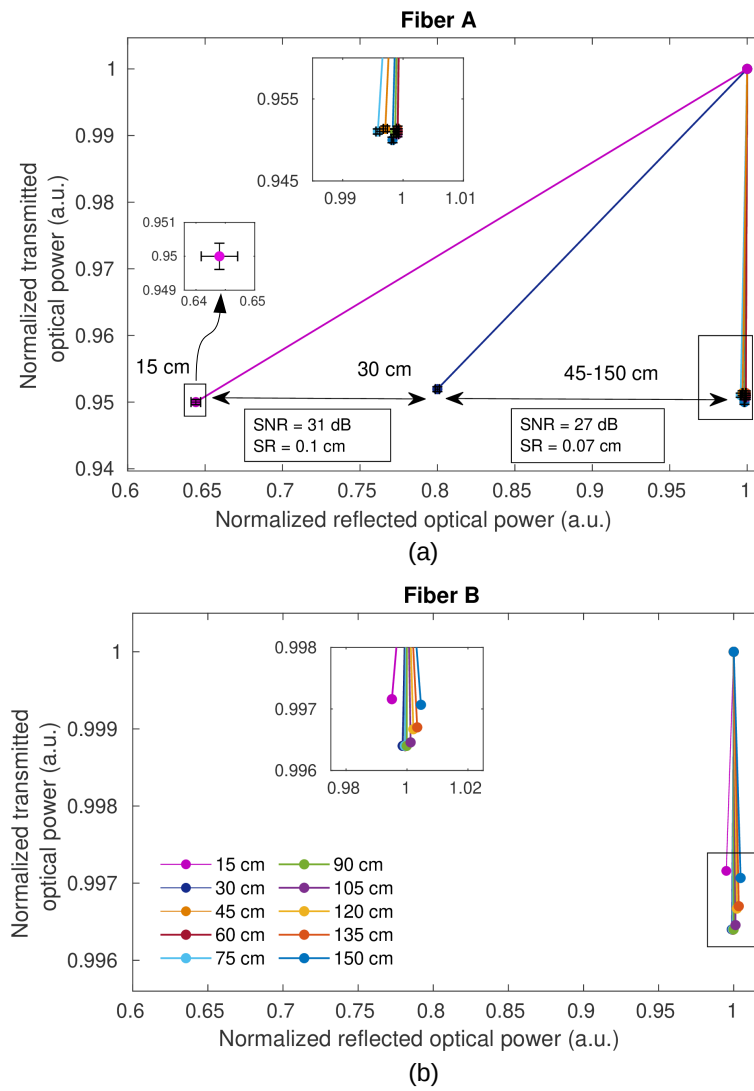


FIGURE 4.11: Relationship between the normalized reflected and transmitted optical powers at different disturbance locations. (a) Fiber A. (b) Fiber B.

Figure 4.13. The distributed sensor using the Fiber C presented the following results: SR (worst case: 0.8 cm and best case: 0.2 cm) and SNR (worst case: 23 dB and best case: 32 dB).

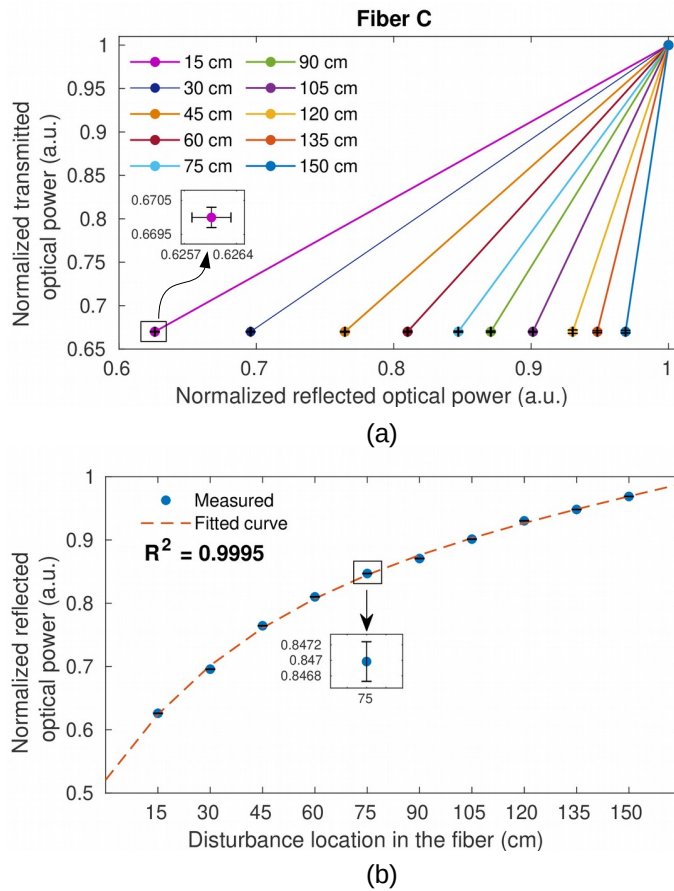


FIGURE 4.12: Results of disturbance location characterization using the Fiber C. (a) Relationship between the normalized reflected and transmitted optical powers at different disturbance locations. (b) Behavior of the normalized reflected optical power related to the disturbance location.

The Fibers D and E presented similar behavior in their responses: both presented negligible variation in the transmitted and reflected optical powers. Thus, the reflected power could not be related to the disturbances along the fiber. Figure 4.14 shows the relation between the normalized reflected and transmitted optical powers with respect to the disturbance location. Regarding the Fiber E, an attenuation of 275 dB/m was reported in [67]. This may be related to the higher particles' diameter in contrast to the size of the particle found in fibers A, B and C. Results using the Fiber E presented low reflected power variation at different disturbances locations ($\Delta r \approx 0.0011$ a.u.).

In summary, this section presented an experimental characterization of a TRA-based sensor using five different DNP-doped fibers applied on a disturbance location protocol. The performance of each sensor is evaluated according to the composition of the nanoparticles incorporated to the fiber core, as presented in Tab. 4.1. The mean size of the nanoparticles incorporated in the Fiber D was not reported (NR*). Also, Tab. 4.1 presented the attenuation (α) of each fiber, based on measurements or previous works. Fibers with big particles presented high attenuation, demanding

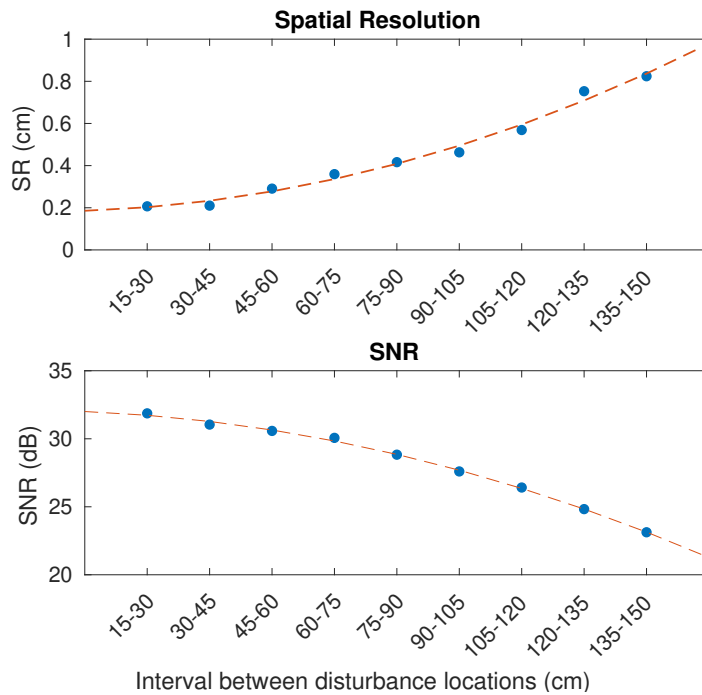


FIGURE 4.13: SR and SNR parameters during the disturbance location characterization using the Fiber C.

the use of short fibers. On the other hand, fibers containing small nanoparticles in its core presented a high sensitivity, with exponential relation between the Rayleigh backscattering and the disturbance location. In addition to a good SR (worst case: 0.8 cm and best case: 0.2 cm) and SNR (worst case: 23 dB and best case: 32 dB), which presents better results when compared to single-mode fibers [133]–[135]. The results shown that Fiber A and C are good candidates for TRA-based wearable sensors, whereas fibers B, D and E are not compatible with this method, since they presented negligible changes in the reflected optical power.

TABLE 4.1: Comparison of different DNP fibers employed in this work.

Fiber	A	B	C	D	E
DNP	<i>SrO</i>	<i>CaO</i>	<i>MgO</i>	<i>La₂O₃</i>	<i>ZnGa₂O₄</i>
NP size (nm)	100	100	40	NR*	150
α (dB/m)	~40	~55	0.4 [136]	>1000	275 [67]
SR (cm)	0.1/0.07	-	0.2/0.8	-	-
SNR (dB)	31/27	-	32/23	-	-

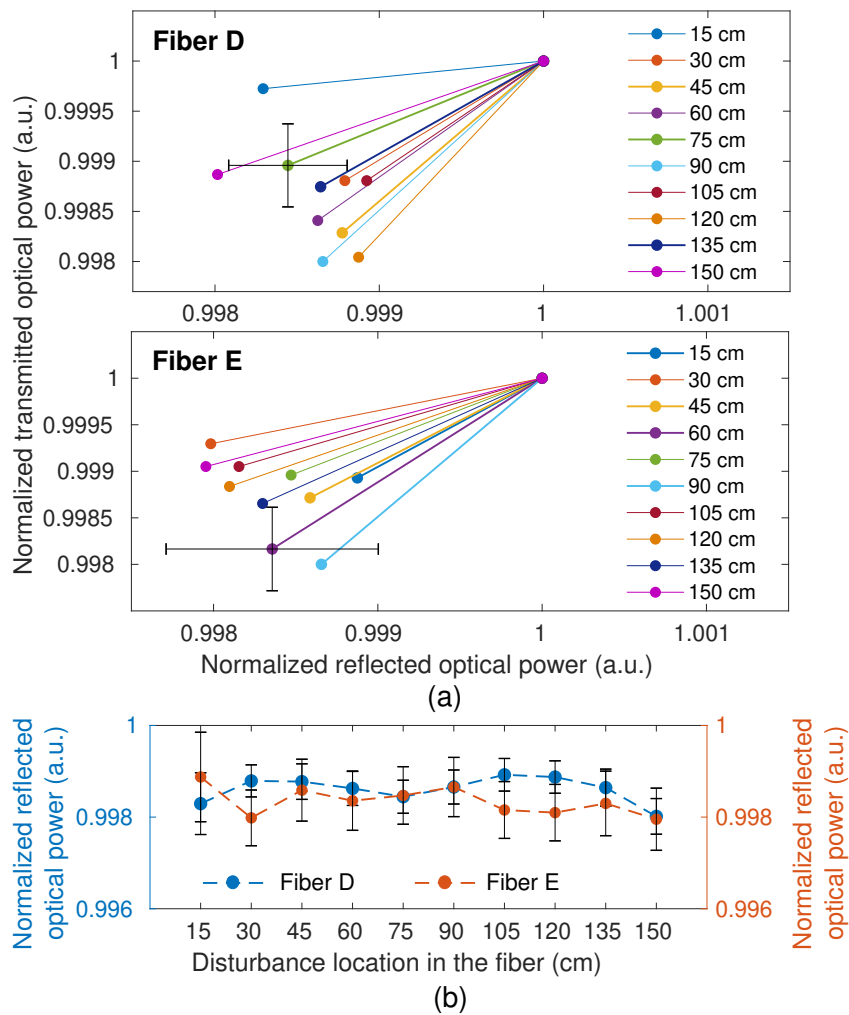


FIGURE 4.14: Results of Fiber D and Fiber E. (a) Relationship between the normalized reflected and transmitted optical powers at different disturbance locations for Fibers D (top panel) and E (bottom panel). (b) Normalized reflected power variation for Fibers D and E related to the disturbance location.

4.4 TRA-based Distributed Sensor using a DNP-doped Fiber: Multiple Simultaneous Disturbances Analysis

4.4.1 Materials and Methods

The materials used in this setup are the same as to the one used in the Section 4.3. The optical fiber used in this setup is the Fiber C, as presented in the Section 4.3, which contains MgO oxide in its composition in addition to erbium ions incorporated into the DNP to broad the emission spectrum, germanium (1.85 mol%) and small amounts of phosphorus (0.8 mol%) to raise the core refractive index and ease the fabrication of these fibers.

4.4.2 Experimental procedures

Multiple simultaneous disturbances characterization is performed to evaluate the transmitted and reflected optical power when disturbances are applied on different points along the fiber, simultaneously. The characterization consists of different combinations of disturbances using the same force, including single and multiple simultaneous disturbances. Six points of disturbances are defined, separated by 15 cm. The goal of this characterization is to identify the disturbance points by analyzing the transmitted and reflected optical powers. Figure 4.15 presents the experimental setup of this characterization. The disturbances combination is presented in Table 4.2, where 1 represents a disturbance at the respective point (P_x , $1 \leq x \leq 6$) and 0 represents no disturbance at the point.

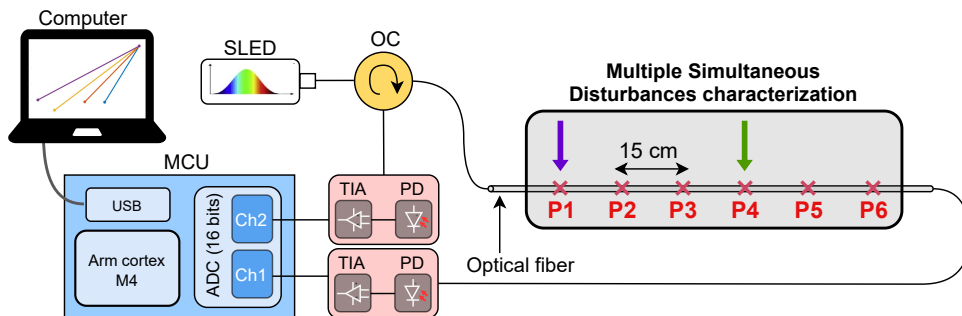


FIGURE 4.15: Experimental setup of the multiple simultaneous disturbances characterization.

An FFNN is designed to classify the disturbance event at 6 predefined points (output) by analyzing the transmitted and reflected powers (input). Two hidden layers, Hidden Layer 1 and Hidden Layer 2, are included with 600 and 300 neurons, respectively. The activation function used in the hidden layers is the rectified linear activation function (ReLU), whereas the activation function used in the output layer is the sigmoid, since it is a multilabel classification. The data is divided into training (80%) and testing (20%), and randomly permuted. Also, the input data are normalized between -1 and 1 . The batch size is 50 and 40 epochs were defined to this model, and the adaptive moment estimation (adam) optimization algorithm was employed. The loss and the accuracy are used as the classification metrics. Moreover, confusion matrices are calculated for different trials (10) with the data randomly permuted. Figure 4.16 presents the FFNN model applied in this experiment.

TABLE 4.2: Combination of the multiple simultaneous disturbances.

Combination	P1	P2	P3	P4	P5	P6
1	1	0	0	0	0	0
2	0	1	0	0	0	0
3	0	0	1	0	0	0
4	0	0	0	1	0	0
5	0	0	0	0	1	0
6	0	0	0	0	0	1
7	1	1	0	0	0	0
8	1	0	1	0	0	0
9	1	0	0	1	0	0
10	1	0	0	0	1	0
11	1	0	0	0	0	1
12	0	1	1	0	0	0
13	0	1	0	1	0	0
14	0	1	0	0	1	0
15	0	1	0	0	0	1
16	0	0	1	1	0	0
17	0	0	1	0	1	0
18	0	0	1	0	0	1
19	0	0	0	1	1	0
20	0	0	0	1	0	1
21	0	0	0	0	1	1
22	1	1	1	0	0	0
23	0	1	1	1	0	0
24	0	0	1	1	1	0
25	0	0	0	1	1	1

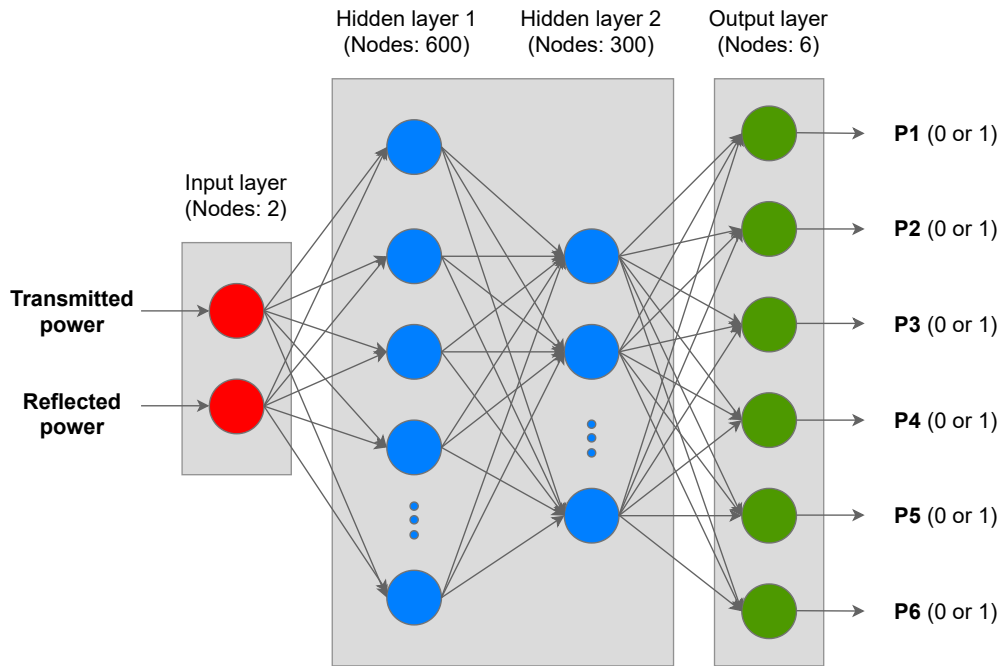


FIGURE 4.16: Feed-forward neural network (FFNN) model.

4.4.3 Results and Discussion

The normalized transmitted and reflected optical powers are the inputs to the FFNN model as shown in Figure 4.16, which pass through two hidden layers and, then, results in the outputs, i.e., the classification among the 6 possible positions. This approach addresses a critical drawback in TRA-based systems, i.e., the issue of assessing simultaneous perturbations along the fiber. Conventionally, TRA-based systems use the transmission and reflection data to estimate the position of a mechanical perturbation in the fiber, the use of this approach in conjunction with deep learning enables the detection of multiple perturbation (3 simultaneous perturbations, in this case) along the optical fiber. Furthermore, the spatial resolution of 15 cm is obtained, which is the distance between 2 consecutive classification regions. Figure 4.17 shows the transmission and reflection optical powers for 3 cases: (i) single point perturbation, (ii) 2-points perturbation and (iii) 3-points perturbation.

The results in Figure 4.17 shows that both reflected and transmitted optical powers varied with the position and number of perturbations along the fiber. Thus, the use of FFNN classification model enables the correct classification of each perturbation even when multiple perturbations are applied in the DNP optical fiber. The results of the FFNN classification model are presented in Figure 4.18. The accuracy value converged to 99.43% and the loss value to 0.0144. Such results indicate the suitability of the proposed approach for multiple impact classification, where the high accuracy indicates negligible errors in the perturbation detection. In order to verify the classification at each position, Figure 4.19 shows the confusion matrices (for each label/position) for the single and multiple perturbation detection using deep learning/TRA-based systems. Therefore, these results in conjunction with the centimeter-scale spatial resolution make this approach suitable for the smart environment application presented in the Chapter 7, where the DNP-doped fiber is embedded at different textiles/objects to the development of a smart environment that enables the detection of the user position inside the environment.

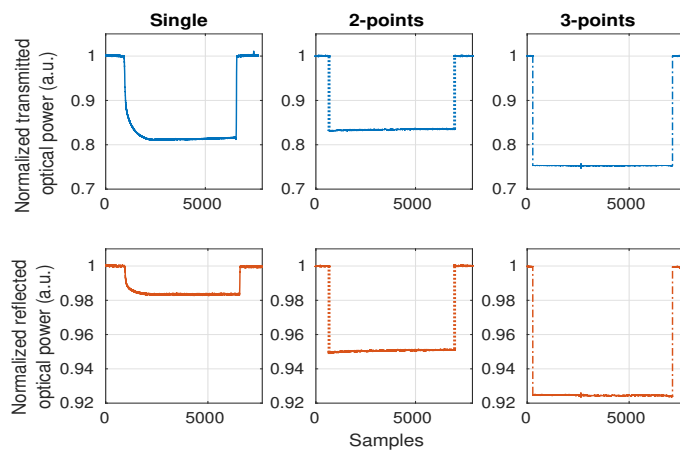
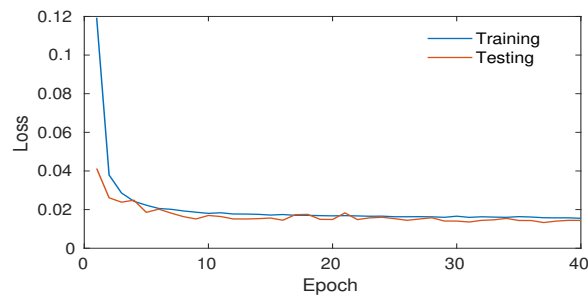
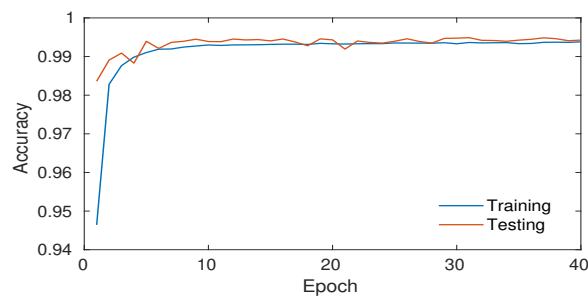


FIGURE 4.17: Transmitted and reflected optical powers under three conditions. (a) Single point perturbation. (b) 2-points perturbation. (c) 3-points perturbation.



(a)



(b)

FIGURE 4.18: Metrics of the designed model for 40 epochs. (a) Loss. (b) Accuracy

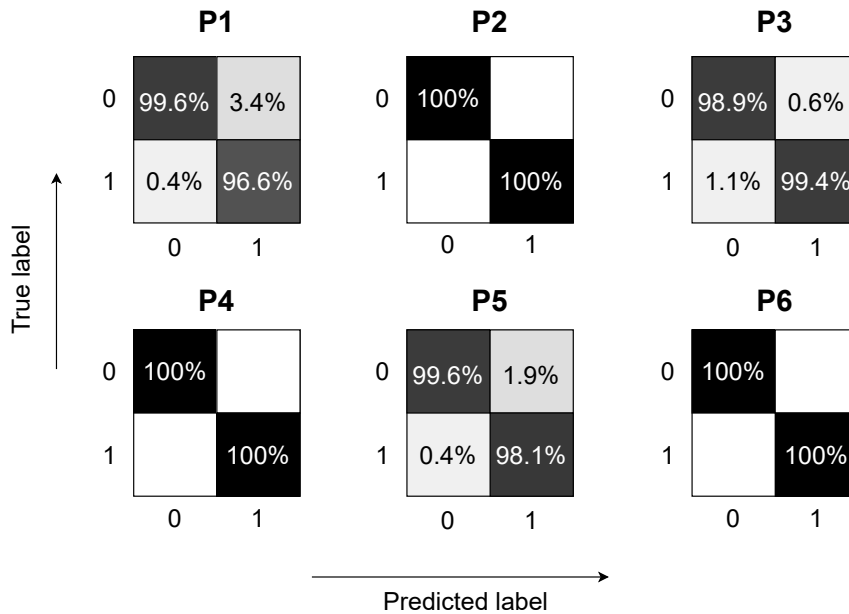


FIGURE 4.19: Confusion matrices of each label for the single and multiple perturbation detection using FFNN model.

4.5 Final Remarks

This Chapter presented the development of optical fiber sensors integrated into textiles or flexible structures for different applications. Moreover, the performance analysis of each proposed sensor is performed. First, intensity variation-based multiplexed sensors using a highly stretchable fiber were integrated into textile and characterized under different temperatures, forces, and angles. These first analyses consisted of a preliminary study using a smart textile for future applications.

Second, 10 FBGs inscribed in 2 silica fibers (5 FBGs in each fiber) were embedded in a rubber blanket. The force characterization was performed by applying different weights on the top of each FBG. The sensors were normalized by their sensitivities. Also, the spatial characterization was performed by applying the same force at the predefined points and associating the sensors' responses with the respective location. A neural network model was designed using the training data to classify new data. The classification presented an accuracy of 99.58%, which confirms the feasibility of identifying the location of the disturbance applied on the rubber blanket.

Finally, this Chapter presented a TRA-based sensor which was evaluated under two scenarios: (i) using different DNP-doped fibers to evaluate the sensors' responses under single disturbances along the fiber, and (ii) using the DNP-doped fiber which presented the best performance under simultaneous perturbations. The SNR and SR were used to evaluate the sensor's performance using five DNP-doped fibers. The DNP-doped fiber with the best performance was selected to the second scenario. Single, 2-points and 3-points disturbances were performed in six different fiber locations. A neural network model was developed to classify the disturbance locations. These results make this approach suitable for textile and smart environment applications.

Chapter 5

Optical Fiber Sensors in a Balance Assessment Protocol

This Chapter presents different POF-based systems for a balance assessment protocol. This protocol consists of disturbances on the back, front, right side and left side of a human body with different magnitudes in order to destabilize the volunteer during gait and to analyze the balance responses under perturbations on different regions and with different forces. The systems are divided into two key elements: (1) a portable smart perturbator, which can provide pushes to the human upper body and quantify the force applied on each push; and (2) a smart garment, which determines the location of the generated disturbance in relation to the human. In this Chapter, the balance assessment protocol is presented as well as the development, characterization and validation of both systems.

5.1 Balance assessment protocol

The balance assessment protocol is related to the BenchBalance project, developed for the EUROBENCH consortium¹. The BenchBalance project is a benchmarking solution proposed to conduct reproducible assessments of balance in various conditions, mainly focused on wearable robots. The main goal of this testbed is to improve the current methods of balance assessment and stabilization capability of wearable exoskeletons designed for assistance of people with motor disorders. Figure 5.1 presents the balance assessment overview. In this context, the use of optical fiber sensors is beneficial, since they can be embedded in the textiles, clothing accessories and objects. Moreover, the multiplexing capabilities of optical fiber sensors enable the development of portable and transparent smart textiles that do not inhibit the user's natural movement. Similarly, the small dimensions of the optical fibers enable their embedment in different objects without leading to weight increase in the object. For this reason, the textiles and objects in the protocol are instrumented with the optical fiber sensors, and based on the preliminary studies presented in the Chapters 3 and 4.

The following sections present the development, characterization and validation of the perturbator system and the smart garment used in the aforementioned protocol.

¹European project EUROBENCH2020, grant number n779963.

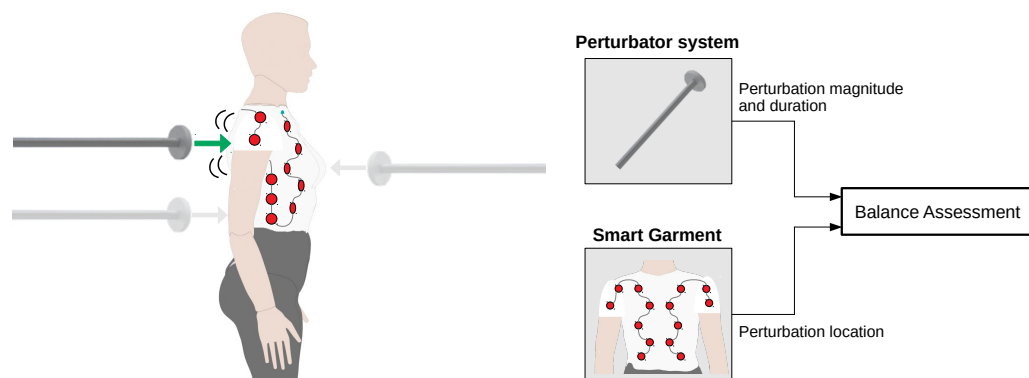


FIGURE 5.1: Balance assessment overview.

5.2 Perturbator System based on POF-embedded Force Sensor

5.2.1 Materials and Methods

The force sensor is comprised of a LPS-POF encapsulated in a flexible material, polydimethylsiloxane (PDMS), and positioned in a 3D printed support made of ABS plastic (see Figure 5.2(a)). The LPS-POF has a diameter of $580 \mu\text{m} \pm 30 \mu\text{m}$ with a core refractive index of 1.54 and a cladding, with $20 \mu\text{m}$ thickness and a refractive index of 1.45. An annealing treatment was performed to reduce the internal stress created in the fiber manufacturing process, and hence decrease the sensors' hysteresis to physical parameters [137]. The sensing approach is based on intensity variation and is comprised by a light source and a photodetector. The light source is a LED IF-E97 (Industrial Fiber Optics, USA) with central wavelength at 660 nm and the optical power variation is acquired by the phototransistor IF-D92 (Industrial Fiber Optics, USA). The signal acquisition is performed by a microcontroller FRMD-KL25Z (NXP Semiconductors, Netherlands) at 100 Hz .

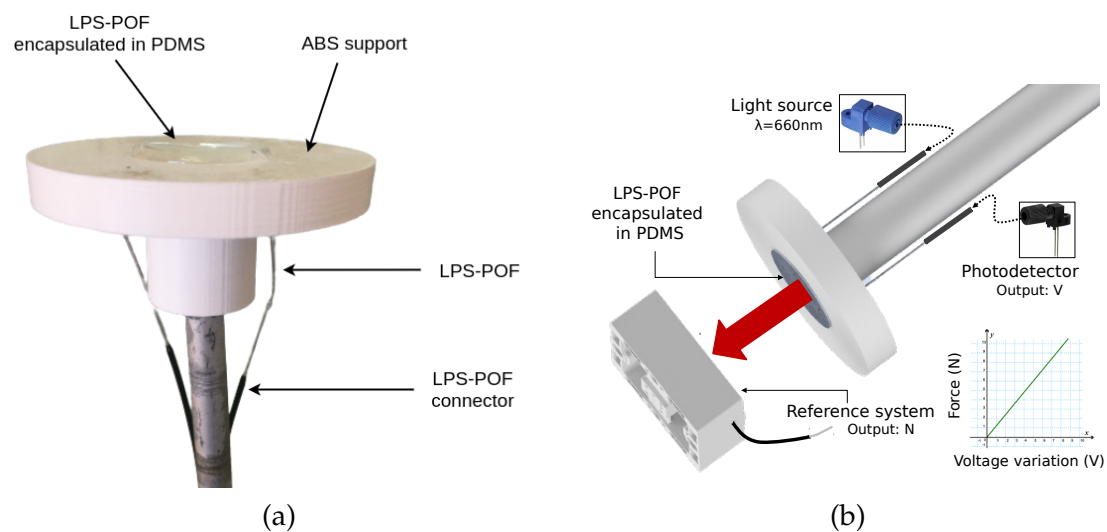


FIGURE 5.2: LPS-POF force sensor. (a) System description. (b) Characterization setup.

5.2.2 Experimental procedures

The evaluation of the POF force sensor was divided in two parts: force characterization and sensor response time analysis. A 3-axis force sensor K3D60a $\pm 500\text{N}/\text{VA}$ (ME Systeme, Germany) was used to characterize the POF force sensor, relating its output force to the output voltage variation in the phototransistor connected to the optical fiber. Tests with vertical forces were performed, as shown in Figure 5.2(b).

The analysis of the sensor response time was performed to characterize the phase delay under an applied force. As the sensor is composed of viscoelastic materials, its response presents a time-varying relationship of stress and strain [138]. The creep/recovery test is employed to characterize the viscoelastic parameters and viscoelastic materials present exponential decay of the strain response with time, as shown in Figure 5.3.

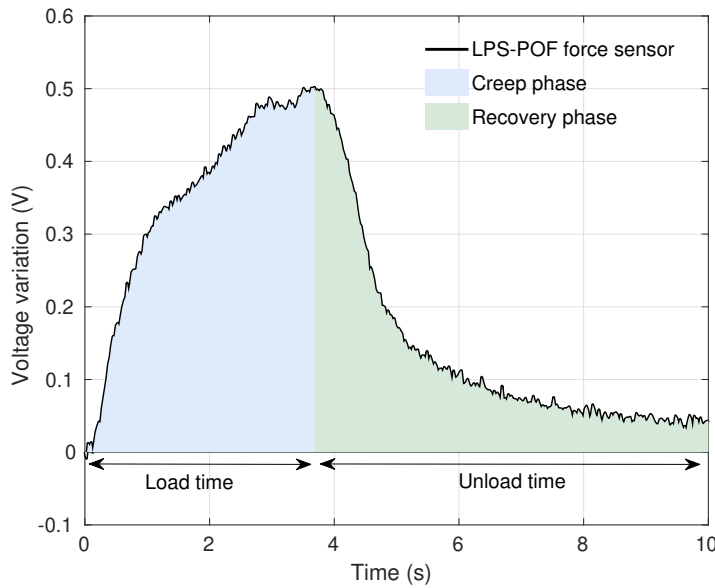


FIGURE 5.3: Viscoelastic transient pattern: creep and recovery.

Due to the non-constant POF response with stress or strain, dynamic tests are important to understand and evaluate the viscoelastic properties of POFs under different conditions, which can involve short or long-term analysis [139]. In this context, different force application frequencies in dynamic tests can change the sensors' response, e.g., hysteresis and relaxation time [140], [141]. In addition, techniques such as pre-straining method can decrease the hysteresis and provide an improvement of the sensor response on a real-time monitoring under strain application [139].

The viscoelastic response can be modeled with the Maxwell's viscoelastic model [138]. As the POF force sensor includes two viscoelastic materials (LPS-POF and PDMS), the sensor response present a exponential decay with degree 2 leading to a phase delay, hysteresis and errors. Equation 5.1 present the relation between transient (σ) and static (σ_0, σ_1) components for each material, which can be obtained in creep/recovery tests such as the one presented in [142]. In addition, t is the time and, τ_0 and τ_1 are the time constant of polymers LPS-POF and PDMS, respectively.

$$\sigma(t) = \sigma_0 \cdot e^{\left(\frac{-t}{\tau_0}\right)} + \sigma_1 \cdot e^{\left(\frac{-t}{\tau_1}\right)} \quad (5.1)$$

Therefore, to overcome these drawbacks and to improve the sensor performance, a compensation model was proposed in this work based on the viscoelastic model presented in the Equation 5.1. The compensation model comprises in decreasing the phase delay which the LPS-POF force sensor presents in the recovery phase after a load application and annulling the stationary errors, as shown in Figure 5.4, where the solid lines represent the viscoelastic response, whereas the dashed lines show the desired response, i.e., without the viscoelastic effects.

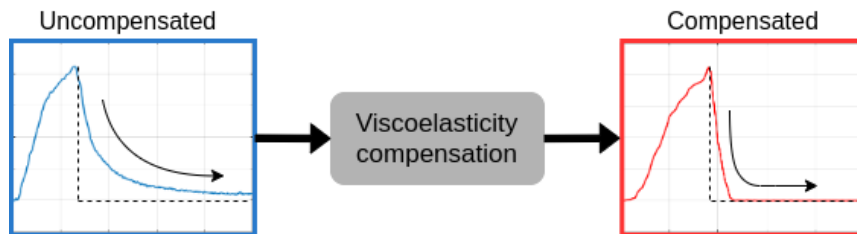


FIGURE 5.4: Viscoelasticity compensation model to improve the sensor recovery response.

After the characterization of the POF force sensor, it was used as a gait perturbation system in a balance assessment protocol, as presented in Figure 5.5. This application aims to analyze the ability of the system to identify the impact and to measure its magnitude.

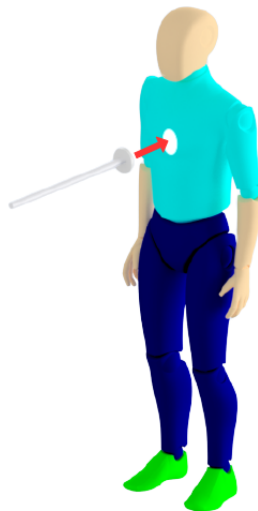


FIGURE 5.5: Perturbator system using the LPS-POF force sensor.

5.2.3 Results and Discussion

The POF force sensor characterization was performed with a reference system and the sensor voltage variation was related to the measured force of the reference system. The POF force sensor presented a linear behavior ($R^2 = 0.9974$, $RMSE = 0.7223N$), as shown in Figure 5.6. In addition, it presented a sensitivity of $40N/V$, approximately.

Figure 5.7 shows the sensor responses of both systems. In this characterization test, the force was applied in a short time (approximately 1s). For this reason, the

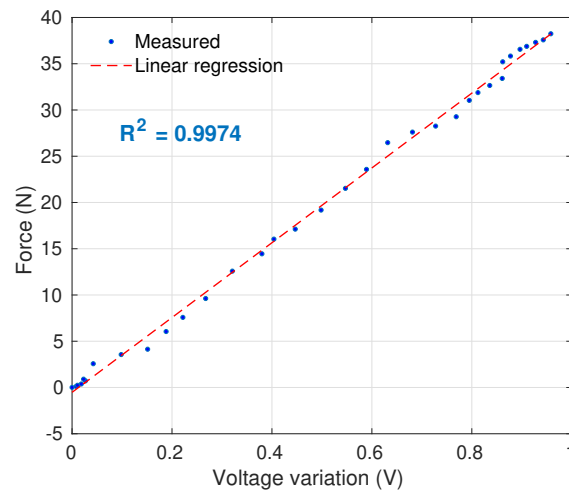


FIGURE 5.6: LPS-POF force sensor characterization.

creep phase is similar to the reference system. However, it is noticeable that the sensor presented a high phase delay in the recovery phase and a stationary error.

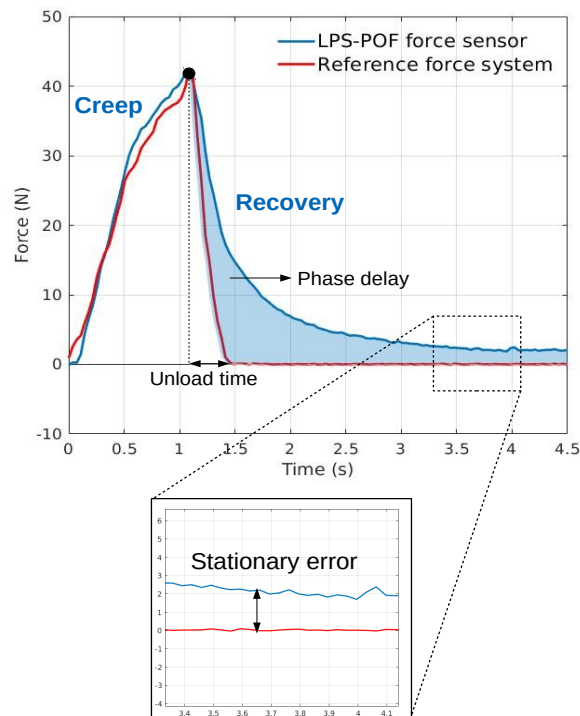


FIGURE 5.7: Viscoelastic behavior of the POF force sensor.

The compensation model was designed based on POF and PDMS materials and this model was applied in the sensor response to decrease the sensor phase delay, hysteresis and measurement errors. Figure 5.8 shows the uncompensated and compensated responses with respect to the reference system. The result shows that the compensated response has a smaller RMSE of 2.03 N, more than a twofold reduction when compared with the uncompensated RMSE (5.75 N), and a smaller phase delay with a reduction of 0.6 s in the unloading time.

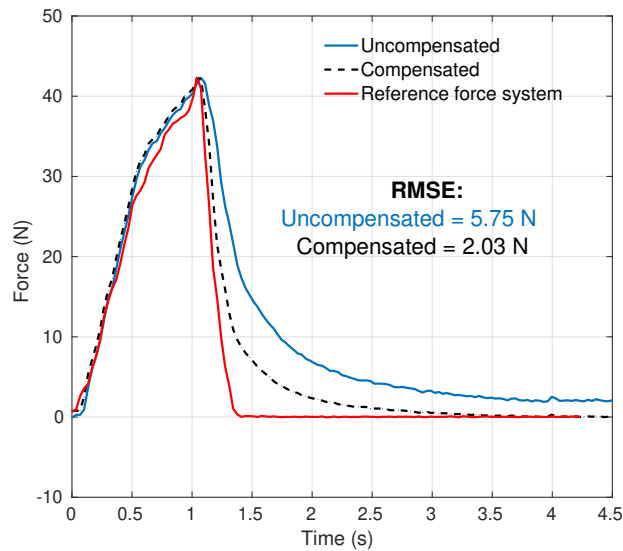


FIGURE 5.8: Uncompensated and compensated responses of LPS-POF force sensor compared to reference system.

The results of using the embedded POF force sensor as a gait perturbation system are presented in the Figure 5.9. The solid circles represent the maximum applied force during the perturbation on the subject. The viscoelastic behavior is noticeable in the recovery phase, which exhibits a delay to return to initial value, also shown in Figure 5.7. In addition, occasionally the sensor value does not return to the zero value, due to the viscoelastic behavior, and another load is applied, which generates accumulated errors.

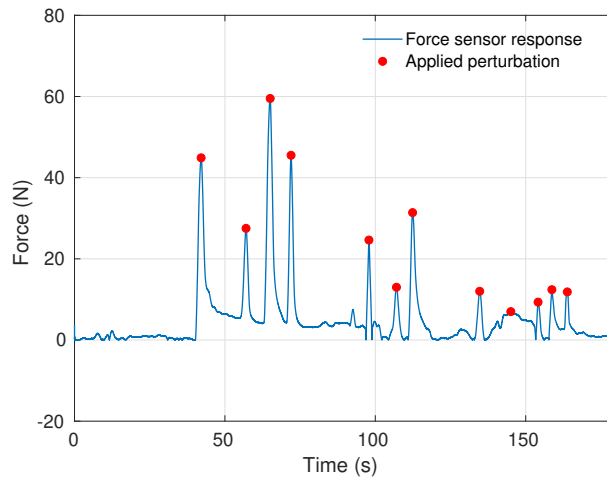


FIGURE 5.9: Results of the LPS-POF force sensor used as gait perturbation system without compensation.

The sensor has no significant phase delay in responding to load application, since the responses of the sensor and the reference system are similar in the creep phase. However, the sensor delay in the recovery phase can be a problem in this application, if perturbations are repeatedly performed at short intervals, it can lead to accumulated errors which are reflected in the numerical integration calculation. Therefore,

the numerical integration of the uncompensated and compensated responses were used as performance parameter to compare accumulated errors.

Figure 5.10 shows the results of the perturbation test with and without the proposed viscoelasticity compensation. The most significant difference is the correction of offset error and, consequently, the reduction of the delay in the recovery response. This is reflected in the calculation of the numerical integration of both responses, which is $I_{uncomp} = 900.09 \text{ N}\cdot\text{s}$ for the uncompensated response and $I_{comp} = 464.63 \text{ N}\cdot\text{s}$ for the compensated response.

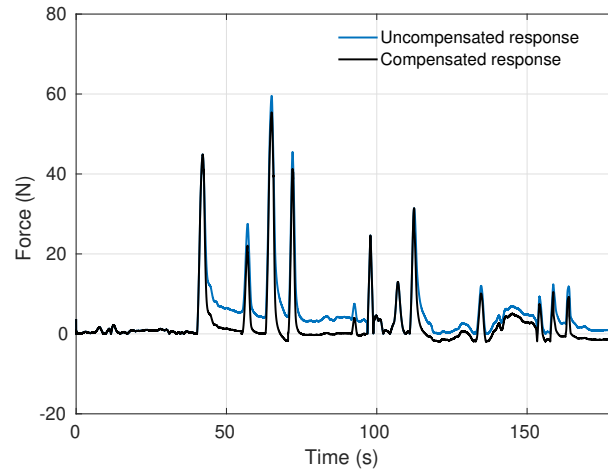


FIGURE 5.10: Results of the perturbation test with uncompensated and compensated responses.

5.3 POF Smart Garment for Impact Identification

5.3.1 Development of the POF Smart Garment

The Smart Garment structure is based on four POFs embedded in a vest with 30 sensors arranged as shown in Figure 5.11. Four photodetectors IF-D92 (Industrial Fiber Optics, USA) are used to acquire the optical power variation. The light source used was a light-emitting diode, LED ($\lambda = 615 - 630 \text{ nm} / 590 \text{ mcd} / 20 \text{ mA}$) positioned on the side cuts. A 3D-printed facet with an aluminum foil is placed to increase the reflectivity on the end facet of each POF, increasing the luminous flux, and the optical power in the phototransistor. In addition, the system is composed of an Inertial Measurement Unit (IMU) MTi-3 (Xsens Technologies B.V., NL) located on the middle of the back to monitor the trunk 3D motion. A Micro SD card module was added in the electronic system to enable the data storage during the tests for offline data processing. Also, a battery and a battery gauge are added to power the system and monitor the battery level, respectively. The signal acquisition and the LEDs control are performed by the microcontroller FRMD-KL25Z (NXP Semiconductors, NL).

Sensors' design

The POF is made of polymethyl methacrylate, PMMA (HFBR-EUS100Z, Broadcom Limited) with a core diameter of $980 \mu\text{m}$, a cladding of fluorinated polymer with $20 \mu\text{m}$ thickness and a polyethylene coating that results on a total diameter of 2.2 mm . As shown in Figure 5.12, the sensors fabrication process is divided into 3 stages: (i)

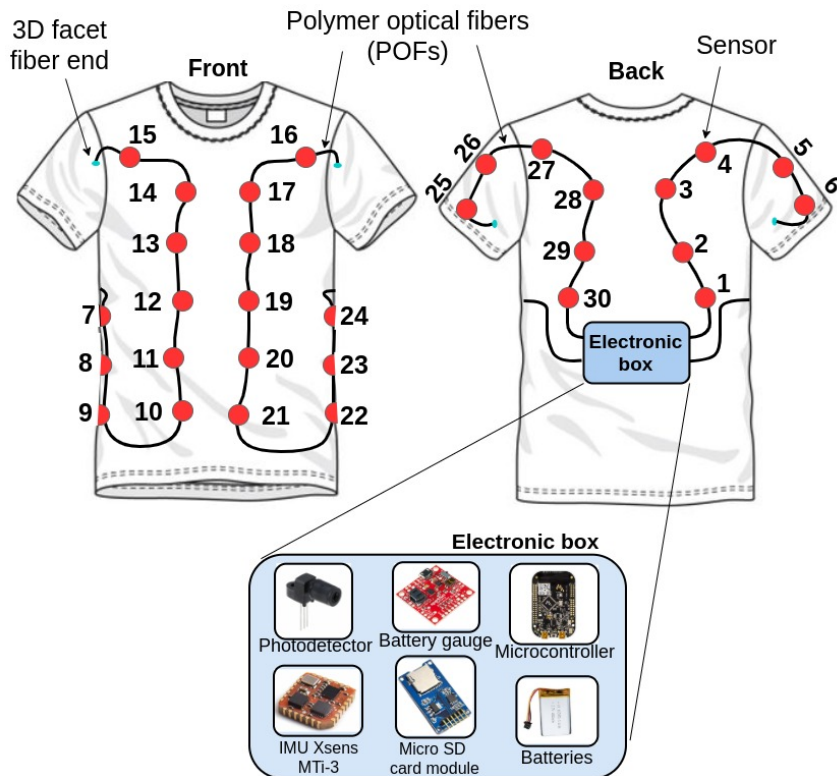


FIGURE 5.11: Smart Garment overview: Sensors arrangement in the Smart Garment.

lateral section creation by removing part of the fiber material (see Figure 5.12(a)), (ii) LED coupling to the sensitive zone (see Figure 5.12(b)) and (iii) sensor encapsulation using clear urethane rubber mixture in a 3D printed part (see Figure 5.12(c)). The fiber lateral section is created through a curved razor blade and afterwards, the optical fiber is attached to the 3D printed part (diameter = 30 mm / height = 7 mm) with the lateral section pointed towards the LED, which is already attached to the 3D part base. With the fiber lateral section coupled to the LED, the clear urethane rubber mixture is spilled into the part and reserved for 24h at room temperature to be cured. Figure 5.12(d) presents the encapsulated sensor when the clear urethane rubber is cured and Figure 5.12(e) shows the sensor incorporated in the textile. The stages (i), (ii) and (iii) can result in sensor-to-sensor differences. The lateral section parameters, the coupling distance and the clear urethane rubber mixture might be different for each sensor, and for this reason, a normalization is necessary.

Data processing and analysis

The multiplexing technique proposed by [79] comprises of a sequential activation of each LED with a predefined frequency and activation sequence. In this case, predefined LEDs are activated at a time and a microcontroller controls the activation frequency and sequence. The acquisition sequence is from the first LED to the last LED of each fiber with a sample time of 2 ms for each activation, as discussed in 2.2.1. In addition, the microcontroller is responsible for the acquisition of the optical power measured by each photodetector when each LED is active, resulting in four matrices, one for each P_x , as shown in Figure 5.13, in which the columns represent the optical power acquired by the photodetectors when a predefined LED is

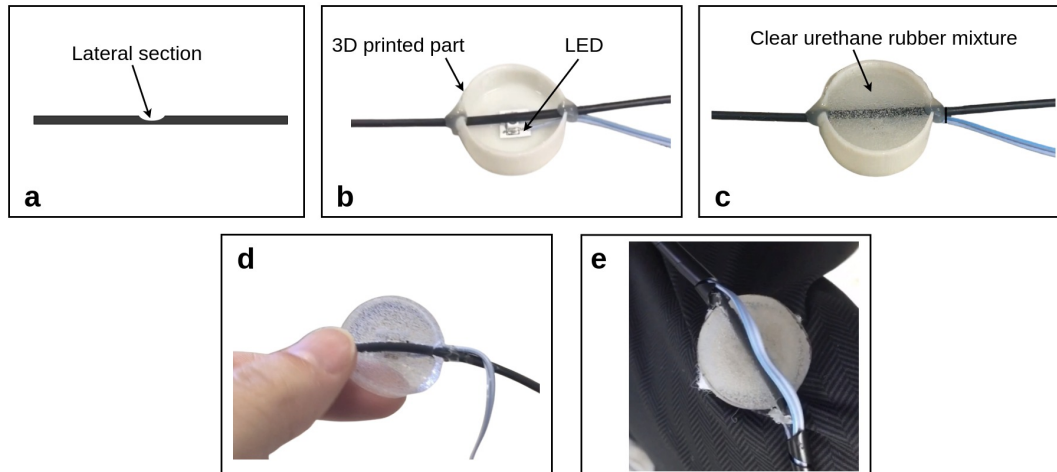


FIGURE 5.12: Sensors fabrication process. (a) Removal of part of the fiber material creating a lateral section. (b) LED coupling to the fiber lateral section in a 3D printed part. (c) Sensor encapsulation using clear urethane rubber mixture. (d) Encapsulated sensor. (e) Sensor incorporated in the garment.

active, and the row represents the temporal acquisition, resulting in a matrix with 30 columns and n rows (samples).

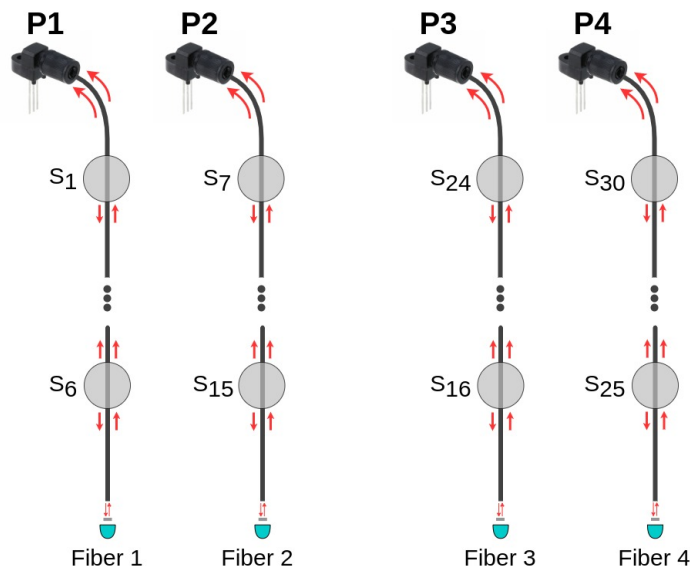


FIGURE 5.13: POF pressure sensors operating setup.

Based on the sensors' responses, the following technique is proposed to identify impacts. Since the smart garment consists of intensity variation-based sensors, when a sensor is pressed during a short time interval, the optical power varies during this time and then returns to the initial value. Thus, when the derivative of the sensors' optical power is analyzed, there are outliers in the data which corresponds to the impact on the respective sensor. Figure 5.14 shows the plots of the optical power and of the optical power derivative of the sensor 18, which are used to identify an impact. The body natural movement also causes a signal variation. However, the variation at the impact moment is higher and its sample is considered an outlier in

the sensors' data. Therefore, the Grubbs's test, which is introduced by [143] and has been widely applied for the detecting of outliers in the data, is used in the derivative of the sensors' optical power data to identify impacts on the sensors.

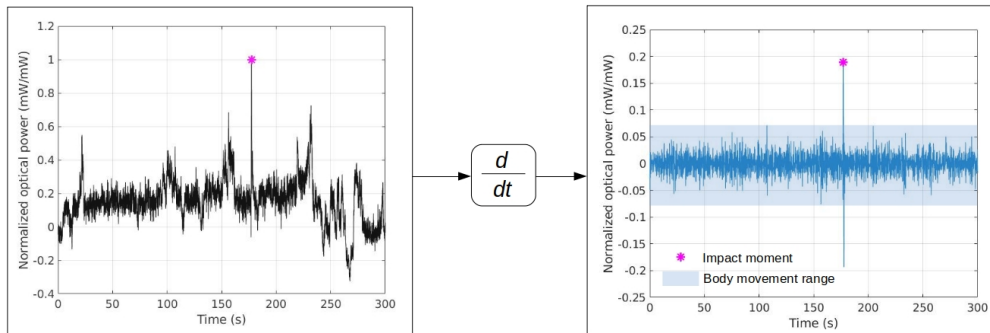


FIGURE 5.14: Proposed technique to identify impacts on the sensors by using outliers identification algorithm in the derivative of the sensors' optical power: example using the sensor 18.

5.3.2 Experimental procedures

In order to characterize the optical fiber sensors, two tests are performed: (i) force characterization and (ii) impact location identification characterization, see Figure 5.15. First, the force characterization aims to characterize the force of each POF pressure sensor. A load cell K3D60a (ME Systeme, Germany) is used as reference force sensor, and the characterization consists of applying the vertical force of the reference force sensor on the top of each sensor on the range of 20 N to 120 N with steps of 20 N. The transmitted optical power is correlated with the force applied on each sensor.

Then, the impact location identification characterization aims to validate the proposed technique using the sensors' responses to identify the impact location on the body, as previously mentioned in the Section 5.3.1. This characterization consists of several perturbations on known areas of the body and the use of the proposed technique to identify these areas. Finally, a perturbation protocol was proposed to evaluate the balance under a instability condition. The perturbation protocol consists of impacts on the back, front, right side and left side of a human body with different magnitudes in order to destabilize the volunteer and to analyze the balance responses under perturbations on different regions and with different forces. The system which perform the perturbations consists of the load cell K3D60a, also used in the force characterization of the smart garment' sensors, and the normal force is analyzed. Using this system, it is possible achieve the force magnitude feedback during the tests. In this protocol, the mediolateral, anteroposterior and longitudinal angles of the volunteer are acquired by the IMU, since the analysis of these angles improves the evaluation of the balance responses during the perturbation protocol. Figure 5.15 presents the experimental setup, including the three proposed tests.

As shown in Figure 5.15(c), the perturbation protocol is divided in four main regions of the human body: back, front, right and left. Each main region is subdivided into upper and lower part. The upper part represents the upper half of the trunk, whereas the lower part represents the lower half one. For this reason, the predefined sub-regions are lower back (B1), upper back (B2), lower front (F1), upper front

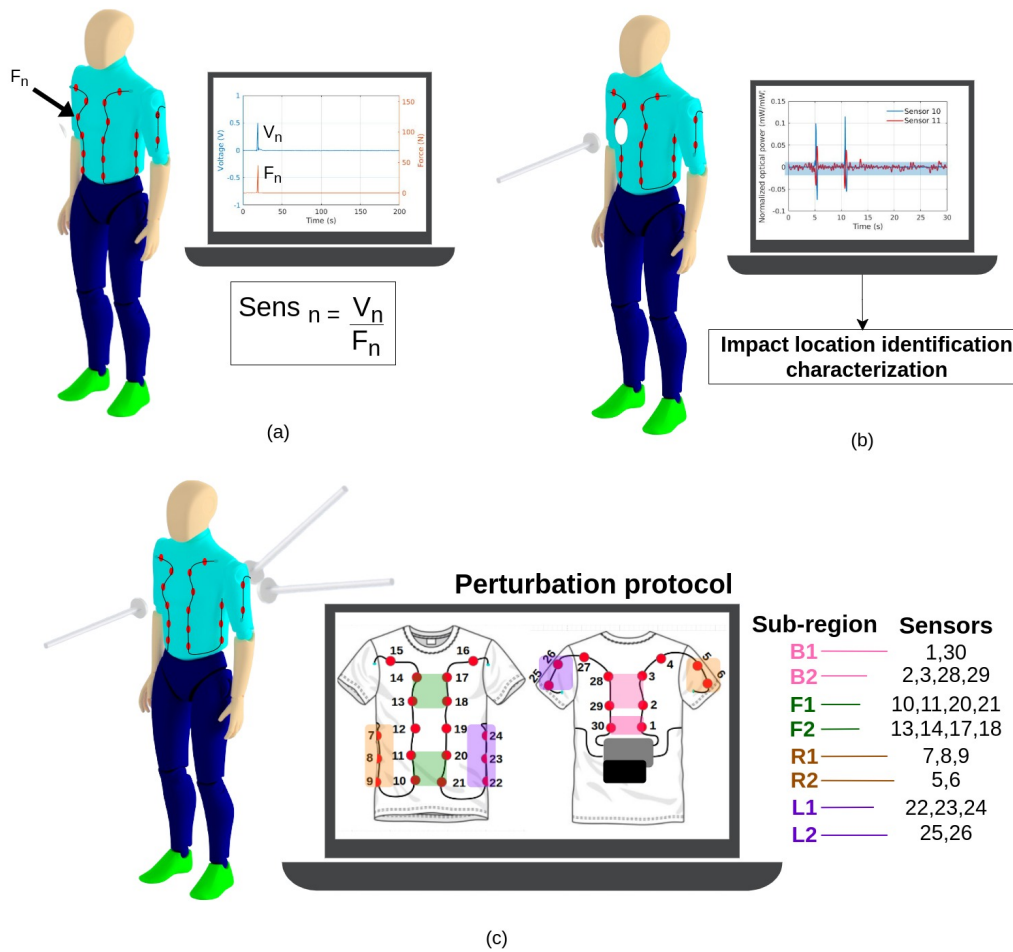


FIGURE 5.15: Experimental setup. (a) Force characterization and sensitivity calculation based on the optical power variation and reference system. (b) Impact location identification with a sample of the sensors responses. (c) Perturbation protocol with the back, front, right and left perturbations in the volunteer. All sub-regions are also presented.

(F2), lower right (R1), upper right (R2), lower left (L1) and upper left (L2). Each sub-region corresponds to sensors groups, and by the variation of the sensor's responses, using the proposed technique mentioned in the Section 5.3.1, it is possible to identify which region is perturbed. In addition, perturbations are applied on each sub-region with two different magnitudes, so-called small and large perturbations, in order to analyze the influence of the force magnitude on the balance response.

5.3.3 Results and Discussion

Sensors' characterization

The analysis of the sensor's responses was based on the intensity variation. Figure 5.14 shows the analysis method of one sensor (sensor 18), since it is close to the chest region, where the impact is applied. The top graphic represents the sensor temporal response and the down graphic presents the sensor's derivative. In this analysis, it is important to observe that the body natural movement provokes a signal variation. However, the variation at the impact moment is higher and its sample is considered an outlier of the sensor's data. As presented in the Figure 5.14, the shaded region represents the body movement range and the marker represents the impact moment. Thus, this method used to detect the outlier comprises the impact identification technique.

Figure 5.16 shows the responses derivative of the 10 sensors (left axis) under forces applied by a reference system (right axis, red curve). The reason of using 10 sensors is to provide better visualization of the curve. However, the actual sensors responses include 30 sensors. The sensors are manufactured and for this reason they present physical differences. Thus, each sensor has a different response under similar applied forces, resulting in different sensitivities. Due to this difference between the sensors, they were normalized by their sensitivities, to achieve similar responses by each sensor.

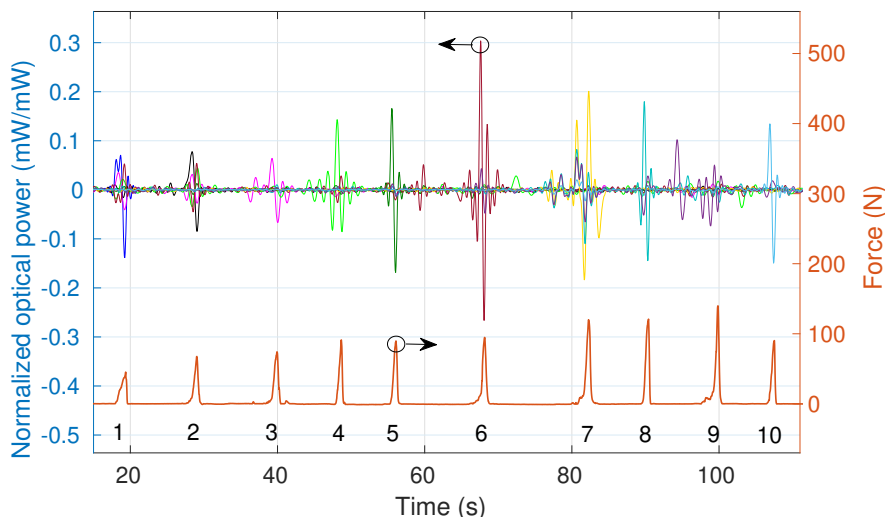


FIGURE 5.16: Force characterization of 10 sensors, where the right axis shows the force measured in the reference system and left axis shows the derivative normalized optical power for 10 sensors, which indicates the signal variation of the active sensors during the impacts.

The sensor's sensitivities are defined as the angular coefficient of the linear regression obtained by the relation between the sensor's output (Volts) and the applied forces (Newtons) during the force characterization. Table 5.1 shows the sensitivities of each sensor used for the sensor's normalization. Sensors present sensitivities from 0.11 up to 15.40 and it may be related to the sensor's fabrication, since some sensitive zone geometries and the clear urethane rubber mixture which encapsulate the sensitive zone and the LED may favor the increase of the transmitted lumens to the core under a force application. The different sensors sensitivities are not an issue for the impact identification and the balance assessment, since it is possible to acquire the individual sensors' responses using the multiplexing technique and even when a small force is applied between two sensors with different sensitivities, both responses present variation at the same time. A sensor with higher sensitivity presents a higher variation under the same applied force. However, by normalizing the sensors, the responses are balanced and the highest resultant response represents an impact closer to the respective sensor.

TABLE 5.1: Sensor's sensitivities of all 30 sensors in the smart garment.

Sensor	Sensitivity (mV/N)	Sensor	Sensitivity (mV/N)
1	11.95	16	8.15
2	0.15	17	9.19
3	0.11	18	0.14
4	0.99	19	0.39
5	1.74	20	5.51
6	0.25	21	4.27
7	2.25	22	0.15
8	1.65	23	2.33
9	1.43	24	0.19
10	8.64	25	9.92
11	0.44	26	7.83
12	8.05	27	15.40
13	9.44	28	6.67
14	0.23	29	5.05
15	0.14	30	7.02

Experimental protocol validation

In the impact location identification characterization, four impacts were performed to analyze the sensor responses and to validate the impact location identification technique. Figure 5.17 shows the results of impacts on 4 different body regions. The red area consists of the impacts on the sensor 10 and the blue area consists of the impacts on the sensor 11. The selected body region 1 corresponds to a region between the sensors 10 and 11, and the body region 2 corresponds to the top of the sensor 11. The shaded regions represent the impact peaks, and since the sensor's responses are normalized, a higher magnitude means a closer impact, i.e., the response magnitude of the sensor 11 is lower than the sensor 10, and it demonstrates that the impact is closer to the sensor 10 (3 cm distance) than the sensor 11 (7 cm distance). The yellow and orange curves consist of the response of the sensors 5 and 6, whereas the violet and green curves consist of the response of the sensor 25 and 26. The impact on the

body region 3 is similar to the impact on the body region 1, since both regions include two sensors. As the magnitude of the sensor 6 is higher than the one of sensor 5 after the normalization, it indicates that the impact was closer to the sensor 6. The impact on the region 4 is similar to the impact on the body region 2, since it is performed only on one sensor (sensor 26). However, this sensor presents a higher force magnitude.

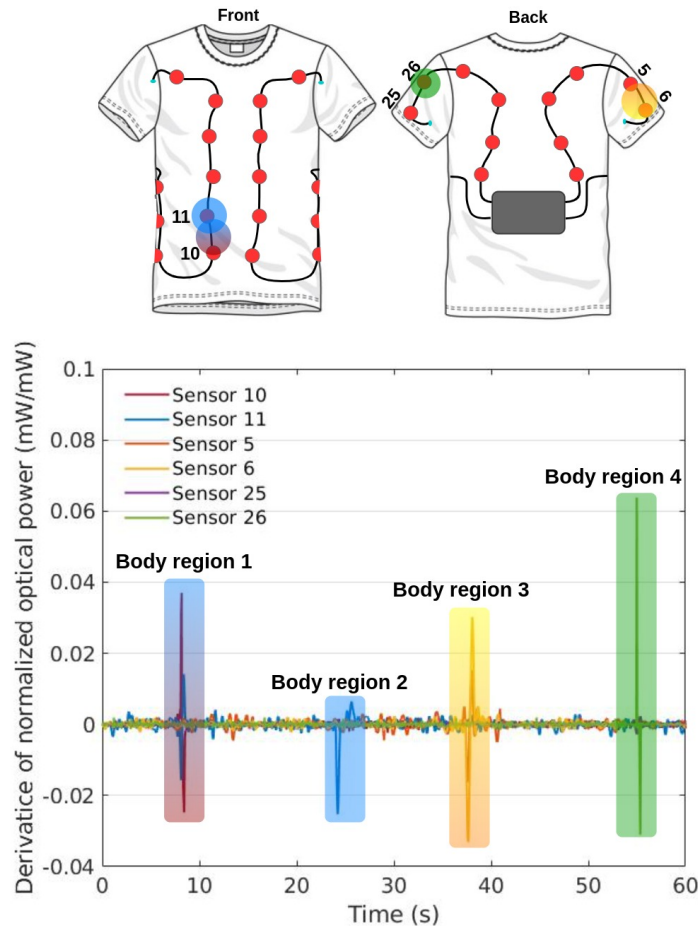


FIGURE 5.17: Impacts on different body regions.

The results presented in Figure 5.17 show the ability to distinguish not only which sensor was activated, such as the body region 2 and 4, but also if the impact was performed between two sensors, such as the body region 1 and 3. It enables the identification of regions where perturbations were applied on the top of a sensor and also the perturbations applied between consecutive sensors, increasing the spatial resolution of the system. Based on the sensor with the lowest sensitivity (sensor 3) and the smaller force applied on sensor 3 (20 N in the force characterization), and considering the sensor noise, the estimated spatial resolution is 1.7 cm, which was estimated from the signal-to-noise ratio and the sensors sensitivities.

The distance between the applied force to the activated sensor can be estimated based on a continuous beam model, in which the adjacent sensors correspond to the supports and the fiber correspond to the beam, as presented in [144] for similar application. The optical power response for the force applied along the fiber in the region between these adjacent sensors is inversely proportional to the distance of this force to the sensor, i.e., as the distance increases the optical power decreases,

when compared to the case in which the force is applied on the top of the sensor, which is the maximum optical power response.

Another important issue to be discussed is the sensor positioning and its influence on the sensors' responses. The human body has regions with different stiffness and an impact on a more flexible region leads to a higher fiber bending when compared to a more rigid region (e.g. the back region), under a same applied force. It means that the sensors positioned on flexible regions can identify impact with smaller forces or have higher deflections for the same force. However, the proposed technique was able to identify impacts even on the sensors positioned on rigid regions, within the force range (20 N to 120 N) applied in this work. Thus, the stiffness issue of the body regions do not alter the impact identification. In fact, if a known force is applied, it is possible to estimate the stiffness of each body region with previously calibrated sensors.

Finally, the results of the perturbation protocol are presented in the Figure 5.18, Figure 5.19, Figure 5.20 and Figure 5.21. Each figure is divided into 3 parts: (a) the garment with the description of the impact sub-regions and the sensors related to these sub-regions, (b) two synchronized graphics showing the activated sensors of the sub-regions and the vertical forces (force z) applied by the reference force sensor during the perturbation protocol, and (c) the IMU results, presenting the mediolateral, anteroposterior and longitudinal angles during the protocol. The shaded regions represent the different force magnitudes, in which the clearest one is the small perturbation and the darkest one is the large perturbation.

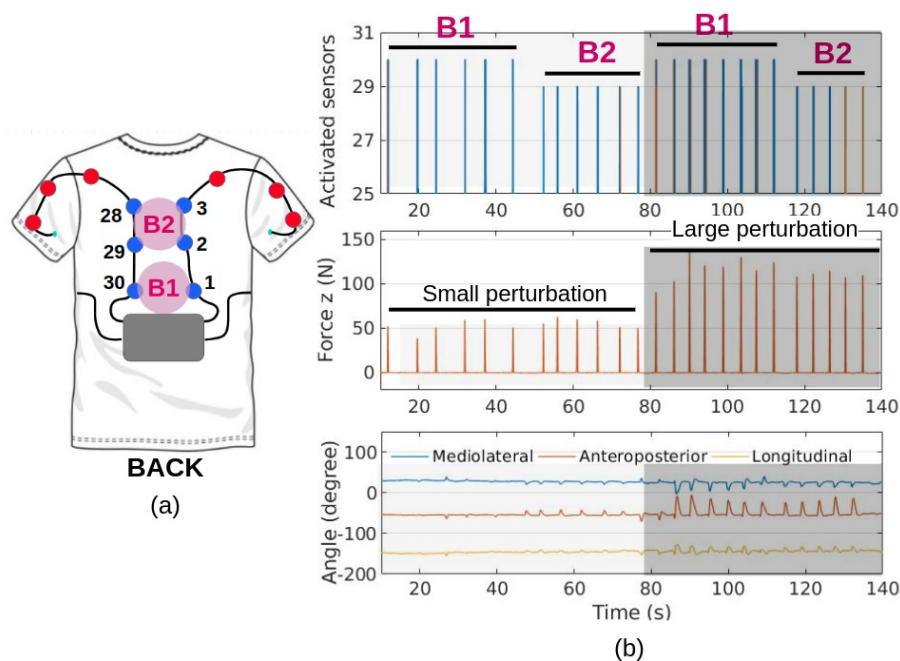


FIGURE 5.18: Results of the perturbation protocol to impacts on volunteer's back. (a) Smart Garment overview with description of the back sub-regions and the sensors related to these sub-regions. (b) Results of the activated sensors, the applied vertical forces (force z) for each sub-region and the volunteer's trunk angles (mediolateral, anteroposterior and longitudinal).

In the results of impacts applied on the back sub-regions, the sensors with highest activation were 30 (B1) and 28, 29 (B2), which implies a left-facing perturbation, as shown in Figure 5.18. Since the impact was not centralized, it leads to a user's

balance response not only in the anteroposterior direction, but also in the mediolateral and longitudinal directions. It is noticeable when the large perturbations are applied, leading to a higher angles of the balance response.

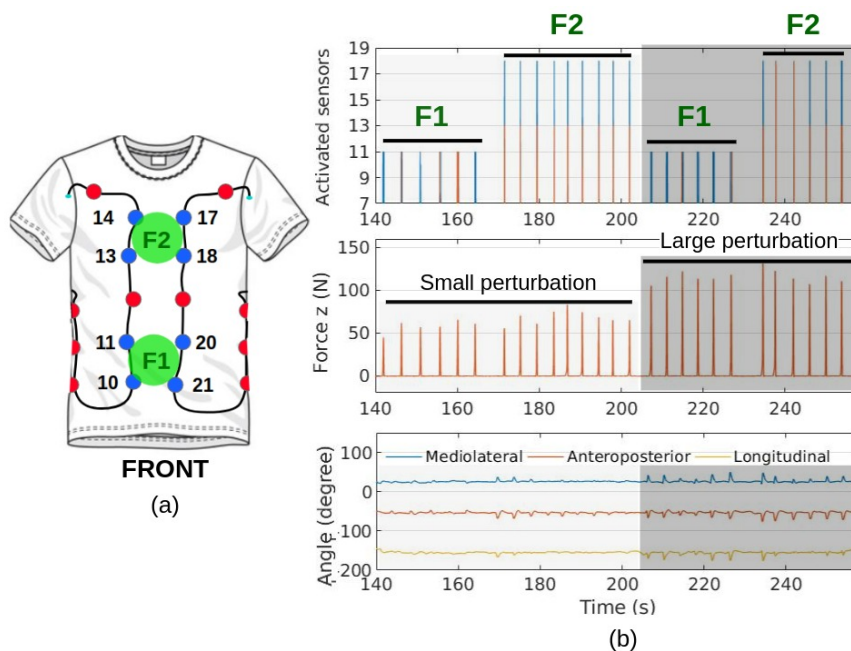


FIGURE 5.19: Results of the perturbation protocol to impacts on volunteer's front. (a) Smart Garment overview with description of the front sub-regions and the sensors related to these sub-regions. (b) Results of the activated sensors, the applied vertical forces (force z) for each sub-region and the volunteer's trunk angles (mediolateral, anteroposterior and longitudinal).

The results of impacts applied on the front sub-regions were different between each other. In the sub-region F1, sensors 10 and 11 are more activated, whereas in the sub-region F2 the sensors 13 and 18 are more activated. It means a left-facing perturbation on the lower front and a central perturbation on the upper front, which is reflected in the results of the mediolateral angles, since for the perturbations that are applied on the center of the body front. The angles of the balance response have lower influence in the mediolateral and longitudinal directions. Results of impacts on the back presented mediolateral angle variations up to 33.12° and mean of 19.21° for large perturbations. On the other hand, results of impacts on the front showed mediolateral angle variations up to 26.59° and mean of 10.90° . In addition, the anteroposterior angles of the balance response under perturbations on the user's front were lower than on the user's back. It is due to the influence of the human's sensory system when the user see and expect the perturbation (front), and can anticipate the balance response, opposed to a perturbation on the back in which the user does not see and anticipate.

The results of impacts applied on the right sub-regions showed a low influence on the anteroposterior direction. The predefined sensors of the sub-region R1 are 7, 8 and 9, as shown in Figure 5.20(a). However, the sensor 10 was also activated in some perturbations, as presented in the first graphic of the Figure 5.20(b). It led to a variation of the longitudinal angles in addition to the mediolateral angles, since the perturbation also rotated the user's body in the longitudinal direction, due to the location of the sensor 10 (right-front of the body). It is also possible to observe

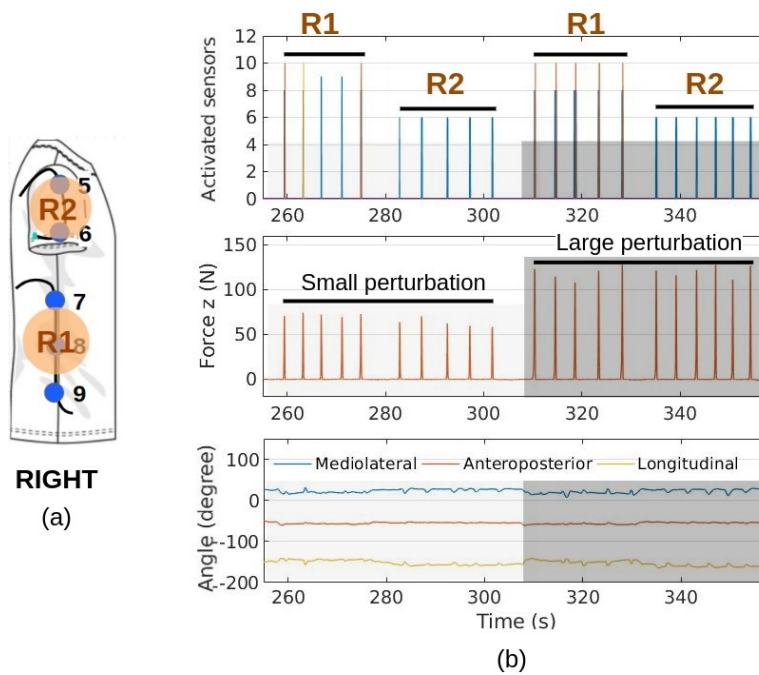


FIGURE 5.20: Results of the perturbation protocol to impacts on volunteer's right. (a) Smart Garment overview with description of the right sub-regions and the sensors related to these sub-regions. (b) Results of the activated sensors, the applied vertical forces (force z) for each sub-region and the volunteer's trunk angles (mediolateral, anteroposterior and longitudinal).

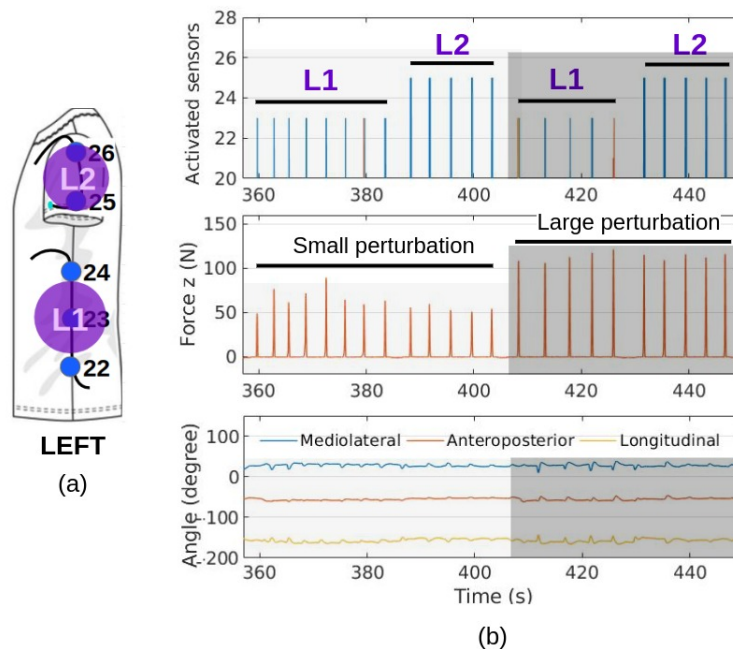


FIGURE 5.21: Results of the perturbation protocol to impacts on volunteer's left. (a) Smart Garment overview with description of the left sub-regions and the sensors related to these sub-regions. (b) Results of the activated sensors, the applied vertical forces (force z) for each sub-region and the volunteer's trunk angles (mediolateral, anteroposterior and longitudinal).

that the perturbations on the mediolateral direction present angle magnitudes much lower than in perturbations on the anteroposterior direction. It is due to the base of support is more stable in the mediolateral direction than on the anteroposterior direction.

The results of impacts applied on the left sub-regions presented similar responses to the previous results (on the right side of the body). The predefined sensors of the sub-region L1 are 22, 23 and 24. However, the sensor 21 was activated, which also led to a angle variation in the longitudinal direction, mainly under large perturbations, whereas the sensors 25 and 26 are activated during the impacts on the sub-region L2, as the predefined sensors, which reflects in the highest influence in the mediolateral direction. In addition, it is possible to observe the difference between the angles during impacts on the lower sub-region (L1) and the upper sub-region (L2), in which the angles provoked by the impacts on L2 were lower than the angles provoked by the impacts on L1, and almost negligible. It means that the impacts on lower sub-region were more destabilizing than on the upper sub-region. This result was different for the other regions, which presented similar responses to the impacts on lower and upper sub-regions, and it can be related to the volunteer's capability to recover to these impacts on the upper left side.

5.4 Final Remarks

This Chapter presented the development of two devices based on optical fiber sensors for a balance assessment application. The balance assessment protocol consisted of applying perturbations on predefined areas of the human trunk to destabilize the volunteer and analyze the balance responses under perturbations on different regions and with different forces.

The first proposed device was a perturbator system with a force intensity variation-based sensor using LPS-POF fiber. The force characterization is performed and, due to the high flexibility and the viscoelastic response, a compensation model is designed to decrease the recovery phase (unload time) and reduce errors. Compensated response presented lower hysteresis, leading to a decrease of the RMSE and numerical integration of approximately 65% and 48%, respectively.

The second proposed device was a smart garment with 30 multiplexed intensity variation-based sensors using PMMA fiber. The sensors were arranged to cover all the regions of the human trunk. Each sensor was characterized under different forces and normalized by their sensitivities. After, several perturbations on known areas of the body were performed and a technique was proposed to identify the impact location on the body. Finally, a balance assessment protocol was performed and the results showed the feasibility of the proposed smart garment to identify the impact region on the body and improve the information during a balance assessment under instability condition.

Chapter 6

Smart Textile for Remote Healthcare Monitoring

This Chapter presents different solutions of photonic textiles (wearable and non-wearable), based on the preliminary studies of Chapters 3 and 4, for application in remote healthcare monitoring. A smart carpet is proposed for acquisition of kinematic and kinetic parameters for gait analysis. By using intensity variation-based POF sensors, it is possible to estimate the ground reaction force as well as the spatio-temporal gait parameters, such as step/stride length, cadence and stance duration. In addition, in a wearable approach, a smart garment is proposed, also using multiplexed intensity variation-based POF sensors. Machine learning algorithms are used to identify different daily activities and to evaluate the demand of the number of sensors employed in the garment fabrication. Different biomedical parameters (biomechanical and physiological) are also estimated when an user is wearing the smart garment. Finally, in the same context a fully portable smart pants is proposed. Gait analysis and activities recognition using deep learning algorithms are presented in this Section. Figure 6.1 summarizes the applications approached in this Chapter.

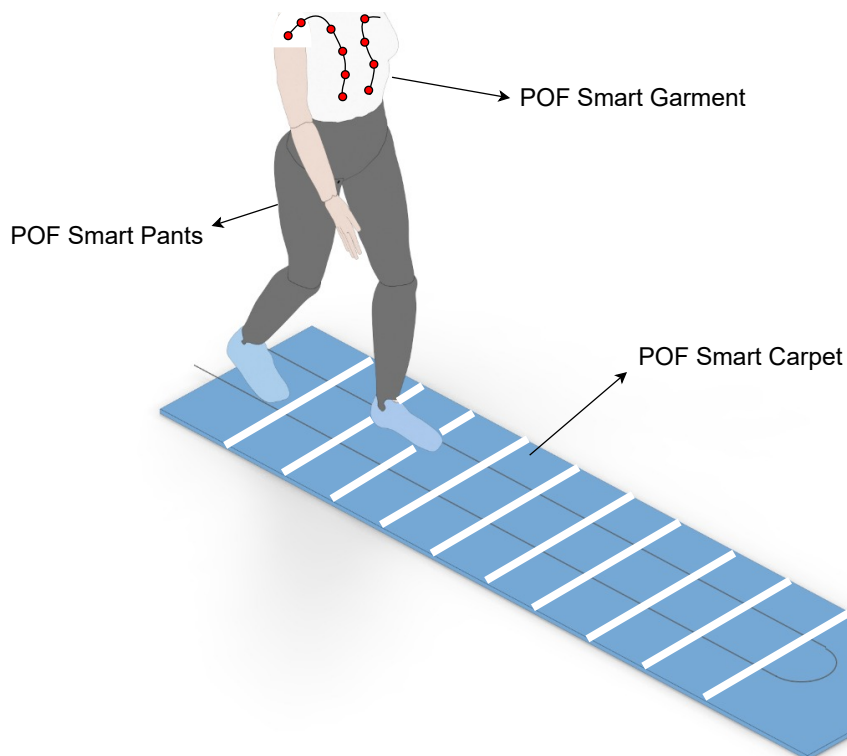


FIGURE 6.1: Chapter 6 overview: Smart Textiles applications.

6.1 POF Smart Garment: Human Activity Classification

6.1.1 POF Smart Garment

The POF smart garment comprises of 30 multiplexed intensity variation-based POF sensors incorporated in a vest, as presented in the Section 5.3. In addition, an IMU MTi-3 (Xsens Technologies B.V., NL) is positioned on the upper region of the smart garment back to estimate the trunk angles. To increase the transmitted optical power, four 3D facets with aluminum foil are positioned at the other end of each fiber, in which the light reflects in the aluminum foil towards the photodetector direction.

6.1.2 Experimental procedures

Human activity recognition protocol

The human activity recognition protocol consists of 4 healthy volunteers wearing the smart garment and performing six different daily activities: standing, sitting, squatting, up-and-down arms, walking and running. This protocol aims to monitor common daily movements and use the smart garment to identify each activity in addition to extract different movement-related parameters during the tests.

Standing represents the activity in which the volunteer is in upright position, whereas the sitting activity involves the volunteer sitting on a chair. The squatting activity is divided into 5 stages (states and transitions): (i) upright position (state), (ii) squatting down (transition between upright to squatting), (iii) squatting (state), (iv) squatting up (transition between squatting to upright) and (v) upright position (state), and these stages are cyclically repeated. The up-and-down arms activity is divided into 4 stages (states and transitions): (i) moving up the right arm (shoulder flexion of 90°), (ii) moving down the right arm (shoulder extension of 90° , back to neutral position), (iii) moving up the left arm (shoulder flexion of 90°) and (iv) moving down the left arm (shoulder extension of 90° , back to neutral position), and they are cyclically repeated. Finally, the walking and running activities were performed on a treadmill to control the velocities and achieve a movement pattern. The walking speed is 0.5 m/s and the running speed is 2.0 m/s . All activities were performed for 2 minutes.

Data processing and Machine Learning training model

The multiplexing technique proposed by [79] consists of a sequential activation of the LEDs and the optical power acquisition in a short time interval. After the activation and optical power acquisition of the last LED, the optical power of all sensors is transmitted to the microcontroller and this process is cyclically repeated. The sensors' signal results in a matrix with 30 columns (corresponding to the 30 sensors) and n rows (corresponding to the n samples).

For the activity classification, the kNN classifier, previously presented in the Section 2.4.1, was employed. The kNN classifier is a popular method with simple implementation and significant classification performance [112]. Furthermore, the kNN is a supervised method of the machine learning field which does not assume a linear class boundary, since the kNN method determines the class based on the k -nearest neighbor training points. For this reason, it has the advantage of producing classification fits that adapt to any boundary [145]. The kNN input data comprise 30 attributes (response of the 30 sensors), six classes (activities) and each sample is labeled according to the respective activity. The classes are divided into: standing (c_1),

sitting (c_2), squatting (c_3), up-and-down arms (c_4), walking (c_5) and running (c_6). Thus, all data are randomly permuted and divided into training (70%) and testing (30%). The classification processing is repeated for 10 times. Accuracy, recall, precision and confusion matrix are used as model evaluation metrics, comparing the real labels with the labels estimated by the kNN model. Furthermore, by analyzing the eigenvectors matrix (V) from the PCA technique, it is possible to obtain the negligible values associated to the original attributes (sensors) in the calculation of the new attributes [120], and the possibility of reducing the number of sensors while maintaining the algorithm classification performance, resulting in an optimized photonic sensor system.

Human movement-related parameters extraction

In addition to the ability of classifying the human activities, several movement-related parameters can be extracted by analyzing the sensors' responses of the smart garment. During the walking and running activities, the responses of the smart garment sensors and the IMU data (reference) were analyzed. The fast Fourier transform (FFT) of the sensors' temporal response is applied for the cadence estimation. In the up-and-down arms activity, by analyzing the arms movement it is possible to monitor the flexion and extension of each shoulder and evaluate the similarity or not between both sides. An outlier detection algorithm based on z -score calculation [146] is applied on the derivative of the sensors' temporal responses and the identified outliers represent the moment of flexion and extension of each shoulder. During the standing activity, which does not involve movement and the breathing is uniform, the breathing rate was estimated using the FFT of the sensors' temporal response of IMU data (reference) and the POF Smart Garment sensors.

6.1.3 Results and Discussion

Sensors' characterization

The proposed system comprises of the POF Smart Garment using sensors composite structures based on OFS technology. The 30 sensors arranged in the garment are presented in Figure 6.2. The sensors are characterized by applying different forces on each one and all sensors presented similar behavior. Figure 6.2 (figure inset) illustrates the response of one sensor (sensor 10) while forces are loaded and unloaded. The sensor response during the loading and unloading presents a determination coefficient (R^2) of 0.9941 and 0.9865, which indicates high linearity. Based on the sensor noise power and the signal power, the SNR is estimated as 22 dB. The data communication is performed by Bluetooth and all the system electronics is powered by a battery, resulting in a fully portable system.

The sensors presented physical differences resulting from the manufacturing process (as mentioned in the Section 5.3), and as a result, they do not present the same sensitivity. To address this issue, the sensors' responses are normalized by their sensitivities, which leads to similar responses on each sensor. The multiplexing capability of the sensors is confirmed by sequentially applying the same force on adjacent sensors (27, 28, 29 and 30). Figure 6.3 shows a significant difference between the response of the sensor in which the force was applied, and the responses of the adjacent sensors that indicate a negligible crosstalk considering the low optical power variations of the other sensors.

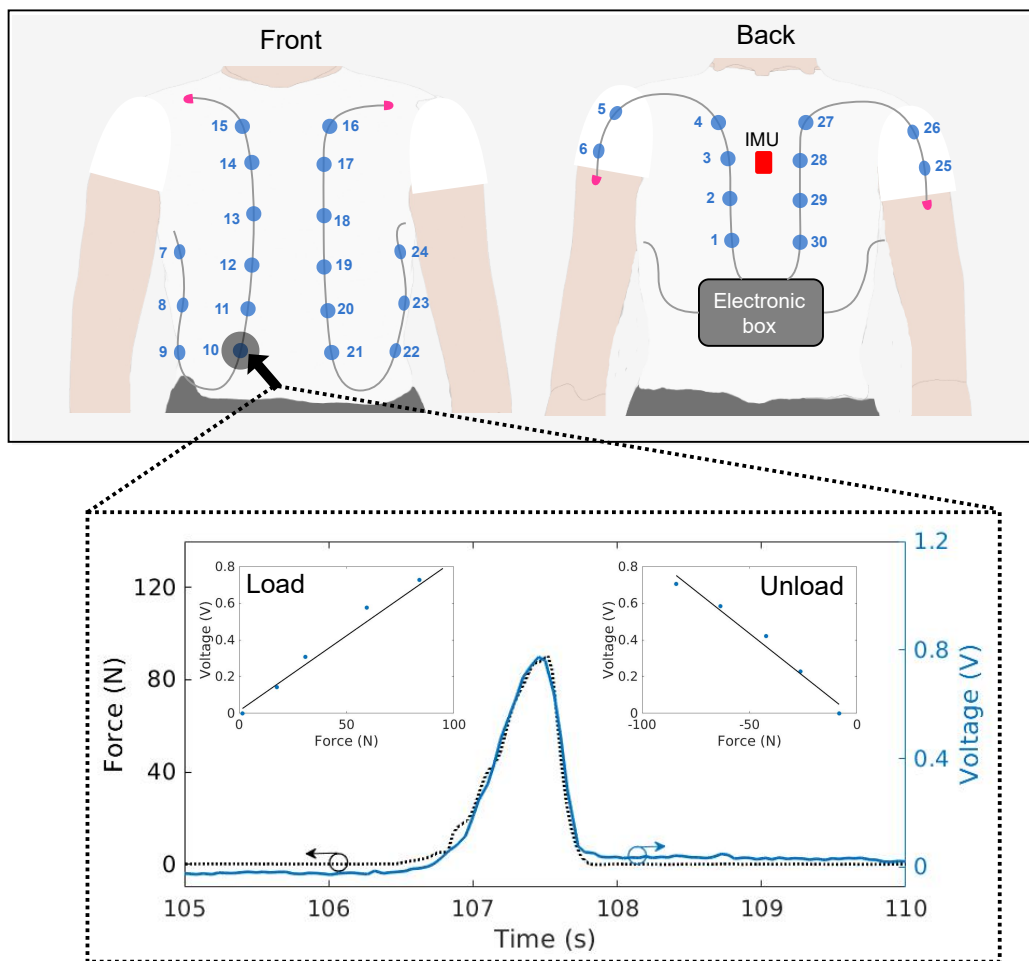


FIGURE 6.2: POF Smart Garment overview and the sensor response when a force is applied on the top of the sensor 10.

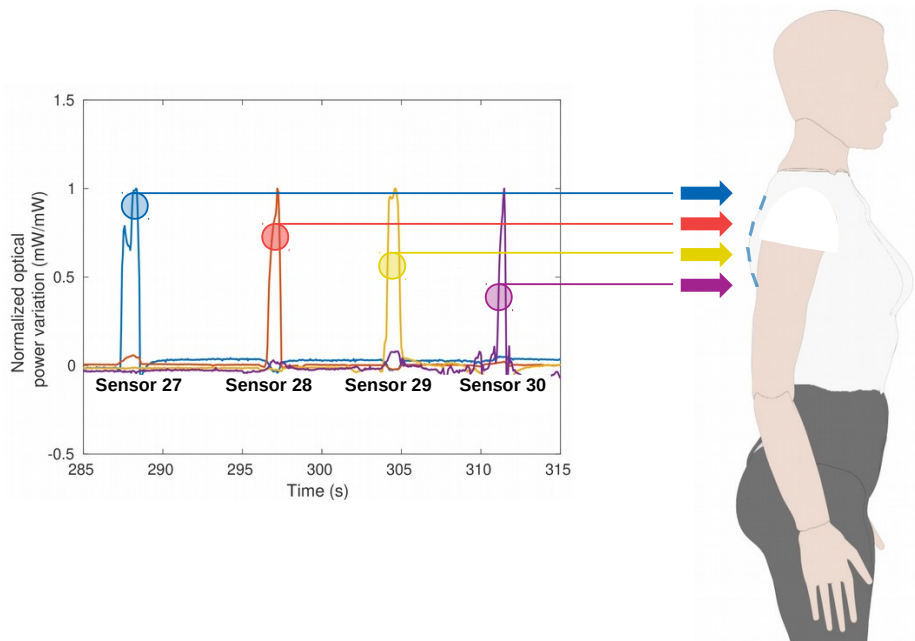


FIGURE 6.3: Response of sensors 27-30 when a predefined loading is applied to each sensor.

Human activities classification

Figure 6.4 shows the responses of 3 sensors (1, 26 and 29) positioned on different places of the body divided into 6 classes (activities). Differences between some classes, such as the c_1 (standing) and c_2 (sitting), are highly perceptible. These classes are completely separated from the other ones by using only these 3 sensors' responses. Standing is a stationary activity, with no movement, which does not involve pressure on any sensor. Sitting is also a stationary activity, however it involves the hip flexion and the activation of the back sensors, due to the chair back support. Since Figure 4 presents the sensors' responses of two sensors located on the back (1 and 29), the variation of these sensors leads to a separation of the data related to the c_2 (sitting).

The classes c_3 (squatting) and c_4 (up-and-down arms), as well as c_5 (walking) and c_6 (running), present similar clusters when the responses of these 3 sensors are evaluated. The activities of the classes c_3 (squatting) and c_4 (up-and-down arms) are not similar. Class c_3 (squatting) represents the squatting activity, which involves a knee flexion/extension and a hip flexion/extension. On the other hand, class c_4 (up-and-down arms) represents the up-and-down arms, which involves a great shoulder flexion/extension and a short longitudinal rotation. However, since there are no significant variation in the trunk movement, the responses of the two selected sensors (1 and 29) located on the back are similar for both movements. On the other hand, the response of the sensor 26 (located on the left arm) presents a bigger movement range for c_4 (up-and-down arms). The activities that represent classes c_5 (walking) and c_6 (running) comprise gait-related movements, yielding similar movement pattern of the limbs (hip, trunk and arms) which influence the smart garment sensors. The significant differences consist of the speed and the intensity level of the movement.

This 3-dimensional evaluation is limited by the analysis of 3 sensors' responses to

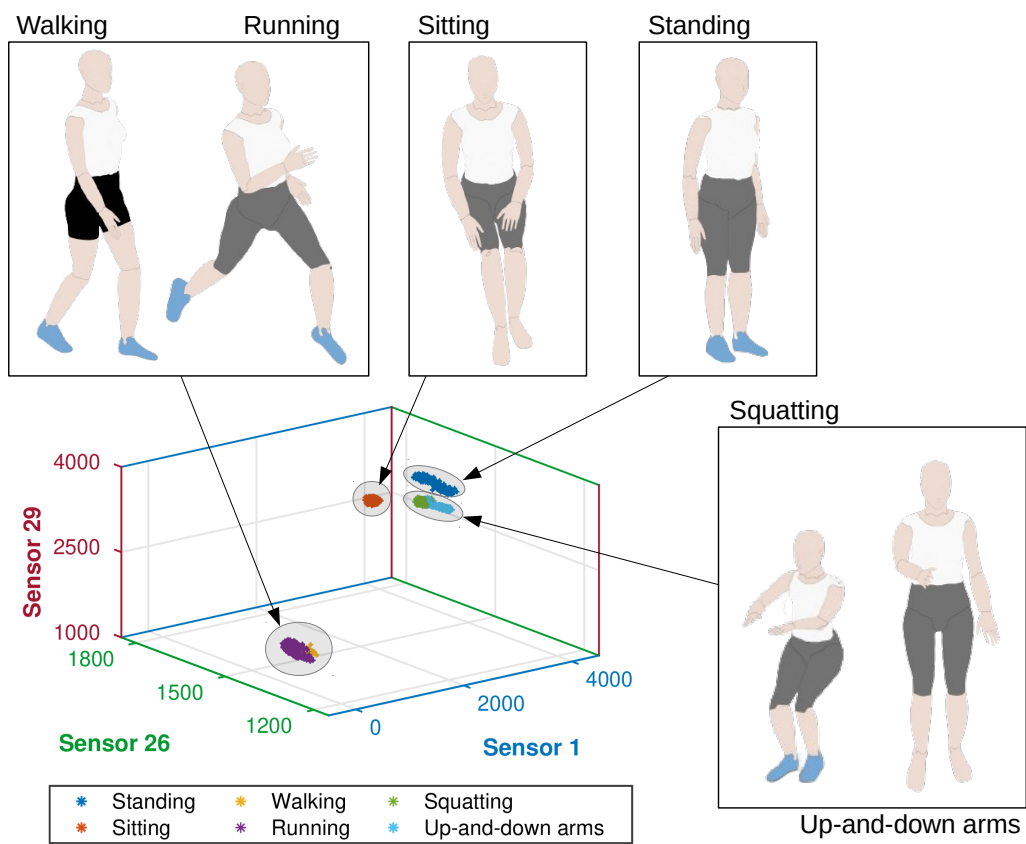


FIGURE 6.4: Clustering of six classes (activities) using the response of 3 sensors.

illustrate a graphical result, which may lead to a weak classification performance if only these 3 sensors are used, since visually some classes contain overlapping data. However, in the classification process, the responses of the 30 sensors are initially employed until the minimal number of sensors is identified. The kNN dataset was randomly permuted and divided into training (70%) and testing (30%). The training data were the base data to classify the testing data, i.e., each new sample was compared with all training data. Thus, the predominant label of the k nearest samples was defined as the label of this new sample, and this was applied to all testing data. The euclidean distance was used as distance metric.

The model evaluation metrics were divided into accuracy, recall and precision. Furthermore, the confusion matrix of each trial was analyzed. Accuracy refers to the percentage of samples correctly classified. Recall represents the percentage of samples of a class correctly classified with respect to all samples of that class, whereas precision represents the percentage of samples of a class correctly classified with respect to all samples predicted for that class. The results of the classifications for each volunteer are presented in Table 6.1. The accuracies of 10 random trials for all the volunteers dataset are higher than 90%. The different classification accuracies in different volunteers is related to the movements performed by each volunteer during the activities of the protocol, since each person perform the movements in a particular way. This means that volunteer 1 performs well-defined movements for each activity which facilitates the classification, whereas volunteer 3 presents errors in the classification activities, mainly involving the walking and running activities which are the movements most similar to each other of this protocol. In addition, the recall and precision results are presented in Table 6.1. It is possible to observe that some classes present better performance in the classification than others. For all volunteers, the classes c_1 (standing) and c_2 (sitting) present higher differences when compared with the other classes. This also confirms the previous analysis in which only three sensors (1, 26 and 29) were analyzed. Differently, the data regarding classes c_3 (squatting) and c_4 (up-and-down arms), and the data regarding c_5 (walking) and c_6 (running) are different for each volunteer, which is related to the individual movement of each person.

Volunteer		1	2	3	4
Accuracy (%)		99.96 (0.04)	92.04 (0.45)	91.34 (0.36)	94.86 (0.25)
Recall (%)	c_1	100 (0.00)	98.31 (0.36)	99.50 (0.18)	99.91 (0.03)
	c_2	100 (0.00)	99.56 (0.19)	100 (0.00)	100 (0.00)
	c_3	100 (0.00)	89.69 (0.77)	94.25 (0.62)	89.77 (1.17)
	c_4	100 (0.00)	89.93 (1.40)	99.98 (0.04)	92.98 (0.75)
	c_5	99.87 (0.00)	93.94 (0.69)	82.62 (1.98)	94.50 (0.66)
	c_6	99.87 (0.00)	78.69 (1.73)	64.91 (1.61)	91.46 (1.22)
Precision (%)	c_1	100 (0.00)	96.02 (0.71)	94.92 (0.60)	98.34 (0.46)
	c_2	100 (0.00)	96.56 (0.66)	100 (0.00)	100 (0.00)
	c_3	100 (0.00)	92.08 (1.01)	98.97 (0.20)	91.56 (1.04)
	c_4	100 (0.00)	91.67 (0.63)	100 (0.00)	93.48 (0.84)
	c_5	99.87 (0.00)	82.50 (1.21)	69.48 (1.15)	91.77 (1.03)
	c_6	99.87 (0.00)	92.44 (0.72)	79.53 (1.91)	93.19 (0.44)

TABLE 6.1: Classification results for each volunteer.

By analyzing the volunteer 1, who presented the best classification results, it is possible to notice that the walking (c_5) and running (c_6) classes presented higher

classification errors, which resulted in a recall and precision of 99.87 (0.00)%, for both classes. Gait speeds for walking and running activities are different, and hence the intensity level of the movement changes, resulting in a different variation of the sensors' responses. However, the gait cycles for walking and running activities are similar, thereby the sensors' responses present a similar pattern and, for this reason, some samples are misclassified. Similarly, the squatting (c_3) and up-and-down arms (c_4) activities are related to similar upper limbs movements and presented misclassified samples.

Data from each volunteer are combined into a single dataset to analyze overall system classification performance, yielding an average accuracy (across participants) of 94.00 (0.14)%. Moreover, by analyzing the confusion matrix, it is possible to observe the influence and classification success of each class. Figure 6.5 shows the confusion matrix of the kNN classification for the whole dataset, including all volunteers. On the diagonal of each matrix are the percentage of the samples correctly classified.

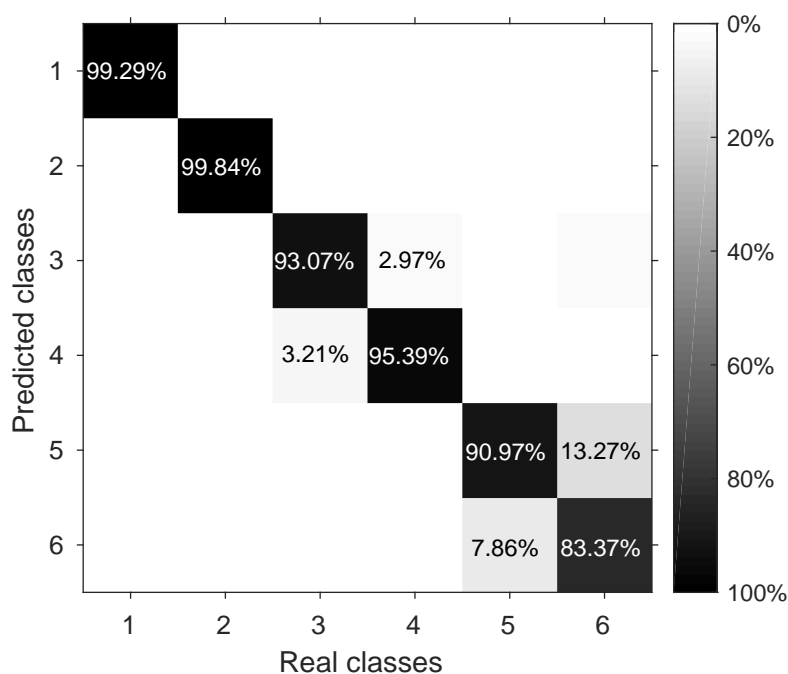


FIGURE 6.5: Confusion matrix regarding 10 trials including the dataset of all volunteers in the kNN classification.

Data dimensionality reduction

Depending on the activity, some sensors are not activated, i.e., they do not present a significant optical power variation when compared to the sensors' response in the standing activity. The activation of different sensors for each activity occurs due to the fact that the activities consist of the movement combination of different body regions. Figure 6.6 presents the sensors activation for each activity.

In the sitting activity there are variations in the response of sensors located on the back and lower region of the trunk (sensors 21 and 10), close to the user's hip, since this activity involves the hip flexion of approximately 90° and the contact of

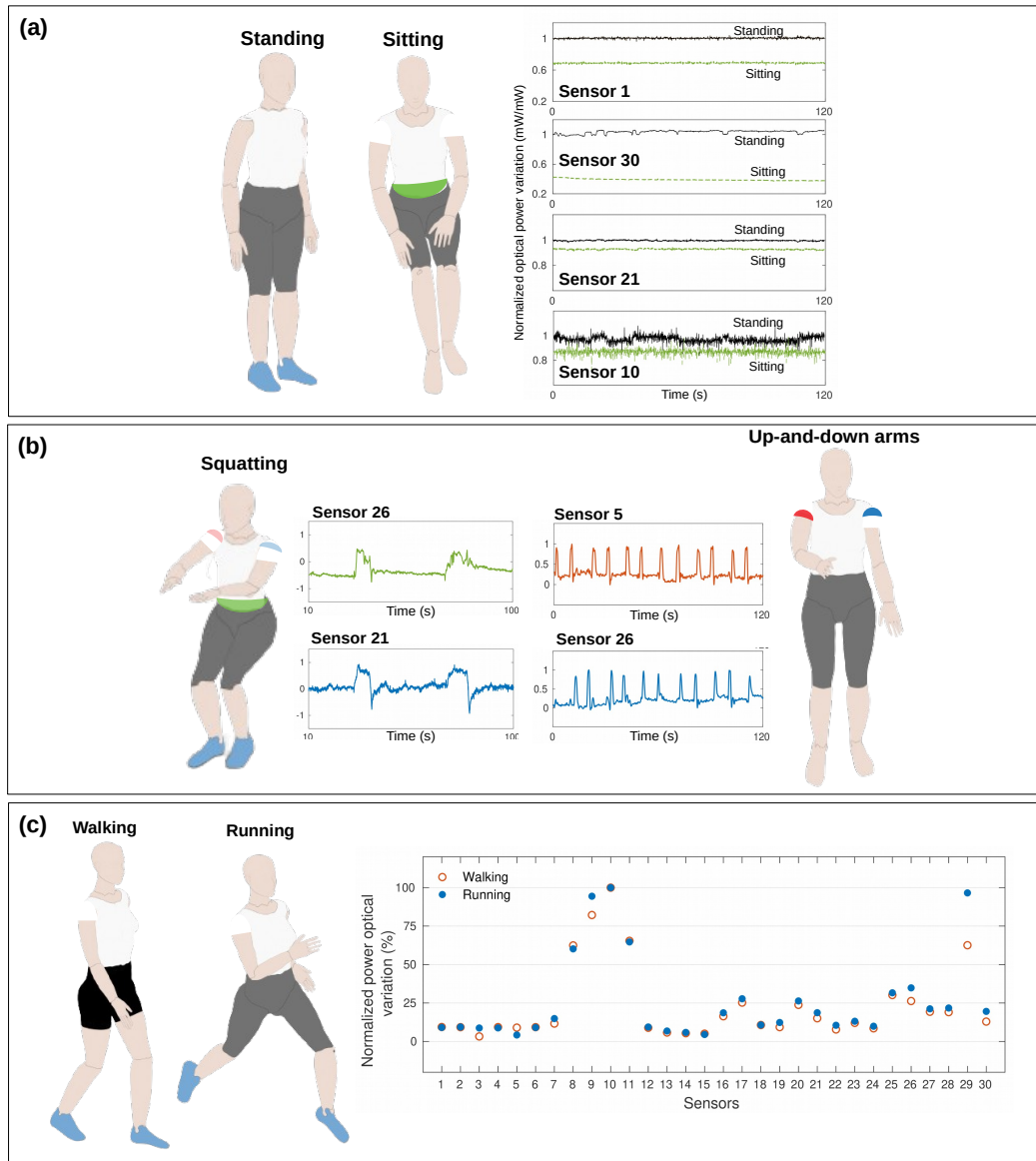


FIGURE 6.6: Sensors activation for each activity. (a) Optical power variation between the standing and sitting activities of sensors 1, 30, 21 and 10. (b) Response of sensors 26 and 21 during the squatting activity and response of sensors 5 and 26 during the up-and-down arms activity. (c) Sensors activation during the walking and running activities.

the user's back to a chair (sensors 1 and 30), as shown in Figure 6.6(a). Figure 6.6(b) shows the temporal response of the most activated sensors during the squatting (sensors 26 and 21) and up-and-down arms (sensors 5 and 26). In sitting and squatting activities the sensor positioned on the hip region (sensor 21) is activated and this is due to the high hip flexion during both activities. In the same way, the sensor positioned close to the shoulder (sensor 26) is activated during the squatting, since the volunteers used the arms to achieve the balance of the body. During the up-and-down arms activity the sensors positioned on the right and left shoulders (sensors 5 and 26) presented the highest normalized optical power variation and this is due to the flexion and extension of each arm which leads to a high bending in the fiber. The walking and running activities comprise the intercalated legs movement, which involves the cyclic hip rotation, and hence, a higher optical variation in the response of sensors located on the lateral and close to the hip. Figure 6.6(c) presents the percentage of the optical power variation of each sensor during walking and running.

In order to analyze the demand of the sensors' amount in the activities classification, the attributes are reduced and the classification performance is calculated. By applying the PCA technique to the volunteer 1 dataset, the attributes were reduced to 10 new attributes, obtained by the linear combination of the 30 sensors' response, and presented a variance explained of 99.84%. The mean of the classification accuracy for 10 trials using the new 10 attributes was 99.02 (0.16)%, which demonstrates that a dataset linearly uncorrelated and 3 times smaller (with better processing performance) still presents a high accuracy (approximately 99%). By analyzing the eigenvectors matrix (V) used by the PCA technique, which represents the coefficients of the linear combination of the original attributes to compose this new dataset (10 attributes) and hence represents the weight of each attribute (sensor), and considering the most significant coefficients, the original attributes were arranged in descending order. By selecting the most significant 14 attributes, the accuracy is 99.71 (0.08)% in 10 trials. By selecting the most significant 12 attributes, the accuracy is 99.46 (0.17)% in 10 trials. Finally, when the most significant 10 attributes are selected the accuracy decreases to 98.14 (0.31)% in 10 trials. It means that the reduction of the smart garment to 10 sensors still provides an accuracy close to 99%, since the 10 sensors cover the body regions which move effectively in these activities for this volunteer in particular. The selected sensors were: 3, 5, 8, 11, 14, 17, 20, 23, 26 and 28. In this way, it is possible to optimize the number of smart garment sensors according to each volunteer, by analyzing their results in a predefined activity, since each person performs the movement differently.

Human movement-related parameters extraction

For the **cadence** estimation, the sensors' responses during the walking and running activities were analyzed. An inertial measurement unit (IMU) was incorporated in the upper back of the garment, and the yaw data obtained from the IMU were compared with the POF Smart Garment (sensor 8, since this sensor is located on the lateral of the body and presents a great variation in the response during walking and running). By applying the FFT to the temporal response of the yaw data and the one of sensor 8 (positioned on the lower right side of the body), both results presented frequency peaks of 35.98 cycles/min and 71.97 cycles/min, as shown in Figure 6.7. These frequencies correspond to cycles of stride per minute, which leads to a double value of cycles of steps per minute, since a stride consists of two steps.

Thus, by analyzing the FFT results, the estimated cadence is 71.96 steps/min (walking) and 143.94 steps/min (running), presenting no error between the results of POF Smart Garment sensors and the IMU.

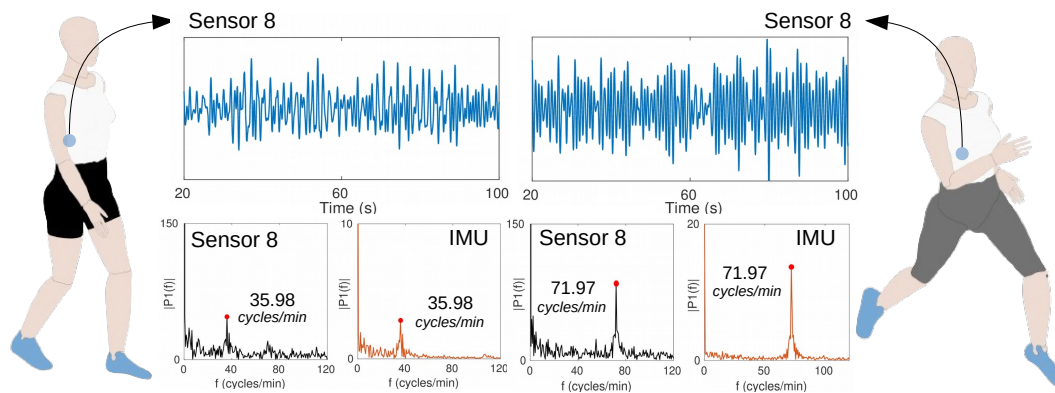


FIGURE 6.7: Results of walking and running tests of the volunteer 1 for cadence estimation: temporal response and FFT of the IMU data (yaw) and the response of sensor 8.

To estimate the **breathing rate**, the sensors' responses during the standing test were analyzed. The volunteer was in upright position and performed no movement to reduce the influence of artifacts. A 0.3 - 0.7 Hz bandpass filter was applied to attenuate external noises. The pitch data obtained by the IMU were compared with the smart garment (sensor 17, since this sensor is positioned on the middle of the body and presents a high variation during the breathing task). By applying the FFT on the temporal response of sensor 17 and pitch data, results presented peaks of 13.20 and 13.19 cycles/min, respectively, which lead to the estimated breathing rates of 26.40 and 26.38 cycles in 2 minutes, as presented in Figure 6.8.

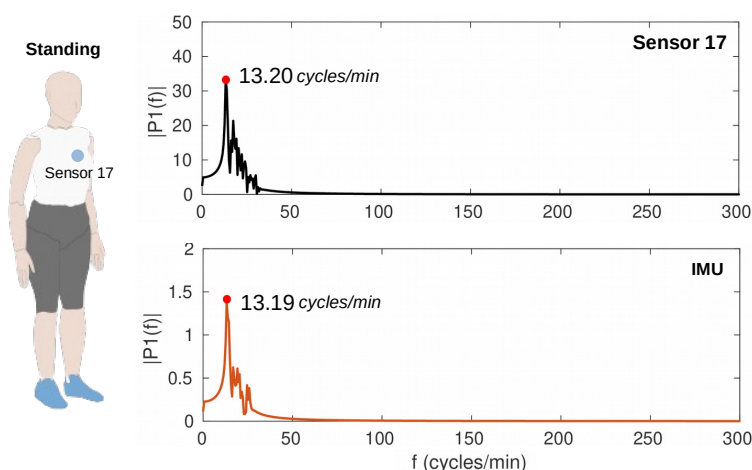


FIGURE 6.8: FFT of the IMU data (pitch) and the response of sensor 17 during standing activity of the volunteer 1 for breathing rate estimation.

The estimated breathing rates from IMU and POF Smart Garment data present high correlation (0.08% relative error). Table 6.2 shows the estimated cadence and breathing rate for all volunteers. The errors between the parameters estimated by the POF Smart Garment sensors and by the IMU occur due to the cross sensitivity of the POF sensors, whereas the IMU is a 3D sensor and the parameters extraction involves data from only one dimension, which reduces the interference of the data from another axes, decreasing the noise in the FFT analysis.

	Volunteer	Cadence (steps/min)		BR (cycles/min)
		Walking	Running	Standing
IMU	1	71.96	143.94	13.19
	2	79.14	155.92	13.79
	3	68.36	125.94	13.79
	4	73.16	146.34	14.39
POF Smart Garment	1	71.96	143.94	13.20
	2	77.38	156.54	13.9
	3	68.60	126.64	14.04
	4	72.12	145.98	14.6
Errors (%)	1	0	0	0.08
	2	2.22	0.40	0.80
	3	0.35	0.56	1.81
	4	1.42	0.27	1.46

TABLE 6.2: Estimated parameters from IMU (reference) and POF Smart Garment sensors: errors between the measurements obtained from the two systems.

The assessment of the **arms movement** was based on the temporal analysis of sensors 5 (right arm) and 26 (left arm), since these sensors are located close to the shoulders and they present a high optical power variation during the up-and-down arms. The responses of both sensors were normalized and can be observed in Figure 6.9. The first curves represent the flexion and extension of each arm. In order to identify the moment of the shoulder flexion and extension, an outlier detection algorithm was employed on the derivative of the sensors' temporal responses (5 and 26); results of the outlier detection are presented in the bottom graphics of Figure 6.9. The shaded areas limited by the dotted lines represent the natural movement range based on the *z-score* calculation ($mean \pm 3 \cdot standard\ deviation$) [146], whereas the markers located outside the areas represent the moment of flexion and extension of the shoulders (outliers).

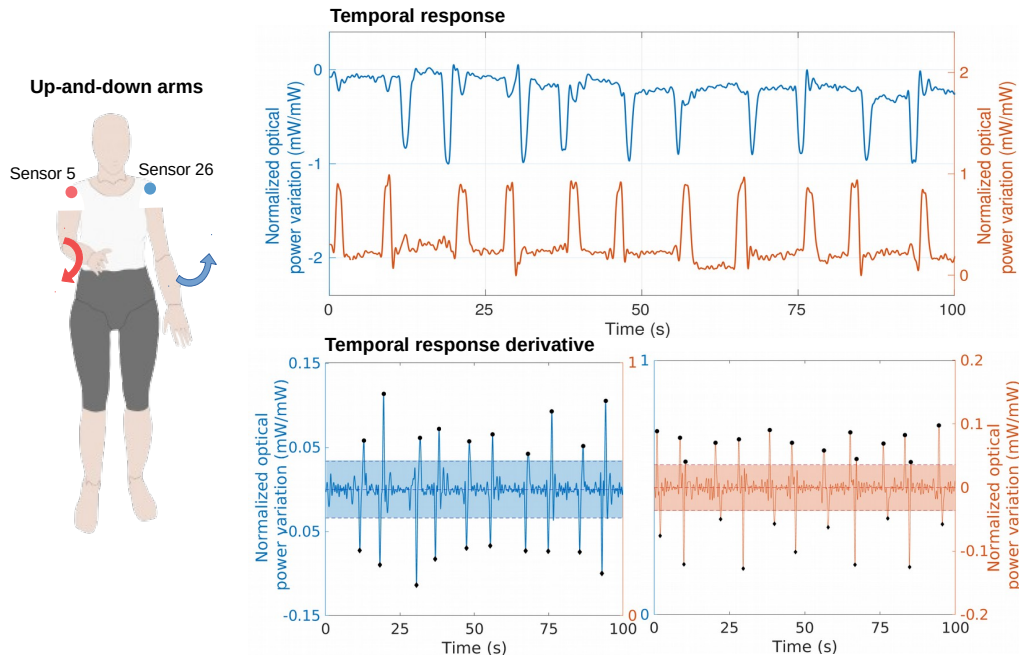


FIGURE 6.9: Results of the up-and-down arms test of the volunteer 1: temporal response of sensors 5 (right arm) and 26 (left arm) and identification of the shoulder flexion and extension by outliers detection using the temporal response derivative.

6.2 POF Smart Pants: Gait Analysis and Movement Recognition

6.2.1 Materials and Methods

The POF Smart Pants comprises an instrumented pants with 2 POFs incorporated in the back parts of the pants (right and left sides) with a total of 60 intensity variation-based multiplexed POF sensors (30 for each leg) encapsulated by a clear urethane rubber mixture. Each sensor is fabricated by laterally coupling a light source to a lateral section, which is made by removing the cladding and part of the fiber core. The light source employed is the addressable RGB LED Strip (1 m, 60 LEDs), which allows controlling which LED turn on and the color by 1 communication bus. It leads to a more compact system using a high number of sensors. The LEDs are activated sequentially and they are controlled by a microcontroller FRMD-KL25Z (NXP Semiconductors, Netherlands). Four photodetectors IF-D92 (Industrial Fiber Optics, USA) are attached in each fiber end to convert the optical power into electrical power. Figure 6.10 presents the POF Smart Pants overview, including the sensors schematic (6.10(a)) and the sensors system incorporated in the pants 6.10(b).

6.2.2 Experimental procedures

A curvature characterization is performed to normalize the sensors according to their sensitivities. The curvature characterization setup, presented in Figure 6.11, consists of applying different curvatures in the sensitive region controlled by the vertical displacement between 1 mm and 5 mm. The sensors responses are related to the different curvatures and the sensors are normalized.

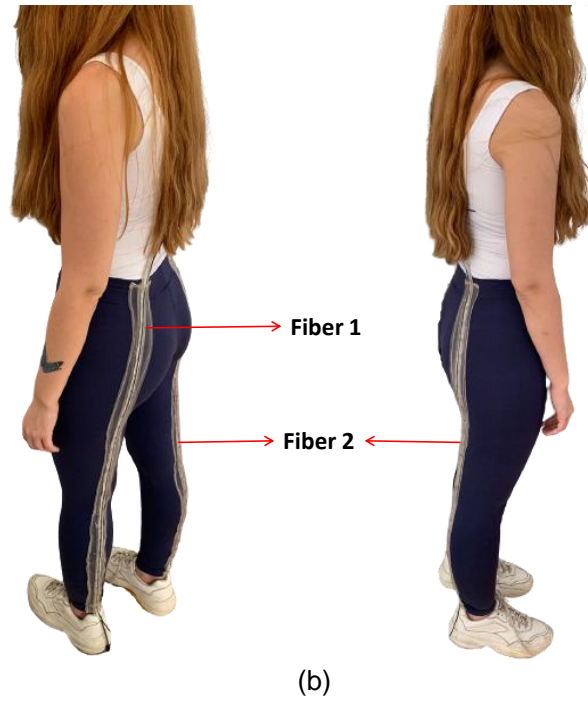
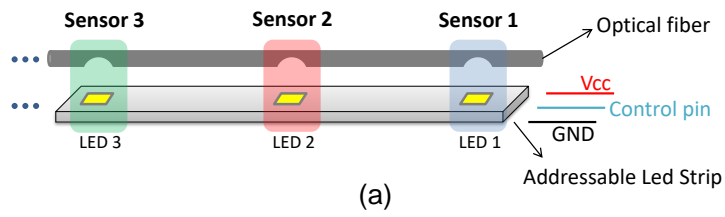


FIGURE 6.10: Smart Pants overview. (a) Sensors system schematic. (b) Sensors system incorporated in the pants.

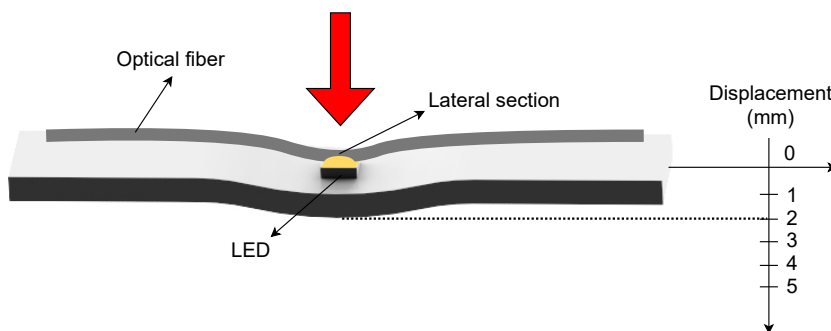


FIGURE 6.11: Curvature characterization setup.

Moreover, 7 different activities involving the lower limbs are performed to evaluate the ability of the smart pants in the identification of different movements, as shown in Figure 6.12. The activities consists of: (i) walking slow, (ii) walking fast, (iii) squatting, (iv) sitting on a chair, (v) sitting on the floor, (vi) front kick and (vii) back kick. A feed-forward neural network (FFNN) is designed to perform the classification of the 7 activities using the 60 sensors (30 for each leg) as input data. In addition, a PCA technique is used to select the most significant sensors and to reduce the number of sensors in the system.

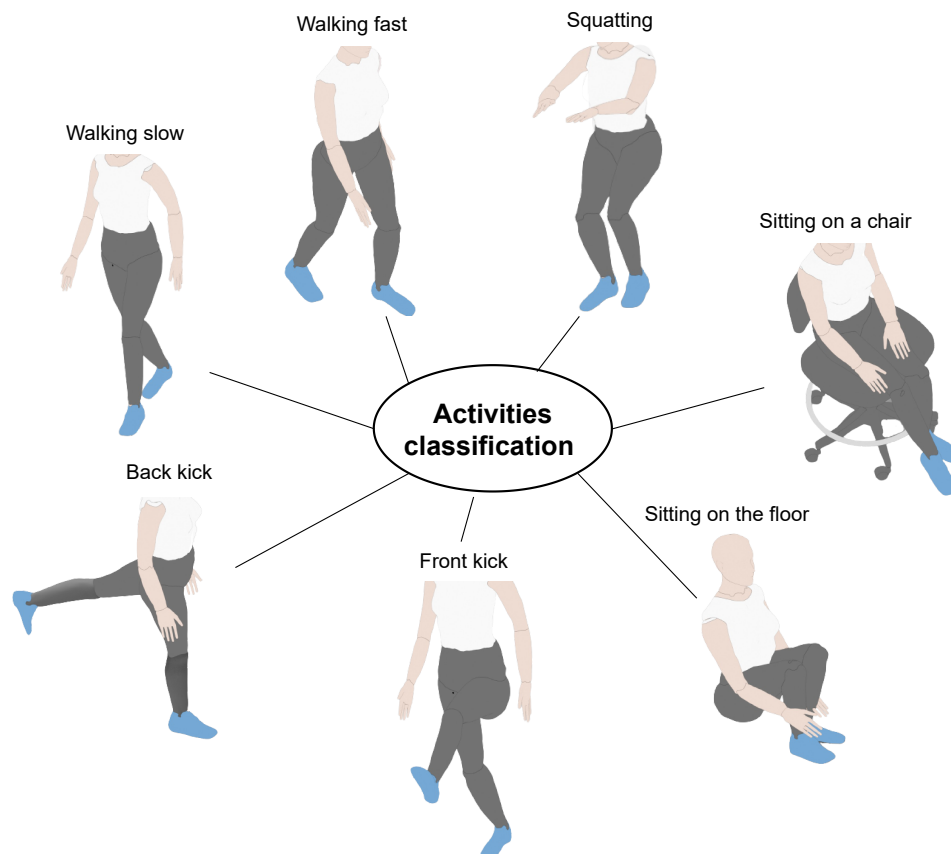


FIGURE 6.12: Activities recognition protocol.

6.2.3 Results and Discussion

Results of the curvature characterization showed different sensors sensitivities. This difference is related to the manufacturing process which eventually presents minor differences between sensors, since lateral section parameters (length and depth) as well as the distance between the LED and the optical fiber's lateral section may have small differences for each sensor, as mentioned in the Section 5.3. All the sensors responses in the characterization are linear fitted ($R^2 > 0.9$). Tables 6.3 and 6.4 present the sensitivities (mV/mm) of the sensors positioned in the both sides of the pants. It is possible to observe the huge differences between the sensors sensitivities. Fabrication stages such as the sensitive zone creation and the encapsulation of clear urethane rubber mixture can lead to differences between sensors, due to the low precision to achieve the same lateral section parameters and the same coupling of the sensitive zones to their respective LEDs during the encapsulation. However, the differences between sensors can be solved with the sensors normalization.

Sensor	Sensitivity (mV/mm)	Sensor	Sensitivity (mV/mm)
1	568.09	16	1.43
2	34.07	17	1.88
3	25.67	18	2.25
4	9.22	19	2.28
5	15.64	20	2.15
6	13.70	21	31.68
7	11.80	22	27.19
8	7.32	23	18.33
9	20.36	24	173.24
10	127.30	25	160.93
11	34.39	26	200.21
12	16.01	27	52.11
13	14.99	28	22.50
14	7.31	29	54.63
15	4.22	30	61.98

TABLE 6.3: Sensitivities of sensors in the fiber 1.

Sensor	Sensitivity (mV/mm)	Sensor	Sensitivity (mV/mm)
1	19.42	16	4.23
2	334.59	17	13.10
3	52.97	18	152.73
4	15.42	19	366.77
5	68.48	20	509.77
6	21.14	21	400.92
7	305.07	22	513.21
8	200.43	23	370.50
9	29.33	24	9.62
10	224.49	25	42.31
11	283.82	26	26.45
12	239.28	27	7.91
13	388.83	28	19.84
14	106.35	29	2.77
15	24.96	30	4.17

TABLE 6.4: Sensitivities of sensors in the fiber 2.

The results of the FFNN classification are presented in Figure 6.13. The accuracy and the loss in 40 epochs are 100% and 0, respectively, which demonstrates that all testing data were correctly classified using the input data from 60 sensors. This shows that the number of sensors can be overestimated, since high accuracy can be achieved with lower number of sensors, which leads to an easier system fabrication. Moreover, excessive number of features in the classification introduces additional computational complexity, which can be solved by reducing the data dimensionality maintaining the high classification performance.

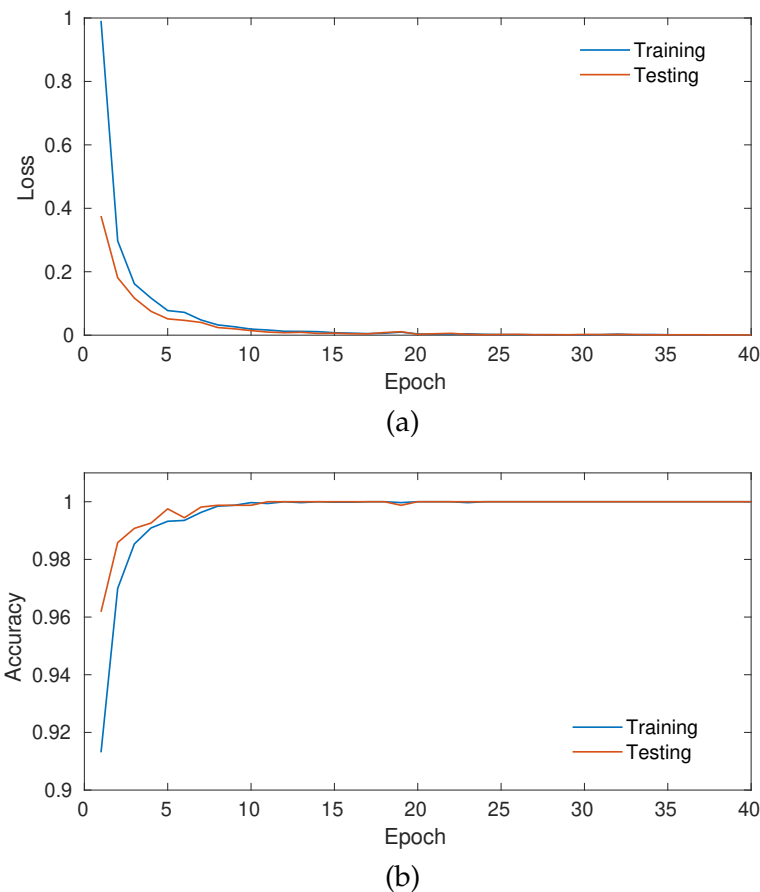


FIGURE 6.13: Metrics of the FFNN model with 40 epochs for activities classification. (a) Loss. (b) Accuracy

By applying the PCA technique to reduce the dimensionality of the classification input data, the results showed that the reduction to 20 principal components led to variance explained of 99.16%, i.e., a third of the number of new features (principal components) represents more than 99% of the data variance in the classification, as presented in Figure 6.14.

Due to the high accuracy of 100% and the high variance explained using only 20 principal components, a selection of the most significant weights (resulted from the PCA) is performed. This selection indicates the most significant sensors without significantly decreasing the classification performance. The selected most significant sensors of the fiber 1, as well as the fiber 2, are: 7, 8, 10, 14, 17, 18, 19, 22, 26, 28 and 29. These 11 indices are related to LED's numbering on the addressable LED strip (top to bottom), as showed in the Figure 6.15, with a total of 22 sensors. This selection illustrates the sensors which present more variability in their responses during the activities performed in this Section.

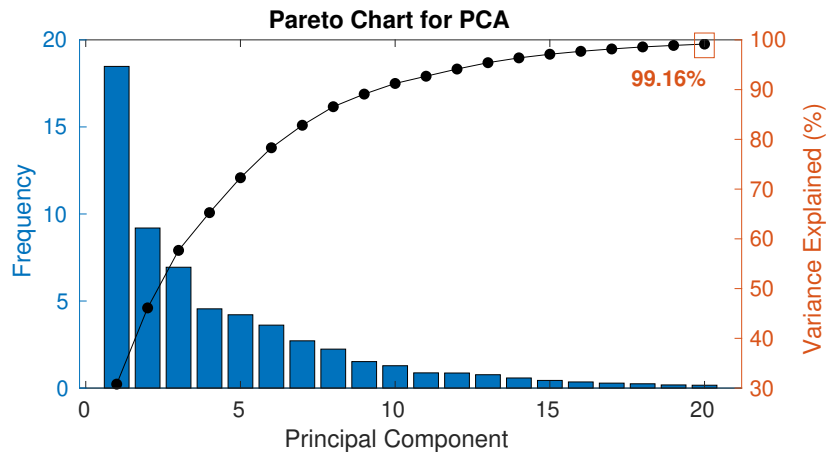


FIGURE 6.14: Pareto chart for the PCA technique.

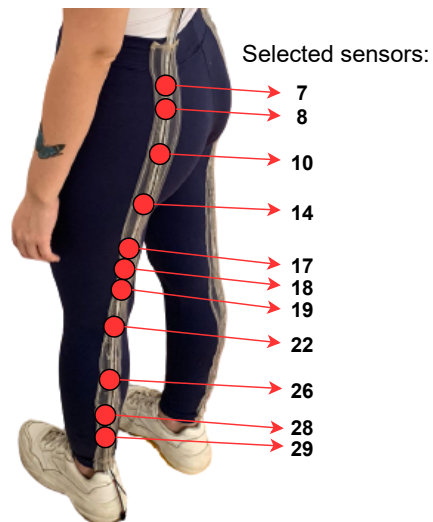


FIGURE 6.15: Selected sensors by analyzing the principal components weights resulted from the PCA technique.

After the sensors selection, the FFNN-based classification process is repeated with 30 epochs, since the preliminary classification process using 40 epochs quickly stabilized and it was not necessary to use so many epochs. The accuracy using 22 sensors converged to 99%, approximately, whereas the loss converged to 0.075, as shown in Figure 6.16. These results showed the possibility of decreasing the number of the sensors, facilitating the manufacturing process and decreasing the data processing cost, providing a similar classification performance.

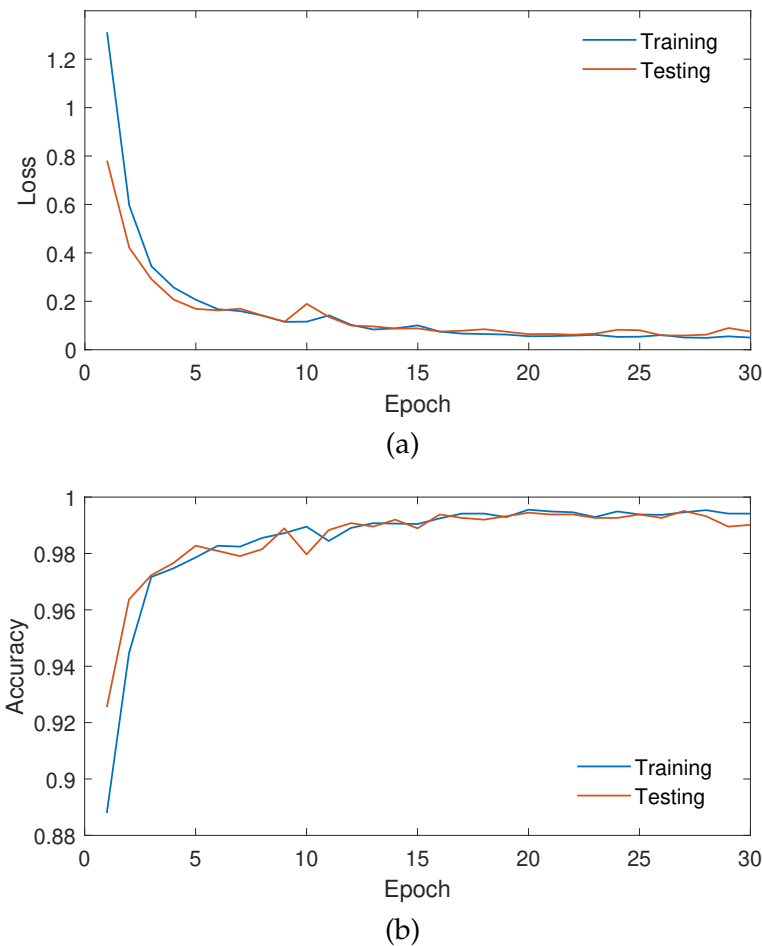


FIGURE 6.16: Metrics of the FFNN model with 30 epochs for activities classification after the sensors selection. (a) Loss. (b) Accuracy

Regarding the gait analysis, Figure 6.17 presents the response of two sensors located at the same position correspondent to each leg in a gait performance. This result shows the ability to identify the steps (left and right) during a gait using only two sensors. Moreover, these sensors responses allow the estimation of the cadence and other spatio-temporal gait parameters, such as the stance and swing phases, and the double support.

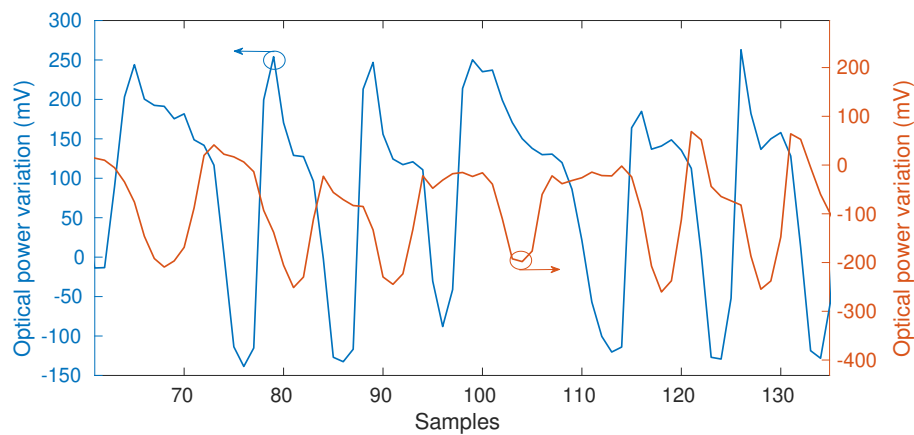


FIGURE 6.17: Selected sensors during the gait performance: left and right legs.

6.3 POF Smart Carpet: Gait Analysis

This Section presents the development of a smart carpet with multiplexed POF sensors for kinematic and kinetic analysis of human gait. The proposed smart carpet can measure the plantar pressure along the device and to estimate the spatio-temporal gait parameters using the sensors distributed throughout carpet. The proposed POF Smart Carpet is an interesting low-cost alternative with high scalability for gait analysis.

6.3.1 Development of the POF Smart Carpet

The POF Smart Carpet structure is based on one POF arranged parallel to the walking direction in between two polyethylene layers, 60 cm wide and 2-m long (see Figure 6.18). The POF was made of PMMA (HFBR-EUS100Z, Broadcom Limited) with a core diameter of $980\ \mu\text{m}$, a cladding of fluorinated polymer with $20\ \mu\text{m}$ thickness and a polyethylene coating that results on a total diameter of $2.2\ \text{mm}$ for the fiber considering its coating. The light source used is a light-emitting diode (LED) flexible lamp belt, horizontally arranged, and the sensors responses, i.e., the optical power variation, were acquired by the photodetectors IF-D92 (Industrial Fiber Optics, USA). The signal acquisition and the LEDs control are performed by the microcontroller FRMD-KL25Z (NXP Semiconductors, Netherlands).

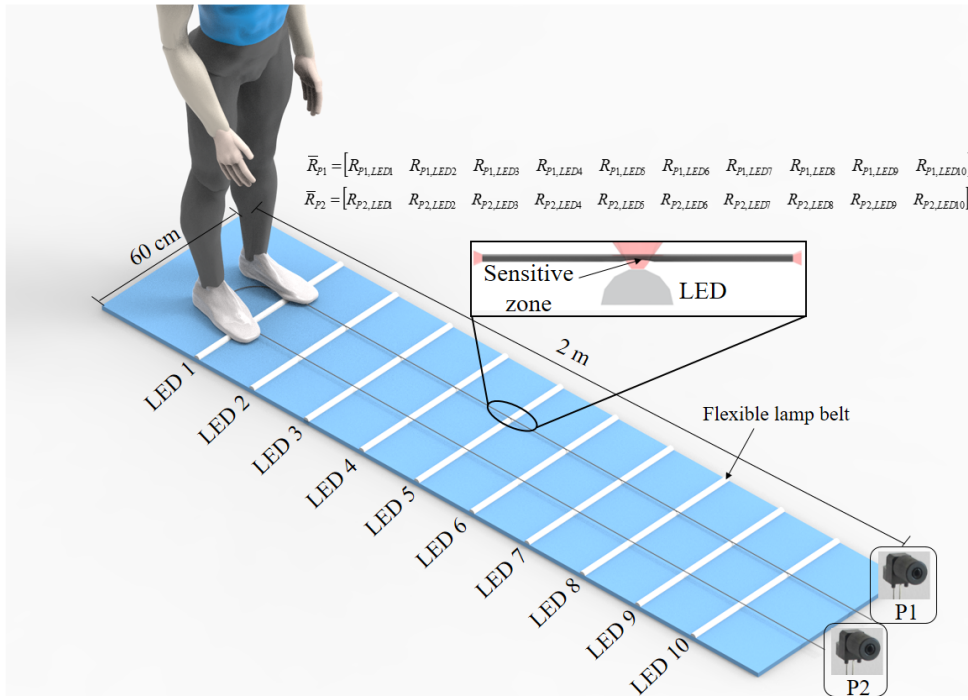


FIGURE 6.18: POF Smart Carpet overview.

To enable the side-coupling of the light source and, at the same time, increase the sensor sensitivity, a lateral section is made on the fiber, where the cladding and part of the core are removed, creating the sensitive zones demonstrated in Figure 6.18 inset. The lateral section length, depth and surface roughness were made through abrasive removal of material following the guidelines presented in [30]. The sensitive zone is created using a sandpaper connected to a rotary tool.

In this case, 20 lateral sections were produced on the fiber with 20 cm separation from each other. Then, the fiber was turned in 180° (as shown in Figure 6.18), which results in 2 rows with 10 sensors each, where there is a 15 cm horizontal separation between the rows. In addition, the LED flexible lamp belts are positioned on each lateral section. When the pressure is applied on each lateral section, there is an optical power variation, which is acquired by P1 and P2.

Two photodetectors were employed, one at each end of the fiber, to acquire the optical power variation of all 20 sensors R_{LEDn} . Thus, the responses of 10 sensors (\bar{R}_{p1}) are acquired by P1 and the other 10 sensors (\bar{R}_{p2}) are acquired by P2, as schematically demonstrated in Figure 6.18.

The multiplexing technique comprises of a sequential activation of each LED with a predefined frequency and activation sequence (as discussed in Section 2.2.1). In this case, one LED flexible lamp belt is activated at a time, illuminating two sensors n simultaneously (right and left), where a microcontroller controls the activation frequency and sequence. The acquisition sequence is from LED 1 to 10 with an activation frequency of 30 Hz for each LED. In addition, the microcontroller is responsible for the acquisition of the optical power measured by each photodetector when each LED is active, resulting in two matrices, one for the P1 and the other for P2, as shown in Figure 6.18. In this case, each matrix has 10 columns, where the columns represent the optical power acquired by P1 and P2 when a predefined LED is active, and each row represents the temporal acquisition.

6.3.2 Experimental procedures

To perform the force and the spatial characterization of the carpet, two experimental protocols were applied. The first protocol is the force characterization, based on positioning of calibrated weights on top of each sensor on the range of 0 N to 50 N with steps of 10 N. The sensors responses are acquired by the photodetectors. Figure 6.19(a) shows the setup for force characterization. The second protocol is the spatial characterization, which is based on positioning of the foot on markers with predefined distances along the carpet. This protocol was performed by two volunteers. The goal of this protocol is to correlate the optical power with the distance along the carpet. This characterization is related to the force characterization, since it is necessary to obtain the sensor response with predefined weights exactly on top of the sensor. Figure 6.19(b) shows the spatial characterization setup.

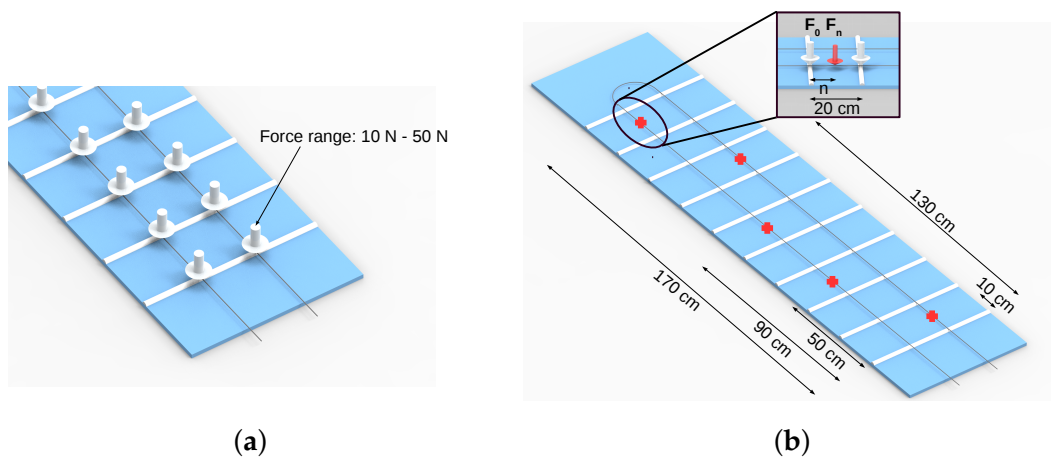


FIGURE 6.19: Characterizations protocols setup: (a) Force characterization. (b) Spatial characterization.

The spatial characterization was based on continuous beam model [147], as shown in Figure 6.19(b), in which the LED flexible lamp belts correspond to the supports and the fiber correspond to the beam. The optical power response for the force applied along the fiber in the region between two consecutive LED flexible lamp belts is inversely proportional to the distance of this force to LED flexible lamp belt. As the distance increases the optical power decreases, when compared to the case where the force is applied on the LED flexible lamp belt, which is the maximum optical power response (as shown in Figure 6.19(a)). Thus, we consider a linear variation of the force along the fiber with the maximum optical power variation when the force is applied in the region of the fiber on the lamp belt and the minimum optical power variation occurs on the region at the middle of two consecutive LED belts as presented in Figure 6.19(b). The relationship between the optical power attenuation and the distance to the sensor was calculated by Equation (6.1), where F_0 is the force applied on top of the sensors, F_n is the force applied along the fiber between the LED flexible lamp belts, n is the distance of F_1 to F_0 and l is the distance between the LEDs, equivalent to 20 cm.

$$n = \frac{F_n \cdot l}{F_0} \quad (6.1)$$

The third experimental protocol consisted of three walking tests, in which the volunteers started the tests with right foot. The goal of this protocol is to validate

the previous characterizations and to estimate the GRF and spatio-temporal gait parameters during walks.

The spatio-temporal gait parameters analyzed in this work consist of the step and stride lengths, cadence, and stance time. Each heel strike is detected by the optical power variation of the sensors and the signals are analyzed in pairs with adjacent sensors. This method allows identification of the heel strike position based on the optical power variation of each sensor. Thus, the distance between the heel strike and the sensors (n) can be calculated by Equation (6.1). The distance of heel strike to carpet start position is the sum of the n with the position of LED flexible lamp belt related to the first stressed sensor in the walking direction. With each heel strike defined, it is possible to calculate the step length through the spatial difference between adjacent heel strikes. Furthermore, the sum of two steps results in the stride length. The cadence is equivalent to number of steps per minute. The time of each test is obtained by ratio between the total samples and activation frequency, while the number of steps is known through step length evaluation. Therefore, the stance time consists of the ratio between optical power variation time and activation time, since the sensor optical power variation only exist when the foot is on the ground pressing the fiber.

6.3.3 Results and Discussion

POF Smart Carpet Characterizations

Figure 6.20 presents the sensors response to the loads applied to 20 sensors (10 for each photodetector) in the force characterization, showing the determination coefficient (R^2) and the relative errors, in which the markers represent the measured output and the continuous lines represent the sensors fit. It is noticeable in Figures 6.20(c) and 6.20(d) the exponential behavior of the curves obtained by P1 and P2, with a linear region from the application of the weights and a saturation tendency for higher weights. Figures 6.20(a) and 6.20(b) show the response of the sensors with higher sensitivity than the other ones. The sensitivity and the linearity are related to the fabrication of each sensor, and for this reason the more sensitive sensors are different for each photodetector. The sensors 1 acquired by each photodetector present polynomial behavior, exceptionally.

Figures 6.21(a) and 6.21(b) present the sensors' sensitivities as a function of the sensor positions. It is possible to observe that generally, the sensitivity decreases as the distance between the sensors and the photodetectors increases. The reason for this behavior is the optical power attenuation at each lateral section leading to a lower detected optical power by the photodetector. This results in a lower sensitivity for the sensor with higher distance from the photodetectors. However, it is important to mention that the lateral section length and depth also influence the sensor sensitivity [30], which can explain the higher sensitivity of the sensor 3 acquired by P2 when compared with sensor 2 acquired by the same photodetector (P2).

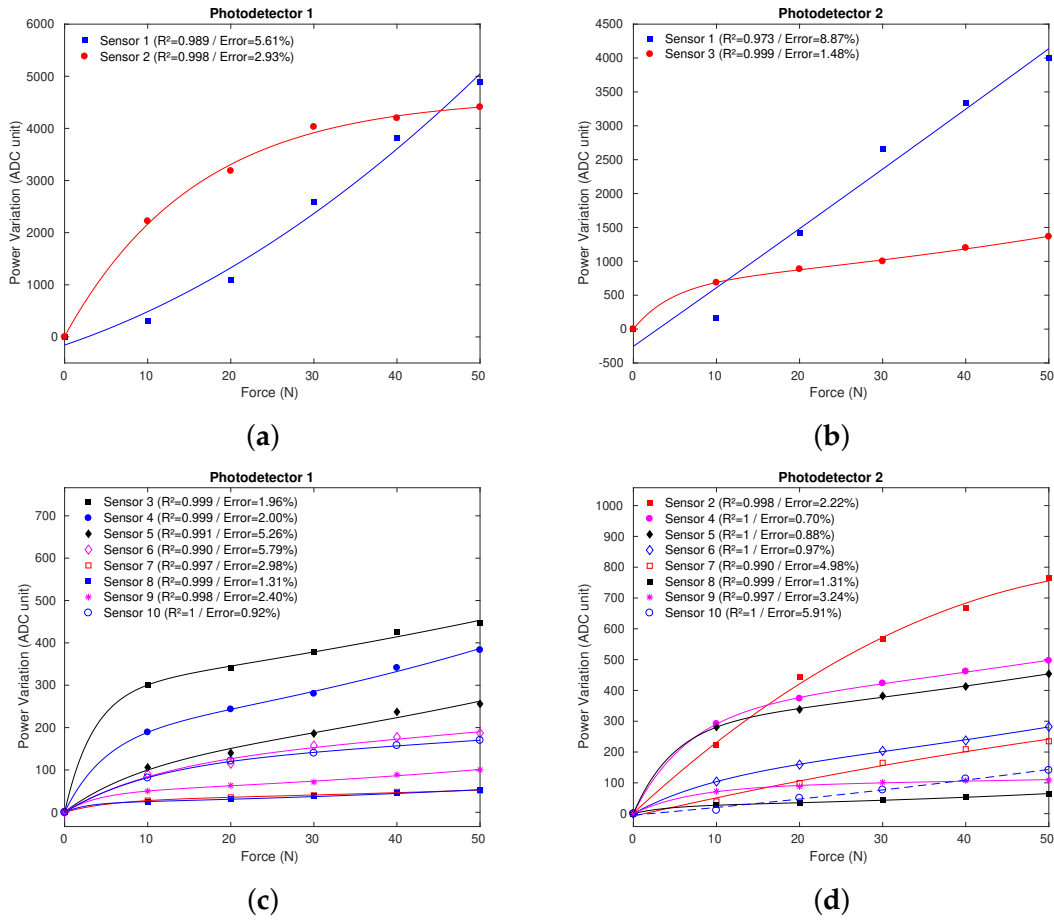


FIGURE 6.20: Sensor’s response in the force characterization with fitted curves: (a) Right sensors 1 and 2 using photodetector P1. (b) Left sensors 1 and 3 using photodetector P2. (c) Right sensors 3-10 using photodetector P1. (d) Left sensors 2 and 4-10 using photodetector P2.

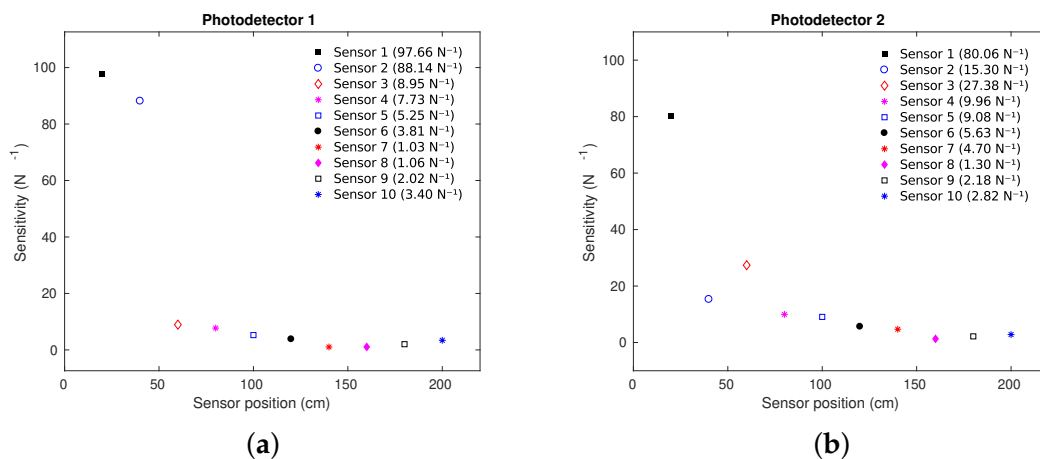


FIGURE 6.21: Sensitivity as a function of the sensor position: (a) Right sensors using photodetector P1. (b) Left sensors using photodetector P2.

Figure 6.22 shows a significant difference between the response of sensor 3, where the force was applied, and the responses of the adjacent sensors (sensors 1, 2, 4, and

5). Considering the low power variation of the other sensors, the crosstalk between sensors is negligible. The cross-sensitivity between both photodetectors is only observed in sensor 10 due to the proximity of this sensor to photodetectors P1 and P2. However, human gait comprises of sequential contralateral steps [18], in which the foot will be placed in one fiber at a time. For this reason, we can identify if the sensor 10 variation was caused by the left or right region of the fiber by analyzing the previous steps. It is noticeable that the power variation decreases as the weight increases. This is due to the exponential behavior of the sensor with saturation tendency, showed in Figure 6.20.

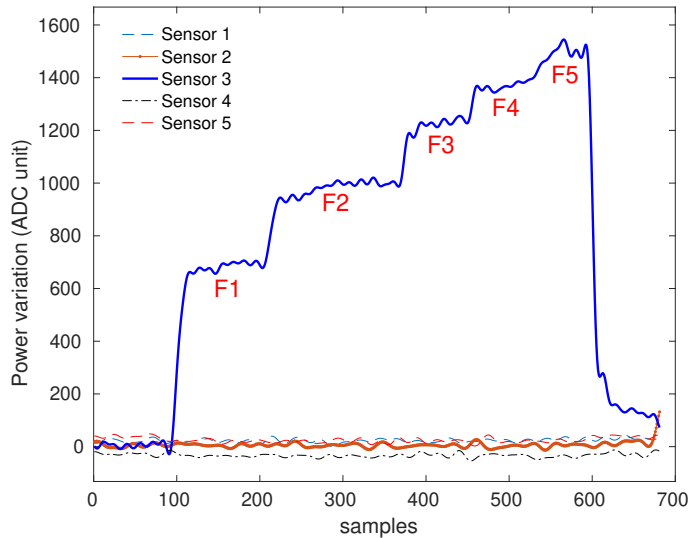


FIGURE 6.22: Response of sensors 1–5 when a loading is applied to sensor 3. The applied forces are of 10 N to 50 N, respectively, with steps of 10 N.

Two volunteers were asked to place their foot on predefined points of the carpet, which are defined in Figure 6.19(b). Figure 6.23 shows the results of spatial characterization, where the maximum error of 6.7 cm was obtained in the marker 1 during the first test. The errors can be related to low sensitivity and/or nonlinearities of the sensors at the region of the first marker (sensors 9–10). On the other hand, the lowest error obtained was 1.5 cm, which occurred in the marker 3. The mean error on this characterization was 4.6 ± 1.7 cm, which, considering the whole range of spatial characterization (160 cm), represents a relative error of 2.9%. The differences between tests 1 and 2 can be related not only to the sensor repeatability, but also to the minor differences on the foot positioning of the volunteers during the tests.

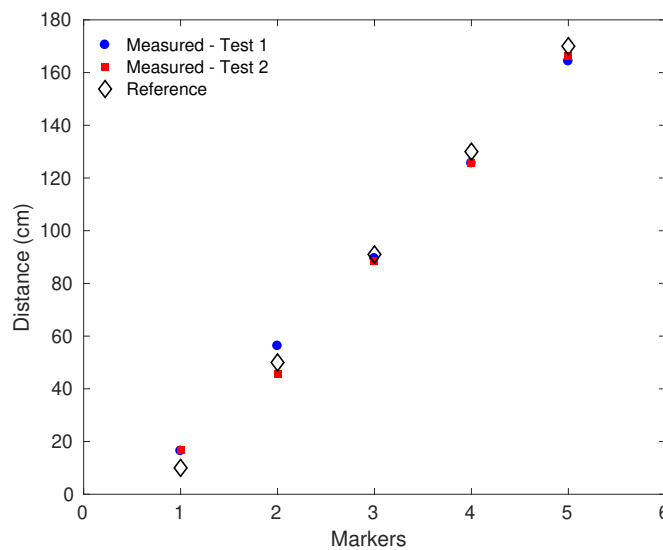


FIGURE 6.23: Results of spatial characterization in the two tests.

POF Smart Carpet Validation in Walking Test

To validate the POF Smart Carpet, three walking tests were performed by three volunteers (two males and one female), age of 26.3 ± 2.1 years. The weight of each voluntary did not influence the results, since the sensor response was normalized for each weight and the purpose of this work is a qualitative analysis. The results of walking tests were divided into GRF data and spatio-temporal gait parameters, including step and stride lengths, cadence and stance duration, in % related to total walking duration. Figure 6.24(a) shows the normalized GRF curves of right and left foot and Figure 6.24(b) shows the foot placement including step lengths during one walking test. The GRF curves present similarity with normal M-shaped GRF pattern [18] and is possible to identify the gait events on the stance phase. It is noticeable that the curve pattern changes along the walking and can also be related to the type of foot strike, which can be neutral, pronated, or supinated. Furthermore, these deviations can also be related with lateral misplacement of the foot on the fiber leading to a variation on the stress transmission to the fiber resulting in different responses of the sensors, may distort the M-shaped. Nevertheless, it is still possible to identify the stance and swing phases, distinguishing the gait events on the stance phase, as well as the double support period in all analyzed cases.

Table 6.5 presents the results of spatio-temporal gait parameters. The volunteers were asked to perform four steps on each walking test. Since the tests were performed by young adults, the step and stride lengths were shorter than the ones commonly obtained in other gait experiments [94]. For walking tests applied to kids or older people, the step and stride lengths would be naturally shorter than the obtained results and can be analyzed with the same system due to the system modular configuration and high spatial resolution. The version of the POF Smart Carpet has 180 cm, which presumably results in a mean of step length of about 45 cm. It is worth noting that the step lengths presented in Table 6.5 generally are close to 45 cm, with a few deviations from this mean value due to the intrinsic variability of the gait [148]. The cadence variability can be related to self-selected pace, which results in a different velocity patterns for each test. However, it is possible to observe similarities on the cadence if the tests of each volunteers are analyzed (see Table 6.5).

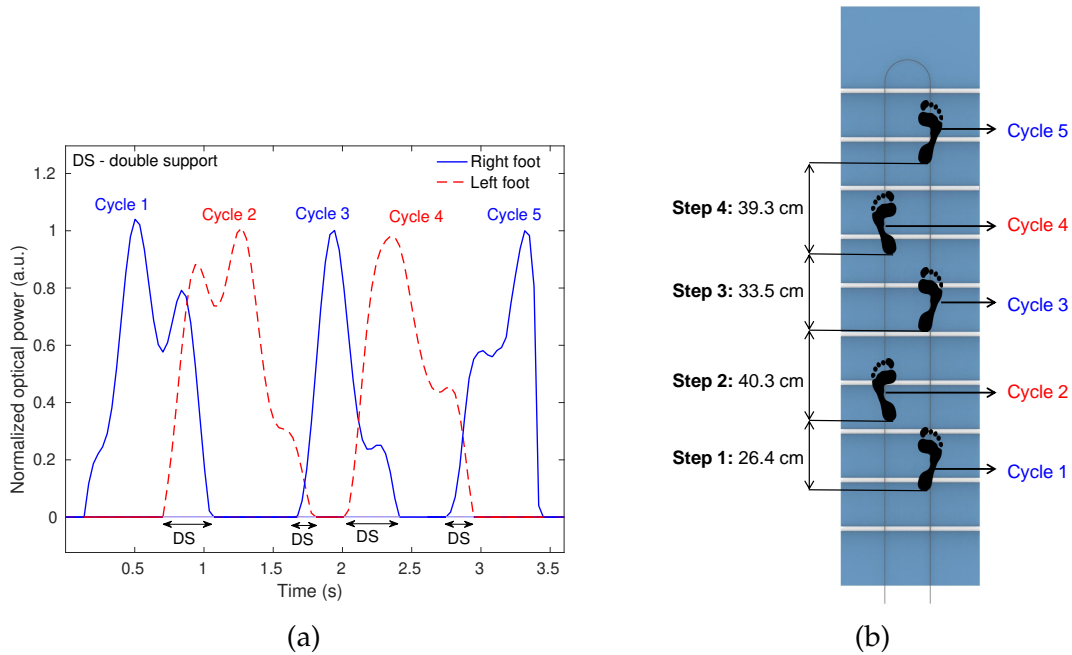


FIGURE 6.24: Results of one walking test: (a) Normalized GRF curves. (b) Foot placement including the step lengths.

Regarding to the stance duration, a mean and standard deviation of $63\% \pm 5\%$ was obtained considering the total walking duration in all performed tests. It is important to mention that the normal stance duration during the gait is 60% according to the literature [18].

TABLE 6.5: Spatio-temporal gait parameters in three walking tests.

		Voluntary 1			Voluntary 2			Voluntary 3		
		T1	T2	T3	T1	T2	T3	T1	T2	T3
Step length (cm)	Step 1	26.4	42.9	16.5	46.5	35.2	30.3	56.5	39.5	38
	Step 2	40.3	31.9	56.9	35.5	35.6	51.1	31.0	35.2	31.1
	Step 3	33.5	42.1	48.1	27.0	39.0	34.7	40.6	55.0	56.4
	Step 4	39.3	37.1	27.2	35.7	34.8	27.8	31.7	10.7	14.9
Stride length (cm)	Stride 1	66.7	74.9	73.5	82.0	70.8	81.4	87.5	74.7	69.1
	Stride 2	73.8	74.1	105.0	62.5	74.6	85.8	71.6	90.2	87.5
	Stride 3	72.9	79.3	75.3	62.7	73.8	62.6	72.3	65.7	71.3
Cadence (steps/min)	-	81.8	62.5	63.4	44.3	44.8	46.9	59.6	60.0	65.7
Stance duration (%)	-	60.9	69.4	58.0	54.3	60.2	65.4	65.8	68.5	64.9

6.4 Final Remarks

This Chapter presented three systems (wearable and non-wearable) based on photonic textiles for monitoring different movement-related parameters in healthcare applications. The systems consisted of a garment, a pair of pants, and a carpet instrumented with intensity variation-based POF sensors.

The POF Smart Garment (presented in Section 5.3) was employed in a human activity recognition protocol to evaluate the ability to identify human activities by analyzing the sensors' responses. A kNN model was designed to classify the activities of 4 volunteers, and an average accuracy of 94% was obtained. The PCA technique was employed for 1 volunteer to evaluate the demand of the number of sensors. Results showed that the reduction from 30 to 10 sensors led to a reduction of 1.82% in the accuracy, i.e. using 30 sensors the accuracy was 99.96% and using one third of the sensors the accuracy was 98.14%, which still provides an accuracy close to 99%. In addition, two movement-related parameters were estimated using the sensors' responses and compared to a reference system (IMU). Minimum error of 0% and maximum error of 2.22% were obtained.

The POF Smart Pants was developed using 60 sensors (30 for each leg), and it is also applied to identify activities, however, the activities are more related to lower limbs movements. A neural network is designed to classify the activities resulting in an accuracy of 100%. The PCA technique was also employed to reduce the number of sensors, resulting in a total of 22 sensors (11 for each leg), and an accuracy of 99%. Results of the POF Smart Pants also allows the estimation of the cadence and other spatio-temporal gait parameters, such as the stance and swing phases, and the double support.

Finally, the POF Smart Carpet was developed for kinetic and kinematic analysis through the monitoring of GRF and spatio-temporal gait parameters. The carpet comprises of low-cost intensity variation-based POF sensors with multiplexing technique and can be an alternative to the high cost systems commonly used for gait analysis. Other advantage of the proposed system is the carpet length, which enables a gait analysis with more steps, with additional possibility of scalability, i.e., a longer carpet can be designed according to the necessities of the user. Results showed that GRF curves are similar with literature, making it possible to identify gait events, stance duration, and double support periods. In addition, it was possible to estimate the step and stride lengths as well as the cadence.

Chapter 7

Heterogeneous OFS Network for Smart Environment

This Chapter presents the integration of optical fiber sensors based on three different approaches for remote healthcare monitoring at home, namely TRA-based systems, FBGs and multiplexed intensity variation sensors. A 6m x 6m room, simulating a small house, is instrumented with a DNP-doped fiber and the TRA system setup (as presented in Section 4.3) is used. Moreover, an FBG-based instrumented carpet (as presented in Section 4.2) is included in this room for gait analysis with the measurement of spatial-temporal parameters and ground reaction forces. Furthermore, the person is wearing the POF Smart Pants, presented in Section 6.2, as a wearable approach for biomechanics analysis and remote activity monitoring. Therefore, the proposed heterogeneous optical fiber sensors system is a flexible and integrated approach for the development of smart environments in Healthcare 4.0. Figure 7.1 summarizes the Smart Environment approach proposed in this Chapter.

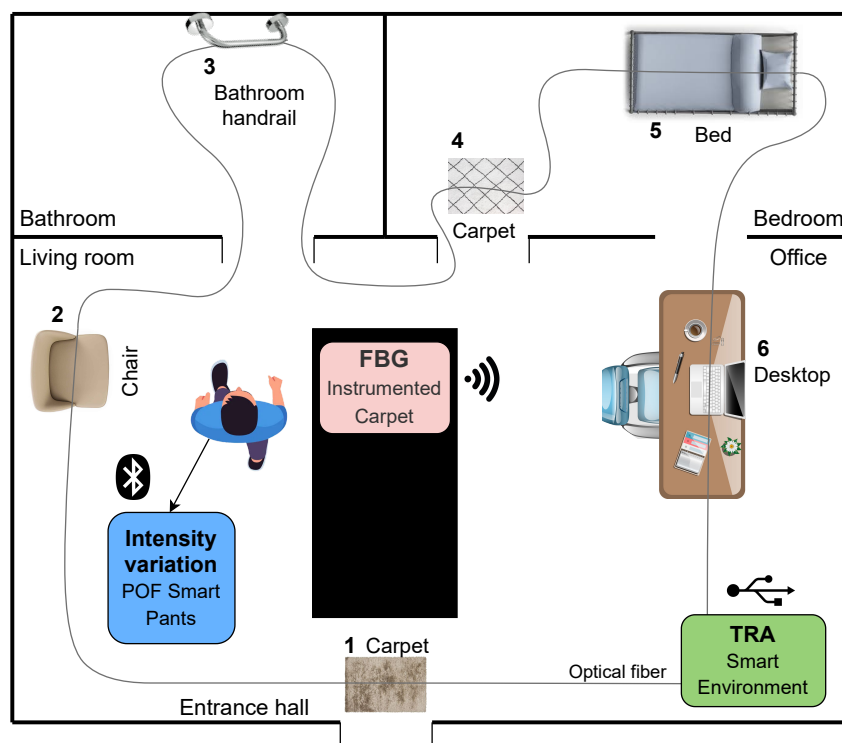


FIGURE 7.1: Chapter 7 overview: heterogeneous OFS network for smart environment.

A graphical interface was developed to perform the synchronization of the systems by the button control to start and stop the acquisition. The graphical interface allows online data visualization in addition to the option to save data and send for offline analysis.

The combination of these three sensors and deep learning algorithms increases the potential of making intelligent decisions in real-time, which enhances the quality of remote healthcare monitoring. It enables collecting medical data, tracking progress, and indicating anomalies, improving the communication between patients and clinicians, and leading to a better everyday quality of life in the end-user community.

7.1 Smart Environment using a TRA-based Sensor

Home is an uncontrolled environment, since it is not usually an instrumented place and there is no health professionals to monitor the subjects who live in such place. The instrumentation of the patient's home is the first stage of remote health monitoring, which allows identifying the place in the house at which the patient is in and presuming which activity he/she is performing. Since more than one person may live in the house, the environment instrumentation must be able to identify multiple people performing simultaneous movements.

As previously presented in the Section 4.4, it is possible to identify multiple simultaneous disturbances in a TRA-based sensor using deep learning techniques. Notable advantages in using this technique include the lower cost by comparing to other distributed systems and the simple acquisition system.

7.1.1 Experimental procedures

Thus, the Smart Environment comprises six principal places: entrance carpet, chair, bathroom handrail, bedroom carpet, bed and, desktop. The DNP-doped fiber is incorporated in all these places. In the TRA setup (presented in the Section 4.3), the transmitted and reflected optical powers indicate the position of the person in the environment, since previous results showed the ability in identifying the disturbance location in the fiber. In this way, the Smart Environment protocol is divided into two parts. The first part consists of one person accessing all the predefined places sorted in ascending order (1 to 6) while the transmitted and reflected optical powers are acquired. The second part consists of two persons accessing different places randomly.

An FFNN model is designed to identify the places in the house where the person (or persons) accessed by using the transmitted and reflected optical powers as input data. The data are divided into training (80%) and testing (20%), and they are associated with their respective classes (places). The input data is normalized between -1 to 1. The FFNN model is evaluated by the accuracy and loss. With the designed model, it is possible to perform the online classification of new data.

7.1.2 Results and Discussion

Figure 7.2 presents the results of the transmitted and reflected optical powers during the Smart Environment protocol. The data are normalized by the results of the unstrained fiber. It is possible to identify the events that the volunteer accesses the

places ordered in the Figure 7.1, previously presented in the beginning of this Chapter. The first place (1, entrance carpet) is the nearest point to the reflection photodetector, whereas the last place (6, desktop) is the farthest one. It leads to a higher reflected optical power variation for places closer to this photodetector, as presented in Figure 7.2.

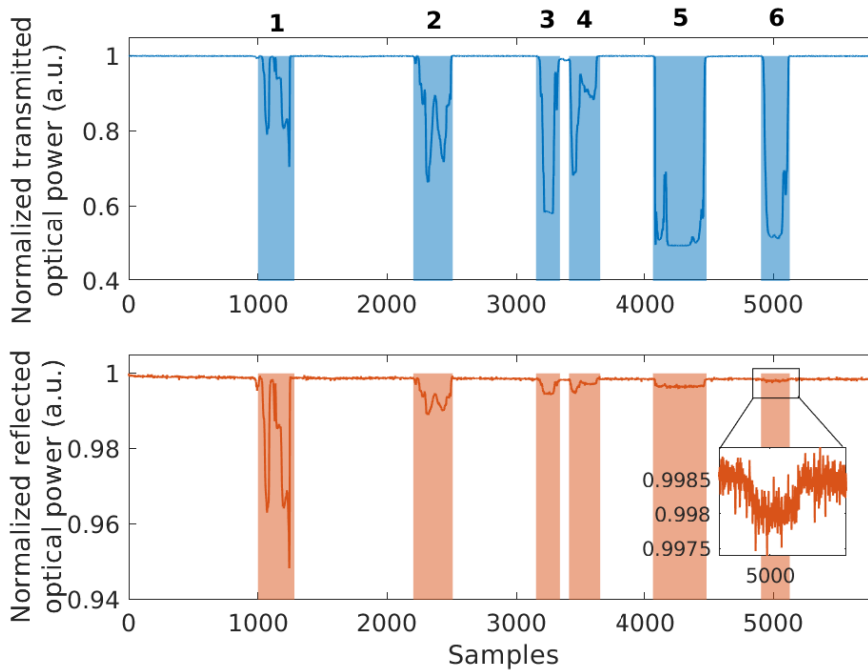


FIGURE 7.2: Results of transmitted and reflected optical power using the TRA setup for place identification in the smart environment.

The transmitted optical power is related to the force applied on the optical fiber whereas the reflected optical power is related to the location of this force. The disturbance points of each place require different forces, i.e., on the carpets, the force applied on the fiber is proportional to the volunteer's weight, whereas, on the bathroom handrail, the force can vary with the need of the user to control his/her balance. For this reason, the transmitted optical power variation does not present a pattern. On the other hand, the reflected optical power variation decreases as the distance from the reflection photodetector increases. It is possible to observe that the reflected optical power variation is lower when compared with the results of Section 4.3. This is because the fiber length is longer, which leads to a weaker reflected signal than when using shorter fiber lengths.

The results of the FFNN model are presented in Figure 7.3. The accuracy and the loss converged to approximately 100% and 0.01, respectively. The convergence of the model to an accuracy of 100% represents the ability to identify the places where the person (or two persons) accessed. This identification can be processed online, and it allows remote monitoring by clinicians located in hospitals with high accuracy.

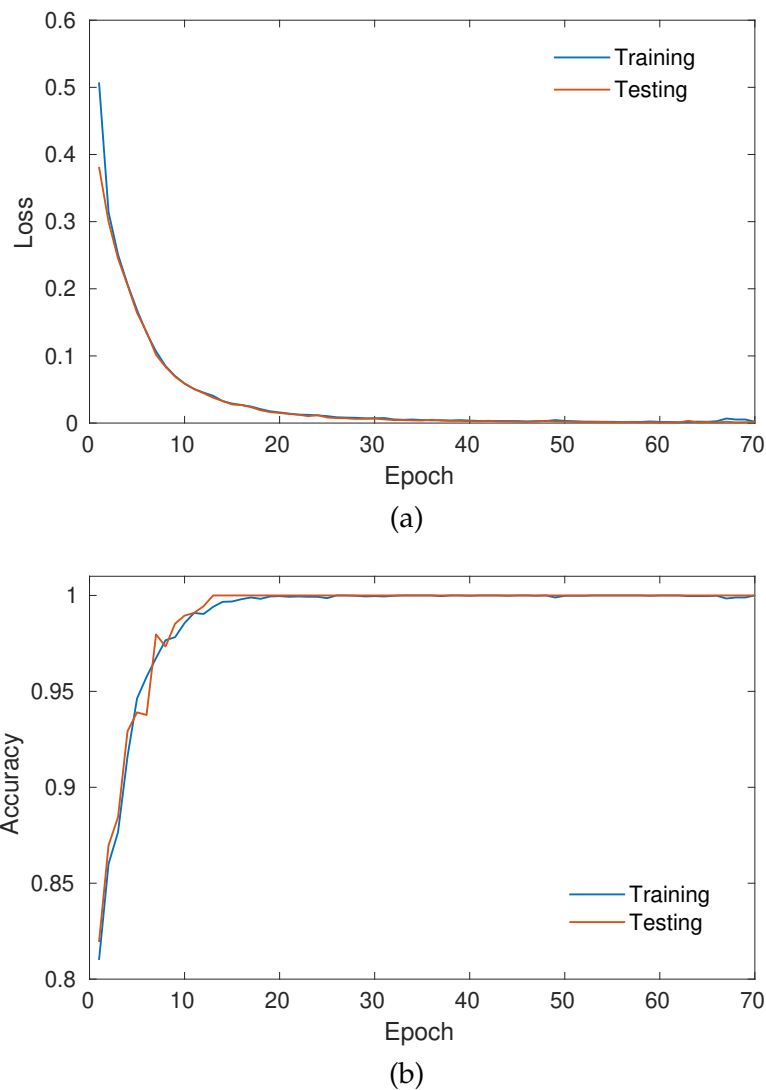


FIGURE 7.3: Metrics of the FFNN model with 70 epochs for the identification of the accessed places in the house. (a) Loss. (b) Accuracy

Based on the results of the classification metrics, the FFNN model can be used as the classifier of new data and identify the places accessed. Figure 7.4 presents an example of the result of the new data classification using the designed FFNN model. The input data is normalized between -1 to 1, as previously mentioned, and the first value corresponds to the transmitted optical power, whereas the last value corresponds to the reflected optical power. The real output consists of binary numbers in which 1 represents when a place is accessed and 0 when no place is accessed. The predicted output is the result of the FFNN model based on an input sample and corresponds to the probabilities of each class. These probabilities are rounded for accuracy estimation.

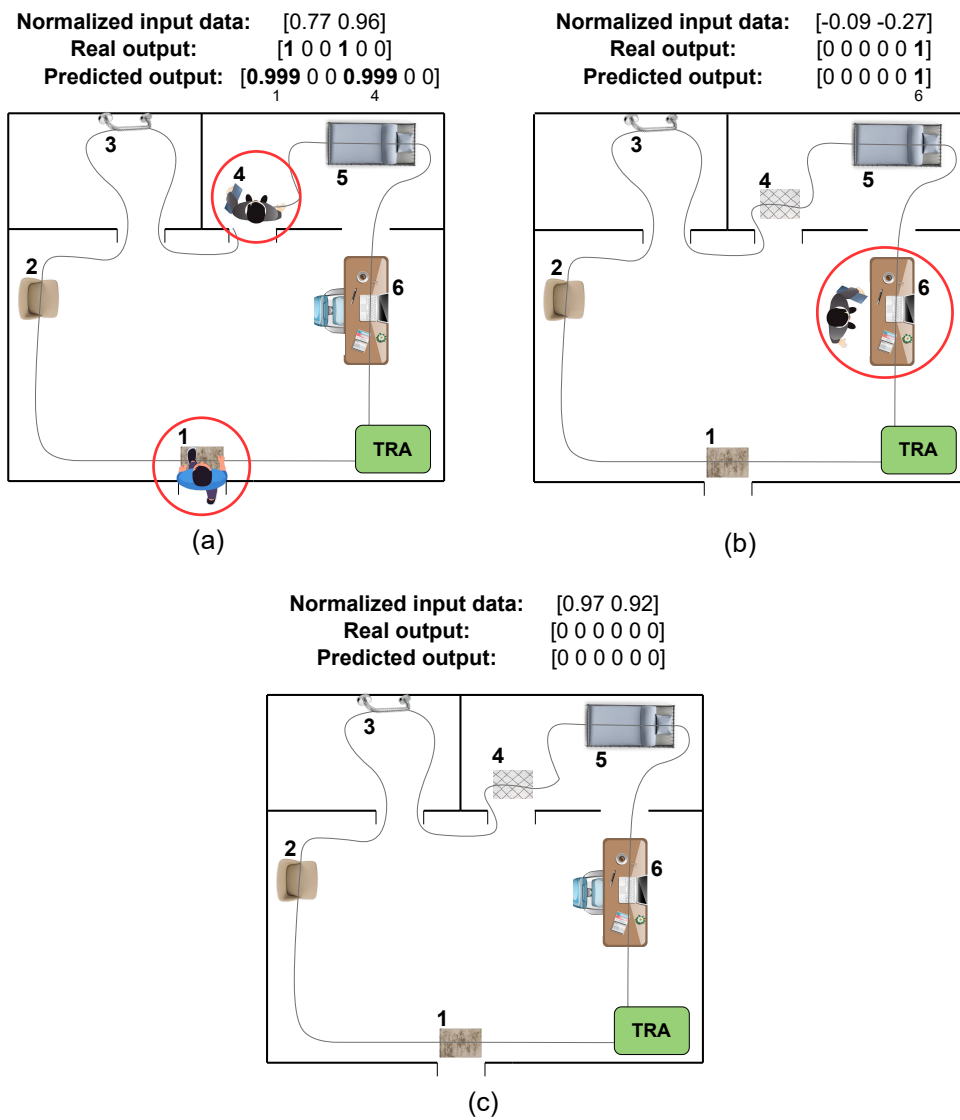


FIGURE 7.4: Results of the classification of new data using the designed FFNN model for three different conditions. (a) Two persons at home. (b) One person at home. (c) No person at home.

7.2 Instrumented Carpet based on FBG Matrix for Gait Analysis

The Instrumented Carpet is a valuable approach incorporated in the Smart Environment since it enables the remote monitoring of gait parameters and provides an objective evaluation of the volunteer's gait, leading to a more accurate and quick response for the clinicians. The evaluation of gait in patients after interventions or elderly with risk of fall are examples of the application of the instrumented carpet at home. Remote gait monitoring facilitates communication between patients and clinicians without the need for face-to-face medical consultation.

7.2.1 Materials and Methods

As shown in Section 4.2, 2 silica fibers with 5 FBGs inscribed in each fiber are embedded in a rubber blanket. Each fiber is positioned in one side (right or left) and the rubber blanket is used as a carpet for gait analysis. In the system setup of this Section, the FBG interrogator (HYPERION si255, Micron Optics) is connected to a router to allow wireless acquisition of FBG data that increases the portability of the proposed system through a wireless connection with the computer which manages all data, as shown in Figure 7.5.

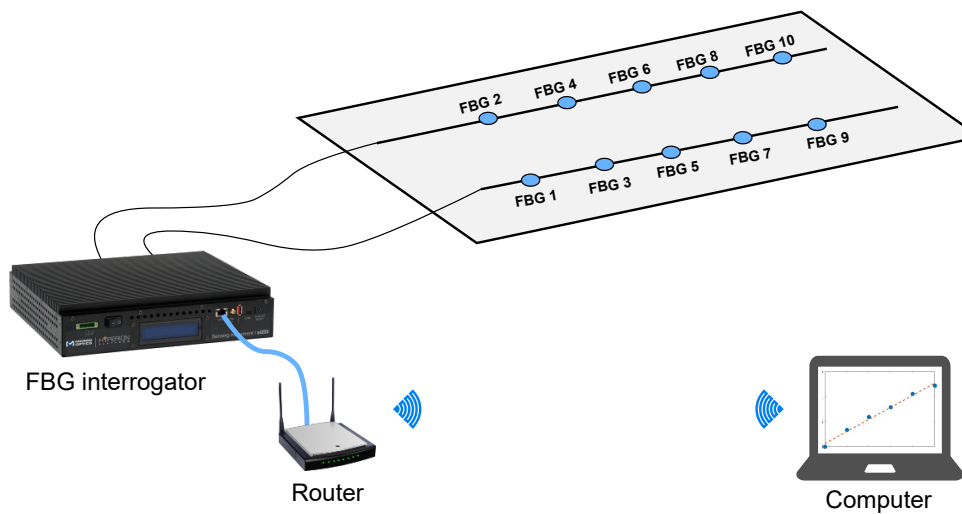


FIGURE 7.5: System setup for the FBG-based Instrumented Carpet in the Heterogeneous OFS network protocol.

7.2.2 Experimental procedures

As presented in Section 4.2, 23 locations of the rubber blanket were characterized for one volunteer by using an FFNN model. With new data, it is possible to identify the points pressed by the volunteer during his/her locomotion in the smart environment. With the foot location identification, it is possible to estimate some spatio-temporal gait parameters, such as step and stride length. Moreover, kinetic parameters of the gait can be estimated by the response of the FBG sensors matrix. The GRF can be obtained by the analysis of the FBG sensors responses, which are converted to force (see the force characterization curves in Section 4.2), and represent the GRF

during the gait. In addition, by analyzing the GRF of each foot it is possible to estimate single and double support duration. In this Section, a gait is performed on the instrumented carpet. The FFNN model designed in Section 4.2 is applied on new data to classify the foot locations during the gait. Thus, some parameters previously mentioned (step and stride length, double support and stance phase duration, GRF) are estimated by the results of the FFNN classification and the FBGs raw data.

7.2.3 Results and Discussion

As presented in Section 4.2, the sensors presented different sensitivities in the force characterization. Table 7.1 shows the estimated sensitivity to force of each FBG sensor. Differences between sensitivities are related to the FBG positioning in the carpet, which has minor differences in its thickness, leading to variations in sensors sensitivities depending on their positions in the rubber carpet. This can be solved by normalizing the sensors' sensitivity.

FBG	Sensitivity (pm/N)	FBG	Sensitivity (pm/N)
1	2.12	6	0.79
2	3.87	7	2.46
3	2.45	8	4.12
4	3.06	9	0.88
5	0.49	10	2.43

TABLE 7.1: FBGs sensors' sensitivities.

After the sensors normalization, the GRF during the gait performance was analyzed. The temporal response of each sensor is presented in Figure 7.6. The GRF data indicate the single and double support periods since there are samples in which only one sensor is pressed and samples in which two sensors are simultaneously pressed. It also leads to the evaluation of stance and swing phases of each foot.

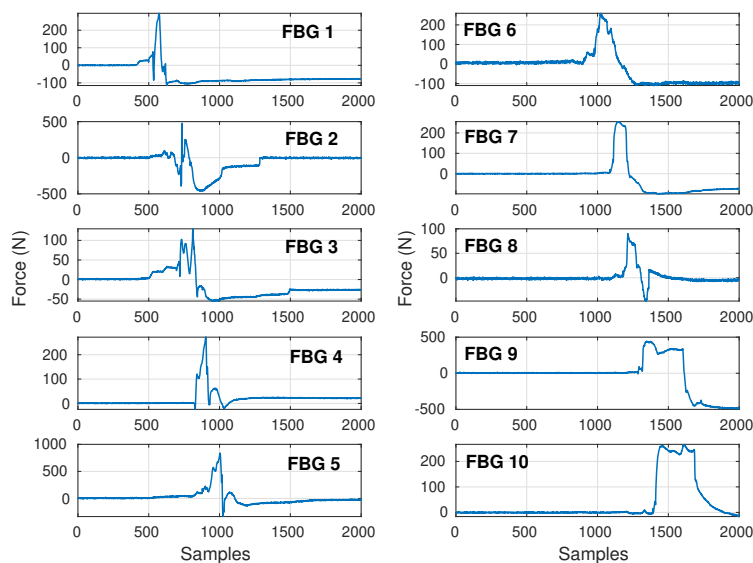


FIGURE 7.6: Sensors responses after normalization during a gait performance.

Figure 7.7 presents the temporal responses of these sensors relating them to the support moments (single or double) of two steps (left and right) during the gait. The responses were presented using FBGs 4 and 5 as an example due to their positioning in the middle region of the carpet. It is possible to observe that the sensors responses during the transition of the foot in the gait presents characteristics that enable the identification of the gait phases. Each FBG curve consists of two different peaks. This behavior corresponds to the body load transition during the gait, i.e., the first single support (left foot) initiates with a heel strike in which the body weight is concentrated on the heel and finishes when the right foot goes to the floor and divides the body weight with the left foot. Thereafter, the double support is initiated with heel strike of the right foot while the left foot is finishing the stance phase with toe-off, and for this reason, the second peak of the left foot is lower than the first one. The double support finishes when the left foot leaves the ground, and the single support of the right foot initiates.

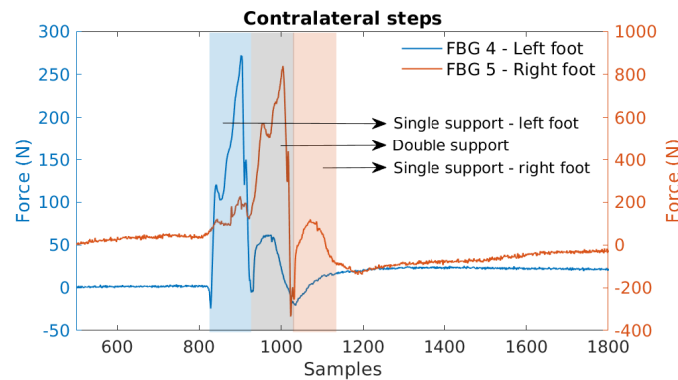


FIGURE 7.7: Sensors responses of FBG 4 and FBG 5, and the estimation of support periods (single and double) of two consecutive contralateral steps during the gait.

By analyzing consecutive contralateral steps, as presented in Figure 7.7, it is possible to estimate the percentage of double support during the stance phase, commonly used in scientific literature to identify gait anomalies. The double support period indicates bilateral floor contact, but not equal load sharing [149]. In the same context, in the analysis of consecutive ipsilateral steps, it is possible to estimate the percentage of stance and swing phases duration, also commonly used for gait assessment, as presented in Figure 7.8.

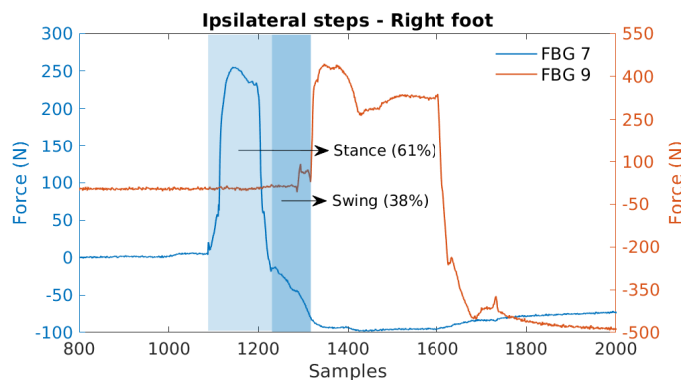


FIGURE 7.8: Sensors responses of FBG 7 and FBG 9 and the estimation of stance and swing phase duration during a gait cycle.

By using the FFNN model previously designed for this application, the locations in the instrumented carpet during a new gait performance were classified using new input data. Figure 7.9 presents the classification results in three different moments in the gait along the carpet (beginning, middle and end of the carpet) with the real output and the output predicted by the designed FFNN model. The FFNN output presents the probabilities of each class (location). Even if the probabilities are not 1, they can indicate the correct classification by using a threshold, since the locations that are not pressed always present probabilities equal to 0.

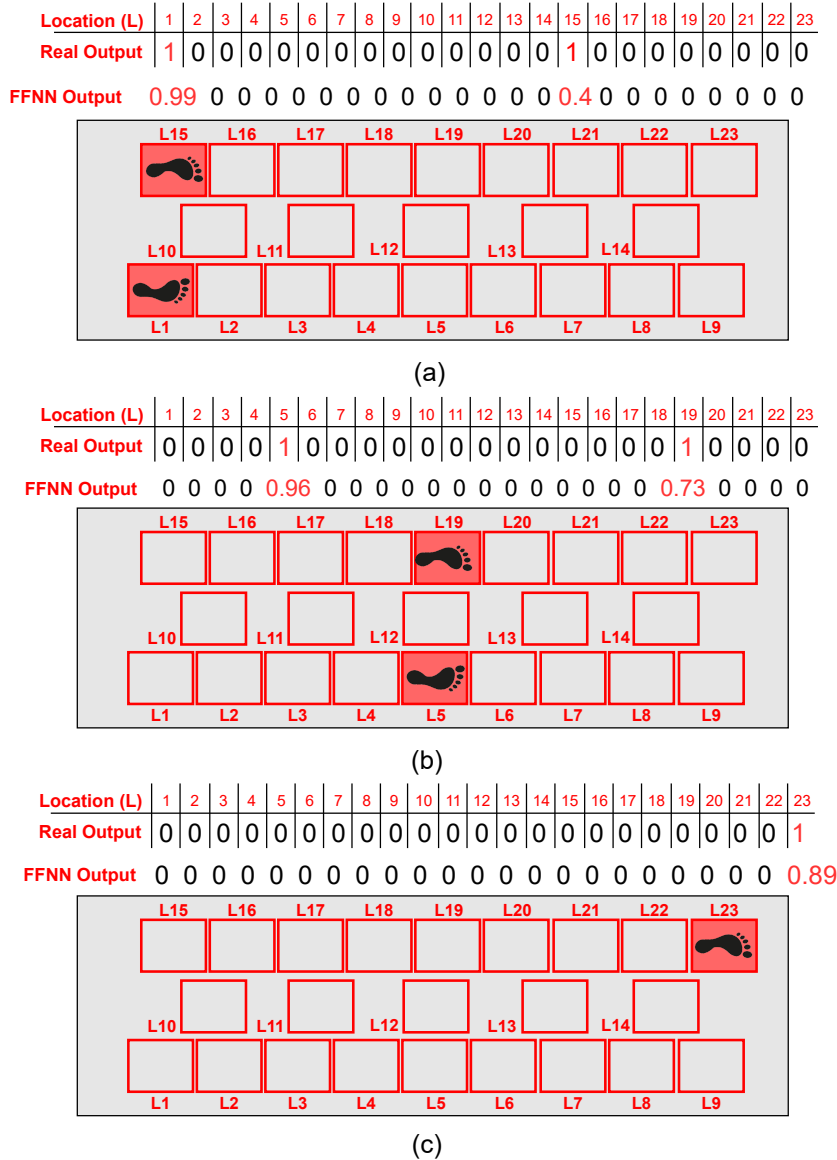


FIGURE 7.9: Examples of the classification of locations pressed by the volunteer during a gait performance using the designed FFNN model: comparison between the real output and the FFNN output, which presents the probabilities of each class. (a) Double support at locations L1 and L15. (b) Double support at locations L5 and L19. (c) Single support at location L23.

7.3 Heterogeneous OFS Network based on FBG, Intensity Variation and TRA techniques

Each system included in the Smart Environment provides valuable information to the healthcare assessment. The results of each technology were presented in the previous sections. Therefore, this Section presents the integration of the systems in the Smart Environment with the simultaneous operation of the whole system. This Section aims to develop an integrated system with a heterogeneous OFS network that can provide different information about a subject (such as a patient) in real-time and remotely communicates with a clinician avoiding face-to-face consultations.

7.3.1 Materials and Methods

The three systems are synchronized and the data acquisition are managed by a graphical interface developed for this protocol. This interface enables online and offline acquisition. FBGs data are transmitted via Wifi, the POF Smart Pants data are transmitted via Bluetooth and the TRA-based Smart Environment data are transmitted via serial communication. All data are received at same global time and operate at different clocks. The interface works with three threads that process the data from each system simultaneously at their respective clocks.

7.3.2 Experimental procedures

The protocol performed using the three systems is similar to the Smart Environment protocol, previously presented in Section 7.1. The difference is the use of the POF Smart Pants and the walking on the Instrumented Carpet before accessing the places of the Smart Environment. During the protocol, the data from all systems are acquired and showed in the graphical interface.

7.3.3 Results and Discussion

The graphical interface developed for the Smart Environment protocol using the three systems (FBG, Intensity-variation and TRA) is presented in Figure 7.10. The left part of the interface is used to connect devices and control the data acquisition (start, stop or save file for offline analysis). The central part of the interface is used for online visualization. The interface was implemented using Python and JavaScript/HTML.

Figure 7.11 presents the results of the three systems during a protocol performance. As mentioned, each system provide an important information. Figure 7.11(a) shows the responses of the activated FBGs of the Instrumented Carpet during the protocol. Since only FBG1, FBG2, FBG3 and FBG6 presented significant variation correspondent the GRF, this result indicates the path performed by the volunteer during the protocol. Figure 7.11(b) shows the sensors' responses of the POF Smart Pants. This result led to the identification of the user's activities during the protocol. Also, Figure 7.11(c) shows the transmitted and reflected optical powers, indicating the places accessed by the volunteer.

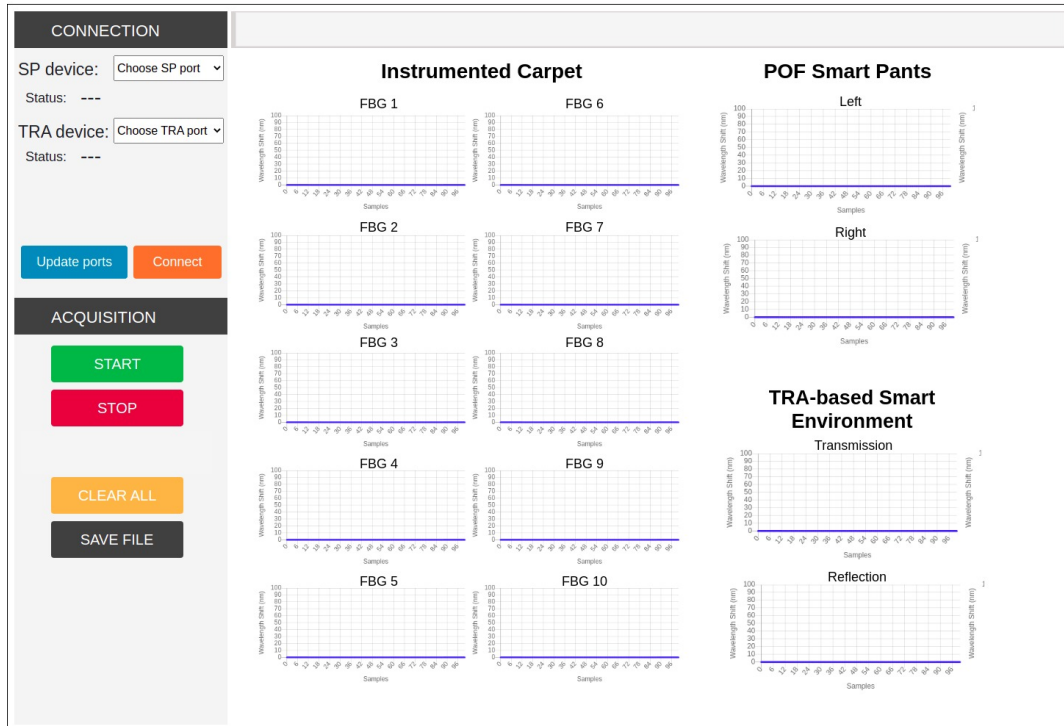


FIGURE 7.10: Graphical interface for data management and acquisition control.

7.4 Final Remarks

This Chapter presented the integration of three sensors using different OFS techniques for simulation of the remote healthcare monitoring at home. The three systems provide different information acquired with the different sensors systems: identification of the place where the volunteer is in the house; analysis of the user's movements, and identification of the activities; assessment of the volunteer's gait during daily activities. The TRA-based system enable the identification of the user's position in the smart environment, whereas the results from the smart pants indicate which activity the user is performing. Furthermore, the FBG-embedded rubber carpet is in a region of the smart environment at which the GRF and spatio-temporal parameters of user's gait are acquired. Thus, the FBG-embedded carpet in the smart environment is a region at which the gait of the user is analyzed and excludes the necessity of patient transportation to clinical environment for this end. The combination of these data provides a higher level of health monitoring at home when compared with isolated systems. This can be useful for clinicians to acquire more information about patients' health, be able to diagnose the correct treatment and even anticipate health issues (specially the gait-related ones).

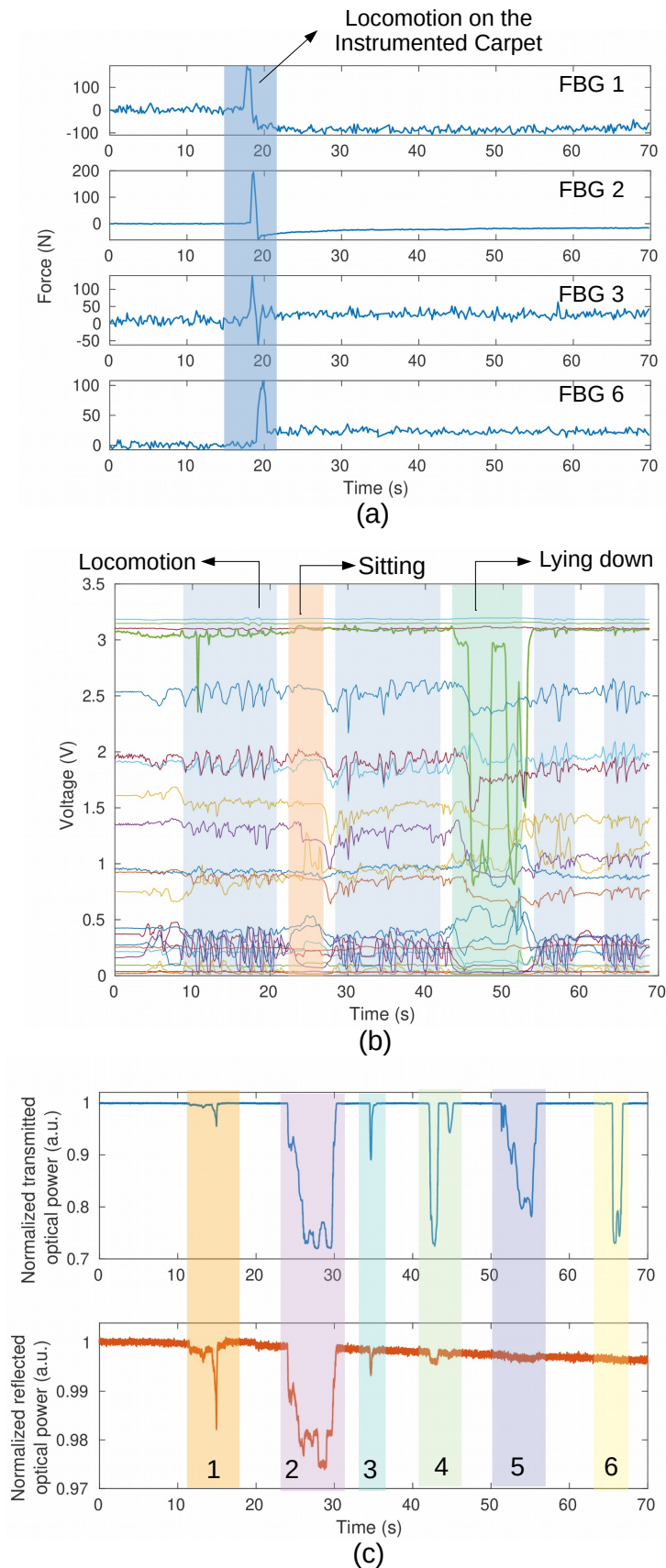


FIGURE 7.11: Result of the Smart Environment protocol using the synchronized systems. (a) FBG-based Instrumented Carpet. (b) POF Smart Pants. (c) TRA-based Smart Environment.

Chapter 8

Conclusions and Future Works

8.1 Summary and Final Remarks

This PhD Thesis presented novel instrumentation approaches for integration of OFS with textiles and flexible structures for healthcare applications. In addition, the combination of different sensors with AI technology resulted in the increase of real-time decisions (such as on the activities classification) and enhancement of the sensors performances. The motivation of this work is the limitations of conventional electronic sensors, which include electromagnetic sensitivity, high hysteresis, high costs and the inability of being embedded or positioned in flexible structures, in most cases. These disadvantages are undesirable for wearable systems, developed in this Thesis and specially undesirable for applications at home, which compact and lower costs are required. Thus, sensors using different sensing techniques for measurement of several physical parameters are developed and analyzed under kinematic and kinetic conditions. In this way, after the performance analysis of the proposed sensors, this PhD Thesis presented the integration of these sensors in smart textiles for wearable or non-wearable applications, such as the POF Smart Garment for activities identification or the FBG-based Instrumented Carpet for gait analysis, respectively. In addition, the DNP optical fiber integration in smart textiles/objects and the use of TRA-based systems for simultaneous multiple detection of mechanical perturbation was also presented. Furthermore, AI techniques covering from Machine Learning to Deep Learning for data classification are employed in different scenarios to improve the sensors performances and classify the activities.

To achieve the mentioned goals, first, a theoretical background and state of the art review of different sensing approaches are presented in Chapter 2. In addition, the fundamentals and overview of optical fibers are also depicted in this Chapter. Then, the biomechanics and their concepts are described. Also, AI concepts and the theory behind the techniques addressed in this Thesis are presented. Thus, Chapter 2 provides the knowledge required for the developments proposed in the following chapters.

Thereafter, Chapters 3 and 4 present the evaluation of proposed sensors for measurement of different parameters. In Chapter 3, sensors are developed for measurement of kinematic (angle) and kinetic (force) parameters are described. These sensors are developed using CYTOP fiber and they are based on intensity-variation technique. The curvature sensor for angle measurement is evaluated under different conditions (angular velocities and source light wavelengths) to evaluate performance factors (sensitivity, hysteresis, linearity). On the other hand, the force sensor is proposed to estimate stiffness for wearable applications. Chapter 4 presents the preliminary studies of sensors integrated in textiles or flexible structures. This Chapter includes 3 different sensing techniques: intensity-variation, FBG and TRA. The

intensity variation-based textile is a preliminary study for user's activities classification. The textile is evaluated under different temperature, force and angular conditions. The FBG-based system is a preliminary study for gait analysis using neural network. Ten (10) FBG sensors are incorporated into two layers of rubber blanket. The sensors are characterized by force and a neural network model is designed to identify predefined locations pressed by the volunteer. Finally, a TRA-based system is evaluated under two conditions: using different DNP-doped fibers to select a suitable DNP fiber composition for the analysis and, applying simultaneous multiple disturbance on a fiber.

In Chapter 5, two devices based on intensity variation POF sensors are developed for a balance assessment protocol. The first device is a perturbator system fabricated using LPS-POF to perform disturbances on a volunteer in order to destabilize him/her. The second system is a smart garment capable of identifying the disturbance points performed by the perturbator system. The goal of this Chapter is to relate the disturbance force (perturbator system) and the disturbance location (smart garment) to assess the human balance.

Chapter 6 presents Smart Textiles for remote healthcare monitoring including the POF Smart Garment, the POF Smart Pants and the POF Smart Carpet. All these systems are developed using multiplexed POF sensors and each sensor has a different proposal during the health monitoring. The POF Smart Garment and the POF Smart Pants are wearable systems developed to evaluate the human movement and to identify different activities related to the upper or lower limbs. On the other hand, the POF Smart Carpet is developed to evaluate different gait parameters, including kinetic (GRF) and kinematic (step and stride length, stance and double support duration) parameters.

Finally, Chapter 7 presents the integration of three different type of sensors in a home for creation of a Smart Environment. The systems consist of: TRA-based Smart Environment, FBG-based Instrumented Carpet and the POF Smart Pants. A graphical interface is developed to perform the systems' synchronization, manage the data acquisition and visualize data online. Data are acquired simultaneously and different healthcare information is provided online or offline.

In summary, this Thesis aimed to develop, analyze and apply different OFS integrated into textiles and flexible structures combined with AI techniques to achieve interesting solutions for remote healthcare monitoring. Therefore, this Thesis is aligned with Healthcare 4.0 technology, which includes smart sensors network, wireless communication, AI technology, resulting in intelligent decision-making.

8.2 Future Works

This Thesis paved the way for a multitude of applications in healthcare and wearable instrumentation. For these reasons, many research fields and future works are available on each of the 3 main themes of this PhD Thesis (new sensors approaches, textiles integration and heterogeneous sensors networks).

The future works perspectives for development and analysis of new sensors (Chapter 3 and 4) are listed as follows:

1. **Development and performance analysis of wavelength multiplexed sensors:**

The improvement of the multiplexing technique in intensity variation-based sensors includes the wavelength multiplexing using light sources with different wavelengths in addition to the temporal multiplexing (presented in different works in this Thesis) in order to enable the addition of more sensors in a unique fiber.

2. Development of new multiplexing techniques using light source modulation:

In addition to the temporal multiplexing technique, new light source modulations will be developed to improve the system architecture and enables higher number of sensors.

3. Development of biosensors for biomarkers and hormone detection:

The monitoring of biomechanical and physiological parameters is presented in this Thesis using different technologies. However, the monitoring of new parameters (such as stress hormone and fatigue) is valuable for healthcare applications since it increases the complexity of the protocols and enables the hormonal feedback of the subjects.

The future works involving integration of new sensors in textiles for measurement of new biomedical parameters in different protocols (Chapter 5 and 6) are listed below:

1. Integration of sensors in textiles for vital signs monitoring:

In addition to breathing rate parameter (presented in the Section 6.1), other vital signs are interesting parameters to monitor, such as heart rate, blood pressure and oximetry.

2. Development of spatial-temporal 3D Human Pose Reconstruction using OFS data and AI techniques:

Another interesting approach is to use OFS combined with AI techniques for 3D human pose reconstruction, which can be relevant in the biomedical field for monitoring patients' posture or lower limb shape reconstruction during the human gait to assist in rehabilitation.

3. Novel textile applications in healthcare devices:

This Thesis presented the development and application of different textiles. Moreover, future work involves the development of new smart textiles for different applications, including clinical assessment.

4. Applications in soft robotics and intelligent multifunctional structures:

Based on the works presented in this Thesis, the development of intelligent multifunctional structures for application in soft robotics is an attractive approach to increase the feedback information through OFS sensors and improve the human-robot interface.

Finally, regarding perspectives of future works using OFS in Healthcare 4.0:

1. Development of cloud storage and computing to store and manage data on Internet application:

Future work includes cloud services development to compute and store a large amount of data from OFS combined with AI techniques in real-time, to improve data management and enable internet applications.

2. Integration of optical fiber sensors network in Smartphones:

Finally, future work involves the integration of OFS networks with smartphones. In this case, the smartphone will act as an interrogation unit, which decreases the system complexity and the costs, and increases the portability and the simplicity of the data acquisition. Also, this approach will enable internet applications.

Bibliography

- [1] P. Uhlenberg, *Handbook of Population Ageing*. 2009, vol. 1, ISBN: 9788578110796. arXiv: [arXiv:1011.1669v3](https://arxiv.org/abs/1011.1669v3).
- [2] P. D. United Nations, Department of Economic and Social Affairs, *World Population Ageing 2019, Highlights*. 2019, pp. 1–111, ISBN: 9789211483260.
- [3] E. Jaul and J. Barron, *Age-Related Diseases and Clinical and Public Health Implications for the 85 Years Old and Over Population*, 2017. DOI: [10.3389/fpubh.2017.00335](https://doi.org/10.3389/fpubh.2017.00335).
- [4] C. Franceschi, P. Garagnani, C. Morsiani, *et al.*, *The continuum of aging and age-related diseases: Common mechanisms but different rates*, 2018. DOI: [10.3389/fmed.2018.00061](https://doi.org/10.3389/fmed.2018.00061).
- [5] W. Huo, S. Mohammed, J. C. Moreno, and Y. Amirat, “Lower Limb Wearable Robots for Assistance and Rehabilitation: A State of the Art,” *IEEE Systems Journal*, vol. 10, no. 3, pp. 1068–1081, 2016, ISSN: 19379234. DOI: [10.1109/JSYST.2014.2351491](https://doi.org/10.1109/JSYST.2014.2351491).
- [6] A. Nag, S. C. Mukhopadhyay, and J. Kosel, “Wearable Flexible Sensors: A Review,” *IEEE Sensors Journal*, vol. 17, no. 13, pp. 3949–3960, 2017, ISSN: 1530437X. DOI: [10.1109/JSEN.2017.2705700](https://doi.org/10.1109/JSEN.2017.2705700).
- [7] I. Korhonen, J. Pärkkä, and M. V. Gils, “Health Monitoring in the Home of the Future,” *IEEE Engineering in Medicine and Biology Magazine*, vol. 22, no. 3, D. M. Ojcius, Ed., pp. 66–73, Aug. 2003, ISSN: 1932-6203. DOI: [10.1371/journal.pone.0237004](https://doi.org/10.1371/journal.pone.0237004).
- [8] S. Majumder, T. Mondal, and M. J. Deen, “Wearable sensors for remote health monitoring,” *Sensors (Switzerland)*, vol. 17, no. 1, 2017, ISSN: 14248220. DOI: [10.3390/s17010130](https://doi.org/10.3390/s17010130).
- [9] M. Böhm, J. C. Reil, P. Deedwania, J. B. Kim, and J. S. Borer, “Resting heart rate: Risk indicator and emerging risk factor in cardiovascular disease,” *American Journal of Medicine*, vol. 128, no. 3, pp. 219–228, 2015, ISSN: 15557162. DOI: [10.1016/j.amjmed.2014.09.016](https://doi.org/10.1016/j.amjmed.2014.09.016).
- [10] A. Leal-Junior, A. Frizera, C. Marques, and M. José Pontes, “Polymer-optical-fiber-based sensor system for simultaneous measurement of angle and temperature,” *Applied Optics*, vol. 57, no. 7, p. 1717, 2018, ISSN: 1559-128X. DOI: [10.1364/ao.57.001717](https://doi.org/10.1364/ao.57.001717).
- [11] H. Dejnabadi, B. M. Jolles, and K. Aminian, “A new approach to accurate measurement of uniaxial joint angles based on a combination of accelerometers and gyroscopes,” *IEEE Transactions on Biomedical Engineering*, vol. 52, no. 8, pp. 1478–1484, 2005, ISSN: 00189294. DOI: [10.1109/TBME.2005.851475](https://doi.org/10.1109/TBME.2005.851475).
- [12] M. Nishyama, M. Miyamoto, and K. Watanabe, “Respiration and body movement analysis during sleep in bed using hetero-core fiber optic pressure sensors without constraint to human activity,” *Journal of Biomedical Optics*, vol. 16, no. January, pp. 1–7, 2011. DOI: [10.1117/1.3528008](https://doi.org/10.1117/1.3528008).

- [13] R. Strauß, S. Ewig, K. Richter, T. König, G. Heller, and T. T. Bauer, "The prognostic significance of respiratory rate in patients with pneumonia: A retrospective analysis of data from 705 928 hospitalized patients in Germany from 2010-2012," *Deutsches Arzteblatt International*, vol. 111, no. 29-30, pp. 503–508, 2014, ISSN: 18660452. DOI: [10.3238/arztebl.2014.0503](https://doi.org/10.3238/arztebl.2014.0503).
- [14] C. Erdmier, J. Hatcher, and M. Lee, "Wearable device implications in the healthcare industry," *Journal of Medical Engineering and Technology*, vol. 40, no. 4, pp. 141–148, 2016, ISSN: 1464522X. DOI: [10.3109/03091902.2016.1153738](https://doi.org/10.3109/03091902.2016.1153738).
- [15] V.-T. Tran, C. Riveros, and P. Ravaud, "Patients' views of wearable devices and AI in healthcare: findings from the ComPaRe e-cohort," *npj Digital Medicine*, vol. 2, no. 1, pp. 1–8, 2019, ISSN: 2398-6352. DOI: [10.1038/s41746-019-0132-y](https://doi.org/10.1038/s41746-019-0132-y).
- [16] L. A. Bove, "Increasing Patient Engagement Through the Use of Wearable Technology," *Journal for Nurse Practitioners*, vol. 15, no. 8, pp. 535–539, 2019, ISSN: 15554155. DOI: [10.1016/j.nurpra.2019.03.018](https://doi.org/10.1016/j.nurpra.2019.03.018).
- [17] The Commission of The European Communities, "Smart Wearables: Reflection and Orientation Paper," *Digital Industry Competitive Electronics Industry*, vol. 121, no. 17, pp. 4592–4599, 2016, ISSN: 1520-6106.
- [18] C. Kirtley, *Clinical Gait Analysis: Theory and Practice*, 1st ed. London, UK: Elsevier B.V., 2006, p. 328, ISBN: 9780443103100. DOI: [10.1016/B978-0-7020-1767-4.50001-1](https://doi.org/10.1016/B978-0-7020-1767-4.50001-1).
- [19] D. Knudson, *Fundamentals of Biomechanics*, 2.ed. 2007, ISBN: 978-0-387-49311-4.
- [20] C. Wong, Z. Q. Zhang, B. Lo, and G. Z. Yang, "Wearable Sensing for Solid Biomechanics: A Review," *IEEE Sensors Journal*, vol. 15, no. 5, pp. 2747–2760, 2015, ISSN: 1530437X. DOI: [10.1109/JSEN.2015.2393883](https://doi.org/10.1109/JSEN.2015.2393883).
- [21] A. Muro-de-la-Herran, B. Garcia-Zapirain, and A. Mendez-Zorrilla, "Gait Analysis Methods: An Overview of Wearable and Non-Wearable Systems, Highlighting Clinical Applications," *Sensors*, vol. 14, no. 2, pp. 3362–3394, Feb. 2014, ISSN: 1424-8220. DOI: [10.3390/s140203362](https://doi.org/10.3390/s140203362).
- [22] M. El-Gohary and J. McNames, "Shoulder and elbow joint angle tracking with inertial sensors," *IEEE Transactions on Biomedical Engineering*, vol. 59, no. 9, pp. 2635–2641, 2012, ISSN: 00189294. DOI: [10.1109/TBME.2012.2208750](https://doi.org/10.1109/TBME.2012.2208750).
- [23] D. Hawkins, "A new instrumentation system for training rowers," *Journal of Biomechanics*, vol. 33, no. 2, pp. 241–245, 2000, ISSN: 00219290. DOI: [10.1016/S0021-9290\(99\)00139-6](https://doi.org/10.1016/S0021-9290(99)00139-6).
- [24] M. J. Mueller, K. E. Smith, P. K. Commean, D. D. Robertson, and J. E. Johnson, "Use of Computed Tomography and Plantar Pressure Measurement for Management of Neuropathic Ulcers in Patients With Diabetes," *Physical Therapy*, vol. 79, no. 3, pp. 296–307, Mar. 1999, ISSN: 0031-9023. DOI: [10.1093/ptj/79.3.296](https://doi.org/10.1093/ptj/79.3.296).
- [25] L. Ballaz, M. Raison, and C. Detrembleur, "Decomposition of the vertical ground reaction forces during gait on a single force plate.," *Journal of musculoskeletal & neuronal interactions*, vol. 13, no. 2, pp. 236–43, Jun. 2013, ISSN: 1108-7161.

- [26] L. Shu, T. Hua, Y. Wang, Q. Qiao Li, D. D. Feng, and X. Tao, "In-shoe plantar pressure measurement and analysis system based on fabric pressure sensing array," *IEEE transactions on information technology in biomedicine: a publication of the IEEE Engineering in Medicine and Biology Society*, vol. 14, no. 3, pp. 767–775, 2010, ISSN: 1558-0032. DOI: [10.1109/TITB.2009.2038904](https://doi.org/10.1109/TITB.2009.2038904).
- [27] A. H. Abdul Razak, A. Zayegh, R. K. Begg, and Y. Wahab, "Foot plantar pressure measurement system: A review," *Sensors (Switzerland)*, vol. 12, no. 7, pp. 9884–9912, 2012, ISSN: 14248220. DOI: [10.3390/s120709884](https://doi.org/10.3390/s120709884).
- [28] S. Chandra Mukhopadhyay, "Wearable Sensors for Human Activity Monitoring," *IEEE Sensors Journal*, vol. 15, no. 3, pp. 1321–1330, 2015.
- [29] D. J. Sanderson, I. M. Franks, and D. Elliott, "The effects of targeting on the ground reaction forces during level walking," *Human Movement Science*, vol. 12, no. 3, pp. 327–337, May 1993, ISSN: 01679457. DOI: [10.1016/0167-9457\(93\)90022-H](https://doi.org/10.1016/0167-9457(93)90022-H).
- [30] A. G. Leal-Junior, A. Frizera, and M. José Pontes, "Sensitive zone parameters and curvature radius evaluation for polymer optical fiber curvature sensors," *Optics & Laser Technology*, vol. 100, pp. 272–281, Mar. 2018, ISSN: 00303992. DOI: [10.1016/j.optlastec.2017.10.006](https://doi.org/10.1016/j.optlastec.2017.10.006).
- [31] K. Peters, "Polymer optical fiber sensors—a review," *Smart Materials and Structures*, vol. 20, no. 1, p. 013 002, Jan. 2011, ISSN: 0964-1726. DOI: [10.1088/0964-1726/20/1/013002](https://doi.org/10.1088/0964-1726/20/1/013002).
- [32] L. Alwis, T. Sun, and K. Grattan, "[INVITED] Developments in optical fibre sensors for industrial applications," *Optics & Laser Technology*, vol. 78, pp. 62–66, Apr. 2016, ISSN: 00303992. DOI: [10.1016/j.optlastec.2015.09.004](https://doi.org/10.1016/j.optlastec.2015.09.004).
- [33] V. Mishra, N. Singh, U. Tiwari, and P. Kapur, "Fiber grating sensors in medicine: Current and emerging applications," *Sensors and Actuators A: Physical*, vol. 167, no. 2, pp. 279–290, Jun. 2011, ISSN: 09244247. DOI: [10.1016/j.sna.2011.02.045](https://doi.org/10.1016/j.sna.2011.02.045).
- [34] A. Theodosiou, M. Komodromos, and K. Kalli, "Carbon Cantilever Beam Health Inspection Using a Polymer Fiber Bragg Grating Array," *Journal of Lightwave Technology*, vol. 36, no. 4, pp. 986–992, Feb. 2018, ISSN: 0733-8724. DOI: [10.1109/JLT.2017.2768414](https://doi.org/10.1109/JLT.2017.2768414).
- [35] Y. Guo, X. Hu, B. Hu, J. Cheng, M. Zhou, and R. Y. K. Kwok, "Mobile Cyber Physical Systems: Current Challenges and Future Networking Applications," *IEEE Access*, vol. 6, pp. 12 360–12 368, 2018, ISSN: 2169-3536. DOI: [10.1109/ACCESS.2017.2782881](https://doi.org/10.1109/ACCESS.2017.2782881).
- [36] N. Zhong, M. Zhao, L. Zhong, *et al.*, "A high-sensitivity fiber-optic evanescent wave sensor with a three-layer structure composed of Canada balsam doped with GeO₂," *Biosensors and Bioelectronics*, vol. 85, pp. 876–882, Nov. 2016, ISSN: 09565663. DOI: [10.1016/j.bios.2016.06.002](https://doi.org/10.1016/j.bios.2016.06.002).
- [37] X. Cheng, J. Bonafacino, B. O. Guan, and H. Y. Tam, "All-polymer fiber-optic pH sensor," *Optics Express*, vol. 26, no. 11, p. 14 610, May 2018, ISSN: 1094-4087. DOI: [10.1364/OE.26.014610](https://doi.org/10.1364/OE.26.014610).
- [38] A. G. Leal-Junior, A. Frizera, and M. J. Pontes, "Dynamic Compensation Technique for POF Curvature Sensors," *Journal of Lightwave Technology*, vol. 36, no. 4, pp. 1112–1117, Feb. 2018, ISSN: 0733-8724. DOI: [10.1109/JLT.2017.2752361](https://doi.org/10.1109/JLT.2017.2752361).

- [39] N. Zhong, Q. Liao, X. Zhu, M. Zhao, Y. Huang, and R. Chen, "Temperature-independent polymer optical fiber evanescent wave sensor," *Scientific Reports*, vol. 5, no. 1, p. 11 508, Sep. 2015, ISSN: 2045-2322. DOI: [10.1038/srep11508](https://doi.org/10.1038/srep11508).
- [40] A. Leal-Junior, A. Theodosiou, A. Frizera-Neto, *et al.*, "Characterization of a new polymer optical fiber with enhanced sensing capabilities using a Bragg grating," *Optics Letters*, vol. 43, no. 19, p. 4799, 2018, ISSN: 0146-9592. DOI: [10.1364/ol.43.004799](https://doi.org/10.1364/ol.43.004799).
- [41] G. Rajan, Y. Mohd, B. Liu, E. Ambikairaja, D. J. Webb, and G.-d. Peng, "Sensors and Actuators A : Physical A fast response intrinsic humidity sensor based on an etched singlemode polymer fiber Bragg grating," *Sensors & Actuators: A. Physical*, vol. 203, pp. 107–111, 2013, ISSN: 0924-4247. DOI: [10.1016/j.sna.2013.08.036](https://doi.org/10.1016/j.sna.2013.08.036).
- [42] A. Stefani, S. Andresen, W. Yuan, N. Herholdt-Rasmussen, and O. Bang, "High Sensitivity Polymer Optical Fiber-Bragg-Grating-Based Accelerometer," *IEEE Photonics Technology Letters*, vol. 24, no. 9, pp. 763–765, May 2012, ISSN: 1041-1135. DOI: [10.1109/LPT.2012.2188024](https://doi.org/10.1109/LPT.2012.2188024).
- [43] D. Vilarinho, A. Theodosiou, C. Leitão, *et al.*, "POFBG-Embedded Cork Insole for Plantar Pressure Monitoring," *Sensors*, vol. 17, no. 12, p. 2924, Dec. 2017, ISSN: 1424-8220. DOI: [10.3390/s17122924](https://doi.org/10.3390/s17122924).
- [44] Z. Chen, D. Lau, J. T. Teo, S. H. Ng, X. Yang, and P. L. Kei, "Simultaneous measurement of breathing rate and heart rate using a microbend multimode fiber optic sensor," *Journal of Biomedical Optics*, vol. 19, no. 5, p. 057 001, May 2014, ISSN: 1083-3668. DOI: [10.1117/1.JBO.19.5.057001](https://doi.org/10.1117/1.JBO.19.5.057001).
- [45] M. Krehel, M. Wolf, L. F. Boesel, R. M. Rossi, G.-l. Bona, and L. J. Scherer, "Development of a luminous textile for reflective pulse oximetry measurements," *Biomedical Optics Express*, vol. 5, no. 8, p. 2537, Aug. 2014, ISSN: 2156-7085. DOI: [10.1364/BOE.5.002537](https://doi.org/10.1364/BOE.5.002537).
- [46] M. Krehel, M. Schmid, R. Rossi, L. Boesel, G.-l. Bona, and L. Scherer, "An Optical Fibre-Based Sensor for Respiratory Monitoring," *Sensors*, vol. 14, no. 7, pp. 13 088–13 101, Jul. 2014, ISSN: 1424-8220. DOI: [10.3390/s140713088](https://doi.org/10.3390/s140713088).
- [47] D. Graham-Rowe, "Photonic fabrics take shape," *Nature Photonics*, vol. 1, no. 1, pp. 6–7, 2007, ISSN: 17494885. DOI: [10.1038/nphoton.2006.35](https://doi.org/10.1038/nphoton.2006.35).
- [48] H. Li, H. Yang, E. Li, Z. Liu, and K. Wei, "Wearable sensors in intelligent clothing for measuring human body temperature based on optical fiber Bragg grating," *Optics Express*, vol. 20, no. 11, p. 11 740, May 2012, ISSN: 1094-4087. DOI: [10.1364/OE.20.011740](https://doi.org/10.1364/OE.20.011740).
- [49] M. Ciocchetti, C. Massaroni, P. Saccomandi, *et al.*, "Smart Textile Based on Fiber Bragg Grating Sensors for Respiratory Monitoring: Design and Preliminary Trials," *Biosensors*, vol. 5, no. 3, pp. 602–615, Sep. 2015, ISSN: 2079-6374. DOI: [10.3390/bios5030602](https://doi.org/10.3390/bios5030602).
- [50] B. M. Quandt, L. J. Scherer, L. F. Boesel, M. Wolf, G.-l. Bona, and R. M. Rossi, "Body-Monitoring and Health Supervision by Means of Optical Fiber-Based Sensing Systems in Medical Textiles," *Advanced Healthcare Materials*, vol. 4, no. 3, pp. 330–355, Feb. 2015, ISSN: 21922640. DOI: [10.1002/adhm.201400463](https://doi.org/10.1002/adhm.201400463).
- [51] T. Islam, S. C. Mukhopadhyay, and N. K. Suryadevara, "Smart Sensors and Internet of Things: A Postgraduate Paper," *IEEE Sensors Journal*, vol. 17, no. 3, pp. 577–584, Feb. 2017, ISSN: 1530-437X. DOI: [10.1109/JSEN.2016.2630124](https://doi.org/10.1109/JSEN.2016.2630124).

- [52] M. F. Domingues, N. Alberto, C. S. J. Leitao, *et al.*, "Insole Optical Fiber Sensor Architecture for Remote Gait Analysis—An e-Health Solution," *IEEE Internet of Things Journal*, vol. 6, no. 1, pp. 207–214, Feb. 2019, ISSN: 2327-4662. DOI: [10.1109/JIOT.2017.2723263](https://doi.org/10.1109/JIOT.2017.2723263).
- [53] D. Li, "5G and intelligence medicine—how the next generation of wireless technology will reconstruct healthcare?" *Precision Clinical Medicine*, vol. 2, no. 4, pp. 205–208, Dec. 2019, ISSN: 2096-5303. DOI: [10.1093/pcmedi/pbz020](https://doi.org/10.1093/pcmedi/pbz020).
- [54] L. Na and J. E. Streim, "Psychosocial Well-Being Associated With Activity of Daily Living Stages Among Community-Dwelling Older Adults," *Gerontology and Geriatric Medicine*, vol. 3, p. 233 372 141 770 001, Jan. 2017, ISSN: 2333-7214. DOI: [10.1177/2333721417700011](https://doi.org/10.1177/2333721417700011).
- [55] J. G. Webster and H. Eren, *Measurement, Instrumentation and Sensors Handbook*, 2ed. 2014, ISBN: 9781439848890.
- [56] G. Rajan, *Optical fiber sensors: Advanced Techniques & Applications*, 1. 2015, p. 575, ISBN: 978-1-4822-2829-8.
- [57] L. Bilro, N. Alberto, J. L. Pinto, and R. Nogueira, "Optical Sensors Based on Plastic Fibers," *Sensors*, vol. 12, no. 9, pp. 12 184–12 207, Sep. 2012, ISSN: 1424-8220. DOI: [10.3390/s120912184](https://doi.org/10.3390/s120912184).
- [58] O. Ziemann, J. Krauser, P. E. Zamzow, and W. Daum, *POF Handbook*. Springer US, 2008, ISBN: 978-3-540-76628-5. DOI: [10.1007/978-3-540-76629-2](https://doi.org/10.1007/978-3-540-76629-2).
- [59] J. Zubia and J. Arrue, "Plastic Optical Fibers: An Introduction to Their Technological Processes and Applications," *Optical Fiber Technology*, vol. 7, no. 2, pp. 101–140, Apr. 2001, ISSN: 10685200. DOI: [10.1006/ofte.2000.0355](https://doi.org/10.1006/ofte.2000.0355).
- [60] A. Leal-Junior and A. Frizzera-Neto, *Optical Fiber Sensors for the Next Generation of Rehabilitation Robotics*. Elsevier, 2022, p. 305, ISBN: 9780323859523.
- [61] C. Broadway, R. Min, A. G. Leal-Junior, C. Marques, and C. Caucheteur, "Toward Commercial Polymer Fiber Bragg Grating Sensors: Review and Applications," *Journal of Lightwave Technology*, vol. 37, no. 11, pp. 2605–2615, Jun. 2019, ISSN: 0733-8724. DOI: [10.1109/JLT.2018.2885957](https://doi.org/10.1109/JLT.2018.2885957).
- [62] A. Leal-Junior, L. Avellar, A. Frizzera, and C. Marques, "Smart textiles for multimodal wearable sensing using highly stretchable multiplexed optical fiber system," *Scientific Reports*, vol. 10, no. 1, p. 13 867, Dec. 2020, ISSN: 2045-2322. DOI: [10.1038/s41598-020-70880-8](https://doi.org/10.1038/s41598-020-70880-8).
- [63] W. Yuan, L. Khan, D. J. Webb, *et al.*, "Humidity insensitive TOPAS polymer fiber Bragg grating sensor," *Optics Express*, vol. 19, no. 20, p. 19 731, Sep. 2011, ISSN: 1094-4087. DOI: [10.1364/OE.19.019731](https://doi.org/10.1364/OE.19.019731).
- [64] W. Blanc and B. Dussardier, "Formation and applications of nanoparticles in silica optical fibers," *Journal of Optics (India)*, vol. 45, no. 3, pp. 247–254, 2016, ISSN: 09746900. DOI: [10.1007/s12596-015-0281-6](https://doi.org/10.1007/s12596-015-0281-6).
- [65] A. Veber, Z. Lu, M. Vermillac, F. Pigeonneau, W. Blanc, and L. Petit, "Nanostructured optical fibers made of glass-ceramics, and phase separated and metallic particle-containing glasses," *Fibers*, vol. 7, no. 12, 2019, ISSN: 20796439. DOI: [10.3390/f7120105](https://doi.org/10.3390/f7120105).
- [66] W. Blanc, V. Mauroy, L. Nguyen, *et al.*, "Fabrication of rare earth-doped transparent glass ceramic optical fibers by modified chemical vapor deposition," *Journal of the American Ceramic Society*, vol. 94, no. 8, pp. 2315–2318, 2011, ISSN: 00027820. DOI: [10.1111/j.1551-2916.2011.04672.x](https://doi.org/10.1111/j.1551-2916.2011.04672.x).

- [67] M. Vermillac, H. Fneich, J. F. Lupi, *et al.*, "Use of thulium-doped LaF₃ nanoparticles to lower the phonon energy of the thulium's environment in silica-based optical fibres," *Optical Materials*, vol. 68, pp. 24–28, 2017, ISSN: 09253467. DOI: [10.1016/j.optmat.2016.11.042](https://doi.org/10.1016/j.optmat.2016.11.042).
- [68] A. Beisenova, A. Issatayeva, S. Korganbayev, C. Molardi, W. Blanc, and D. Tosi, "Simultaneous Distributed Sensing on Multiple MgO-Doped High Scattering Fibers by Means of Scattering-Level Multiplexing," *Journal of Lightwave Technology*, vol. 37, no. 13, pp. 3413–3421, 2019, ISSN: 15582213. DOI: [10.1109/JLT.2019.2916991](https://doi.org/10.1109/JLT.2019.2916991).
- [69] A. Beisenova, A. Issatayeva, I. Iordachita, W. Blanc, C. Molardi, and D. Tosi, "Distributed fiber optics 3D shape sensing by means of high scattering NP-doped fibers simultaneous spatial multiplexing," *Optics Express*, vol. 27, no. 16, p. 22 074, Aug. 2019, ISSN: 1094-4087. DOI: [10.1364/OE.27.022074](https://doi.org/10.1364/OE.27.022074).
- [70] Z. Ashikbayeva, A. Aitkulov, M. Jelbuldina, *et al.*, "Distributed 2D temperature sensing during nanoparticles assisted laser ablation by means of high-scattering fiber sensors," *Scientific Reports*, vol. 10, no. 1, p. 12 593, Dec. 2020, ISSN: 2045-2322. DOI: [10.1038/s41598-020-69384-2](https://doi.org/10.1038/s41598-020-69384-2).
- [71] M. Sypabekova, S. Korganbayev, W. Blanc, *et al.*, "Fiber optic refractive index sensors through spectral detection of Rayleigh backscattering in a chemically etched MgO-based nanoparticle-doped fiber," *Optics Letters*, vol. 43, no. 24, p. 5945, 2018, ISSN: 0146-9592. DOI: [10.1364/ol.43.005945](https://doi.org/10.1364/ol.43.005945).
- [72] M. Cen, V. Moeyaert, P. Mégret, and M. Wuilpart, "Localization and quantification of reflective events along an optical fiber using a bi-directional TRA technique," *Optics Express*, vol. 22, no. 8, p. 9839, Apr. 2014, ISSN: 1094-4087. DOI: [10.1364/OE.22.009839](https://doi.org/10.1364/OE.22.009839).
- [73] M. Silveira, A. Frizera, A. Leal-Junior, *et al.*, "Transmission–Reflection Analysis in high scattering optical fibers: A comparison with single-mode optical fiber," *Optical Fiber Technology*, vol. 58, no. July, p. 102 303, Sep. 2020, ISSN: 10685200. DOI: [10.1016/j.yofte.2020.102303](https://doi.org/10.1016/j.yofte.2020.102303).
- [74] W. Blanc, I. Martin, H. Francois-Saint-Cyr, *et al.*, "Compositional Changes at the Early Stages of Nanoparticles Growth in Glasses," *The Journal of Physical Chemistry C*, vol. 123, no. 47, pp. 29 008–29 014, Nov. 2019, ISSN: 1932-7447. DOI: [10.1021/acs.jpcc.9b08577](https://doi.org/10.1021/acs.jpcc.9b08577).
- [75] M. Vermillac, J.-F. Lupi, F. Peters, *et al.*, "Fiber-draw-induced elongation and break-up of particles inside the core of a silica-based optical fiber," *Journal of the American Ceramic Society*, vol. 100, no. 5, pp. 1814–1819, May 2017, ISSN: 00027820. DOI: [10.1111/jace.14774](https://doi.org/10.1111/jace.14774).
- [76] D. Tosi, C. Molardi, W. Blanc, T. Paixão, P. Antunes, and C. Marques, "Performance Analysis of Scattering-Level Multiplexing (SLMux) in Distributed Fiber-Optic Backscatter Reflectometry Physical Sensors," *Sensors*, vol. 20, no. 9, p. 2595, May 2020, ISSN: 1424-8220. DOI: [10.3390/s20092595](https://doi.org/10.3390/s20092595).
- [77] D. Tosi, C. Molardi, and W. Blanc, "Rayleigh scattering characterization of a low-loss MgO-based nanoparticle-doped optical fiber for distributed sensing," *Optics & Laser Technology*, vol. 133, no. April 2020, p. 106 523, Jan. 2021, ISSN: 00303992. DOI: [10.1016/j.optlastec.2020.106523](https://doi.org/10.1016/j.optlastec.2020.106523).

- [78] L. Renqiang, F. Zhuang, Z. Yanzheng, C. Qixin, and W. Shuguo, "Operation Principle of a Bend Enhanced Curvature Optical Fiber Sensor," in *2006 IEEE/RSJ International Conference on Intelligent Robots and Systems*, IEEE, Oct. 2006, pp. 1966–1971, ISBN: 1-4244-0258-1. DOI: [10.1109/IR0S.2006.282403](https://doi.org/10.1109/IR0S.2006.282403).
- [79] A. G. Leal-Junior, C. R. Díaz, C. Marques, M. J. Pontes, and A. Frizera, "Multiplexing technique for quasi-distributed sensors arrays in polymer optical fiber intensity variation-based sensors," *Optics & Laser Technology*, vol. 111, no. August 2018, pp. 81–88, Apr. 2019, ISSN: 00303992. DOI: [10.1016/j.optlastec.2018.09.044](https://doi.org/10.1016/j.optlastec.2018.09.044).
- [80] Y. Fu, H. Di, and R. Liu, "Light intensity modulation fiber-optic sensor for curvature measurement," *Optics & Laser Technology*, vol. 42, no. 4, pp. 594–599, Jun. 2010. DOI: [10.1016/j.optlastec.2009.10.009](https://doi.org/10.1016/j.optlastec.2009.10.009).
- [81] K. Hill and G. Meltz, "Fiber Bragg grating technology fundamentals and overview," *Journal of Lightwave Technology*, vol. 15, no. 8, pp. 1263–1276, 1997, ISSN: 07338724. DOI: [10.1109/50.618320](https://doi.org/10.1109/50.618320). arXiv: [arXiv:1011.1669v3](https://arxiv.org/abs/1011.1669v3).
- [82] D. Sáez-Rodríguez, K. Nielsen, O. Bang, and D. J. Webb, "Photosensitivity mechanism of undoped poly(methyl methacrylate) under UV radiation at 325 nm and its spatial resolution limit," *Optics Letters*, vol. 39, no. 12, p. 3421, Jun. 2014, ISSN: 0146-9592. DOI: [10.1364/OL.39.003421](https://doi.org/10.1364/OL.39.003421).
- [83] A. Pospori, C. A. F. Marques, O. Bang, D. J. Webb, and P. André, "Polymer optical fiber Bragg grating inscription with a single UV laser pulse," *Optics Express*, vol. 25, no. 8, p. 9028, Apr. 2017, ISSN: 1094-4087. DOI: [10.1364/OE.25.009028](https://doi.org/10.1364/OE.25.009028).
- [84] Z. Ding, C. Wang, K. Liu, *et al.*, "Distributed Optical Fiber Sensors Based on Optical Frequency Domain Reflectometry: A review," *Sensors*, vol. 18, no. 4, p. 1072, Apr. 2018, ISSN: 1424-8220. DOI: [10.3390/s18041072](https://doi.org/10.3390/s18041072).
- [85] P. Shrestha, J. H. Kim, Y. Park, and C. G. Kim, "Impact localization on composite structure using FBG sensors and novel impact localization technique based on error outliers," *Composite Structures*, vol. 142, pp. 263–271, 2016, ISSN: 02638223. DOI: [10.1016/j.compstruct.2016.01.088](https://doi.org/10.1016/j.compstruct.2016.01.088).
- [86] V. V. Spirin, "Transmission-reflection analysis for localization of temporally successive multipoint perturbations in a distributed fiber-optic loss sensor based on Rayleigh backscattering," *Applied Optics*, vol. 42, no. 7, p. 1175, Mar. 2003, ISSN: 0003-6935. DOI: [10.1364/AO.42.001175](https://doi.org/10.1364/AO.42.001175).
- [87] V. V. Spirin, F. J. Mendieta, S. V. Miridonov, M. G. Shlyagin, A. A. Chtcherbakov, and P. L. Swart, "Localization of a Loss-Inducing Perturbation With Variable Accuracy Along a Test Fiber Using Transmission-Reflection Analysis," *IEEE Photonics Technology Letters*, vol. 16, no. 2, pp. 569–571, 2004, ISSN: 10411135. DOI: [10.1109/LPT.2003.821048](https://doi.org/10.1109/LPT.2003.821048).
- [88] R. M. López, V. V. Spirin, S. V. Miridonov, M. G. Shlyagin, G. Beltrán, and E. A. Kuzin, "Fiber optic distributed sensor for hydrocarbon leak localization based on transmission/reflection measurement," *Optics and Laser Technology*, vol. 34, no. 6, pp. 465–469, 2002, ISSN: 00303992. DOI: [10.1016/S0030-3992\(02\)00043-9](https://doi.org/10.1016/S0030-3992(02)00043-9).

- [89] V. V. Spirin, M. G. Shlyagin, S. V. Miridonov, and P. L. Swart, "Alarm-condition detection and localization using Rayleigh scattering for a fiber-optic bending sensor with an unmodulated light source," *Optics Communications*, vol. 205, no. 1-3, pp. 37–41, 2002, ISSN: 00304018. DOI: [10.1016/S0030-4018\(02\)01310-X](https://doi.org/10.1016/S0030-4018(02)01310-X).
- [90] A. G. Leal Junior, A. Frizera, and M. J. Pontes, "Analytical model for a polymer optical fiber under dynamic bending," *Optics & Laser Technology*, vol. 93, pp. 92–98, Aug. 2017, ISSN: 00303992. DOI: [10.1016/j.optlastec.2017.02.009](https://doi.org/10.1016/j.optlastec.2017.02.009).
- [91] A. G. Leal-Junior, C. A. Diaz, L. M. Avellar, M. J. Pontes, C. Marques, and A. Frizera, "Polymer optical fiber sensors in healthcare applications: A comprehensive review," *Sensors (Switzerland)*, vol. 19, no. 14, pp. 1–30, 2019, ISSN: 14248220. DOI: [10.3390/s19143156](https://doi.org/10.3390/s19143156).
- [92] D. A. Winter, *Biomechanics and Motor Control of Human Movement*. Hoboken, NJ, USA: John Wiley & Sons, Inc., Sep. 2009, p. 386, ISBN: 9780470549148. DOI: [10.1002/9780470549148](https://doi.org/10.1002/9780470549148).
- [93] J. Taborri, E. Palermo, S. Rossi, and P. Cappa, "Gait partitioning methods: A systematic review," *Sensors*, vol. 16, no. 1, pp. 40–42, 2016, ISSN: 14248220. DOI: [10.3390/s16010066](https://doi.org/10.3390/s16010066).
- [94] M. Whittle, *Gait analysis: an introduction*, 4th ed., M. Whittle, Ed. Oxford: Butterworth-Heinemann, 2007, p. 255, ISBN: 0750688831.
- [95] C. Vaughan, B. Davis, and J. O'Connor, *Dynamics of human gait*. 1999, ISBN: 0620235586.
- [96] A. Muro-de-la-Herran, B. Garcia-Zapirain, and A. Mendez-Zorrilla, "Gait Analysis Methods: An Overview of Wearable and Non-Wearable Systems, Highlighting Clinical Applications," *Sensors*, vol. 14, no. 2, pp. 3362–3394, Feb. 2014, ISSN: 1424-8220. DOI: [10.3390/s140203362](https://doi.org/10.3390/s140203362).
- [97] D. Winter, "Human balance and posture control during standing and walking," *Gait & Posture*, vol. 3, no. 4, pp. 193–214, Dec. 1995, ISSN: 09666362. DOI: [10.1016/0966-6362\(96\)82849-9](https://doi.org/10.1016/0966-6362(96)82849-9).
- [98] V. Lugade, V. Lin, and L.-s. Chou, "Center of mass and base of support interaction during gait," *Gait & Posture*, vol. 33, no. 3, pp. 406–411, Mar. 2011, ISSN: 09666362. DOI: [10.1016/j.gaitpost.2010.12.013](https://doi.org/10.1016/j.gaitpost.2010.12.013).
- [99] L. Guo and S. Xiong, "Accuracy of Base of Support Using an Inertial Sensor Based Motion Capture System," *Sensors*, vol. 17, no. 9, p. 2091, Sep. 2017, ISSN: 1424-8220. DOI: [10.3390/s17092091](https://doi.org/10.3390/s17092091).
- [100] F. Madehkhaksar, J. Klenk, K. Sczuka, K. Gordt, I. Melzer, and M. Schwenk, "The effects of unexpected mechanical perturbations during treadmill walking on spatiotemporal gait parameters, and the dynamic stability measures by which to quantify postural response," *PLOS ONE*, vol. 13, no. 4, J. M. Haddad, Ed., e0195902, Apr. 2018, ISSN: 1932-6203. DOI: [10.1371/journal.pone.0195902](https://doi.org/10.1371/journal.pone.0195902).
- [101] J. Mueller, T. Engel, S. Mueller, S. Kopinski, H. Baur, and F. Mayer, "Neuromuscular response of the trunk to sudden gait disturbances: Forward vs. backward perturbation," *Journal of Electromyography and Kinesiology*, vol. 30, pp. 168–176, Oct. 2016, ISSN: 10506411. DOI: [10.1016/j.jelekin.2016.07.005](https://doi.org/10.1016/j.jelekin.2016.07.005).

- [102] C. Walsh, "Human-in-the-loop development of soft wearable robots," *Nature Reviews Materials*, vol. 3, no. 6, pp. 78–80, Jun. 2018, ISSN: 2058-8437. DOI: [10.1038/s41578-018-0011-1](https://doi.org/10.1038/s41578-018-0011-1).
- [103] V. Monaco, P. Tropea, F. Aprigliano, *et al.*, "An ecologically-controlled exoskeleton can improve balance recovery after slippage," *Scientific Reports*, vol. 7, no. 1, p. 46721, Sep. 2017, ISSN: 2045-2322. DOI: [10.1038/srep46721](https://doi.org/10.1038/srep46721).
- [104] M. Cianchetti, C. Laschi, A. Menciassi, and P. Dario, "Biomedical applications of soft robotics," *Nature Reviews Materials*, vol. 3, no. 6, pp. 143–153, Jun. 2018, ISSN: 2058-8437. DOI: [10.1038/s41578-018-0022-y](https://doi.org/10.1038/s41578-018-0022-y).
- [105] Y. Long, Z. Du, L. Cong, W. Wang, Z. Zhang, and W. Dong, "Active disturbance rejection control based human gait tracking for lower extremity rehabilitation exoskeleton," *ISA Transactions*, vol. 67, pp. 389–397, Mar. 2017, ISSN: 00190578. DOI: [10.1016/j.isatra.2017.01.006](https://doi.org/10.1016/j.isatra.2017.01.006).
- [106] L. Capineri, "Resistive Sensors with Smart Textiles for Wearable Technology: From Fabrication Processes to Integration with Electronics," *Procedia Engineering*, vol. 87, no. September, pp. 724–727, 2014, ISSN: 18777058. DOI: [10.1016/j.proeng.2014.11.748](https://doi.org/10.1016/j.proeng.2014.11.748).
- [107] C. Gonçalves, A. F. da Silva, J. Gomes, and R. Simoes, "Wearable e-textile technologies: A review on sensors, actuators and control elements," *Inventions*, vol. 3, no. 1, pp. 1–13, 2018, ISSN: 24115134. DOI: [10.3390/inventions3010014](https://doi.org/10.3390/inventions3010014).
- [108] A. G. Leal-Junior, A. Frizzera-Neto, M. J. Pontes, and T. R. Botelho, "Hysteresis compensation technique applied to polymer optical fiber curvature sensor for lower limb exoskeletons," *Measurement Science and Technology*, vol. 28, no. 12, p. 125103, Dec. 2017, ISSN: 0957-0233. DOI: [10.1088/1361-6501/aa946f](https://doi.org/10.1088/1361-6501/aa946f).
- [109] P. Roriz, O. Frazão, A. B. Lobo-Ribeiro, J. L. Santos, and J. A. Simões, "Review of fiber-optic pressure sensors for biomedical and biomechanical applications," *Journal of Biomedical Optics*, vol. 18, no. 5, p. 050903, May 2013, ISSN: 1083-3668. DOI: [10.1117/1.JBO.18.5.050903](https://doi.org/10.1117/1.JBO.18.5.050903).
- [110] J. Chanchaichujit, A. Tan, F. Meng, and S. Eaimkhong, *Optimization, Simulation and Predictive Analytics in Healthcare*. 2019, pp. 95–121, ISBN: 9789811381133. DOI: [10.1007/978-981-13-8114-0_5](https://doi.org/10.1007/978-981-13-8114-0_5).
- [111] J. D. Rudie, A. M. Rauschecker, R. N. Bryan, C. Davatzikos, and S. Mohan, "Emerging Applications of Artificial Intelligence in Neuro-Oncology," *Radiology*, vol. 290, no. 3, pp. 607–618, 2019, ISSN: 15271315. DOI: [10.1148/radiol.2018181928](https://doi.org/10.1148/radiol.2018181928).
- [112] S. Zhang, X. Li, M. Zong, X. Zhu, and R. Wang, "Efficient kNN Classification With Different Numbers of Nearest Neighbors," *IEEE Transactions on Neural Networks and Learning Systems*, vol. 29, no. 5, pp. 1774–1785, May 2018, ISSN: 2162-237X. DOI: [10.1109/TNNLS.2017.2673241](https://doi.org/10.1109/TNNLS.2017.2673241).
- [113] Y. LeCun, Y. Bengio, and G. Hinton, "Deep learning," *Nature*, vol. 521, no. 7553, pp. 436–444, May 2015, ISSN: 0028-0836. DOI: [10.1038/nature14539](https://doi.org/10.1038/nature14539).
- [114] N. Syam and A. Sharma, "Waiting for a sales renaissance in the fourth industrial revolution: Machine learning and artificial intelligence in sales research and practice," *Industrial Marketing Management*, vol. 69, no. January, pp. 135–146, 2018, ISSN: 00198501. DOI: [10.1016/j.indmarman.2017.12.019](https://doi.org/10.1016/j.indmarman.2017.12.019).

- [115] Y. Bengio, P. Simard, and P. Frasconi, "Learning long-term dependencies with gradient descent is difficult," *IEEE Transactions on Neural Networks*, vol. 5, no. 2, pp. 157–166, Mar. 1994, ISSN: 1045-9227. DOI: [10.1109/72.279181](https://doi.org/10.1109/72.279181).
- [116] Y. Ho and S. Wookey, "The Real-World-Weight Cross-Entropy Loss Function: Modeling the Costs of Mislabeling," *IEEE Access*, vol. 8, pp. 4806–4813, 2020, ISSN: 2169-3536. DOI: [10.1109/ACCESS.2019.2962617](https://doi.org/10.1109/ACCESS.2019.2962617).
- [117] L. Li, M. Doroslovacki, and M. H. Loew, "Approximating the Gradient of Cross-Entropy Loss Function," *IEEE Access*, vol. 8, pp. 111 626–111 635, 2020, ISSN: 2169-3536. DOI: [10.1109/ACCESS.2020.3001531](https://doi.org/10.1109/ACCESS.2020.3001531).
- [118] G. T. Reddy, M. P. K. Reddy, K. Lakshmana, *et al.*, "Analysis of Dimensionality Reduction Techniques on Big Data," *IEEE Access*, vol. 8, pp. 54 776–54 788, 2020, ISSN: 21693536. DOI: [10.1109/ACCESS.2020.2980942](https://doi.org/10.1109/ACCESS.2020.2980942).
- [119] S. Ayesha, M. K. Hanif, and R. Talib, *Overview and comparative study of dimensionality reduction techniques for high dimensional data*, 2020. DOI: [10.1016/j.inffus.2020.01.005](https://doi.org/10.1016/j.inffus.2020.01.005).
- [120] M. Ringnér, "What is principal component analysis?" *Nature Biotechnology*, vol. 26, no. 3, pp. 303–304, Mar. 2008, ISSN: 1087-0156. DOI: [10.1038/nbt0308-303](https://doi.org/10.1038/nbt0308-303).
- [121] I. Industrial Fiber Optics, *Plastic Fiber Optic Phototransistor IF-D92*, 2006.
- [122] A. G. Leal-Junior, A. Frizera, L. M. Avellar, and M. J. Pontes, "Design considerations, analysis, and application of a low-cost, fully portable, wearable polymer optical fiber curvature sensor," *Applied Optics*, vol. 57, no. 24, p. 6927, Aug. 2018, ISSN: 1559-128X. DOI: [10.1364/AO.57.006927](https://doi.org/10.1364/AO.57.006927).
- [123] A. Chinpon, K. Thamaphat, M. Hansuparnusorn, and P. Limsuwan, "A force measurement method using the optical fibre beam," *Procedia Engineering*, vol. 32, pp. 989–993, 2012, ISSN: 18777058. DOI: [10.1016/j.proeng.2012.02.043](https://doi.org/10.1016/j.proeng.2012.02.043).
- [124] J. Walton and S. Russell, "Physiotherapy assessment of shoulder stiffness and how it influences management," *Shoulder & Elbow*, vol. 7, no. 3, pp. 205–213, Jul. 2015, ISSN: 1758-5732. DOI: [10.1177/1758573215586152](https://doi.org/10.1177/1758573215586152).
- [125] E. Rocon, A. F. Ruiz, R. Raya, *et al.*, "Human–Robot Physical Interaction," in *Wearable Robots*, Chichester, UK: John Wiley & Sons, Ltd, 2008, pp. 127–163, ISBN: 9780470512944. DOI: [10.1002/9780470987667.ch5](https://doi.org/10.1002/9780470987667.ch5).
- [126] C. Yang, C. Zeng, P. Liang, Z. Li, R. Li, and C.-Y. Su, "Interface Design of a Physical Human–Robot Interaction System for Human Impedance Adaptive Skill Transfer," *IEEE Transactions on Automation Science and Engineering*, vol. 15, no. 1, pp. 329–340, Jan. 2018, ISSN: 1545-5955. DOI: [10.1109/TASE.2017.2743000](https://doi.org/10.1109/TASE.2017.2743000).
- [127] X. Roselló-Mechó, M. Delgado-Pinar, A. Díez, and M. V. Andrés, "Measurement of Pockels' coefficients and demonstration of the anisotropy of the elasto-optic effect in optical fibers under axial strain," *Optics Letters*, vol. 41, no. 13, p. 2934, Jul. 2016, ISSN: 0146-9592. DOI: [10.1364/OL.41.002934](https://doi.org/10.1364/OL.41.002934).
- [128] A. G. Leal-Junior, A. Theodosiou, C. R. Diaz, *et al.*, "Simultaneous Measurement of Axial Strain, Bending and Torsion With a Single Fiber Bragg Grating in CYTOP Fiber," *Journal of Lightwave Technology*, vol. 37, no. 3, pp. 971–980, Feb. 2019, ISSN: 0733-8724. DOI: [10.1109/JLT.2018.2884538](https://doi.org/10.1109/JLT.2018.2884538).

- [129] C. A. R. Diaz, A. G. Leal-Junior, P. S. B. Andre, *et al.*, "Liquid Level Measurement Based on FBG-Embedded Diaphragms With Temperature Compensation," *IEEE Sensors Journal*, vol. 18, no. 1, pp. 193–200, Jan. 2018, ISSN: 1530-437X. DOI: [10.1109/JSEN.2017.2768510](https://doi.org/10.1109/JSEN.2017.2768510).
- [130] A. G. Leal-Junior, C. A. Díaz, A. Frizera, C. Marques, M. R. Ribeiro, and M. J. Pontes, "Simultaneous measurement of pressure and temperature with a single FBG embedded in a polymer diaphragm," *Optics & Laser Technology*, vol. 112, no. September 2018, pp. 77–84, Apr. 2019, ISSN: 00303992. DOI: [10.1016/j.optlastec.2018.11.013](https://doi.org/10.1016/j.optlastec.2018.11.013).
- [131] Y. Luo, B. Yan, Q. Zhang, G.-D. Peng, J. Wen, and J. Zhang, "Fabrication of Polymer Optical Fibre (POF) Gratings," *Sensors*, vol. 17, no. 3, p. 511, Mar. 2017, ISSN: 1424-8220. DOI: [10.3390/s17030511](https://doi.org/10.3390/s17030511).
- [132] J.-F. Lupi, M. Vermillac, S. Trzesien, M. Ude, W. Blanc, and B. Dussardier, "Gradual-Time Solution Doping for the Fabrication of Longitudinally Varying Optical Fibres," *Journal of Lightwave Technology*, vol. 36, no. 10, pp. 1786–1791, May 2018, ISSN: 0733-8724. DOI: [10.1109/JLT.2017.2785862](https://doi.org/10.1109/JLT.2017.2785862).
- [133] R. López, V. Spirin, S. Miridonov, M. Shlyagin, G. Beltrán, and E. Kuzin, "Fiber optic distributed sensor for hydrocarbon leak localization based on transmission/reflection measurement," *Optics & Laser Technology*, vol. 34, no. 6, pp. 465–469, Sep. 2002, ISSN: 00303992. DOI: [10.1016/S0030-3992\(02\)00043-9](https://doi.org/10.1016/S0030-3992(02)00043-9).
- [134] V. Spirin, F. Mendieta, S. Miridonov, M. Shlyagin, A. Chtcherbakov, and P. Swart, "Localization of a Loss-Inducing Perturbation With Variable Accuracy Along a Test Fiber Using Transmission-Reflection Analysis," *IEEE Photonics Technology Letters*, vol. 16, no. 2, pp. 569–571, Feb. 2004, ISSN: 1041-1135. DOI: [10.1109/LPT.2003.821048](https://doi.org/10.1109/LPT.2003.821048).
- [135] P. L. Swart, "20-km-length distributed fiber optical loss sensor based on transmission-reflection analysis," *Optical Engineering*, vol. 44, no. 4, p. 040 501, Apr. 2005, ISSN: 0091-3286. DOI: [10.1117/1.1883585](https://doi.org/10.1117/1.1883585).
- [136] W. Blanc, V. Mauroy, and B. Dussardier, "Erbium-doped nanoparticles in silica-based optical fibres," *International Journal of Nanotechnology*, vol. 9, no. 3-7, pp. 480–487, 2012, ISSN: 14757435. DOI: [10.1504/IJNT.2012.045350](https://doi.org/10.1504/IJNT.2012.045350).
- [137] W. Yuan, A. Stefani, M. Bache, *et al.*, "Improved thermal and strain performance of annealed polymer optical fiber Bragg gratings," *Optics Communications*, vol. 284, no. 1, pp. 176–182, 2011, ISSN: 00304018. DOI: [10.1016/j.optcom.2010.08.069](https://doi.org/10.1016/j.optcom.2010.08.069).
- [138] R. Lakes, *Viscoelastic Materials*. Madison: Cambridge University Press, 2009, p. 461, ISBN: 9780521885683.
- [139] I.-L. Bundalo, K. Nielsen, G. Woyessa, and O. Bang, "Long-term strain response of polymer optical fiber FBG sensors," *Optical Materials Express*, vol. 7, no. 3, p. 967, 2017, ISSN: 2159-3930. DOI: [10.1364/ome.7.000967](https://doi.org/10.1364/ome.7.000967).
- [140] A. Stefani, S. Andresen, W. Yuan, and O. Bang, "Dynamic characterization of polymer optical fibers," *IEEE Sensors Journal*, vol. 12, no. 10, pp. 3047–3053, 2012, ISSN: 1530437X. DOI: [10.1109/JSEN.2012.2208951](https://doi.org/10.1109/JSEN.2012.2208951).
- [141] A. Leal-Junior, A. Frizera, M. J. Pontes, *et al.*, "Dynamic mechanical characterization with respect to temperature, humidity, frequency and strain in mPOFs made of different materials," *Optical Materials Express*, vol. 8, no. 4, p. 804, Apr. 2018, ISSN: 2159-3930. DOI: [10.1364/OME.8.000804](https://doi.org/10.1364/OME.8.000804).

- [142] A. G. Leal-Junior, A. Frizera, C. Marques, and M. J. Pontes, "Viscoelastic features based compensation technique for polymer optical fiber curvature sensors," *Optics & Laser Technology*, vol. 105, pp. 35–40, Sep. 2018, ISSN: 00303992. DOI: [10.1016/j.optlastec.2018.02.035](https://doi.org/10.1016/j.optlastec.2018.02.035).
- [143] F. E. Grubbs, "Sample Criteria for Testing Outlying Observations," *The Annals of Mathematical Statistics*, vol. 21, no. 1, pp. 27–58, 1950, ISSN: 0003-4851. DOI: [10.1214/aoms/1177729885](https://doi.org/10.1214/aoms/1177729885).
- [144] L. M. Avellar, A. G. Leal-Junior, C. A. R. Diaz, C. Marques, and A. Frizera, "POF Smart Carpet: A Multiplexed Polymer Optical Fiber-Embedded Smart Carpet for Gait Analysis," *Sensors*, vol. 19, no. 15, p. 3356, Jul. 2019, ISSN: 1424-8220. DOI: [10.3390/s19153356](https://doi.org/10.3390/s19153356).
- [145] D. Bzdok, M. Krzywinski, and N. Altman, "Points of significance: Machine learning: Supervised methods," *Nature Methods*, vol. 15, no. 1, pp. 5–6, 2018, ISSN: 15487105. DOI: [10.1038/nmeth.4551](https://doi.org/10.1038/nmeth.4551).
- [146] I. F. Ilyas and X. Chu, *Data Cleaning*. ACM Books, 2019, p. 260, ISBN: 9781450371520.
- [147] R. C. Hibbeler, *Mechanics of Materials*, 7.ed, c. Pearson, 2008, p. 637, ISBN: 9788576053736.
- [148] J. M. Hausdorff, "Gait variability: methods, modeling and meaning," *Journal of NeuroEngineering and Rehabilitation*, vol. 2, no. 1, p. 19, Dec. 2005, ISSN: 1743-0003. DOI: [10.1186/1743-0003-2-19](https://doi.org/10.1186/1743-0003-2-19).
- [149] J. Perry, *Gait Analysis - Normal and Pathological Function*. 1992, pp. 1–19, ISBN: 9781556421921. DOI: [10.1017/CB09781107415324.004](https://doi.org/10.1017/CB09781107415324.004). arXiv: [arXiv:1011.1669v3](https://arxiv.org/abs/1011.1669v3).